



This work is protected by copyright and other intellectual property rights and duplication or sale of all or part is not permitted, except that material may be duplicated by you for research, private study, criticism/review or educational purposes. Electronic or print copies are for your own personal, non-commercial use and shall not be passed to any other individual. No quotation may be published without proper acknowledgement. For any other use, or to quote extensively from the work, permission must be obtained from the copyright holder/s.

Investigating the natural attenuation and fate of a
trichloroethene plume at the groundwater-surface water
interface of a UK lowland river

John James Weatherill

Thesis submitted for the degree of Doctor of Philosophy

December 2015

Keele University

Abstract

Legacy industrial contaminants, such as trichloroethene (TCE), that have been released to aquifers in the last century, now threaten the quality of groundwater baseflow to lowland rivers and streams. Before reaching these receptors, contaminant plumes must first transit the heterogeneous environment of the aquifer-river interface. This research investigates the fate and potential for in-situ natural attenuation at this interface where a poorly-defined TCE plume potentially threatens a ‘gaining’ lowland river in the UK. It was possible to reveal a well-defined discharge zone of the plume in the riverbed with limited dispersion occurring in the low-permeability floodplain deposits. Through electrical resistivity imaging and intrusive sampling, this alluvial aquitard was revealed to be laterally extensive along the river corridor. A dissolved TCE flux of 0.43–1.5 g d⁻¹ to the river was estimated, with most of this discharge occurring over a 40 m long reach, centred on a meander bend in the floodplain. The location and magnitude of this flux is influenced by continuity of stratified silt and peat deposits extending riverward from the floodplain, which provide significant retardation capacity. Metre-scale heterogeneity in the spatial variability of the groundwater discharge through these deposits was revealed with riverbed temperature mapping. A dominance of aerobic and nitrate-rich water throughout the aquifer-river system maintains a large stoichiometric demand for organic carbon and prevents the onset of reducing conditions required for significant dechlorination of the plume. However, at discrete shallow locations in the riverbed and parts of the alluvium, partial dechlorination of the plume was observed. A grid of pore water samplers revealed more enhanced dechlorination to *cis*-1,2-dichloroethene and vinyl chloride in methanogenic zones of the shallow sediment that was influenced by river macrophyte growth. Although in-situ natural attenuation does exceed the up-gradient aquifer in places, overall these processes are unlikely to prevent migration of the majority of the contaminant mass to the river. However, surface water impacts from this particular plume are unlikely with the large dilution available in the river itself.

Acknowledgements

I wish to express gratitude to Keele University and the Environment Agency who provided the funding to make this research possible. I would like to kindly thank my supervisors Dr Stefan Krause, Dr Nigel Cassidy and Dr Sami Ullah for their helpful guidance, support and enthusiasm throughout the project. I am very grateful to Dr Falko Drijfhout for his technical support in developing the GC-MS method and always being on hand to troubleshoot issues. I am also grateful to Mr Ian Wilshaw for solving frequent problems with the ion chromatograph and always dealing with my consumable orders on time. I thank Mr Kevin Voyce at the Environment Agency in Shrewsbury for allowing me access to the agency's boreholes, supplying data and providing helpful discussions. I thank Ms Amy Cowles and Dr Vladimir Zholobenko for their assistance with the ICP-OES analysis. I also thank the University of Birmingham for the use of their TOC analyser. I am very grateful to the land owners at Helshaw Grange and Heathbrook Farm for allowing me to install equipment on their property and permitting access to the River Tern at all times.

For taking the time out to come to the River Tern and help install infrastructure or collect data, grateful thanks go to Amir Levy, Liliana Rose, April Fitzgerald-Hudson, Liam Bullock, Kelly Ross, Henry Dick and Austin Haffenden. I thank undergraduate students Amy Ward, Helen Prosser, Tom Elbourne and Michael Grimes who collected data for their dissertations at the field site. I acknowledge the Keele Postgraduate Association for providing funding for conference attendance and analytical costs. I also acknowledge the contributions of Mr Andrew Pearson and Mr Ian Edwards at the Environment Agency.

Last but not least, I thank my family and friends for their on-going support and encouragement throughout the project.

Table of Contents

Chapter 1. Introduction	1
1.1 Research context	1
1.1.1 Introduction	1
1.1.2 TCE in groundwater	1
1.1.3 Contaminant properties of TCE	2
1.2 Research motivation	4
1.2.1 Pressures on rivers from CE contamination	4
1.2.2 Legislative drivers	6
1.2.3 Knowledge gaps and scientific rationale	7
1.3 Research scope	8
1.3.1 Aims and objectives	8
1.3.2 Thesis structure	9
Chapter 2. Natural attenuation of chlorinated ethenes at aquifer-river interfaces: a review	11
2.1 Chapter Introduction	11
2.2 The aquifer-river interface	12
2.2.1 Hydrological framework	12
2.2.2 Biogeochemical importance of the aquifer-river interface	13
2.3 Non-destructive natural attenuation processes	15
2.3.1 Advection and dispersion	15
2.3.2 Hydrophobic sorption	16
2.3.3 In-situ dilution	20
2.3.4 Volatilisation	22
2.4 Destructive natural attenuation processes	23
2.4.1 Reductive dechlorination	23
2.4.1.1 <i>Dehalorespiration</i>	23
2.4.1.2 <i>Carbon and electron donors for reductive dechlorination</i>	26
2.4.1.3 <i>Redox controls on reductive dechlorination</i>	28
2.4.2 Fate of lower-chlorinated ethenes	32
2.4.2.2 <i>Biological oxidation of cDCE</i>	32
2.4.2.2 <i>Biological oxidation of VC</i>	33
2.4.3 Cometabolic transformation of CEs	35
2.4.4 Abiotic dechlorination by natural reductants	36
2.5 Approaches to investigate CE plume fate at aquifer-river interfaces	39
2.5.1 Characterising groundwater discharge pathways	39
2.5.1.1 <i>Geophysical methods</i>	39
2.5.1.2 <i>Temperature as tracer</i>	40

2.5.2	Delineating plume discharge zones	41
2.5.2.1	<i>Passive sampling</i>	41
2.5.2.2	<i>Multi-level sampling</i>	42
2.5.3	Estimating plume fluxes to rivers	43
2.5.3.1	<i>Initial studies of discharging plumes</i>	44
2.5.3.2	<i>Temperature methods</i>	44
2.5.3.3	<i>Combined approaches</i>	45
2.5.4	Demonstrating in-situ transformation at field scale	47
2.5.4.1	<i>Parent-daughter relationships</i>	47
2.5.4.2	<i>Compound-specific isotope analysis</i>	48
2.5.4.3	<i>Novel molecular biomarkers</i>	50
2.5	Chapter summary	52
 Chapter 3. Study area, materials and methods		53
3.1	Chapter introduction	53
3.2	Study area characteristics	54
3.2.1	Physiography of the River Tern catchment	54
3.2.2	Hydrology	54
3.2.3	Geology of the River Tern Valley	56
3.2.3.1	<i>Solid geology</i>	56
3.2.3.2	<i>Unconsolidated geology and 'drift' deposits</i>	58
3.2.4	Hydrogeology	61
3.2.4.1	<i>Permo-Triassic sandstone</i>	61
3.2.4.2	<i>Aquifer-river interactions</i>	62
3.2.5	Groundwater quality issues in the study area	64
3.2.6	Existing monitoring networks	67
3.3	Groundwater investigation methods	71
3.3.1	Passive sampling	71
3.3.1.1	<i>HydraSleeves</i>	71
3.3.1.2	<i>Riverbed diffusion samplers</i>	71
3.3.2	Drive-point mini-piezometers	73
3.3.3	Single-screen monitoring wells and piezometers	76
3.3.3.1	<i>Alluvial monitoring wells</i>	76
3.3.3.2	<i>Riverbed piezometers and stage recorder</i>	79
3.3.4	Direct-push methods	82
3.3.4.1	<i>Porewater samplers</i>	82
3.3.4.2	<i>Temporary piezometer nests</i>	85
3.4	Physical characterisation methods	88
3.4.1	Sediment properties	88

3.4.1.1	<i>Coring</i>	88
3.4.1.2	<i>Fraction organic carbon</i>	89
3.4.1.3	<i>Porosity and bulk density</i>	90
3.4.2	Water level monitoring and hydraulic testing	91
3.4.2.1	<i>Water level measurements</i>	91
3.4.2.2	<i>Hydraulic conductivity determinations</i>	92
3.4.3	Electrical resistivity imaging	93
3.4.3.1	<i>Survey design and data acquisition</i>	94
3.4.3.2	<i>Data processing and inversion</i>	95
3.4.3	Riverbed temperature mapping	97
3.5	Sampling and chemical analysis	99
3.5.1	In-situ measurements	99
3.5.1.1	<i>Dissolved oxygen</i>	99
3.5.1.2	<i>pH and electrical conductivity</i>	99
3.5.2	Volatile organic compounds	100
3.5.2.1	<i>Chlorinated ethenes</i>	100
3.5.2.2	<i>Methane</i>	103
3.5.3	Anions	105
3.5.4	Iron and manganese	106
3.5.5	Dissolved organic carbon	107
3.6	Statistical analysis	108
3.6.1	Parametric tests	108
3.6.2	Non-parametric tests	109
Chapter 4	Plume discharge zone characterisation	110
4.1	Chapter introduction	110
4.2	Delineation of the plume discharge zone	110
4.2.1	Sampling of pre-existing monitoring networks	110
4.2.1.1	<i>Permo-Triassic sandstone boreholes</i>	110
4.2.1.2	<i>Floodplain boreholes and riverbed piezometer network</i>	112
4.2.2	Passive diffusion sampling campaign	113
4.2.3	Riverbed mini-piezometer investigation	116
4.2.3.1	<i>September 2011 snapshot</i>	116
4.2.3.2	<i>December 2011 snapshot</i>	118
4.2.3.3	<i>Daughter product detections in the riverbed</i>	121
4.3	Floodplain hydrogeological investigation	124
4.3.1	Characterisation of the alluvium deposits	124
4.3.1.1	<i>Geological observations from augering at Helshaw Grange</i>	124
4.3.1.2	<i>Geological observations from augering at Heathbrook Farm</i>	125
4.3.1.3	<i>Hydraulic conductivity and head distribution in the floodplain</i>	127

4.3.1.4	<i>Plume distribution in the alluvium</i>	130
4.3.2	Electrical resistivity imaging surveys	131
4.3.2.1	<i>64 m resistivity profiles</i>	131
4.3.2.2	<i>32 m resistivity profiles</i>	136
4.3.2.3	<i>LOCAR resistivity profiles in Heathbrook Farm</i>	138
4.3.3	Hydrogeological interpretation of ERI profiles	139
4.3.3.1	<i>Interpretation approach</i>	139
4.3.3.2	<i>ER2 interpretation</i>	141
4.3.3.3	<i>ER3 interpretation</i>	142
4.3.3.4	<i>ER4 interpretation</i>	144
4.3.3.5	<i>ER5 interpretation</i>	144
4.3.3.6	<i>ER6 interpretation</i>	145
4.3.3.7	<i>ER7 interpretation</i>	146
4.3.3.8	<i>Profiles without ground-truth information</i>	147
4.3	Discussion	154
4.4.1	Delineation of the plume discharge zone in the riverbed	154
4.4.2	Characteristics of the floodplain groundwater system	155
4.4.3	Insights from electrical resistivity imaging	159
4.4.4	Preliminary evidence of in-situ transformation of the plume	161
4.5	Chapter summary	163
Chapter 5.	Controls and drivers of contaminant discharge through the riverbed	164
5.1	Chapter introduction	164
5.2	Flow controls and properties	165
5.2.1	Physical properties of the riverbed	165
5.2.1.1	<i>Surficial sediment mapping</i>	165
5.2.1.2	<i>Shallow riverbed stratigraphy</i>	166
5.2.1.3	<i>Organic carbon content of the riverbed deposits</i>	168
5.2.1.4	<i>Retardation potential of the riverbed</i>	170
5.2.2	Discrete observations of groundwater flow	173
5.2.2.1	<i>Hydraulic conductivity variation</i>	173
5.2.2.2	<i>Vertical hydraulic gradient observations</i>	176
5.2.2.3	<i>Spatial variability of hydraulic conductivity and pressure gradients</i>	179
5.2.3	Continuous monitoring of riverbed pressure gradients	181
5.2.3.1	<i>Temporal variability of hydraulic heads and river stage</i>	181
5.2.3.2	<i>Temporal variability of the VHG in the riverbed</i>	186
5.3	Groundwater and contaminant fluxes through the riverbed	188
5.3.1	Groundwater flux based on Darcian flow	188
5.3.1.1	<i>Darcy flux approach</i>	188
5.3.1.2	<i>Potential groundwater fluxes</i>	190

5.3.2	Groundwater flux based on temperature profiling	192
5.3.2.1	<i>Depth-distribution of temperature</i>	192
5.3.2.2	<i>Spatial patterns of pore water temperature</i>	193
5.3.2.3	<i>Calculated groundwater flux</i>	197
5.3.3	Contaminant flux assessment	201
5.3.3.1	<i>TCE concentrations in the riverbed</i>	202
5.3.3.2	<i>Potential TCE flux based on Darcian flow</i>	203
5.3.3.3	<i>Theoretical dilution within the surface water column</i>	205
5.3.3.4	<i>Potential TCE flux based on temperature mapping</i>	205
5.3.3.5	<i>Comparison of fluxes</i>	207
5.3.3.6	<i>Influence of the sediment matrix contaminant transport</i>	210
5.4	Discussion	212
5.4.1	Flow regime of the riverbed	212
5.4.2	Spatial variability and controls on groundwater fluxes	214
5.4.3	Plume flux assessment	217
5.4.4	Plume transport through the riverbed	220
5.5	Chapter summary	222
 Chapter 6. Redox conditions and controls on in-situ transformation		223
6.1	Chapter introduction	223
6.2	Chlorinated ethene observations	226
6.2.1	River flow conditions during sampling campaigns	226
6.2.2	Variation in groundwater chlorinated ethene concentrations	228
6.2.2.1	<i>Permo-Triassic sandstone</i>	228
6.2.2.2	<i>Alluvial groundwater monitoring network</i>	228
6.2.3	CE distributions in the riverbed	231
6.2.3.1	<i>Spring 2012 snapshot</i>	231
6.2.3.2	<i>Summer 2012 snapshot</i>	233
6.2.3.3	<i>Spatial variability of CEs at ‘plot-scale’</i>	235
6.2.4	Quantification of TCE reductive dechlorination	236
6.2.4.1	<i>Reach-scale reductive dechlorination activity</i>	237
6.2.4.2	<i>Plot-scale reductive dechlorination activity</i>	239
6.3	Variation in redox conditions	241
6.3.1	Groundwater redox conditions	241
6.3.1.1	<i>Permo-Triassic sandstone in Spring 2012</i>	241
6.3.1.2	<i>Alluvial groundwater system in Spring 2012</i>	242
6.3.1.3	<i>Alluvial groundwater system in Summer 2012</i>	245
6.3.2	Redox environment of the riverbed at reach-scale	248
6.3.2.1	<i>Redox conditions in the riverbed in Spring 2012</i>	249
6.3.2.2	<i>Redox conditions in the riverbed in Summer 2012</i>	252

6.3.2.3	<i>Representative redox profiles</i>	257
6.3.3	Redox conditions in the plot-scale sampler array	259
6.3.3.1	<i>Terminal electron acceptors</i>	259
6.3.3.2	<i>Reduced metabolites and DOC</i>	260
6.3.4	Redox interactions with TCE dechlorination	265
6.3.4.1	<i>Redox interactions at reach-scale</i>	266
6.3.4.2	<i>Redox interactions in the plot-scale array</i>	268
6.4	Discussion	270
6.4.1	Spatial variability of redox conditions and transformation patterns	270
6.4.2	Implications of river macrophyte growth on dechlorination potential	276
6.4.3	Impact of diffuse nitrate contamination on TCE transformation	277
6.5	Chapter summary	279
Chapter 7. Conclusions and future research directions		281
7.1	Introduction	281
7.2	Summary of key findings	281
7.3	Wider implications of the research	287
7.4	Future research outlook	290
7.4.1	Numerical simulations	290
7.4.2	Quantification of hyporheic exchange	290
7.4.3	Investigation of TCE-sediment partitioning	291
7.4.4	Further investigation of in-situ biodegradation	291
7.4.5	Passive sampling of CEs and redox indicators beneath vegetation	292
8.	References	293
9.	Appendices	324

List of Figures

1.3.1	Conceptual flow chart outlining thesis layout	10
2.2.1	Groundwater flow to rivers and the hyporheic zone	14
2.2.2	Conceptual models of aquifer-river interactions	15
2.3.1	Transport processes affecting chlorinated ethenes	20
2.3.2	Impact of hyporheic exchange on plume discharge	22
2.4.1	Reductive dechlorination pathways for TCE	25
2.4.2	Electron flow diagram from DOC to microbial redox processes	31
3.2.1	Overview of the River Tern catchment	56
3.2.2	Geology of the River Tern catchment	59
3.2.3	Geological cross-section of the Stafford Basin	60
3.2.4	Permian Bridgnorth sandstone samples	59
3.2.5	Hydrogeology of the study area	63
3.2.6	Hydrogeological cross-section of the TCE plume	66
3.2.7	Depth stratification of TCE in Environment Agency boreholes	66
3.2.8	Historic aerial photography of RAF Ternhill maintenance area	67
3.2.9	Monitoring network of the study area on the floodplain	69
3.3.1	Riverbed diffusion sampler construction and installation	74
3.3.2	Mini-piezometer construction and installation	75
3.3.3	Single-screen monitoring well construction and installation	78
3.3.4	Installed Transect S piezometers	81
3.3.5	Pore water samplers construction and installation	84
3.3.6	Temporary piezometer nests	86
3.3.7	Layout of all new and existing monitoring infrastructure	87
3.4.1	Schematic of Wenner array resistivity survey	95
3.4.2	Temperature probe construction diagram	98
4.2.1	River flow and rainfall over sampling campaigns in Chapter 4	112
4.2.2	TCE concentrations in the existing monitoring network	113
4.2.3	Diffusion sampler results for TCE and cDCE.	115
4.2.4	Spatial variation of TCE in September 2011	117
4.2.5	Spatial variation of TCE in December 2011	119
4.2.6	Longitudinal interpolation of TCE at Transect D	120
4.2.7	Spatial variation of cDCE in September 2011	122
4.2.8	Spatial variation of cDCE in December 2011	123
4.3.1	Resistivity profiles locations on the floodplain and auger hole logs	126
4.3.2	Hydraulic head distribution in the floodplain	129

4.3.3	Chlorinated ethenes in alluvial boreholes	131
4.3.4	64 m electrical resistivity profiles	135
4.3.5	32 m electrical resistivity profiles	137
4.3.6	LOCAR resistivity profiles	139
4.3.7	Hydrogeological interpretation of 64 m resistivity profiles	149
4.3.8	Hydrogeological interpretation of 32 m resistivity profiles	151
4.3.9	Hydrogeological interpretation of LOCAR resistivity profiles	153
4.4.1	Hydrogeological cross-section of the floodplain	158
5.2.1	Riverbed sediment composition map	167
5.2.2	Riverbed stratigraphy	168
5.2.3	Sediment fraction of organic carbon	169
5.2.4	Hydraulic conductivity cumulative frequency and depth variation	175
5.2.5	Vertical hydraulic gradient cumulative frequency and depth variation	178
5.2.6	Spatial variability of hydraulic conductivity and vertical hydraulic gradients	180
5.2.7	Hydrographs for riverbed piezometers and river levels	184
5.2.8	Temporal variability of vertical hydraulic gradients	187
5.3.1	Schematic of flux calculation approach	190
5.3.2	Calculated groundwater baseflow over the reach	191
5.3.3	Depth variation of temperature	193
5.3.4	Spatial variability of riverbed temperature	196
5.3.5	Calculated groundwater fluxes from temperature	199
5.3.6	Spatial variability of groundwater fluxes from temperature	200
5.3.7	Linear interpolation of TCE concentrations in the riverbed	202
5.3.8	Linear interpolation of TCE flux along the reach	204
5.3.9	Spatial variation of TCE discharge based on temperature mapping	207
5.3.10	Comparison of independent Darcy flux estimates	208
5.4.1	Spatial comparison of temperature-derived flux and TCE concentrations	219
5.4.2	Conceptual model of plume transport in the riverbed	221
6.2.1	River flow, rainfall and sampling locations for Chapter 6	227
6.2.2	Chlorinated ethenes in alluvial boreholes	230
6.2.3	Spatial distribution of TCE and cDCE in the riverbed in Spring 2012	232
6.2.4	Spatial distribution of TCE and cDCE in the riverbed in Summer 2012	234
6.2.5	Spatial distribution of TCE and cDCE in the plot scale samplers	236
6.2.6	Reductive dechlorination activity diagrams for TCE at reach scale	238
6.2.7	Reductive dechlorination activity diagrams for TCE at plot scale	240
6.3.1	Redox indicators in the alluvial groundwater system in Spring 2012	244
6.3.2	Redox indicators in the alluvial groundwater system in Summer 2012	247
6.3.3	Variability of redox indicators in the riverbed in Summer 2012	251
6.3.4	Variability of redox indicators in the riverbed in Summer 2012	255

6.3.5	Representative redox profiles in the riverbed	258
6.3.6	Plot scale variability of redox indicators	262
6.3.7	Scatter plots of chlorine numbers with redox indicators at reach scale	267
6.3.8	Scatter plots of chlorine numbers with redox indicators at plot scale	269
6.4.1	Spatial interpolation of nitrate, methane and chlorine number at plot scale	275
7.4.1	Multi-scale and multi-process conceptual model integrating study findings	286

List of Tables

1.1	Physical and chemical properties of TCE	4
3.1	Existing groundwater monitoring network	70
3.2	Single-screen alluvial monitoring well network	77
3.3	Single-screen riverbed monitoring well network	80
3.4	Electrical resistivity data acquisition	96
3.5	Mass spectrometer ions for chlorinated ethene quantitation	102
4.1	HydraSleeve groundwater samples from May 2011	111
4.2	Electrical resistivity values of common geological materials	141
5.1	Riverbed sediment properties and retardation coefficients	172
5.2	Input parameters for Darcy fluxes	189
5.3	Comparison of fluxes and antecedent conditions	209
5.4	Calculated residence times and contaminant velocities for TCE	210
6.1	Criteria for assessment of redox conditions	225
6.2	Concentrations of redox indicators in the Permo-Triassic sandstone	242

List of Equations

2.1	Average linear advective pore water velocity	15
2.2	Distribution coefficient for partitioning contaminants	16
2.3	Sediment-water partition coefficient	17
2.4	Coefficient of retardation	18
2.5	Sorption-modified contaminant velocity	18
2.6	Derivation of a chlorine number	48
3.1	Loss-on-ignition determination	89
3.2	Porosity determination	90
3.3	Bulk density determination	90
3.4	Hvorslev solution for a partially-penetrating well	92
3.5	Henry's law for ideal gases	104
3.6	Density factor methane in for Henry's law calculation	104
3.7	Determination of headspace concentration for methane	105
3.8	Determination of aqueous concentration for methane	105
5.1	Determination of vertical hydraulic gradient	176
5.2	1-D vertical groundwater discharge	188
5.3	Calculation of volumetric groundwater discharge	188
5.4	1-D heat flux solution for vertical groundwater flow	197
5.5	Flow-concentration product for contaminant flux	202
5.6	Calculation of total contaminant flux	202

List of Appendices

A	Mini-piezometer location details	324
B	VHG-derived flux calculations	325
C	Temperature-derived flux calculations	327
D	Supplementary water quality data	334
E	Correlation matrices	336

1. Introduction

1.1 Research context

1.1.1 Introduction

Since the early 1980s, widespread contamination of aquifers by chlorinated ethenes (CEs) has become recognised as a ubiquitous environmental legacy associated with post-industrial and historic urban landscapes in the developed world (Rivett et al., 1990a; Burston et al., 1993; Jackson, 1998). Compounds formerly used as industrial solvents in cleaning and degreasing applications such as trichloroethene (TCE) and tetrachloroethene (PCE), together with their daughter products *cis*-1,2-dichloroethene (cDCE) and vinyl chloride (VC) have now become some of the most frequently detected volatile organic compounds (VOCs) found in groundwater to date (Squillace et al., 2004; Basu et al., 2004; Carter et al., 2008; Yang et al., 2012; Rivett et al., 2012).

1.1.2 TCE in groundwater

TCE is a chemically stable, non-flammable and volatile liquid making it an excellent non-polar solvent for vapour degreasing of metal parts in the aerospace, automotive and electronics industries (Doherty, 2000). Commercial TCE production began in the UK in 1909 and increased significantly after the second world war from approximately 40,000 tons annually in 1949 to a peak of 90,000 tons per annum in 1970 (Rivett et al., 1990b). The first cases of TCE contamination of potable water in UK was documented by Lyne and McLachlan (1949) where contamination was suspected from taste and odour problems associated with public drinking water supply wells as well as deleterious health effects reported by the local population (Rivett et al., 2006). Around this time, the scientific

community considered TCE and other synthetic organic compounds to be innocuous with respect to serious impacts on potable groundwater quality (e.g., Thomas, 1951). It was not until the mid-to-late 1970s that the occurrence of chlorinated solvents in groundwater in parts of Europe and North America became a recognised problem. Technological advances in gas chromatography led to the discovery of trihalomethane disinfection by-products arising from chlorination of drinking water (Bellar et al., 1974) followed by detection of TCE and PCE in municipal water supplies sourced from solvent-contaminated groundwater (Westrick et al., 1984; Folkard, 1986; Misstear et al., 1998). By the late 1980s, TCE had become notorious, with one UK survey detecting it in 78% of groundwater abstractions from the sandstone aquifer underlying Birmingham city (Rivett et al., 1990a). Similarly in the U.S., TCE contamination has been detected in soil and groundwater associated with practically all historic industrial and military sites with the long term costs of remediation estimated to be as great as 1 trillion dollars (NRC, 1994). The modern use of TCE as a degreasing solvent has declined and is subject to stringent controls on handling and disposal (DEFRA, 2005). In Europe, it is now chiefly produced as a chemical feedstock in the fluorocarbon and polyvinyl chloride markets (ECSA, 2011).

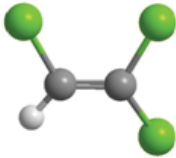
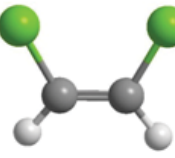
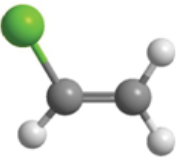
1.1.3 Contaminant properties of TCE

The fluid properties of TCE which renders it an effective degreasing solvent also make it a highly problematic contaminant in aquifers. As an immiscible liquid with poor aqueous solubility and high density (Table 1.1), TCE will enter the subsurface as a dense, non-aqueous phase liquid (DNAPL) capable of penetrating the water table with rapid and often complex migration within the saturated zone (Pankow and Cherry, 1996) sometimes to considerable depths (Darlington et al., 2013). Once in the saturated zone as DNAPL, TCE migration is understood to follow vertical pathways of least resistance through the larger

pores or wider fracture apertures in the matrix under the influence of gravity (Schwille, 1988; Mercer and Cohen, 1990). As a two phase water-DNAPL system, pore or fracture entry pressures arise from capillary resistances at smaller pore throats or narrower fracture apertures which may cause pooling or horizontal migration along stratigraphic controls such as clay lenses (Keuper et al., 1993). The trailing edge of the DNAPL mass will often leave behind imbibed ‘blobs’ and ‘ganglia’ in pores which are effectively immobilised by capillary forces (Mercer and Cohen, 1990). This complex multiphase behaviour creates major technical challenges for engineered remediation efforts at source zones (e.g., Parker et al., 2008). Because of the low solubility of the DNAPL, slow mass transfer to the aqueous phase will occur over time with a solute plume released into the local groundwater flow system which may persist for decades (Johnson and Pankow, 1992). TCE has relatively weak hydrophobicity (Table 1.1) and dissolved-phase plumes are not subject to strong retardation by aquifers with limited organic carbon content (Benker et al., 1997; 1998). TCE often exhibits variable but limited chemical reactivity in groundwater and requires anaerobic conditions in order for significant biodegradation to take place. This occurs when chlorine atoms are sequentially replaced by hydrogen in a process known as reductive dechlorination which produces lower-chlorinated homologues cDCE, VC and finally, non-chlorinated ethene or ethane (Bradley, 2000). Therefore, in aquifers with a high redox potential and limited organic carbon content in the matrix, solute plumes released from DNAPLs are often recalcitrant and can attain lengths of many kilometres (e.g., Jackson, 1997; Rivett et al., 2001). Because of the large cost commitments associated with engineered remediation or containment of solvent plumes, monitored natural attenuation (MNA) is increasingly being considered as a practical and environmentally acceptable management option (e.g., Weidemeier et al., 1998; Witt et al., 2002; Newell et al., 2006). However, it is also accepted that natural attenuation processes over decadal time

scales may not be sufficient to halt migration of solvent plumes towards the natural discharge points of groundwater flow systems (Rivett and Thornton, 2008). This raises important concerns for land owners, environmental managers and regulators regarding the ultimate environmental fate of unmanaged CE plumes migrating along natural hydraulic gradients.

Table 1.1 Physical and chemical properties of TCE and its chlorinated daughter products. Ball-and-stick molecular structures represent chlorine atoms in green, carbon in grey and hydrogen in white.

Property	units	TCE	cDCE	VC
Molecular structure				
Molecular mass	g mol ⁻¹	131.4	96.9	62.5
Boiling point ^a	°C	87	60	-14
Melting point ^a	°C	-87	-81	-153
Aqueous solubility at 25 °C ^b	mg L ⁻¹	1000	3500	2700
Density at 20 °C ^b	g mL ⁻¹	1.46	1.28	0.91
Log K _{ow} ^a	mL mL ⁻¹	2.29	1.86	1.75
Henry's law constant at 20 °C ^a	atm mol ⁻¹	0.314	0.14	0.891

* Octanol-water partition coefficient

^a Sourced from Fetter (1997)

^b Sourced from USEPA (1995)

1.2 Research motivation

1.2.1 Pressures on rivers from CE contamination

Patterns of urbanisation and industrial development in the UK over previous centuries have tended to focus on water courses, some of which are in hydraulic continuity with major urban aquifers (Lerner and Barret, 1996; Tait et al., 2004). There are thought to be upwards

of 100,000 brownfield sites in existence in the UK (Rivett et al., 2002) and underlying the City of Birmingham alone, there are estimated to be approximately 500 individual point-sources of chlorinated solvent contamination (Rivett et al., 2012). In the US, a national survey of 1218 hazardous waste sites found that 51% were releasing VOC plumes to surface water from groundwater (USEPA, 1991). A more recent survey of 45 chlorinated solvent plumes across North America and Europe found one in five were discharging to surface water bodies (McGuire et al., 2004). Given these pressures, it is not surprising that the small number of workers investigating VOCs dissolved in streams and rivers have documented the presence of CEs, with alarming frequency. For example, Yamamoto et al. (1997) conducted a survey of 55 industrial VOCs dissolved in surface and transitional water bodies at a number of monitoring points in the industrialised region of Osaka, Japan. CEs were among the most prevalent contaminant group detected with 57% of 137 samples containing TCE, followed by 50% for cDCE and 40% for PCE. In the US, TCE was found in 51% of 104 samples containing VOCs sampled from seven streams draining a range of land use types in New Jersey (USGS, 1998). More recently in the UK, TCE was the most frequently detected VOC in the waters of the River Tame, Birmingham as part of an extensive ‘city scale’ monitoring program (Ellis, 2003; Ellis and Rivett, 2007). These studies clearly demonstrate the importance of the groundwater pathway in linking historic industrial contamination of aquifers by chlorinated solvents with modern deterioration of surface water quality.

1.2.2 Legislative drivers

A new impetus in hydrological research advocates a greater understanding of the interdependence of groundwater and surface water systems. This is exemplified by the stream-catchment ‘continuum’ concept (Bencala, 1993) where recognition of the need for integrated management stems from awareness of the impact of poor water quality in one catchment ‘compartment’ on the other (Winter et al., 1998; Hancock, 2002; Ellis and Rivett, 2007; Smith et al., 2008; McKnight et al., 2012). Throughout Europe, this integrated approach is mandated by current legislation such as the EU Water Framework Directive (WFD) (2000/60/EC) and Groundwater Daughter Directive (2006/118/EC) (CEC, 2000) which place great emphasis on the preservation and restoration of aquatic ecosystems dependant on groundwater both now and in the future. In Europe, TCE has been included on list one (sometimes referred to as the ‘black list’) of the EU Dangerous Substances Directive (1976/464/EEC) since 1976 (CEC, 1976) because of its environmental persistence and toxicity to aquatic life. It is currently one of 33 hazardous substances listed on annex one of the WFD daughter directive on environmental quality standards (2008/105/EC) (CEC, 2008) and is subject to a regulatory limit of $10 \mu\text{g L}^{-1}$ for inland surface waters, which is 3 orders of magnitude lower than its aqueous solubility (Table 1.1). TCE is both toxic and a suspected human carcinogen with its daughter product, VC, well known to be a human carcinogen (Clewell et al., 2001). Consequently, drinking water standards in Europe are set at $10 \mu\text{g L}^{-1}$ for TCE and $0.5 \mu\text{g L}^{-1}$ for VC (CEC, 1998). The World Health Organisation (WHO) estimates limits of $70 \mu\text{g L}^{-1}$ for TCE and $5 \mu\text{g L}^{-1}$ for VC as maximum exposure levels without significant health risks over a lifetime of exposure through drinking water (WHO, 2004). Therefore, an integrated understanding of the fate of TCE and its daughter products in the environment is essential for the long term management of risks posed by this legacy industrial contaminant.

1.2.3 Knowledge gaps and scientific rationale

Successful implementation of the WFD across EU member states will require improved process-based understanding of the transformation and fate of groundwater pollutants at the aquifer-river interface (Buss et al., 2009). In the UK, research on groundwater-surface water interactions has traditionally focused on upland catchments (e.g. Soulsby et al., 2001). However, lowland rivers receiving baseflow from groundwater bodies impacted by diffuse and point-source contamination pressures which are at risk of failing to achieve WFD targets for water quality have recently become a target for research (Smith, 2005; Fisher et al., 2005). This was borne out by the establishment of an interdisciplinary scientific investigation, the UK Lowland Catchment Research (LOCAR) program which recognised the importance of the groundwater-surface water interface in the management of permeable catchments (Wheater and Peach, 2004). The fate of discharging CE plumes is controlled by physical and chemical processes which operate at this critical catchment interface which includes the bed and banks of river channels but may also extend laterally into the wider riparian zone (Sophocleous, 2002). Although many studies have documented instances of CE contamination of aquifers, detailed investigation of their solute plume behaviour and fate at aquifer-river interfaces is currently limited to just a handful of case studies (Conant et al., 2004; Ellis and Rivett, 2007; LaSage et al., 2008; Abe et al., 2009; Hamonts et al., 2009). These investigations demonstrate a variable but significant potential for in-situ contaminant attenuation along groundwater flow paths through the interface, which often surpasses the underlying groundwater system. This forms the basis of the scientific rationale for this current research.

1.3 Research scope

1.3.1 Aims and objectives

The overarching aim of this study is to provide an integrated conceptual understanding of the fate and potential for in-situ natural attenuation of a poorly characterised TCE plume known to be impacting groundwater quality in one of the UK's principal water supply aquifers. This aim is advanced through interdisciplinary field investigations along a section of the lowland River Tern in Shropshire, selected during the LOCAR program as a type locality for groundwater-fed lowland river reaches in the UK (Adams et al., 2003).

The specific objectives of this research are fourfold:

- (1) To apply a nested monitoring approach to delineate the riparian discharge zone of a TCE plume upwelling from depth in a regional sandstone aquifer.
- (2) To investigate the importance of geological controls on groundwater contaminant discharge at multiple spatial scales in a heterogeneous lowland environment.
- (3) To quantify contaminant mass fluxes from groundwater to surface water using complimentary independent approaches.
- (4) To investigate the biodegradation potential of a rural lowland aquifer-river interface impacted by diffuse nitrate pollution and seasonal macrophyte growth.

1.3.2 Thesis structure

This thesis is divided into 7 chapters. The research strategy and format of the thesis is presented in Fig. 1.3.1. Following on from this chapter, Chapter 2 reviews the importance of the aquifer-river interface, key destructive and non-destructive natural attenuation processes and the relevant field methods to investigate CE transport and fate in the near-river geological environment. Chapter 3 provides a comprehensive overview of the study area, outlines the main field investigation methods, monitoring tools and laboratory analytical procedures used. Chapter 4 applies a multi-scale investigative approach to delineate the discharge zone of the plume and investigates the hydrogeological framework of the river corridor along the discharge zone. Chapter 5 investigates the variability of hydrophysical controls of groundwater and contaminant discharge through the riverbed. Chapter 6 investigates the biogeochemical environment of the discharge zone over two seasonal sampling snapshots using a redox-indicator approach applied over multiple spatial scales to target reactive flow paths through the riverbed. Chapter 7 synthesises the key conclusions from the research, discusses the wider implications of the work and provides an outlook for future research directions.

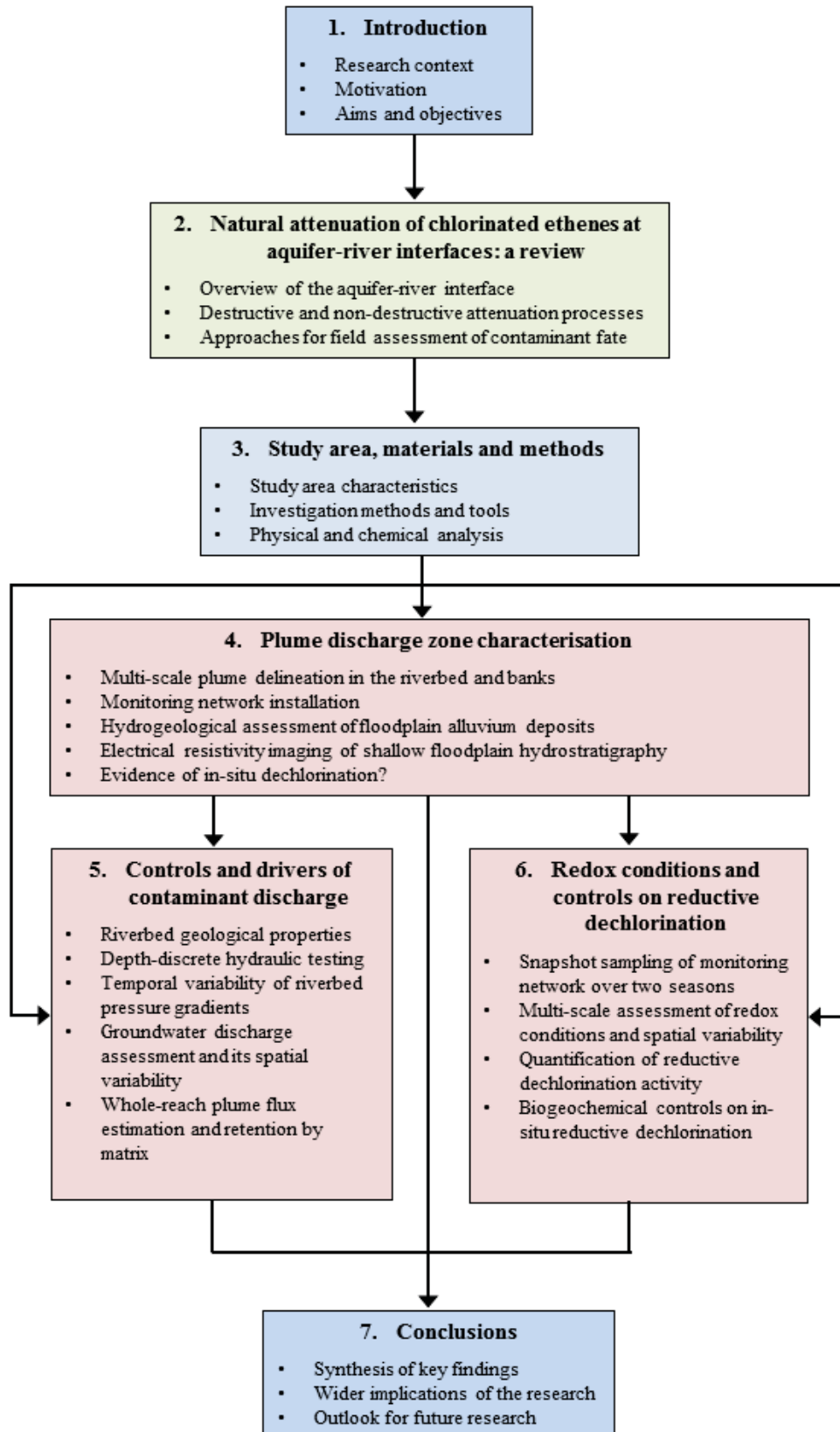


Fig. 1.3.1 Flow diagram outlining the strategy for the research program and structure of the thesis.

2. Natural attenuation of chlorinated ethenes at aquifer–river interfaces: a review

2.1 Introduction

Because of the environmental concerns posed by chlorinated ethenes in groundwater, a significant body of research has emerged that investigates the processes which lead to their natural attenuation in aquifers. This chapter aims to provide a comprehensive synthesis of the current scientific understanding of all destructive and non-destructive attenuation processes documented in the field and laboratory, together with a review of the monitoring approaches available to characterise their fate at aquifer-river interfaces. It begins by providing a conceptual basis for aquifer-river interactions and goes on to review important mass transport processes which may lead to non-destructive attenuation of plumes discharging to surface water bodies. Particular attention is given to reductive dechlorination as a key destructive attenuation process and its coupling with biogeochemical cycling of natural organic carbon as well as its interaction with other microbially-mediated redox processes. The fate of the chlorinated daughter products produced during partial reductive dechlorination is also considered. Where possible, studies which specifically document microbial processes in riverbed sediments are included. The final section of the chapter reviews selected case studies to illustrate the key field-scale investigative approaches that have been used to characterise CE plumes discharging to rivers.

2.2 The aquifer-river interface

2.2.1 Hydrological framework

The groundwater-surface water interface (alternatively known as the hyporheic zone) of streams and rivers has been defined by different disciplines from various perspectives (Krause et al., 2011a) but is generally accepted to comprise the saturated interstices of the riverbed and riparian zone that contains at least some proportion of surface water (White, 1993). It is recognised as a dynamic and biologically diverse ‘ecotone’ in the catchment continuum where exchange of water, energy and solutes readily occurs between groundwater and surface water (Triska et al., 1989; Brunke and Gonser 1997; Dahm et al., 1998; Boulton et al., 1998). From an ecological perspective, this ecotone establishes habitats and refugia for obligate and facultative anaerobes, spawning grounds for fish and a rooting zone for aquatic plants (Buss et al., 2009). From a hydrogeological perspective, the geological framework of the aquifer-river interface is often characterised by a high degree of spatial heterogeneity in sediment composition and structure which contrasts from the often more uniform flow regime of aquifers and is also subject to the dynamics of seasonal erosion and sedimentation patterns (Huggenberger et al., 1998; Woessner et al., 2000; Fleckenstein et al., 2006). Spatial patterns of stream-aquifer exchange are often complex and subject to dynamic, competing driving forces between the regional hydraulic gradient in the surrounding aquifer where regional, intermediate and local flow lines converge (Tóth, 1963; Sophocleous, 2002) and advection of surface water into sediment interstices (known as hyporheic exchange) (Harvey and Bencala, 1993) (Fig. 2.2.1). These driving forces are regulated by the hydrophysical properties of the interface which includes the spatial distribution and magnitude of hydraulic conductivity, geometry of the river channel within the alluvial corridor and hydraulic gradients arising from the relative positioning of

river stage and adjacent water tables (Woessner, 2000) (Fig. 2.2.2). This research is concerned with streams and rivers which receive net accretion in groundwater baseflow contribution where contaminant flow lines emanate from a point source in the up-gradient flow system and solute transport is orientated along a set of flow paths which converge along a discrete river reach. This type of aquifer-river relationship is often described as 'gaining' in conceptual models (Winter et al., 1998; Woessner, 2000; Sophocleous, 2002) because net river flow is increasing and is depicted in Fig. 2.2.2 as Condition A.

2.2.2 Biogeochemical importance of the aquifer-river interface

The hydraulic conductivity of riverbed materials often varies over several orders of magnitude and associated residence times along flow paths can range from hours to days for non-sorbing solutes (Haggerty et al., 2002; Zarnetske et al., 2011) or much longer for sorbing solutes (Conant et al., 2004). Increased microbial biodiversity and the often greater availability of labile organic carbon in this zone in comparison to the deeper aquifer can favour the development of microbially-mediated redox gradients superimposed on flow paths (Baker et al., 2000; Morrice et al., 2000; Lautz and Fanelli, 2008). Because of this, the sediment pore water environment of the aquifer-river interface is recognised as a zone dominated by accelerated microbial activity leading to intensified biogeochemical cycling and turnover rates which lead to steep physicochemical gradients over short (sub-metre) spatial scales (Storey et al., 1997; Fraser and Williams 1998; Franken et al., 2001; Hancock, 2002). Pusch and Schwoerbel (1994) estimated that 95% of whole hyporheic community respiration was due to heterotrophic microbial activity in a third order stream in the Black Forest, Southern Germany. Respiration of oxidisable organic carbon with concurrent reduction of terminal electron acceptors (TEAs) present in groundwater including dissolved oxygen (DO), nitrate (NO_3^-), oxidised forms of manganese and iron

(e.g., Mn^{4+} and Fe^{3+}), sulphate (SO_4^{2-}) and carbon dioxide (CO_2) will occur along flow paths where TEA replenishment rates are exceeded by rates of consumption (Baker et al., 2000). However, because of the temporal dynamics of hyporheic exchange, transient re-oxidation of anaerobic zones in the riverbed may occur or, conversely, labile organic materials may be introduced to sediment interstices. As a result, much interest has arisen in the potential for redox transformation of groundwater contaminants along flow paths through this zone, such as denitrification of NO_3^- -impacted groundwater (Triska et al., 1989; Krause et al., 2009) and attenuation of metalliferous mine waters (Gandy et al., 2004). More recently, microbially-mediated transformation processes operating at the aquifer-river interface have been considered in order to investigate the potential attenuation of a range of VOCs in groundwater including monoaromatic hydrocarbons (Westbrook et al., 2005), polycyclic aromatic hydrocarbons (Morash et al., 2007), fuel oxygenates (Landmeyer et al., 2010), monochlorobenzene (Schmidt et al., 2011) as well as chlorinated ethenes (Conant et al., 2004; Ellis and Rivett, 2007; LaSage et al., 2008; Hamonts et al., 2012).

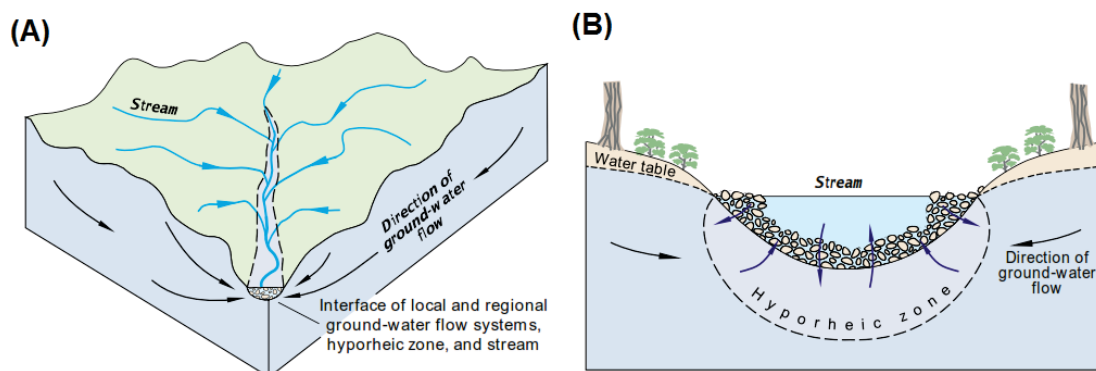


Fig. 2.2.1 (A) Catchment-scale visualisation of groundwater flow line convergence on a connected river. (B) Cross-section of the aquifer-river interface (hyporheic zone) at the river channel scale (after Winter et al., 1998).

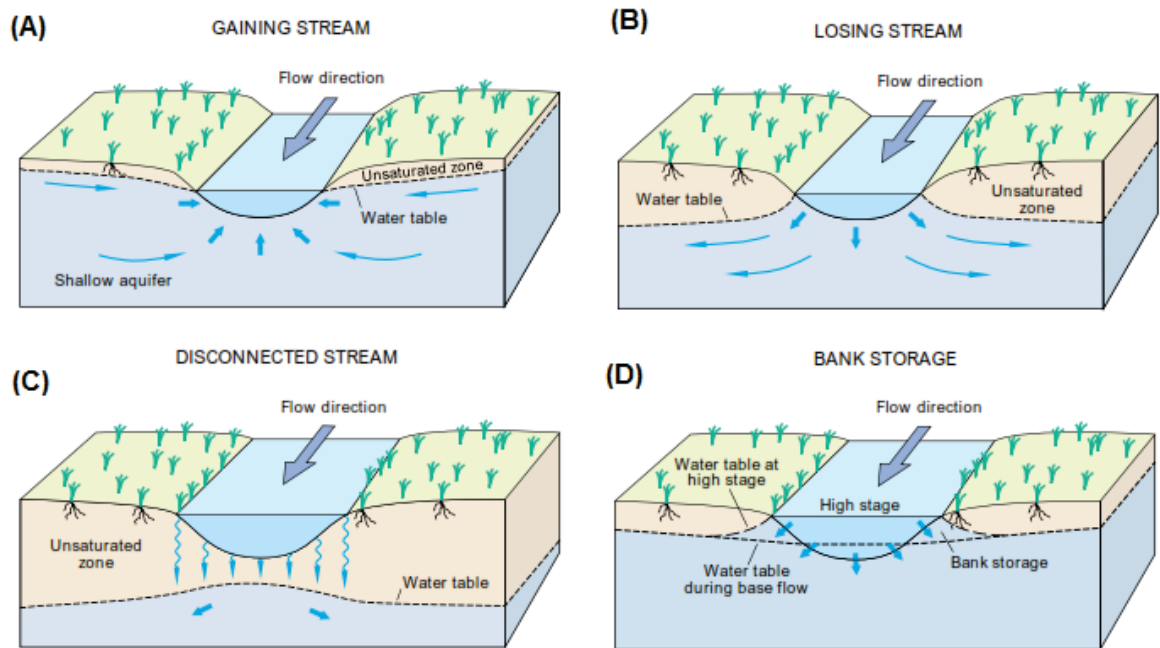


Fig. 2.2.2 Channel-scale conceptual models of aquifer-river interactions based on the relative positioning of water table and stream stage (after Winter et al., 1998). Conditions A, B and C depict steady-state conditions where net stream flow is (A) accreted, (B) lost and (C) groundwater and surface water flow systems are not connected. Condition (D) represents transient conditions during high stream stage events where surface water is temporarily stored within stream bank sediments.

2.3 Non-destructive natural attenuation processes

2.3.1 Advection and dispersion

Advection is the dominant mass transport process which moves dissolved chlorinated ethenes (CEs) towards natural discharge zones, caused by the bulk movement of groundwater along the prevailing hydraulic gradient (Freeze and Cherry, 1979). The average linear pore water velocity (V_a) [$L T^{-1}$] in a direction parallel to groundwater flow caused by advection is given in Equation 2.1 (Weidemeier et al., 1998) which represents the velocity a conservative tracer would experience.

Equation 2.1
$$V_a = \frac{K}{n} \frac{dh}{dl}$$

Where K is the hydraulic conductivity [$L T^{-1}$], n is the effective porosity [$L^3 L^{-3}$] and dh/dl is the hydraulic gradient [$L L^{-1}$]. Solute transport by advection alone produces a sharp concentration front (Fig. 2.3.1). However, hydrodynamic dispersion causes plumes to spread out in directions both parallel and transverse to groundwater flow resulting in a reduction in contaminant mass (Fig. 2.3.1) (Weidemeier et al., 1998). Heterogeneity in sediment sequences causes mechanical dispersion of solutes at microscopic scales where local transport velocities vary around a mean (Domenico and Schwartz, 1990). This arises due to faster groundwater flow through smaller pores, differences in flow path lengths over the same linear distance (tortuosity) and varying friction around pore throats where groundwater travels faster towards the centre of the throat (Freeze and Cherry, 1979). Molecular diffusion also causes dispersion where movement of solutes from areas of high concentration to low concentration occurs under the influence of a concentration gradient. Diffusion is more significant for CE transport through aquitards (e.g., Damgaard et al., 2013) and is often neglected for permeable sediments (Domenico and Schwartz, 1990).

2.3.2 Hydrophobic sorption

Dissolved CEs can be removed from the aqueous phase during adsorption-desorption reactions by partitioning to the sediment matrix. Sorption of CEs and other non-polar organic contaminants is a complex processes which is strongly influenced by the mass fraction of organic carbon (f_{oc}) [$M M^{-1}$] of the solid phase, for hydrophobic contaminants. In various batch experiments, TCE adsorption has been shown to generally follow a linear isotherm (Garbarini and Lion, 1986; Mouvet et al., 1993; Lu et al., 2011). A distribution coefficient (K_d) [$L^3 M^{-1}$] can be derived from the slope of the isotherm according to Equation 2.2 (Weidemeier et al., 1998).

Equation 2.2
$$K_d = \frac{C_a}{C_l}$$

Where C_a is the adsorbed mass concentration [$M M^{-1}$] and C_l is the dissolved concentration [$M L^{-3}$]. Because organic matter dominates adsorption sites for CEs where f_{oc} is greater than 0.1% (Schwarzenbach and Westall, 1981), K_d can be normalised to the organic carbon content of the matrix using Equation 2.3 (Weidemeier et al., 1998) to calculate the sediment-water partition coefficient, K_{oc} [$L^{-3} M$].

Equation 2.3
$$K_{oc} = \frac{K_d}{f_{oc}}$$

This relationship assumes that sorption is independent of initial CE concentration. K_{oc} has been shown to be linearly related to K_{ow} ; the octanol-water partition coefficient which is an indicator of hydrophobicity (Seth et al., 1999). K_{oc} has also been estimated from aqueous solubilities (Chiou et al., 1979). However, the adsorption behaviour of CEs has been shown to not always follow simple empirical relationships, particularly where large dissolved concentration ranges are involved (Ball and Roberts, 1991; Huang et al., 2003). Sorbed concentrations are sometimes found to be far greater than would be otherwise predicted by empirical models (Allen-King et al., 1996). The composition and structure of natural sedimentary organic matter varies greatly as a result of origin, age and degree of diagenetic alteration. This can lead to considerable variation in K_{oc} estimates from equilibrium experiments (Weber et al., 1992). During diagenesis, polymerisation effects can lead to decreases in hydrogen/carbon and oxygen/carbon elemental ratios leading to a greater affinity for hydrophobic organic compound adsorption (Huang and Weber, Allen-King et al., 2002). For example, thermally altered carbonaceous material present in unweathered shale and high-grade coal was found to exhibit a sorption capacity an order of magnitude greater than recent soil organic matter (Grathwohl, 1990). However, where weathering processes subsequently increase oxygen/carbon ratios, the increase in oxygen-containing functional groups can lead to an overall increase in polarity and a reduced affinity for non-

polar, hydrophobic sorbates like CEs (Allen-King et al., 2002). In addition, natural sedimentary organic matter composition can affect sorption equilibrium kinetics. For example, in the case of amorphous humic substances (sometimes called ‘soft’ carbon), linear sorption was found to occur in minutes whereas more condensed, kerogen-dominated carbon (known as ‘hard’ carbon), non-linear sorption over days or longer was observed (Weber et al., 1992; Luthy et al., 1997).

From Table 1.1 (Chapter 1), it can be seen that CEs have generally weak hydrophobicity, indicated by their low log K_{ow} values which decrease with decreasing number of chlorine substituents from 2.29 (for TCE) to 1.75 for VC (Table 1.1). Consequently, they are not capable of being fully immobilised by sorption interactions with the solid phase (Bourg et al., 1992). However, the presence of sedimentary organic matter in the sediment profile will reduce overall migration velocities (V_a) and potential breakthrough to rivers (Fig. 2.3.1). The dimensionless coefficient of retardation (R) can be estimated using Equation 2.4 (Weidemeier et al., 1998).

Equation 2.4
$$R = 1 + \left(\frac{K_d \cdot \rho}{n} \right)$$

Where K_d is already given, ρ is the bulk density of the solid phase [$M L^{-3}$] and n is the porosity. R can then be applied to calculate the sorption-modified contaminant velocity (V_r) [$L T^{-1}$] using Equation 2.5 (Weidemeier et al., 1998).

Equation 2.5
$$V_r = \frac{V_a}{R}$$

At sites where f_{oc} has been determined for both aquifer and riverbed solids, it has been shown that riverbed f_{oc} often exceeds that of the up-gradient groundwater system by between one and three orders of magnitude (e.g., Conant et al., 2004; Ellis and Rivett, 2007; Smith and Lerner, 2008). For example, Conant et al. (2004) calculated R values of

22-88 for PCE transport through semi-confining deposits in the riverbed of the Pine River site, in comparison to 1.2–1.8 for the sand aquifer. This results in a dramatic increase in contaminant residence time in the order of decades to hundreds of years through the top 2 m of the semi-confining low-permeability strata at the site. These findings are comparable to the retardation potential estimated for the River Tame sediments (maximum of retardation factor of 66) in comparison to 1.3 for the Triassic sandstone aquifer in the UK presented by Ellis and Rivett (2007). These observations are supported by another UK study (Smith and Lerner, 2008) where the retardation capacity of riverbed sediments in a number of sandstone catchments (Leith, Tern and Severn) was assessed. Using a high density of f_{oc} measurements from cores, retardation capacity was found to be significantly greater in the top 1–2 m of riverbed than that of the underlying aquifers in all locations. One of the lowland reaches (River Severn) investigated was suggested to provide the equivalent sorption capacity that 190 m of equivalent length of flow path in the sandstone aquifer.

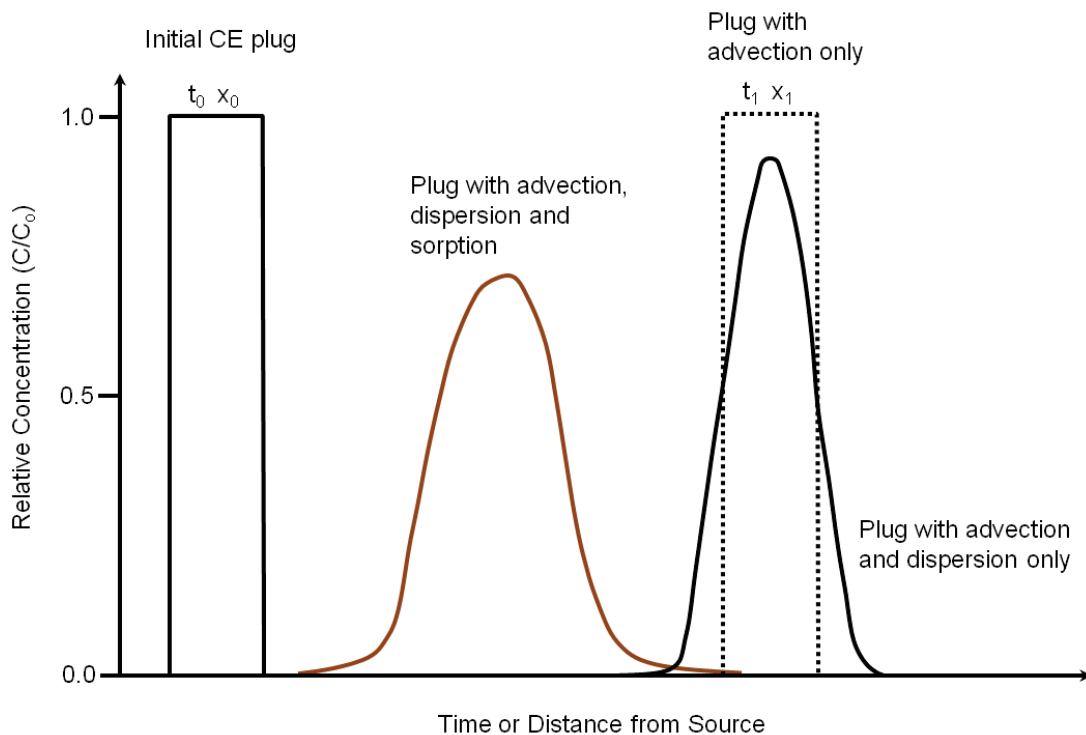


Fig. 2.3.1 Breakthrough curve for an instantaneous release of a CE mass with ‘plug flow’ illustrating the effects of advection, dispersion and sorption on contaminant migration fronts (redrawn from Weidemeier et al., 1998).

2.3.3 In-situ dilution

CE plumes transiting aquifer-river interfaces are subject to transient interactions with other waters types originating from different sources, such as infiltrating surface water and uncontaminated regional groundwater discharge from the surrounding catchment, the relative proportions of which vary temporally and spatially (Woessner et al., 2000). The infiltration of surface water into sediment interstices during hyporheic exchange (Fig. 2.3.2) has been documented as non-destructive process where physical mixing leads to dilution and apparent attenuation in riverbeds receiving CE-contaminated baseflow (e.g., Fryar et al., 2000; Ellis and Rivett, 2007; LaSage et al., 2008; Hamonts et al., 2009, 2012). Conservative solutes can be used to trace the infiltration of surface water into sediment pore water where the resulting decline of contaminant concentrations may be misinterpreted as evidence of degradation. Chloride (Cl^-) shows conservative transport

behaviour and is often present in both groundwater and surface water, and, where these end-members have distinctive concentration ranges, it can be used as a geochemical tracer (Englehardt et al., 2011; Binley et al., 2013; Byrne et al., 2013). Although Cl^- is released during reductive dechlorination and mineralisation reactions, the stoichiometric yield of Cl^- from $\mu\text{g L}^{-1}$ range plumes is likely to be an order of magnitude lower than natural background concentrations. For example, Ellis and Rivett (2007) were able to use Cl^- to trace infiltration of surface water into the bed sediments of the River Tame given the elevated surface water Cl^- concentrations ($>150 \text{ mg L}^{-1}$) relative to groundwater levels (ca. 40 mg L^{-1}). Using Cl^- profiles from piezometers, they were able to attribute groundwater-surface mixing to observed declines in CEs shallow sediment ($<50 \text{ cm}$). Hamonts et al. (2009) used stable isotopes of water ($\delta^{18}\text{O}$ and $\delta^2\text{H}$) to discriminate between apparent attenuation due to dilution of VC and cDCE from mixing of different water sources and active biodegradation along an instrumented section of the Zenne River, Belgium. With the use of environmental isotopes, it was possible to identify pore water signatures of infiltrating surface water and clean groundwater seepage recharged by leakage from a nearby canal. Dilution was observed to significantly attenuate shallow CE concentrations due to physical mixing of unpolluted groundwater and as well as surface water downwelling to depths of 20–60 cm under the influence of riverbed topography (Fig. 2.3.2).

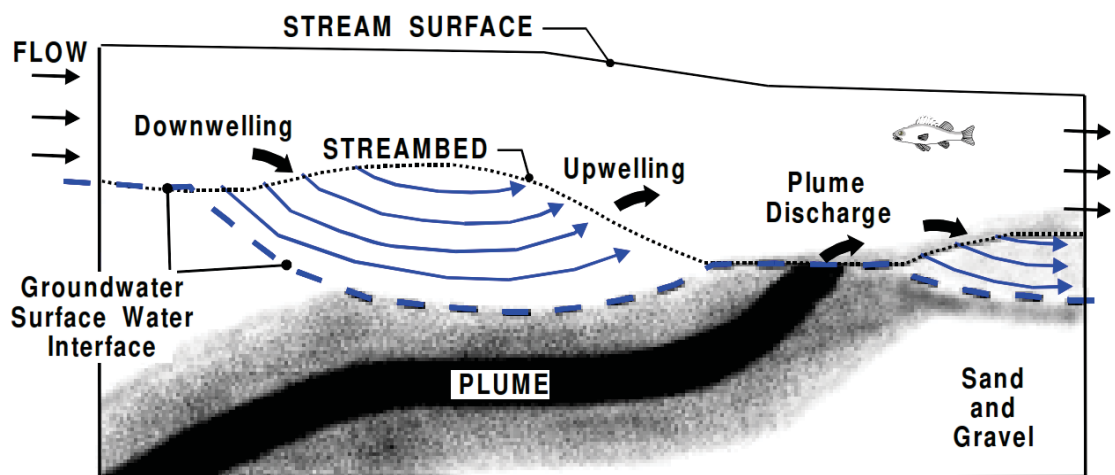


Fig. 2.3.2 Conceptual model illustrating impacts of hyporheic exchange and in-situ dilution on the discharge of a CE plume through a riverbed (after Conant, 2000).

2.3.4 Volatilisation

Loss of dissolved CEs and their volatile metabolites to the atmosphere represents the ultimate sink for groundwater plumes discharging to surface water bodies, which occurs as turbulent or diffusive exchange across the air/water interface (Rathbun, 2000). To date, very few experimental studies have specifically investigated VOC efflux across stream-air interfaces. However, Chapman et al. (2007) considered volatilisation losses to be a major apparent attenuation process at a site where TCE was discharging to a number of small streams and a pond, prior to reaching a major watercourse. In one integrated risk assessment of a CE plume discharging to a stream in Denmark, McKnight et al. (2010) considered volatilisation to be the primary attenuation process for reduction in surface water TCE concentrations. Kim and Hemond (1998) used an innovative, multi-tracer approach to quantify the flux and fate of dissolved VOCs (including TCE and cDCE) in a number of small streams in the industrialised headwaters of the Aberjona catchment (Massachusetts, US). They used a non-volatile tracer (NaCl) to estimate discharge co-injected with propane as a volatile tracer. By comparing the volatilisation of the tracer with

the volatilisation ratio of the tracer and the VOC, they were able to estimate VOC flux accretion from specific reaches assumed to be from lateral groundwater discharges. In a similar approach, Mukherjee et al. (2005) used a propane-Rhodamine WT tracer approach to demonstrate that TCE loss through volatilisation greatly surpassed dilution, sorption and biodegradation in surface water column of a channelised New Jersey stream.

2.4 Destructive natural attenuation processes

2.4.1 Reductive dechlorination

2.4.1.1 Dehalorespiration

CEs are efficiently removed from the environment through reductive dechlorination where organically-bound chlorine atoms are sequentially mineralised via replacement with hydrogen (Fig. 2.4.1) in a process known as hydrogenolysis (Vogel et al., 1987). Under anaerobic conditions, CEs are thermodynamically favourable as TEAs in energy-conserving microbially-mediated terminal electron accepting processes (TEAPs). Their reduction is coupled to synthesis of ATP using externally-sourced hydrogen as a source of electrons or reducing equivalents, in the presence of a carbon source (such as acetate) needed for cellular growth (Mohn and Tiedje, 1992). The term ‘dehalorespiration’ has been coined for this metabolic process (Holliger et al., 1999; Smidt and de Vos, 2004) and the bacteria responsible for it are either obligate or facultative anaerobes, some of which are related to sulphate and sulphur reducers (Bagley and Gosset, 1990). There is also some evidence that methanogenic archaea (*Methanosarcina* spp.) are capable of reductively dechlorinating PCE although it is not certain whether this is a direct biological process or a cometabolic interaction (Fathepure and Boyd, 1988). Reduction of CEs is a step-wise

process where lower-chlorinated homologues are produced after the addition of two electrons from the hydrogen molecule and release of a hydrogen and inorganic chloride (Cl⁻) ion (Fig. 2.4.1). In this way, PCE and TCE may be completely reduced to non-chlorinated environmentally harmless end-products ethene and ethane (Fig. 2.4.1) (Vogel et al., 1987; Freedman and Gossett, 1989; Maymo-Gatell et al., 1997; McCarty, 1997). The DCE produced may be either 1,1-DCE, *cis*-1,2-DCE (cDCE) or *trans*-1,2-DCE (tDCE) (Fig. 2.4.1) with the *cis* isomer being the abundant form produced as a result of biological reduction (Bouwer, 1994), although tDCE has been reported in one culture (Cheng and He, 2009). Among the most important bacterial species which can completely degrade chlorinated ethenes are members of the genus *Dehalococcoides* which belong to the phylum *Chloroflexi*; known informally as green, non-sulphur bacteria (Löffler et al., 2013). This genus contains the highest number of reductive dehalogenase genes which code for the enzymes that act on organically-bound halogen atoms and are thought to be exclusively dependent on organohalogen compounds as TEAs in their strict energy metabolism which uses molecular hydrogen (H₂) as a direct electron donor (Seshadri et al., 2005). Maymo-Gatell et al. (1997) were the first to isolate the bacterium *Dehalococcoides ethenogenes* (strain 195) which is capable of complete reduction of PCE to ethene. Since the early 1990s, a great number of additional bacterial species and strains have been isolated which are known to be capable of reducing PCE or TCE as far as DCE such as *Desulphitobacterium dehalogenans* (Utkin et al., 1994), *Desulfomonile tiedjei* (Cole et al., 1995), *Sulfurospirillum multivorans* (Luijten et al., 2003), *Desulphitobacterium* (Gerritse et al., 1996), *Dehalobacter restrictus* (Holliger et al., 1998), *Desulphitobacterium hafniense* (Christiansen et al., 1996), *Desulfuromonas chloroethenica* (Krumholz, 1997), *Desulphitobacterium frappieri* (Dennie et al., 1998), *Sulfurospirillum halorespirans* (Luijten et al., 2003), *Enterobacter agglomerans* (Sharma and McCarty, 1996),

Desulfuromonas michiganensis (Sung et al., 2003) *Geobacter lovleyi* (Sung et al., 2006) and *Dehalococcoides* strains CBDB1 and MB (Fung et al., 2007; Cheng and He, 2009).

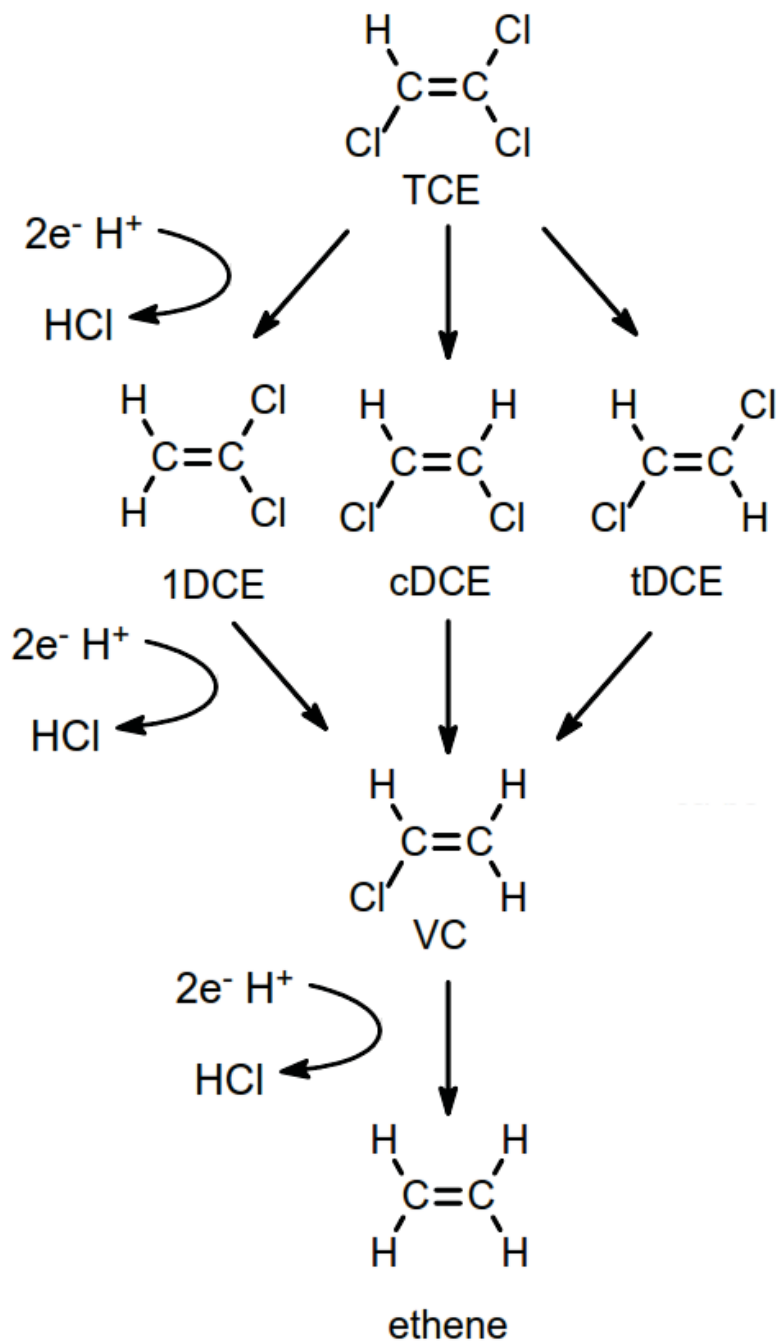


Fig. 2.4.1 Reductive dechlorination pathways of TCE as far as the non-toxic gas ethene (modified from Middeldorp et al., 1999).

2.4.1.2 *Carbon and electron donors for reductive dechlorination*

Dissolved organic carbon (DOC) is a primary driver of heterotrophic metabolism in streambeds and its concentration and quality are thought to be major limiters of whole stream ecosystem respiration (Pusch and Schwoerbel, 1994; Boulton et al., 1997; Baker et al., 1999; Battin et al., 2008). The DOC ‘pool’ available to pore microbes is a complex admixture of mostly reduced carbon species, characterised by a wide range of molecular weights with both refractory and labile components (Baker et al., 1999; Sobczack and Findlay, 2002; Sachse et al., 2005; Romani et al., 2006). Zones of reduced flow along stream corridors as a result of channel morphology or macrophyte density can facilitate sedimentation and accumulation of organic matter in sediments (Sanders et al., 2007). Hyporheic exchange may lead to advection of DOC derived from terrestrial sources (allochthonous) or primary production in the water column (autochthonous) to serve as a source of oxidisable carbon to sediment interstices during settling, mobilisation events and times of high stream stage (Baker and Vervier, 2004; Byrne et al., 2013). Biofilm, microbial and fungal biomass may also present significant autochthonous stores of bioavailable carbon for microbial respiration (Storey et al., 1997; Krause et al., 2011a).

Much research has focused on the role of DOC as carbon source for heterotrophic denitrification (e.g., Brunke and Gonser, 1997; Boulton et al., 1998; Dahm et al., 1998, Baker and Vervier, 2004; Krause et al., 2009). However, much less is known about its role in other anaerobic TEAPs including reductive dechlorination and fermentation in streambed sediments (Morrice et al., 2000; Mermillod-Blondin et al., 2005). Decomposition of complex DOC (Fig. 2.4.2) is initiated by extracellular enzymes produced by fermenters which hydrolyze molecules that cannot pass through the outer membrane of bacteria due to their high molecular weight (Heimann et al., 2010). Fermentation-derived hydrogen is the chief source of electrons for reductive dechlorination

of CEs where it may be utilised directly as H₂ or released from low molecular weight organic molecules produced during fermentation of more complex biopolymers (Fig. 2.4.2). Examples of complex fermentable substrates which have been used to promote reductive dechlorination of chlorinated organic compounds include vegetable oils (Newman and Pelle, 2006) corn cobs (Brennan et al., 2006), wood chips, corn crop residues and newspaper (Wu et al., 1998), and microbial biomass (Yang and McCarty, 2000). In other instances, small, organic monomers such as glucose, methanol and ethanol (Freedman and Gosset, 1989; Fennel et al., 1997) have been shown to readily release H₂ upon endogenous fermentation to drive complete dechlorination. Dechlorinating bacteria, which can reduce PCE or TCE as far as cDCE, are capable of utilising a much wider range of potential electrons donors. For example, the bacterium *Enterobacter* (strain MS-1) was found to be capable of oxidising 58 different organic substrates including a broad range of carbohydrates, amino acids, purines, pyrimidin and organic acids (Holliger et al., 1998).

A wide range of volatile fatty acids (VFAs) formed during intermediate fermentation (Fig. 2.4.2) have been shown to sustain complete dechlorination by providing a steady supply of H₂ including propionate, butyrate, lactate, and formate (Fennel et al., 1997; Azizian et al., 2010; Schneidewind et al., 2014). The role of acetate as a direct electron donor in reductive dechlorination is somewhat controversial. Whilst He et al. (2002) found acetate alone was capable of producing complete dechlorination of PCE (in the absence of H₂), Aulenta et al. (2002) failed to find any evidence of acetate sustaining dechlorination of PCE. Despite the importance of VFAs in the intermediate metabolism of DOC and as a source of H₂ for reductive dechlorination, studies which document their natural production or coupling with biogeochemical cycling in riverbeds, are scarce. Rulík and Hereka (1998) and Rulík et al. (2000) observed high concentrations of lactate and acetate (>300 µg L⁻¹) in the hyporheic zone pore water of a lowland stream in Sitka (Czech Republic). Their work indicated that

overproduction of VFAs was occurring as a result of insufficient supply of consuming TEAs to anaerobic microsites within biofilms, resulting in a net release of VFAs to the advective flow system. Baker and Vervier (2004) quantified VFAs in shallow riparian groundwater where they comprised between 1 and 9% of the measured DOC. They found the VFA content of DOC to be a significant predictor of in-situ denitrification activity in the shallow unconfined groundwater where hydrological linkages formed between floodplain soils during times of high stream stage and water table height.

2.4.1.3 *Redox controls on reductive dechlorination*

Reductive dechlorination of CEs requires anaerobic conditions in order to be thermodynamically favourable as an energy source for dechlorinating organisms (Vogel et al., 1987). Microbial energy derived from oxidation of an electron donor and concomitant reduction of a TEA typically proceeds in a sequence determined by the Gibb's free energy liberated by the reaction (Fig. 2.4.2) to drive synthesis of ATP and cell growth (Holliger et al., 1998). PCE is a potent oxidiser with four chlorine atoms and is known to be rapidly transformed to TCE under all anaerobic TEAPs ranging from denitrifying to methanogenic conditions (Bradley, 2000). As the electronegative chlorine atoms are removed, the redox behaviour of lower chlorinated ethenes becomes more complex (Mohn and Tiedje, 1992). TCE transformation to cDCE is thought to require more reducing conditions (such as Mn reduction), whereas cDCE to VC and VC to ethene proceed more slowly, may not be growth-linked and require highly reducing SO_4^{2-} reducing or methanogenic conditions (Fig. 2.4.2) (Mayamo-Gatell et al., 2001). Channelling of available electrons to denitrifiers, metal reducers, SO_4^{2-} reducers and methanogens will influence the rate and extent of dechlorination reactions in mixed microbial communities which utilise common electron donors (e.g., H_2) with dechlorinators (Aulenta et al., 2007). Inhibition of CE-reduction may

occur where ambient H_2 concentrations are maintained at a level below the threshold necessary to sustain dechlorinators e.g., $<0.05\text{--}0.1$ nM (Lovely et al., 1994; Löffler et al., 1999). At the lowest end of the metabolic energy regime (Fig. 2.4.2), methanogens and SO_4^{2-} reducers have greatest potential to preferentially consume H_2 , particularly in the case of *Dehalococcoides* which relies exclusively on H_2 and can completely detoxify CEs. It has been shown that dechlorinators are capable of out-competing methanogens at low H_2 threshold concentrations (<0.3 nM) with reported thresholds for methanogens in the range of $7\text{--}10$ nM (Ballapragada et al., 1997). Therefore, in sediments where slowly fermenting substrates (such as butyrate or propionate) are present, CE reduction may inhibit methanogenesis. However, Lee et al. (2004) suggest that the initial dechlorinator population size relative to H_2 -utilising methanogens can have a significant effect on the efficacy of reductive dechlorination.

The range of H_2 concentrations utilisable by SO_4^{2-} reducers is much closer to that of dechlorinators (e.g., $1\text{--}4$ nM) (Lovley et al., 1994; Luijten et al., 2004; Heimann et al., 2010) suggesting a possible inhibitory effect from SO_4^{2-} which is a ubiquitous major anion in both groundwater and surface water. Aulenta et al. (2008) observed consistent negative effects of SO_4^{2-} addition on the dechlorination rate of PCE amended with butyrate. Furthermore, sulphur oxyanions were shown to actually inhibit the action of dehalogenase enzymes in the dehalorespiring species *Desulfomonile tiedje* (Townsend and Suflita, 1997). The presence of SO_4^{2-} has also been implicated where incomplete dechlorination leads to accumulation of cDCE and VC (Bagley and Gossett, 1990). Conversely, Aulenta et al. (2007) found that SO_4^{2-} concentrations had no significant effect on dechlorination rates in microcosms amended with multiple electron donors and as well as NO_3^- and Fe^{3+} . However, Nelson et al. (2002) found significant PCE reduction inhibition from both NO_3^-

and SO_4^{2-} in a mixed culture. When H_2 was continuously-fed and non-limiting, a significant lag period was observed before any TCE or methane (CH_4) were detected. In that study, the authors observed that nitrous oxide (N_2O), the intermediate formed during denitrification, was inhibitory to dechlorination at a concentration of 13 μM . CEs themselves may also competitively inhibit steps of the dechlorination chain (Chambon et al., 2013). Yu et al. (2005) investigated self-inhibition of PCE and TCE dechlorination in mixed culture studies. Their findings suggested that higher CEs (PCE and TCE) were capable of competitively inhibiting the reduction of the lower CEs (cDCE and VC). However, PCE did not hinder reductive dechlorination of cDCE and the presence of lower CEs had no or only a very marginal effect on dechlorination of the higher CEs.

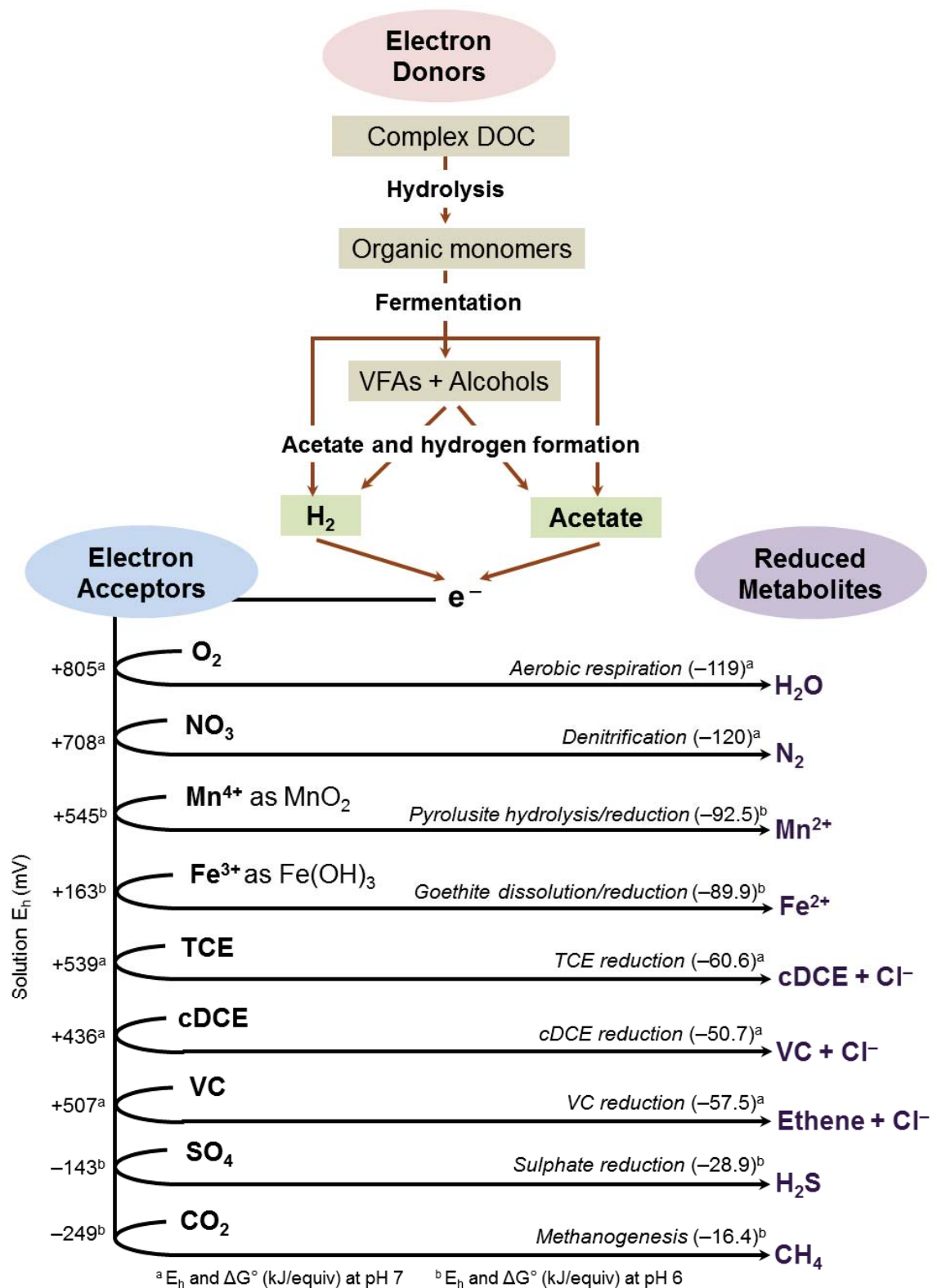


Fig. 2.4.2 Diagram illustrating electron flow from complex DOC to common microbially-mediated TEAPs and dechlorination reactions in order of decreasing energy yield (redrawn from McCarty, 1997). Thermodynamic sequence of TEAPs is predicated from Gibb's free energy (ΔG°) (given in parentheses) taken from half-cell reactions calculated by Weidemeier et al. (1998) at standard temperature and pressure. A negative ΔG° indicates that the reaction is energy-yielding.

2.4.2 Fate of lower-chlorinated ethenes

The build-up of partially dechlorinated daughter products is a major concern where the reductive transformation halts at production of cDCE or VC (e.g., Lorah and Olsen, 1999; Lorah and Voytek, 2004). Due to the electronegativity of the chlorine atoms in the polychlorinated ethenes PCE and TCE, oxidation of the carbon backbone in the ethene molecule is energetically unfavourable to microbes (Vogel et al., 1987). However, as susceptibility to the reductive pathway decreases proportionally with ratio of chlorine to carbon substituents from PCE to VC, both cDCE and VC are potentially amenable to oxidation and complete mineralisation to the non-specific innocuous metabolites chloride and CO₂ (Schmidt and Tiehms, 2008).

2.4.2.2 Biological oxidation of cDCE

Bradley and Chapelle (1998a) were among the first to examine the potential for aerobic degradation of cDCE in sediments and microbial communities indigenous to streambeds. Their study demonstrated biological aerobic mineralisation of [¹⁴C]-DCE (4:1 *cis*-to-*trans* isomers) to CO₂ in microcosms with recovery of [¹⁴C]-DCE ranging from 17–100% after just 8 days with a negative relationship between DCE concentration and mineralisation rate. However, this study used natural sediment media potentially containing a range of other substrates where cometabolic processes could not be ruled out (Bradley and Chapelle, 2000b). Other work has shown aerobic DCE mineralisation is likely to proceed much more slowly in aquifer media (e.g., Klier et al., 1999) where just 3–10% mineralisation was achieved after 180 days incubation. In a more recent study, Abe et al (2008) found no evidence of cDCE removal in aerobic microcosms incubated over 1.5 years. The first unequivocal demonstration of aerobic mineralisation of cDCE to CO₂ by microbes isolated from streambed media was demonstrated by Bradley and Chapelle

(2000a). They used microbes extracted from the aforementioned streambed site in liquid microcosms and the work indicated similar rapid activities to the 1998 study, however, no direct evidence of microbial growth was observed. More recent work using isotopic fractionation and protein quantification has verified that microbial growth is coupled with DCE degradation using various microcosm configurations (e.g., Schmidt et al., 2010).

2.4.2.3 *Biological oxidation of VC*

The accumulation of VC in sediment pore water poses great concerns due to its toxicity and known carcinogenicity. As VC contains only a single chlorine atom, the carbon backbone of the ethene molecule has a greater tendency to undergo oxidation than any other CE. Hartmans et al. (1985) used 1% (v/v) VC in the vapour phase as a substrate which sustained the growth of a population of *Mycobacterium*. Davis and Carpenter (1990) were among the first to document aerobic oxidation of [¹⁴C]-VC to ¹⁴CO₂ in aerobic groundwater samples taken a river bank where no other substrates such as CH₄ were present. They observed 99% removal of amended [¹⁴C]-VC after 108 days with approximately 65% recovered as [¹⁴C]-CO₂. Later work has also demonstrated relatively rapid aerobic oxidation of VC in aquifer microcosms (Bradley and Chapelle, 1996; Bradley et al., 1998a, Bradley and Chapelle, 1998a, b) as well as under anaerobic TEAPs including Fe reduction, SO₄²⁻ reduction and CO₂ reduction (methanogenesis) (Bradley and Chapelle, 1996; Bradley and Chapelle, 1998a). In the aforementioned streambed study, Bradley and Chapelle (1998a) demonstrated mineralisation of 45-100% [¹⁴C]-VC removal in just 8 days. Where DCE was also included in microcosm amendments, VC mineralisation was observed at a greater rate (Bradley and Chapelle, 1998a, b). In a field-scale study, Witt et al. (2002) inferred significant aerobic VC oxidation within a CE-contaminated site associated with the anaerobic-aerobic transition zone of the plume.

Bacteria capable of VC oxidation as a primary substrate in the presence of oxygen and absence of cometabolic substrates are thought to be well distributed in the subsurface (Coleman et al. 2002) and several strains have been isolated including *Mycobacterium aurum* (strain L1) (Hartmans et al., 1985) and *Pseudomonas aeruginosa* (strain MF1) (Verge et al., 2002), *Mycobacterium* (11 individual strains), *Nocardioides* (strain JS614) (Coleman et al., 2002) *Ralstonia* sp. (strain TRW-1) (Elango et al., 2006). Gossett (2010) found that VC oxidation could be sustained by *Mycobacterium* at extremely low (microaerophilic) DO concentrations (e.g. 0.01–0.02 mg L⁻¹) raising the important question as to whether previously reported weakly anaerobic conditions (e.g., metal-reducing) in fact contain low levels of DO which can sustain oxidation of VC. The metabolic interactions between methanogenesis, acetogenesis and VC degradation under highly anaerobic conditions has been shown to be complex. Bradley and Chapelle (1999a) investigated VC metabolism under highly reducing methanogenic bed sediments of a lake and stream. Their work provided evidence that CH₄ can be produced as a terminal metabolite of [¹⁴C]-VC anaerobic oxidation where ¹⁴CH₄ was detected in addition to ¹⁴CO₂. In a follow up study utilising [¹⁴C]-acetate, Bradley and Chapelle (1999b) postulated that VC may be degraded via syntrophic oxidative acetogenesis followed by acetotrophic methanogenesis as a mechanism leading to CH₄ and CO₂ as terminal metabolites. Using radiometric chromatography, transient accumulation [¹⁴C]-acetate as a reactive intermediate was confirmed by Bradley and Chapelle (2000b) indicating a novel coupling of acetogenic fermentation with methanogenic VC degradation. The study also indicated that oxidative acetogenesis may play a significant role catalysing the initial steps of VC mineralisation under reduction of humic substances, Fe³⁺ and SO₄²⁻ as TEAs.

2.4.3 Cometabolic transformation of CEs

CEs can be transformed under aerobic conditions by cometabolic reactions initiated by enzymes produced by a wide range of aerobic microbes (Arp et al., 2001). It is not thought that these reactions provide any benefit to the organism responsible through acquisition of metabolic energy or as a source of carbon for cellular growth (Horvath 1972). Cometabolic oxidation of CEs is a widespread process involving microbial populations that express non-specific monooxygenase or dioxygenase enzymes that catalyze the initial step in oxidation of a carbon co-substrate in the presence of DO and source of reducing equivalents (Bradley, 2003). Some of the first reports of environmental degradation of CEs have been attributed to cometabolism. For example, Wilson and Wilson (1985) demonstrated removal of TCE by biological activity in soil columns fed by a natural gas/air stream composed predominantly of methane. Later work revealed the enzyme methane monooxygenase to be responsible for catalysing the reaction with TCE (e.g., Alvarez-Cohen and McCarty, 1991; Wymore et al., 2007). The lack of enzyme specificity leads to competition between CEs and co-substrates for active sites of oxygenases leading to incorporation of O₂ into the CE molecule via epoxidation (Mattes et al., 2010). TCE, DCE and VC are all amenable to cometabolic aerobic oxidation by the action of oxygenases during syntrophic oxidation of reduced co-substrates. PCE was originally thought to be recalcitrant to aerobic oxidation under environmental conditions (e.g., Weidemeier et al., 1998); however, it has since been shown to be degradable by the enzyme toluene-*o*-xylene monooxygenase (Ryoo et al., 2000). The most important natural co-substrates likely to be present at aquifer-river interfaces include ammonium (Arciero et al., 1989; Kocamei and Cecen, 2010) and methane (Fogel et al., 1986; Conrad et al., 2010). Indeed, Bradley (2000) suggests that aerobic cometabolism could be a significant natural attenuation mechanism for TCE at the groundwater-surface water interface of organic-rich streambeds which are known to

support methanotrophic bacterial communities. Also of interest in CE degradation is the coupling of direct oxidation of lower-chlorinated CEs with cometabolism of higher ones, thereby negating the need for exogenous co-substrates within reactive sediment zones. This is well described for oxidation of VC with simultaneous cometabolism of cDCE (Freedman et al., 2001; Verce et al., 2002). Bradley and Chapelle (1998a, b) do not preclude aerobic cometabolism as an unobserved process partly responsible for the rapid mineralisation of cDCE (presumably utilising VC as a co-substrate), but this has not been repeated to the same extent in later work. Cometabolism of VC and cDCE by ethene and ethane oxidisers is also reported by other authors (Freedman and Herz, 1996; Le and Coleman, 2011). In addition, cometabolic reductive dechlorination has also been cited as a significant degradation process, albeit difficult to distinguish from dehalorespiration at field scale. For example, the final dechlorination step of VC to ethene by *Dehalococcoides ethenogenes* (strain 195) is purported to be a cometabolic process (Maymo-Gatell et al., 1997). The metabolites of aerobic cometabolism such as TCE epoxide are unstable and may abiotically decompose into a variety of non-volatile intermediates including dichloroacetic acid, chloral hydrate, formate, glyoxylate and carbon monoxide which may present significant toxicity to the enzyme-producing microbes (Mattes et al., 2010; Suttinun et al., 2013). The environmental fate of these chlorinated oxidation products is not well understood but they may ultimately be amenable to final biotic or abiotic mineralisation to Cl^- and CO_2 (Bradley, 2003).

2.4.4 Abiotic dechlorination by natural reductants

Reduced phases of iron (e.g. Fe^0 or Fe^{2+}) are known to serve as natural reductants capable of transforming chlorinated ethenes to lower chlorinated forms or non-chlorinated end-products, in the absence of direct biological mediation. Iron minerals such as pyrite (FeS_2),

mackinawite (FeS), troilite (FeS), magnetite (Fe₃O₄), ‘green rusts’ and iron-bearing phyllosilicates (e.g. biotite, montmorillonite and vermiculite) have all been shown to have significant dechlorination activity with PCE, TCE, cDCE and VC (Butler and Hayes, 1999; Lee and Batchelor, 2002a; 2002b; 2004; Ferrey et al., 2004; Jeong and Hayes, 2007; Jeong et al., 2011). Pyrite and mackinawite have been shown to reduce TCE in parallel through β -elimination to chloroethyne (where two chlorine atoms of the CE are reduced to Cl⁻ with the formation of C-C triple bond) or via reductive hydrogenolysis to cDCE (Butler and Hayes, 1999; Jeong and Hayes, 2007). Removal of cDCE and VC using magnetite has been reported by Lee and Batchelor (2002a) and Ferrey et al. (2004) in sterilised batch experiments. He et al. (2010) investigated the reaction kinetics of mackinawite on TCE reduction and found that it was 20-50 times less reactive after freeze-drying due to a reduction in the effective mineral surface area and changes in mineral composition as a result of the treatment process. Jeong et al. (2011) found pronounced dechlorination of cDCE by metastable Fe²⁺-containing oxyhydroxides under iron-reducing conditions and attributed a significant proportion of the reactivity due to the action of surface-complexed Fe²⁺. Also in that study, cDCE degradation was complete to the non-chlorinated ethyne or ethene via β -elimination. Many of these studies document cases of CE degradation in the soil zone, however, abiotic degradation of CEs has also been observed at depth in bedrock aquifers. For example, Darlington et al. (2008) investigated apparent attenuation of cDCE at depths of over 200m in a fractured sandstone aquifer produced from microbial reductive dechlorination of TCE. Abiotic degradation of radiolabeled [¹⁴C]-cDCE was confirmed by anaerobic microcosms prepared from groundwater and drill cores. [¹⁴C]-cDCE degradation to non-volatile products including glycolate, acetate, and formate was observed in sterile microcosms resulting from an as yet unknown abiotic transformation process. From a remediation perspective, the β -elimination pathway is an attractive attenuation mechanism

as it prevents production (and the potential accumulation) of the toxic and carcinogenic intermediate VC. As such, this pathway is often targeted for engineered permeable reactive barriers utilising particulate Fe^0 to treat CE plumes adjacent to DNAPL source areas (e.g. Arnold and Roberts, 2000). At aquifer-river interfaces, iron sulphides may be present in clastic sediment derived from weathering of sulphide-containing rocks, through precipitation of acidic mine effluents (Gandy et al., 2004) and/or under highly reducing conditions as a result of microbial reduction of Fe^{3+} bound in the mineral phase with concomitant bacterial SO_4^{2-} reduction (Morse et al., 1987; Kennedy and Everett, 2001). The later scenario was envisaged by Kennedy et al. (2006) where Fe^{3+} and SO_4^{2-} were naturally abundant in the form of matrix clay minerals and gypsum-rich shale in an aquifer contaminated with high levels of TCE (e.g., $>10 \text{ mg L}^{-1}$) associated with an accidental fuel oil spill at the Altus Air force Base (Oklahoma, US). The introduction of an extraneous organic carbon source from the fuel spill was found to promote highly reducing conditions favouring microbial Fe and SO_4^{2-} reduction and the precipitation of FeS within a clay-rich zone of the plume. Elimination of TCE due to the presence of FeS was observed in equal amounts between live and sterile microcosms without significant detections of either cDCE or VC. After exhaustion of FeS, no further removal of TCE was reported suggesting a coupling of abiotic Fe^{2+} oxidation with geochemical dechlorination of TCE to acetylene and chloride.

2.5 Approaches to investigate CE plume fate at aquifer-river interfaces

2.5.1 Characterising groundwater discharge pathways

2.5.1.1 Geophysical methods

As non-ionic solutes at dilute aqueous concentrations (e.g., 10s–1000s $\mu\text{g L}^{-1}$) CEs do not have sufficiently contrasting geophysical properties to distinguish them from other dissolved constituents in ambient groundwater. Therefore, they are not directly detectable by their geophysical properties alone, in contrast to highly conductive landfill leachate plumes (e.g., Acworth and Jorstad, 2006). However, geophysical ‘imaging’ of the architecture of stream beds and riparian zones is a potentially powerful non-intrusive tool to aid in conceptualising stream-aquifer interactions at reach scale. Binley et al. (2010) review the emerging discipline of ‘hydrogeophysics’ in the context of subsurface hydrological investigations and indicates the potential of such techniques at aquifer-river interfaces. In particular, electrical and electromagnetic methods are capable of delineating important near-stream stratigraphic controls on groundwater discharge, such as the depth to bedrock and the lateral continuity and thickness of hydrofacies, with a measurement density not possible with direct observations from cores (Cardenas and Zlotnik, 2003; Crook et al., 2008). Despite these benefits, only a limited number of studies have applied geophysical methods to characterise plume discharge sites and groundwater-surface water interfaces in general. Conant et al. (2004) used ground-penetrating radar (GPR) deployed in-stream from an inflatable boat to image sub-channel sediments along a reach of the Pine River (Ontario, CA) where a PCE plume emanating from a dry cleaner was suspected to be discharging. They were able to visualise the geometry and lateral extent of semi-confining deposits observed in core samples and as well as identify areas of the riverbed where these

confining layers were absent. Similarly, Lyford et al. (1999) used bank-side GPR profiles to image the thickness and continuity of glacial deposits along the banks of the Royal River (Maine, US) where a TCE plume was known to discharge. Crook et al. (2008) demonstrate the potential of electrical resistivity imaging (ERI) of alluvial groundwater systems. They document examples where ERI could be applied to determine the thickness and extent of an alluvial gravel aquifer overlying a chalk aquifer noted from borehole logs at the River Lambourne (Berkshire, UK). They also used cross-borehole measurements across the river to visualise the lateral continuity of the alluvial aquifer below the channel. Nyquist et al. (2009) is one of the few published examples where ERI was applied directly along a streambed to image sub-channel structure.

2.5.1.2 *Temperature as a tracer*

Groundwater temperature is often seen as a robust natural tracer for understanding spatial and temporal dynamics of groundwater discharge through riverbeds in both contaminated and pristine environments (e.g., Conant, 2000, Lowry et al., 2007; Keery et al., 2007; Kalbus et al., 2009; Krause et al., 2011b). Groundwater temperatures at sufficient depth typically show little annual variability in comparison to surface water, which fluctuates both seasonally and diurnally. Therefore, when a significant contrast exists (e.g., in summer or winter), concentrated zones of groundwater upwelling in riverbeds appear as cold spots, thereby allowing the spatial heterogeneity of groundwater contributions to river flow to be observed along a reach (Stonestrup and Constatz, 2003; Schmidt et al., 2006; Kalbus et al., 2009; Annibas et al., 2009). Temperature measurements have the particular advantage of being technically simple and rapid to acquire over spatial scales of centimetres to 100s of metres with little or no intrusion into bed materials (as well as allowing the water flux to be estimated which is discussed in the next section). Conant

(2000) was one of the first to explore temperature tracing in riverbeds with up to 500 individual measurements arranged as a regular grid covering a 60 m reach at a depth of 0.2 m in the bed of the Pine River site. By using temperature observations, it was possible to characterise groundwater-surface water connectivity at metre-scales in the riverbed deposits and conceptualise five distinct types of groundwater discharge at the site during baseflow. Advances in optical reflectometry have allowed the use of fibre-optic distributed temperature sensors (FO-DTS) to trace patterns of groundwater discharge along river reaches (e.g., Selker et al., 2006; Krause et al., 2012) where concurrent measurements of temperature are taken along a cable buried directly in the riverbed with spatial and temporal resolutions exceeding that practical with manual measurements. In one example in an uncontaminated setting, Lowry et al. (2007) used FO-DTS to identify focussed groundwater discharge to wetland stream through ‘soil pipes’ within peat deposits over an 800 m reach at a spatial resolution of 1 m. These features were presented as spatially discrete and temporally persistent temperature anomalies collected at 1 minute intervals over 48 hours.

2.5.2 Delineating plume discharge zones

Although the methods discussed previously provide for the characterisation of near-river stratigraphy and groundwater discharge patterns, concentration data are required in order to validate assumptions of actual contaminant transport pathways.

2.5.2.1 *Passive sampling*

Diffusion sampling using unobtrusive methods is an attractive tool for the screening of in-situ contaminant concentrations as it allows representative sample acquisition with minimal disruption to the riverbed flow regime (Church et al., 2002). Moreover, passive

sampling provides time-integrated concentrations, which ‘smooths out’ local fluctuations and allows low concentrations to be determined accurately. Passive vapour sampling (utilising partitioning of dissolved VOCs to the vapour phase of a vial covered by a polyethylene film) has been used to map the distribution of CE plumes in plan view in unconsolidated benthic sediments. The approach is advantageous in that it does not require any pre-existing monitoring wells to be in place, thereby significantly reducing investigation costs. Vroblesky et al. (1991) used test tubes containing activated carbon fused to ferromagnetic wires as an adsorbent trap at 40 locations in tidal creek where groundwater contaminated with PCE, TCE and other VOCs was discharging. Later work, using vapour samplers (without requiring an adsorbent trap), have been successfully applied at groundwater/surface water interfaces for high-resolution spatial plume delineation in diffuse-flow aquifer media (Lyford et al., 1999; Church et al., 2002) as well as fractured bedrock systems (Vroblesky and Robertson, 1996; Vroblesky et al., 1996; Church et al., 2002).

2.5.2.2 *Multi-level sampling*

Given the natural heterogeneity of most fluvial deposits, multi-level sampling of the top few metres of the sediment profile is recognised as an important step in discharge zone assessment to delineate the 3-dimensional configuration of discharging plumes and identify reactive zones (Rivett et al., 2008). This has been accomplished using nested piezometers (Norman et al., 1987; Lorah and Olsen, 1999) drive-point mini-piezometers (Conant et al., 2004; Ellis and Rivett, 2007; Roche et al., 2008), multi-level sampler bundles (Conant et al., 2004), the ‘waterloo profiler’ (Pitkin, et al., 1999; Conant et al., 2004) and ‘peepers’ (Lorah and Olsen, 1999; LaSage et al., 2008). Rivett et al. (2008) describe the design and application of cost-effective mini-piezometers that are suitable for vertical profiling when

used to assess urban baseflow quality along a 7 km stretch of the River Tame in Birmingham City, UK. They document the initial detection of TCE and its daughter product *cis*-1,2-dichloroethene (cDCE) during a coarse piezometer survey (100–300 m spacings) that was followed by progressive refinement of the network to include cross-channel transects over a 50 m reach. This revealed a TCE plume discharge zone with significant spatial variability across the reach and concentration changes from <0.1 to $800 \mu\text{g L}^{-1}$ over depths of 10 to 40 cm below the riverbed. Roy and Bickerton (2010) document the use of a simple pore water mini-profiler that could be easily deployed into unconsolidated sediments allowing rapid acquisition of riverbed samples to screen urban groundwater baseflow quality. They applied this technique to a site on the Pine River, Angus (Ontario, CA) where a PCE plume was known to discharge (Conant et al., 2004). They were able to successfully reproduce contaminant distribution patterns along a longitudinal profile which closely resembled that of previous plume delineation at the site (Conant et al., 2004) but with the benefit of minimal costs and labour.

2.5.3 Estimating plume fluxes to rivers

Monitoring contaminant mass flux from groundwater to surface water is an important element in assessing the potential risks posed by CE plumes discharging to surface water bodies. Basu et al. (2006) define contaminant mass discharge for plume-scale studies as the contaminant mass per unit time that migrates across a hypothetical ‘control plane’ situated down-gradient of the source and orientated orthogonal to the mean groundwater flow direction. However, at aquifer-river interfaces, control planes for uncharacterised plumes may not be always be easy to define. Therefore, plume-scale flux assessments are most easily made from point-observations where groundwater fluxes can be estimated (Kalbus et al., 2006) and, where contaminant concentration data are available, a flow-concentration

product approach can be used to quantify mass flux rates (Ellis and Rivett, 2007).

2.5.3.1 *Initial studies of discharging plumes*

Norman et al. (1986) assessed the discharge of a VOC plume containing vinyl chloride (VC) and dichloroethene (DCE) to the Chocato River (Massachusetts, US) using a network of seepage meters and nested single level piezometers. Using groundwater flow calculated from Darcy velocities and seepage meters, they estimated a total VOC load of 1.9 kg y^{-1} to be discharging from groundwater to the river. Avery (1994) used a combination of seepage meters, monitoring wells and a 2-D numerical flow model to estimate a TCE discharge of 2 g d^{-1} to a river emanating from a 'Superfund' toxic waste site. However, only a single monitoring well adjacent to the river was able to provide a concentration term. Although these direct methods are capable of providing local loading estimates, heterogeneity on the scale of metres to centimetres may introduce significant uncertainties when attempting to up-scale and integrate observations over whole river reaches. In addition, there are often practical difficulties installing seepage meters in gravel or cobble bed materials which may significantly bias results (Ellis, 2003).

2.5.3.2 *Temperature methods*

Where contaminant concentrations are known, a mass flux may be calculated from the advective heat flow determined from the three-dimensional distribution of temperature in riverbeds (Kalbus et al., 2007; 2009; Schmidt et al., 2008; Annibas et al., 2009). Estimations of groundwater fluxes to rivers have been accomplished using temperature time series with limited spatial resolution (Hatch et al., 2006; Keery et al., 2007) and synoptic surveys of temperature profiles at high spatial resolutions (Conant, 2000; Schmidt et al., 2006; 2007). The aforementioned Conant (2004) study was the first to use high-

resolution temperature gradient measurements in plan-view to obtain a groundwater flux by deriving a relationship between the measured temperature gradient and the actual measurement of groundwater flux in piezometers, with quantification of hyporheic mixing using geochemical tracers. The study was able to show that groundwater discharge from 7% of the riverbed area contributed to up to 24% of the total discharge through the reach. Later work has used analytical solutions for heat flow equations produced in the 1960s (e.g. Suzuki, 1960; Stallman, 1965), in combination with field measurements of temperature gradients and an estimation of riverbed thermal properties, to calculate the vertical Darcy flow without the need for any additional flux estimation when vertical flow and quasi-steady state conditions can be assumed (Schmidt et al., 2006; 2007). Schmidt et al. (2007) applied an analytical one-dimensional, steady-state heat diffusion-advection equation (Turncotte and Schubert, 1982) to re-analyse the temperature data acquired by Conant (2004) and were able to achieve similar vertical Darcy fluxes and spatial patterns to those of the original study.

2.5.3.3 *Combined approaches*

Many authors advocate a combination of approaches in order to overcome the uncertainties associated with individual methods (Kalbus et al., 2006; Ellis et al., 2007; Milosevic et al., 2012). Kalbus et al. (2007) used a novel combination of integral pumping tests (IPTs) with streambed temperature profiling to estimate fluxes of chlorinated benzenes (chiefly monochlorobenzene and dichlorobenzene) to the Schnachtgraben stream (Bitterfeld, Germany). They used IPTs to accurately determine contaminant concentrations in the groundwater plume discharging laterally through a well-defined control plane situated adjacent to the stream. They achieved this by simultaneously pumping four abstraction wells and continuously monitoring contaminant concentrations in the abstracted

groundwater over wide zones (10s of metres) surrounding wells. By using temperature gradient measurements and heat flow equations (Schmidt et al., 2006), they were able to estimate a flux of $272 \mu\text{g m}^{-2} \text{d}^{-1}$ for monochlorobenzene and $76 \mu\text{g m}^{-2} \text{d}^{-1}$ for dichlorobenzene. However, the possible effects of sorption and biodegradation were not considered in their estimate. Of all studies that have investigated groundwater VOCs discharging to rivers, none to date have considered the ‘city scale’ river reach such as that described in Ellis and Rivett (2007). Their study instrumented a 7.4 km reach of the River Tame (Birmingham, UK) with a network of mini-piezometers along 19 cross-channel transects. They used five flow-concentration product methods including, flow gauging, mean Darcy fluxes from piezometers and falling head tests, baseflow separation curve analysis, incremental flow gauging and incremental changes in surface water quality. By combining these methods they were able to estimate a city scale flux of TCE of 22–200 kg y^{-1} integrated over the instrumented reach. However, their flux estimate approach, based on measurements of surface water VOCs, did not include quantification of volatilisation and the authors accept that (1) entire plumes may have been missed by the configuration of their piezometer network and that (2) occasional high concentrations in piezometers were strongly influencing their Darcy flux estimates. Nevertheless, given the huge uncertainties associated with urban groundwater systems, their estimates were in agreement to within one order of magnitude and this remains the only study to investigate baseflow contamination at such a large scale.

2.5.4 Demonstrating in-situ transformation at field scale

2.5.4.1 Parent-daughter relationships

Observations of declining primary contaminant concentrations and/or production of lower chlorinated metabolites are key lines of evidence to support the occurrence of in-situ natural attenuation within plumes at the field scale (Wiedemeier et al., 1998; Witt et al., 2002). At aquifer-river interfaces, these observations can be made through point sampling along vertical profiles following theoretical plume discharge flow paths. With multi-level concentration information, quantitative metrics can be used to evaluate the extent of in-situ reductive dechlorination where the effects of dilution and dispersion may lead to erroneous interpretation of raw concentration data. For example, Ellis and Rivett (2007) and Roche et al. (2008) used molar ratios of daughter products to parent CEs (e.g., cDCE:TCE, VC:cDCE or TCE:VC) sampled along vertical riverbed profiles. They were able to demonstrate that limited dechlorination of TCE was occurring in shallow anaerobic sediment zones along piezometer profiles in the riverbed of the urban River Tame site. Other metrics have been devised which take into account products of the full dechlorination sequence and integrate them into a single convenient number. Damgaard et al. (2013) calculated the degree of dechlorination (DoD) on high-resolution core sampling in order to determine the performance of enhanced reductive dechlorination of CEs in a fractured clay-rich till. DoD quantifies the completeness of reductive transformation of a primary CE as a function of the stoichiometric fractions of daughter products in the dechlorination chain, where $\text{DoD} = 0$ indicates no degradation and $\text{DoD} = 1$ where complete dechlorination has taken place. In a similar approach, a 'chlorine number' (N_{Cl}) is derived where the CE species present are composited and scaled from ~ 0 to 3, in the

case of TCE (Weaver et al., 1997; Freitas et al., 2015). This can be calculated using Equation 2.6 provided by Weaver et al. (1997).

Equation 2.6
$$N_{Cl} = \frac{\sum W_i C_i}{\sum C_i}$$

Where W_i is the number of chlorine atoms in the CE molecule (e.g., 3 for TCE, 2 for cDCE and 1 for VC, etc.) and C_i is the molar concentration of each CE species present. An N_{Cl} of close to 0 indicates no organically-bound chlorine is present and the plume consists entirely of ethene whereas an N_{Cl} of 3 indicates no degradation has taken place with only TCE present. A reduction in chlorine number along vertical profiles in riverbed piezometers can be used to determine whether any in-situ transformation has taken place (Freitas et al., 2015). Weaver et al. (1997) used this approach to demonstrate in-situ transformation of a TCE plume in Michigan, US where a reduction in chlorine numbers could be attributed to anaerobic and locally methanogenic zones within the plume.

2.5.4.2 *Compound-specific isotope analysis*

Advances in mass spectrometry now allow the measurement of molecular-level isotope ratios of CEs. Compound-specific stable isotopes analysis (CSIA) relies on differences in reaction rates between molecules with light (e.g., ^{12}C , ^{35}C , 1H) and heavy (e.g., ^{13}C , ^{37}C , 2H) isotopes, leading to kinetic isotope fractionation (Meckenstock et al., 2004). Lighter isotopes are preferentially degraded by microbial enzymes leading to a progressive enrichment of heavier isotopes in the remaining substrate, which can be expressed as a ratio e.g. $^{13}C/^{12}C$ ($\delta^{13}C$) of a standard in the per mil notation (‰). CSIA has become a powerful tool as it allows non-reactive processes (which affect contaminant concentrations) such as dilution, dispersion and sorption to be distinguished from biotic attenuation processes within complex plumes such as those containing both primary and

secondary products and/or originating from multiple sources (Song et al., 2002; Hunkeler et al., 2004, 2011; Hamonts et al., 2012). Meckenstock et al. (2004) provide a comprehensive overview of the groundwater-related isotopic fractionation processes of organic contaminants in the context of biodegradation. Hunkeler et al. (1999) were one of the first to apply CSIA in order to characterise the fractionation of carbon in reductive dechlorination of PCE to ethene. They observed significant enrichment of $\delta^{13}\text{C}$ in microcosms during reductive dechlorination of cDCE (-25.7 to -1.5‰) and VC (-37.0 to -2.5‰) and during ethene formation (-60.2‰ to -27.3‰) the latter of which approached the initial PCE $\delta^{13}\text{C}$ signature indicating complete reductive dechlorination. Aerobic degradation of CEs has been shown to produce significant isotopic fractionation. This is of particular importance for demonstrating degradation pathways at the field scale as the non-specific metabolites (e.g., Cl^- and CO_2) produced are often indistinguishable from high background concentrations of these major solutes. Tiehm et al. (2008) observed $\delta^{13}\text{C}$ enrichment factors of -5.4‰ during oxidation of VC and -9.8‰ during cometabolic oxidation of VC. Schmidt et al. (2010) observed an average enrichment of -15.2‰ during the aerobic mineralisation of cDCE as a sole carbon source. Abe et al. (2009) used CSIA to interpret the transformation patterns of a PCE plume in riverbed pore water profiles at the Pine River site. In this case, several PCE source $\delta^{13}\text{C}$ signatures were observed within the discharge zones of the plume where the isotopic variability of PCE was attributed to a mixing of sources. cDCE $\delta^{13}\text{C}$ values were found to be stable in areas where concentrations were varied significantly with values similar to that of the primary PCE contaminant mass indicating complete transformation of PCE to cDCE. In other locations, the $\delta^{13}\text{C}$ signature of ethene was similar to that of PCE indicating complete reductive dechlorination. Hamonts et al. (2012) monitored the $\delta^{13}\text{C}$ of VC impacting a reach of the Zenne River (Belgium) over a 21 month period where previous biotic and abiotic attenuation was

shown to be occurring at certain locations (Hamonts et al., 2008). Using a site-specific $\delta^{13}\text{C}$ enrichment factor for VC, they were able to show that temporal variability in the extent of biotransformation was generally minimal in contrast to reduction in concentrations as a result of in-situ dilution from downwelling surface water.

2.5.4.3 *Novel molecular biomarkers*

Molecular microbiological techniques have recently become available to characterise microbial degradation processes in contaminated aquifers (Weiss and Cozzarelli, 2008). The application of quantitative polymerase chain reaction (qPCR) amplification and sequencing of 16S ribosomal RNA (rRNA) has become an increasingly important tool in characterising indigenous microbial community structure, function and spatial distributions within CE plumes. Of particular interest is demonstrating the presence and activity of populations of *Dehalococcoides* spp. and other dechlorinators where their growth can be linked to sequential production of daughter products and consumption of electron donors (Hendrickson et al., 2002; Sung et al., 2006). The 16S rRNA gene of the *Dehalococcoides* genus and other bacterial groups is highly conserved between species and its amplification and sequencing can be used to distinguish between individual microbial populations and their phylogenies (Löffler et al., 2013; Taş et al., 2010). Recent whole genome sequencing of a number of *Dehalococcoides* strains has allowed functional genes, which encode for specific reductive dehalogenase enzymes, to be identified (Maphosa et al., 2010). Genes include *pceA* and *tceA* (strain 195) (Fung et al., 2007) which dechlorinates PCE and TCE, respectively, and *vcrA* (strain VS) (Muller et al., 2007) and *bvcrA* (strain BAV1) (Krajmalnik-Brown et al., 2007) which are known to reduce VC. In a study investigating the degradation potential of hexachlorobenzene, Taş et al. (2011) used 16S rDNA qPCR-based molecular approaches to quantify the abundance of *Dehalococcoides* spp. from 15

sediment sampling locations across four European catchments, all with a history of organochlorine contamination. Of these sites, *Dehalococcoides* spp. were found to be present at 80% of locations indicating a high prevalence of this environmentally important genus in contaminated riverbed sediments. Similarly, Hamonts et al. (2014) found that the prevalence dehalogenase-encoding genes and microbial community structure did not differ between areas where significant dechlorination and no dechlorination of VC and cDCE was occurring in a eutrophic riverbed in Belgium. At the Pine River site in Canada impacted by a PCE plume, Abe et al. (2009) used PCR-amplifiable primers to detect the presence of *Dehalococcoides* in order to validate the anaerobic reductive dechlorination of VC. In addition, the gene responsible for encoding a key enzyme in the aerobic oxidation of VC and ethene was identified (EaCoMT) by a PCR-based approach. Their work showed that *Dehalococcoides* occurred in the sediment profile where sedimentary organic matter was greater than 2% (g g^{-1}) with stronger signals occurring at greater depths. In contrast, the EaCoMT gene was detected at 35 out of 37 locations in a range of sediment types including sandy areas with no known VC exposure, indicating a high aerobic VC oxidation potential throughout the site.

2.6 Chapter summary

This chapter has outlined the hydrological and biogeochemical framework of the aquifer-river interface through which CE plumes must transit. Sorption is probably the most important non-destructive attenuation mechanism for aquifer-river interfaces but has not been widely investigated in field studies. Where organic matter is present, retardation is likely to significantly surpass the up-gradient aquifer. A wide range of microbes potentially present in riverbeds are capable of dechlorinating TCE as far as cDCE. Electron donors are likely to be derived from the fermentation products of DOC, however detailed field investigations of the role of DOC in reductive dechlorination are lacking. Further dechlorination to VC or ethene may be subject to competition for available H₂ between SO₄²⁻ reducers and methanogens. VC is rapidly oxidised by DO but cDCE is likely to be more persistent in aerobic riverbeds. Cometabolism may be a significant transformation mechanism in riverbeds where methanogenesis is occurring. However, because no stable metabolites are generated by this process, demonstrating its activity at field-scale is problematic. Passive sampling and environmental geophysics offer cost-effective, non-intrusive approaches to delineate plume discharge zones and characterise the geological framework of aquifer-river interfaces. Flow-concentration product approaches can be used to estimate mass fluxes from plumes, however uncertainty in the flow or concentration terms is introduced by local heterogeneity. Where a thermal gradient exists, temperature can be a robust natural tracer of groundwater discharge through riverbeds which can be applied at a spatial resolution that would be impractical with more intrusive methods. New isotopic and molecular biological techniques provide powerful new tools to assess in-situ transformation pathways of CEs. Alternatively, simple quantitative metrics can be applied to concentration data in order to quantify the extent of reductive dechlorination of a parent compound which removes the confounding effects of dilution and dispersion.

3. Study area, materials and methods

3.1 Chapter introduction

An integrated conceptual understanding of groundwater contaminant fate at lowland aquifer-river interfaces requires multi-scale observations of geological properties, groundwater flow, surface water interactions and hydrochemical gradients. This chapter begins by providing a comprehensive overview of the study area from river basin-scale to reach-scale and characterises the hydrological, geological and hydrogeological setting which frames this research. The prior understanding of the nature of the TCE contamination is described and details of the existing monitoring networks available are provided. This chapter goes on to describe the construction and deployment of the different groundwater investigation tools and documents the establishment of new monitoring networks and techniques to investigate water flow and the hydrochemistry at the aquifer-river interface. A scientific rationale for their application is also outlined. The key methods used to acquire primary physical, hydrological and chemical data are then provided together with quality control measures and analysis of uncertainties. Where the subsequent analysis of primary datasets was undertaken, the details are included at the start of the relevant chapter sections. The statistical procedures used for quantitative data analysis are briefly discussed. The majority of field data collection was undertaken from 2011–2012 and in the summer of 2013. The specific dates of individual campaigns are indicated in the relevant chapter sections.

3.2 Study area characteristics

3.2.1 Physiography of the River Tern catchment

The River Tern is a major tributary of the River Severn and from its source in the Maer Hills drains a total basin area of 852 km². It is joined by two principal tributaries; the River Roden and River Meese as well as numerous smaller brooks and rivers (Fig. 3.2.1). The catchment lies in the North Shropshire plain and is generally low-lying with subdued relief, although some higher ground is present in the north. Elevations are generally between 50 and 90 m AOD (Streetly and Shepley, 2005). Population density in the catchment is quite low with Telford and Market Drayton forming the most significant urban centres (Fig. 3.2.1). The study area is located close to the headwaters of the catchment (Fig. 3.2.1) where the upriver basin area is 92.6 km² and the river is joined by a small tributary known as the Bailey Brook (Fig. 3.2.1) (Marsh and Hannaford, 2008). The course of the River Tern in the study area is largely natural and has not been significantly modified by human activities since the mid-19th century (Keery, 2005). According to the UK Land cover 2000 survey data, the upper catchment is predominantly semi-intensive agricultural with grassland accounting for the majority of the land area (53%) followed by arable and horticultural (30%), woodland (12%) and urban areas (5%) (Fuller et al., 2002).

3.2.2 Hydrology

The Tern catchment has a moderate climate with a long-term mean annual rainfall of 740 mm (1957–2007) upstream of the study area decreasing to 583 mm at lower elevations (Hannah et al., 2009). The majority of rainfall occurs from December to March (Blackwell, 2002) whilst the long-term average air temperature is 9.3 °C (1957–2007). January is the coldest month with a mean minimum of 3.7 °C and July the warmest, with an average

maximum of 15.8 °C (Hannah et al., 2009). The River Tern is gauged approximately 5 km upriver of the study area (NGR SJ 629316) at Ternhill hydrometric station (Fig. 3.2.1) which records a long term (1972–2005) mean daily flow of 0.86 m³ s⁻¹ (Marsh and Hannaford, 2008). The river exhibits a baseflow-dominated flow regime with a high baseflow index (BFI) of 0.77 (Marsh and Hannaford, 2008). Groundwater seepage from the highly permeable Permo-Triassic sandstones (PTS), which underlie much of the catchment, maintains the high baseflow rate during dry weather periods (Shepley and Streetly, 2007). This is reflected by the substantial 95th exceedance percentile flow (Q₉₅) of 0.41 m³ s⁻¹ which is approximately half of mean flow (Marsh and Hannaford, 2008). Using stable isotopes of water as a tracer, Clay et al. (2004) demonstrated that river's flow was dominated by groundwater discharge in summer but autumn/winter were more influenced by precipitation. Hydrographs for the River Tern and Bailey brook typically show event flows superimposed over a seasonal groundwater baseflow oscillation with 'flashy' responses occurring after prolonged rainfall. Runoff is generated from the low-permeability Triassic mudstone in the upper catchment (Streetly and Shepley, 2005). However, overbank flooding is considered to be rare (Keery, 2005). The 10 km reach of the River Tern near the study area has a biological water quality rating of Class A (or 'very good') as measured between 2005–2009 by the Environment Agency (EA) (www.environment-agency.gov.uk). Invertebrate assemblages characteristic of an unpolluted river have been documented in this period (Wright et al., 2000) which represents an improvement from Class B 'good' in the years 2001–2004. However, the river suffers from severe nitrate pollution with the worst nitrate grade of Class 6 (>40 mg NO₃⁻ L⁻¹) held consistently from 1990–2009.

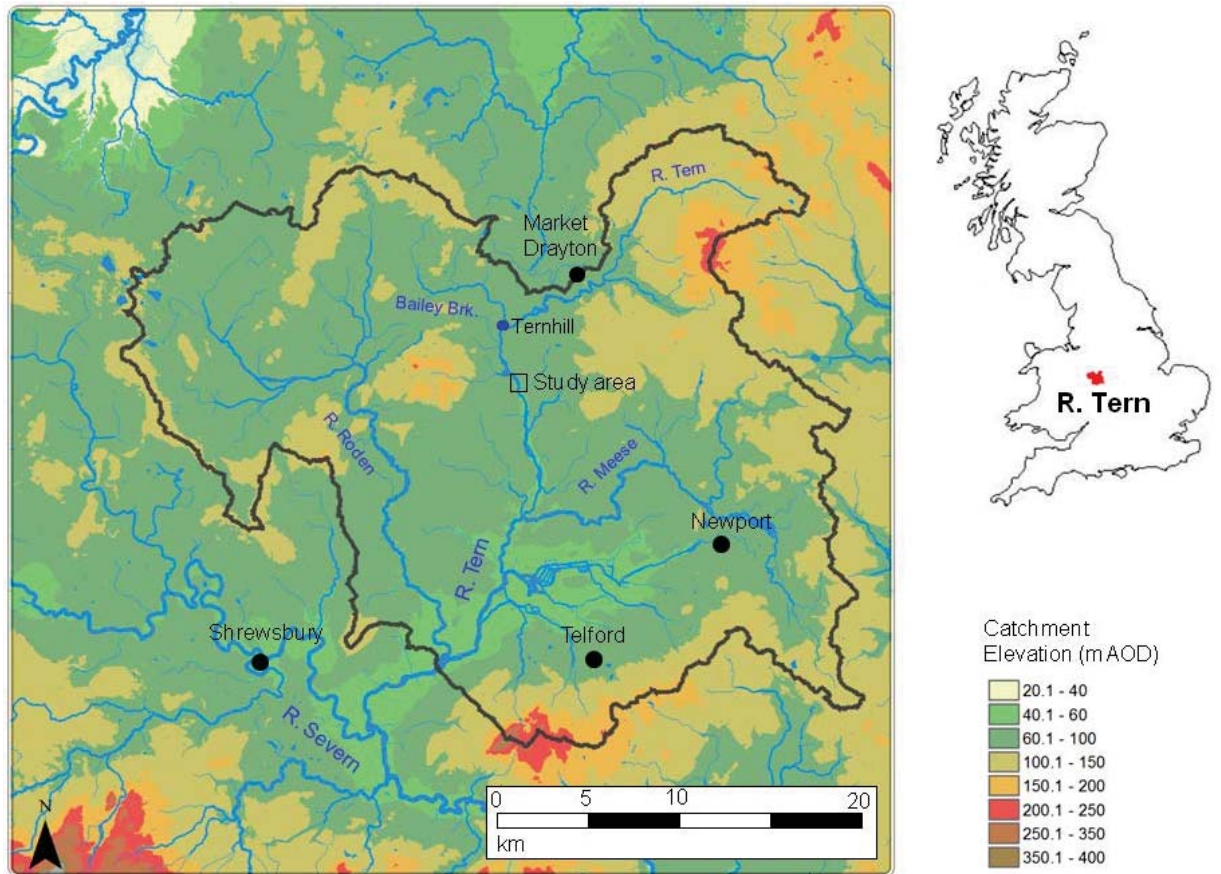


Fig. 3.2.1 Geographical context, topography and drainage network of the River Tern catchment from the UK National River Flow Archive spatial data (<http://ww.ceh.ac.uk/data/nrfa>). The study area is outlined with a square symbol whilst the blue circle indicates the position of Ternhill hydrometric station.

3.2.3 Geology of the River Tern Valley

3.2.3.1 *Solid geology*

The River Tern and its tributaries are mostly underlain by Permo-Triassic sedimentary rocks which are divided between the Cheshire Basin in the northwest and Stafford Basin towards the east, although minor Carboniferous and Jurassic sediments also outcrop (Fig. 3.2.2). The nomenclature differs for the two depositional basins despite having similar ages and lithostratigraphic sequences, with the Hodnet fault (Fig. 3.2.2) used to demarcate the boundary (Bridge et al., 2002). A desert-like, arid environment existed in the West

Midlands region during the Permian Period (approximately 252–292 Ma) and the early Triassic (252–201 Ma) (Zeigler, 1990). In the early Permian, basin development was initiated by crustal extension producing a series of northeast–southwest trending depositional troughs across the West Midlands region, bounded by basement-controlled faults. Aeolian deposition of wind-blown sands dominated in the mid-to-late Permian with increasing fluvial influences in the form of braided rivers at the start of the Triassic (producing pebble beds and conglomeritic sandstones). Deposition was restricted later in the Triassic where fine-grained sediments of the Mercia Mudstone Group (formerly known as the Keuper Marl) were laid down in saline, playa lake conditions (Warrington, 1970). The Permo-Triassic succession are mainly feldspathic and lithic arenites which form a series of fault-bounded blocks that dip 5–10° northeast and overlap onto older Carboniferous argillaceous sediments (Smedley et al., 2005; Bouch et al., 2006). Locally, the study area is underlain by the Permian Bridgnorth sandstone (Lower Mottled Sandstone) and thinly capped in the east by Kidderminster sandstone (Bunter Pebble Beds) (Fig. 3.2.2). This forms the base of the Triassic Sherwood Sandstone Group (Papatolios and Lerner, 1993) in the area. The whole sequence is underlain at depth by the Carboniferous Salop Formation (Warwickshire Group) which is downthrown against the Mercia Mudstone group by the Hodnet Fault (Fig. 3.2.3). The Bridgnorth sandstone (equivalent to the Kinnerton sandstone of the Cheshire Basin) is represented by red-to-brown, fine or medium-grained, pebble-free, cross-bedded sandstones with accumulation considered a consequence of aeolian processes within a large dune complex (Karpeta, 1990). Although poorly exposed in the study area, borehole evidence (ECL, 2009) indicates that the Permian Bridgnorth sandstone is moderate or poorly cemented and semi-friable (Fig. 3.2.4) with sparse conglomeritic horizons and a substantial weathered layer at its surface (Adams et al., 2003). The Kidderminster formation is of fluvio-deltaic origin

and comprises sand, conglomerate, marl bands as well as more argillaceous sediments which are typically well-cemented (Papatolios and Lerner, 1993).

3.2.3.2 *Unconsolidated geology and 'drift' deposits*

The unconsolidated deposits of the River Tern's catchment are mostly Pleistocene age (2.8 Ma to 11.7Ka) sub-glacial tills and glaciofluvial sands and gravels deposited in the Late Devensian (28 to 18 Ka) during retreat and decoupling of ice masses towards centres in the Irish Sea and Wales (Cook, 2010). The thickness of these drift deposits varies spatially across the catchment and are generally thicker in the west with up to 30 m of till recorded (Streetley and Shepley, 2005). In the study area, the deposits are patchy or absent immediately to the east of the river (Adams et al., 2003). Holocene to recent deposits (11.7 Ka to present) consist of re-worked glaciogenic sediments which are incorporated into river terrace deposits and alluvium. Terraces have a distinctive bench-like geomorphology and a continuous river gravel terrace is present on the eastern boundary of the River Tern floodplain in the study area (Blackwell, 2002). The alluvium deposits line the river corridor and range up to 8 m in thickness but are commonly less than 5 m thick. The alluvium typically consists of clay, silt, sand/gravel as well as peat or humic deposits and may have gravel bars at the base of the sequence (Streetley and Shepley, 2005). Locally, borehole evidence indicates that the alluvium ranges from 3–5 m in thickness and contains occasional peat and clay lenses (Adams et al., 2003). Bank exposures along the course of the river in the study area reveal the alluvium to be composed on cross-bedded sands with silt bands and gravel (Blackwell, 2002).

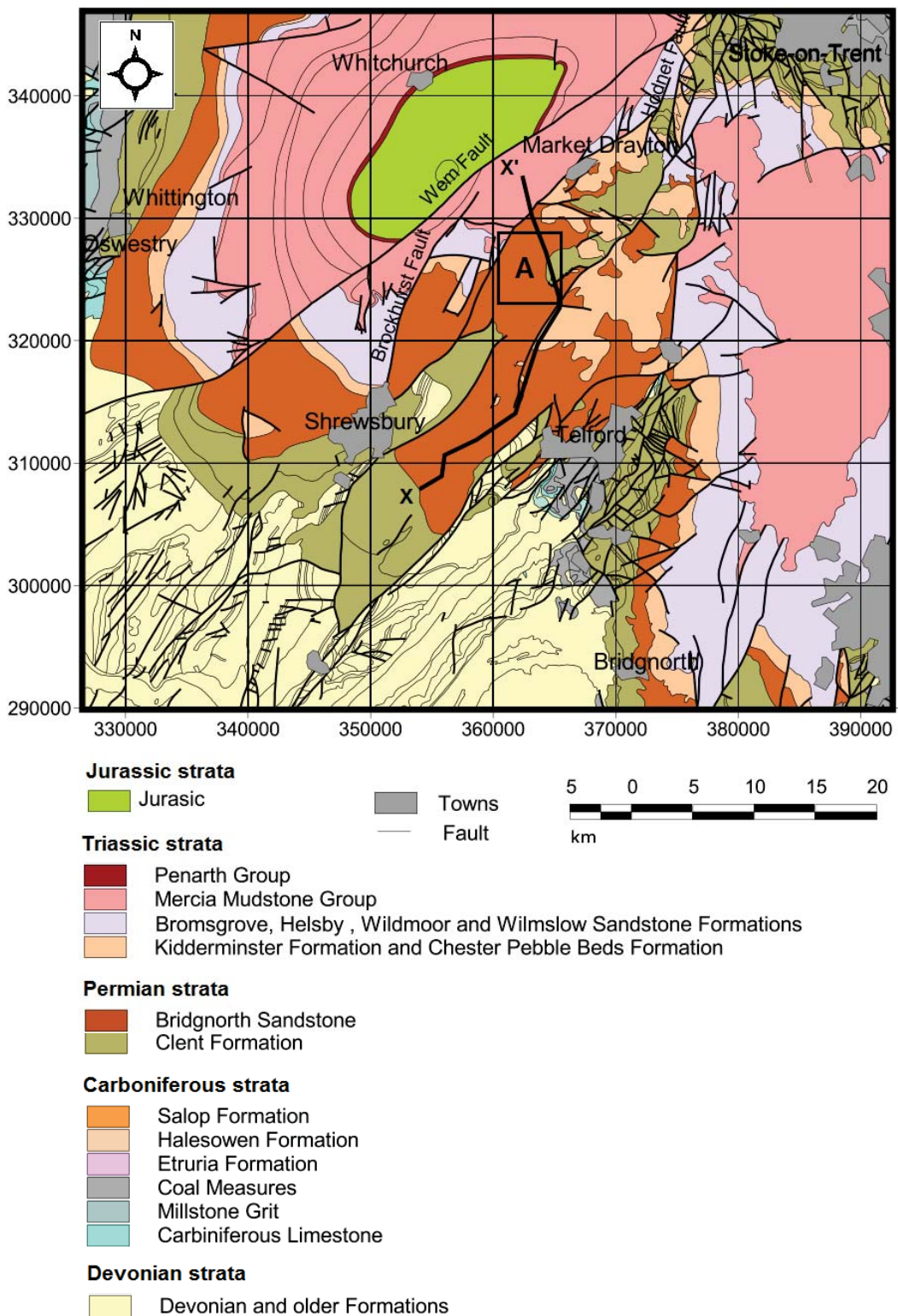


Fig. 3.2.2 Regional geology of the River Tern catchment and the surrounding areas of North Shropshire, Shropshire and South Cheshire (modified from Smedley et al., 2005). The study area featured in Fig. 3.1.4 is denoted by the letter A. The line of the cross-section given in Fig. 3.2.5 is indicated by X-X'.

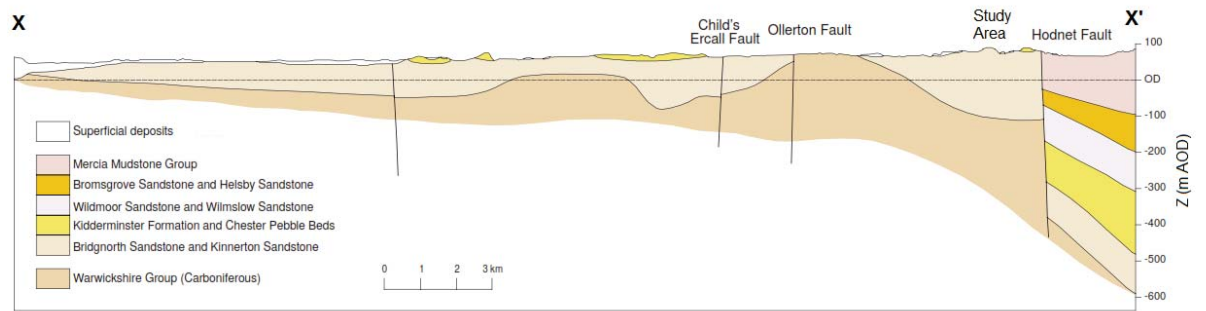


Fig. 3.2.3 Geological cross-section through the Stafford Basin showing formation thicknesses and principal structural features (after Smedley et al., 2005). The location of the study area (close to the Hodnet Fault) is indicated. Refer to Fig. 3.2.2 for the location and orientation of this cross-section in the River Tern Valley.

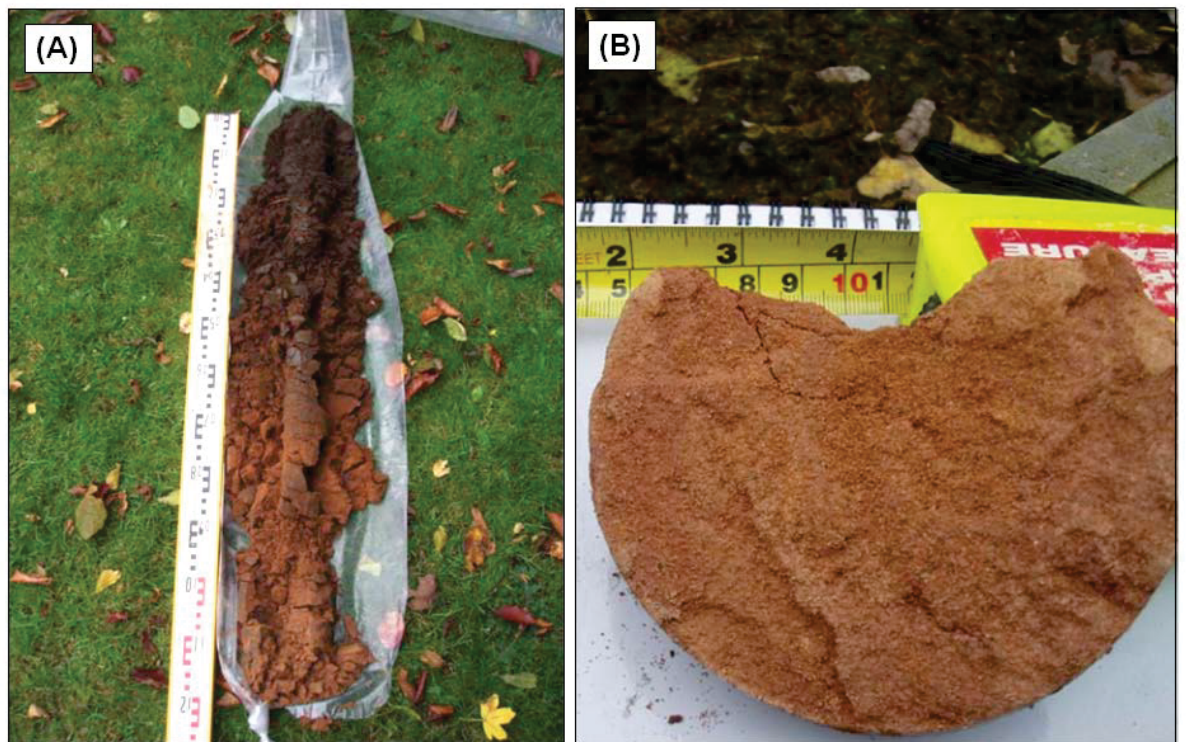


Fig. 3.2.4 Core samples of the Bridgnorth sandstone in (A) drill core sample and (B) hand specimen (after ECL, 2009). Note the red-to-brown colour, friable consistency and texturally uniform nature of the sandstone.

3.2.4 Hydrogeology

3.2.4.1 Permo-Triassic sandstone

The Permo-Triassic sandstone (PTS) in the area forms a regionally significant aquifer and is considered to be the second most important groundwater resource in the UK, after the Cretaceous chalk (Allen et al., 1997). Groundwater is abstracted by Severn Trent Water to serve the major population centres of Telford and Market Drayton (domestic and industrial use). Seasonal abstraction for spray irrigation is common as are small private supplies (Streetly and Shepley, 2005). Groundwater is also occasionally abstracted from the PTS (in combination with release of surface water from Clywedog and Vyrnwy reservoirs in Wales) to alleviate low-flows in the River Severn after extended periods of dry weather. The Shropshire Groundwater Scheme (SGS), operated by the Environment Agency, comprises a network of abstraction and observation boreholes licensed to withdraw up to 180,000 m³ d⁻¹ from the regional PTS groundwater system (Voyce, 2008). In the study area, the Bridgnorth and Kidderminster sandstones are unconfined and constitute a single groundwater body (Fig. 3.2.5) with an interpreted saturated thickness of approximately 110 m, overlain by a relatively thin unsaturated zone of <10 m (Rahman and Shepley, 2005). The poorly cemented nature of the Bridgnorth sandstone produces high porosity values (16.6–33.6% v v⁻¹) representing a large groundwater storage potential (Allen et al., 1997). Recharge typically occurs in the autumn and winter months when rainfall is greatest and potential evapotranspiration rates are lowest with average annual recharge estimated at 231 mm for modelling purposes (EA, 2008). The Helshaw Grange Abstraction borehole (HGA) forms part of the SGS in the study area with associated monitoring wells including Helshaw Grange observation borehole (HGO), Heathbrook East (HBE) and Heathbrook West (HBW) situated down-gradient on the floodplain of the river (Fig. 3.2.5). The

groundwater flow regime in the area is matrix-dominated and intergranular with relatively uniform hydraulic properties. Where present, however, preferential flow through interconnected fractures may be locally important (Brereton, 1976). Streetly and Shepley (2005) estimate that the bulk hydraulic conductivity of the Bridgnorth formation ranges from 0.1–26.6 m d⁻¹ with geometric mean of 3 m d⁻¹, which is similar to that of Allen et al. (1997) at 0.09–25 m d⁻¹ and a geometric mean of 6.9 m d⁻¹.

3.2.4.2 *Aquifer-river interactions*

Regional groundwater flow from the PTS aquifer to the Tern is the dominant mode of aquifer-river interaction at catchment scale, with annual recharge ultimately discharging as baseflow along the river corridor. However, the River Tern is incised through the alluvium deposits underlying the valley floor which form an important local-scale control on river-aquifer interaction. Riverbed permeability was studied in detail by Clark (1976) along a 10 km stretch of the river (which included the reach investigated in this study). Stratified alluvial deposits of peat and clay were found to provide significant hydraulic ‘sealing’ of the riverbed. Krause et al. (2012) and Angermann et al. (2012) found these clay and peat lenses to act as semi-confining layers to upwelling groundwater discharge to the river. A number of pumping tests were carried out at abstraction well HGA (during the SGS development in the 1970s) to investigate the hydraulic connectivity between the PTS and the River Tern (Joseph and Brereton, 1975; Brereton, 1976). HGA was pumped at a rate of ~7,000 m³ d⁻¹ for 26 days with heavy rainfall occurring on a number of occasions. A strong correlation was observed between rainfall, river and groundwater levels monitored at adjacent wells HBE and HBW. An analysis of the data indicated that the river acted as a recharge boundary and that hydraulic continuity of the PTS with the River Tern was apparently greater at high flows than low flows (Streetly and Shepley, 2005).

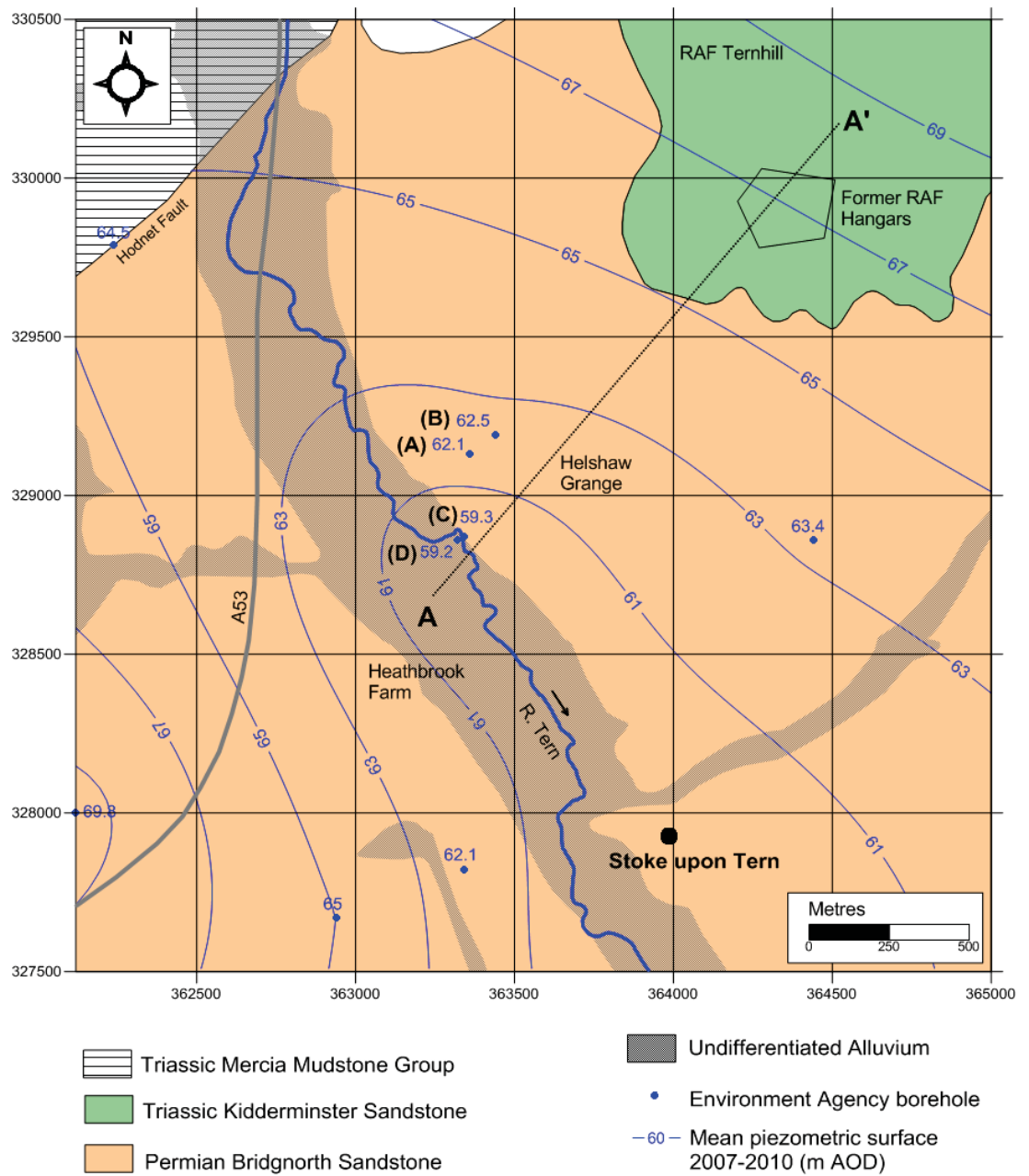


Fig. 3.2.5

Hydrogeology of the study area showing the Permo-Triassic sandstones which form the regional aquifer. The hydraulic head contours are based on mean monthly groundwater levels measured in the Environment Agency observation boreholes (2007–2010, not all measurement points shown, EA, 2010, unpublished data). Features labelled; (A) Helshaw Grange abstraction borehole (HGA), (B) Helshaw Grange observation borehole (HGO) (C) Heathbrook East borehole (HBE) (4) Heathbrook West borehole (HBW). The line A–A' denotes the location of the cross-section in shown in figure Fig. 3.2.6.

3.2.5 Groundwater quality issues in the study area

The limited extent of the unsaturated zone and thin drift deposits in the study area makes the unconfined PTS aquifer extremely vulnerable to potentially polluting activities. Natural groundwater quality has been impacted by diffuse nitrate (NO_3^-) contamination from agricultural activities with NO_3^- concentrations often in excess of 50 mg L^{-1} (EA, 2010; unpublished data). Large areas of the unconfined PTS in the region (including in the study area) are designated nitrate vulnerable zones (DEFRA, 2004). Much of this NO_3^- leached from the soil zone discharges in groundwater baseflow to the river (Krause et al., 2013). Chlorinated ethene contamination of the PTS aquifer was first revealed in 2003 during routine groundwater quality sampling at HGA (Rahman and Shepley, 2005). TCE concentrations in the range of $35\text{--}48 \text{ }\mu\text{g L}^{-1}$ were observed in bulk pumped samples. This abstraction well has since been excluded indefinitely from operational use in the SGS. TCE was also found in boreholes down hydraulic gradient including HGO, HBE and HBW. These are situated approximately 500 m southwest of the abstraction borehole suggesting the presence of a dissolved phase plume (Fig. 3.2.6). Passive sampling exercises using ‘HydraSleeve’ samplers and ‘Equilibrator’ diffusion samplers (Waterra, UK) were carried out on HGA (Fig. 3.2.7A) and HGO (Fig. 3.2.7B) in the summer of 2009 to characterise the depth-stratification of the potential plume by targeting specific fracture zones. Maximum TCE concentrations were found between 60 and 80 m depth in HGA, close to the interpreted base of the Bridgnorth sandstone aquifer (Fig. 3.2.6). The plume differs from other individual sites reported in the literature in that no specific source area is known. A particle tracking study was carried out in 2005 (Rahman and Shepley, 2005) using the EA’s regional water resources model of the PTS aquifer (Streetly and Shepley, 2005). This examined the potential impact of operational pumping on the direction and velocity of the TCE migration and its natural migration through the sandstone aquifer. The

simulations suggested an up-gradient source for the plume (based on an advective travel time to HGA of 37 years) originating somewhere in the area of former aircraft maintenance hangars associated with RAF Ternhill approximately 1.5 km northeast of HGA (Figs. 3.2.5 and 3.2.8). This is supported by tritium (^3H) aging conducted on pumped samples from HGA (during development of the SGS in 1972) where groundwater age was interpreted to be in excess of 20 years based on a ^3H unit value of 9.8 (Severn Water Authority, 1974). Although the mixing of water types of differing ages is a distinct possibility, this and the modelling results suggests the original contamination event most likely occurred sometime in the 1950s. A recent particle tracking study by Perkins (2013), which used a greater level of mesh refinement than the 2005 study, also indicated that the former RAF maintenance area was a possible source area (Fig. 3.2.8). However, an intrusive site investigation in this area (Fig. 3.2.5) did not reveal the presence of any DNAPL source material (ECL, 2009), and, to date, the source of the contamination has yet to be confirmed.

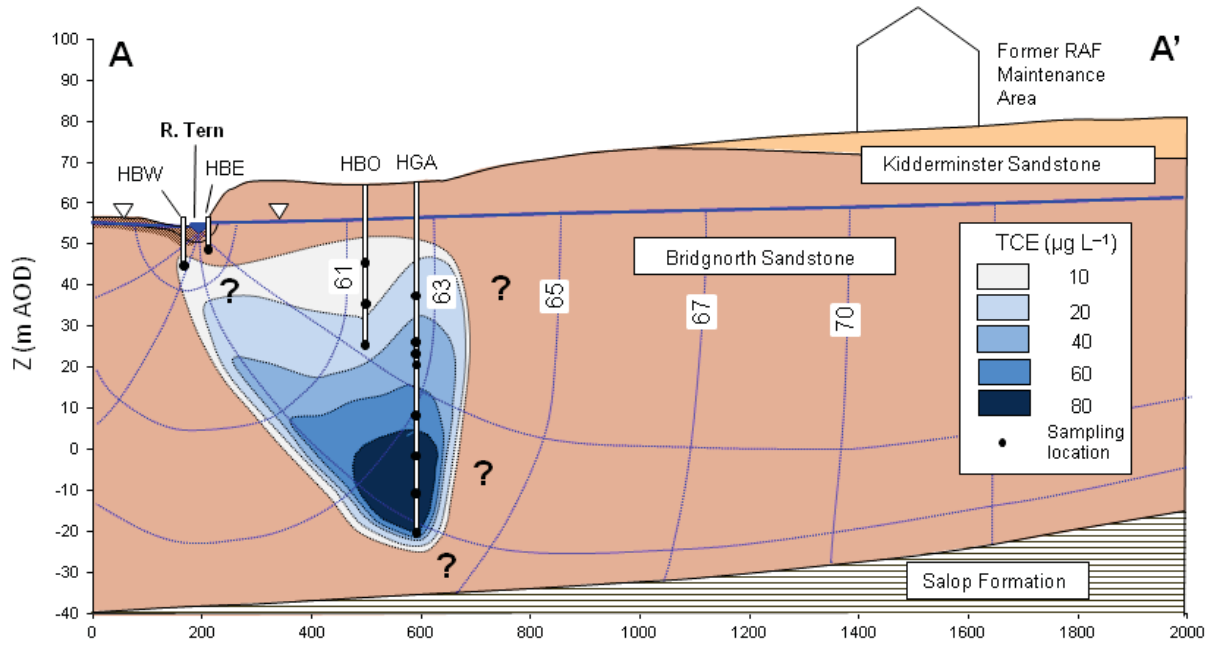


Fig. 3.2.6 Hydrogeological cross-section based on the passive sampling carried out by the Environment Agency in 2009 illustrating the known extent of the plume (Kevin Voyce, EA, 2010, personal communication). Question marks denote areas of uncertainty. Refer to Fig. 3.2.5 for the location of the cross-section line.

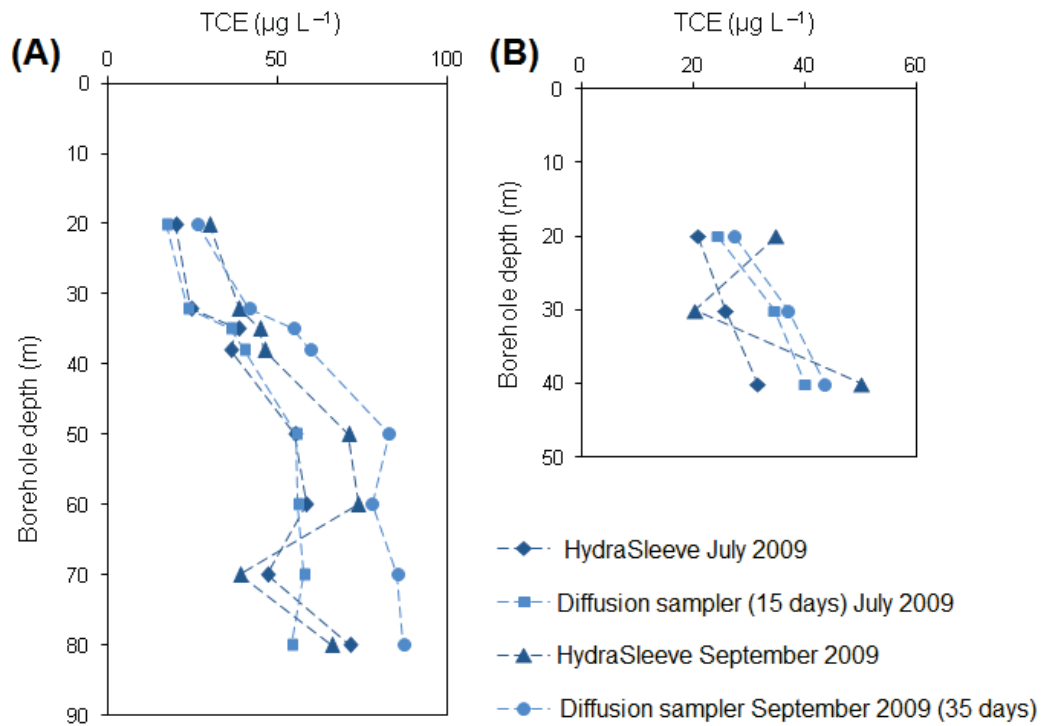


Fig. 3.2.7 Detailed depth-concentration profiles for the passive sampling conducted at (A) HGA and (B) HGO (EA, 2010; unpublished data).

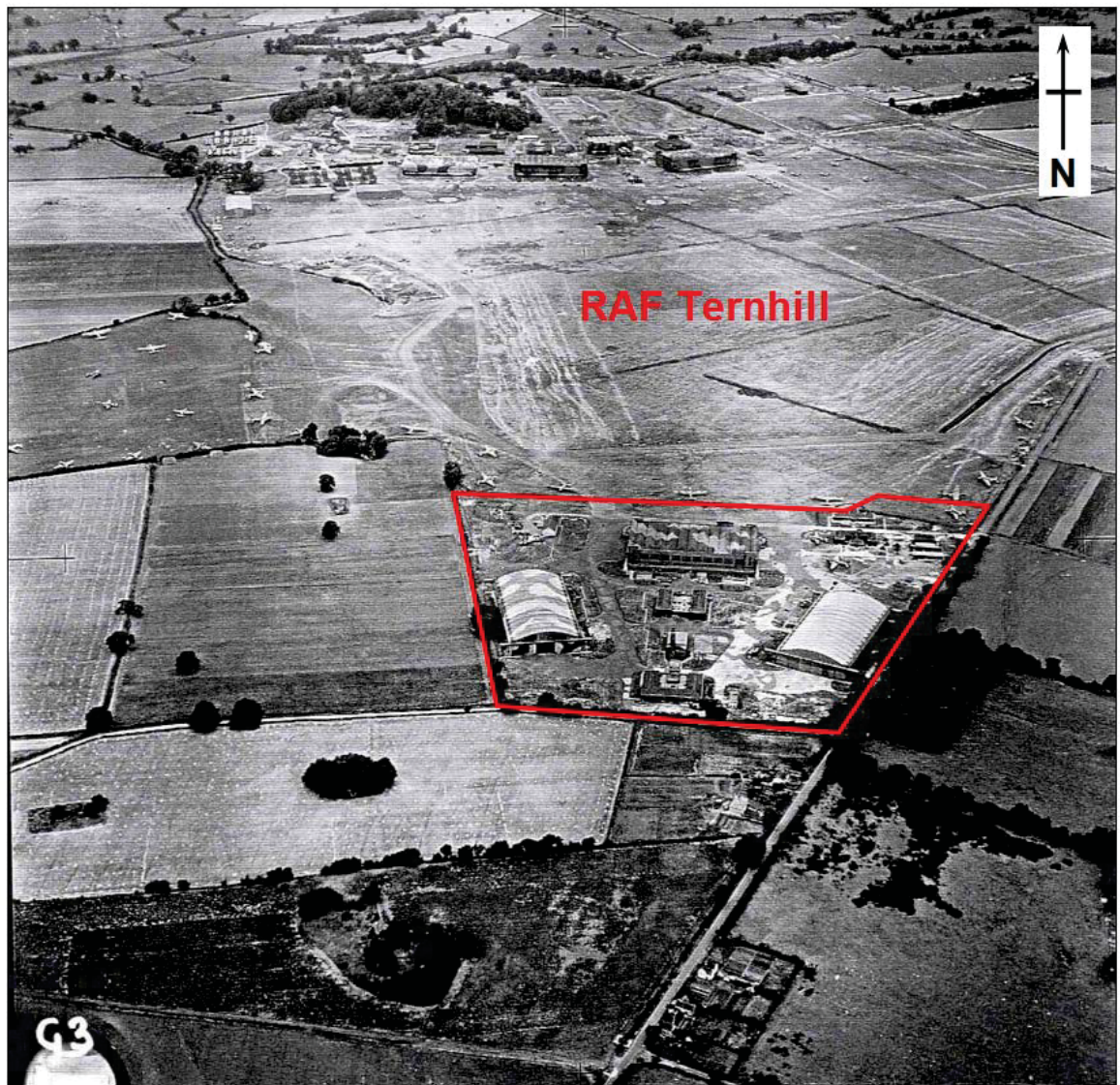


Fig. 3.2.8 Aerial photography of the suspected source area of the TCE contaminant plume (circa. 1940) as indicated by the red boundary line (after ECL, 2009). The active RAF base is in the background whilst the study area of the River Tern is located approximately 1.5 km to the southeast. The boundary of this area is given in Fig. 3.2.5.

3.2.6 Existing monitoring networks

Other than occasional abstraction associated with operation of the SGS, the area of the Tern catchment in the study area is considered to be relatively pristine with largely natural hydraulic gradients maintaining ‘gaining’ flow conditions (Clay et al., 2004; Hannah et al.,

2009; Krause et al., 2012). In light of this, the reach was selected as one of a number of important type localities by the UK's Natural Environment Research Council (NERC) in their lowland catchment research (LOCAR) thematic program and is considered to be one of the best examples of a lowland river draining a highly permeable Permo-Triassic sequence in the UK (Wheater and Peach, 2004). During this program, a borehole array was installed on the floodplain (in 2000) to investigate groundwater recharge through the drift deposits (Adams et al., 2003). In combination with additional observation boreholes already present (Figs. 3.2.5 and 3.2.8) the groundwater is subject to on-going monitoring by the Environment Agency (Table 3.1). This study mainly focuses on a 250 m long meandering section of the river characterised by steep-sided vegetated banks with a channel width between 3 and 6 metres (Fig. 3.2.9). A number of morphologically distinctive units have been identified including runs, pools and several riffle sequences (Smith and Lerner, 2008; Krause et al., 2011b). The importance of the reach as an experimental field site is reflected by the high density of monitoring infrastructure already present at the time of this study (Table 3.1).



Fig. 3.2.9 Overview of floodplain investigation area with the locations of pre-existing monitoring networks installed at the site, prior to this investigation (GetMapping Plc., 2009; copyright).

Table 3.1 Details of all existing groundwater monitoring infrastructure sampled during this investigation. Water table is denoted by ‘wt’.

Name	Installation date	Total depth	Response zone	Aquifer lithology	Reference
<i>SGS Boreholes</i>					
		(m)	(m)		
HGA	1972	85	15-85	Bridgnorth SST	Streetly and Shepley, 2005
HGO	1976	40	14-40	Bridgnorth SST	Streetly and Shepley, 2005
HBE	1976	9	6-9	Bridgnorth SST	Streetly and Shepley, 2005
HBW	1976	12	6.5-12	Bridgnorth SST	Streetly and Shepley, 2005
<i>LOCAR borehole array</i>					
T08 (drift)	2001	4.5	wt-4.5	Sand	Adams et al., 2003
T08 (bedrock)	2001	25	22-25	Bridgnorth SST	Adams et al., 2003
T11A	2001	50.8	9.5-50.8	Bridgnorth SST	Adams et al., 2003
T11B (drift)	2001	2.7	wt-2.7	Sand, silt	Adams et al., 2003
T11B (bedrock)	2001	22.4	19.1-22.4	Bridgnorth SST	Adams et al., 2003
T11C (drift)	2001	3.5	wt-3.5	Peat, sand	Adams et al., 2003
T11C (bedrock)	2001	23.8	21.1-23.8	Bridgnorth SST	Adams et al., 2003
T11D (drift)	2001	3.5	2.45-3.5	Silt, sand	Adams et al., 2003
T11D (bedrock)	2001	23	20.3-23	Bridgnorth SST	Adams et al., 2003
<i>Shallow monitoring wells</i>					
GW1-GW10	2009	3	2.8-3	Alluvium	Angermann et al., 2012
<i>In-river piezometers</i>					
P1-27	2009	1.5	1.35-1.5	stratified deposits	Krause et al., 2012

3.3 Groundwater investigation methods

3.3.1 Passive sampling

3.3.1.1 HydraSleeves

Groundwater from wells installed in the PTS aquifer was sampled using HydraSleeve (Waterra, UK) discrete interval passive samplers. These devices withdraw a grab sample or ‘core’ from the water column in long screened or open boreholes from a discrete depth (<http://www.waterra-in-situ.com>). The technique offers advantages over traditional pumped or packer-based sampling in that there is (1) minimal disruption to the natural flow regime of the formation and (2) the need for the purging and management of large volumes of potentially contaminated water is negated (ITRC, 2006).

3.3.1.2 Riverbed diffusion samplers

A bespoke passive diffusion sampler was designed for deployment in the shallow riverbed sediments (see Chapter 4) using a semi-permeable low-density polyethylene (LDPE) membrane based on the designs of Church et al. (2002) and Divine and McCray (2004). LDPE is an inexpensive polymer that undergoes transient cavitations in its molecular structure allowing small non-polar molecules to diffuse across thin (e.g. <0.1 mm) films, in response to local concentration gradients (Vrana, 2005). It is also known to be compatible with all chlorinated ethenes (Vroblesky and Campbell, 2001; Ehlke et al., 2004) and therefore ideal for TCE passive sampling. Each sampler was formed from 30 µm films cut from ‘layflat’ LDPE tubing (Polybags, UK) and 20 mL borosilicate vials filled with VOC-free water to form a positive meniscus over the vial opening (where a rubber o-ring was fitted to form a gasket). The LDPE film was then pulled down over the opening and

secured with self-locking nylon ties and the excess film trimmed off (Fig. 3.3.1A). If large air bubbles developed under the membrane, the film was discarded and the process repeated. Completed samplers were attached via surveyor's flags to facilitate relocation. In total, 46 samplers were deployed in the main channel of the River Tern and a drainage ditch (locations given in Chapter 4). Each sampler was emplaced by hand to a depth of 15 cm (± 3 cm) in the surficial sediment with care taken to ensure each device was fully covered by sediment. Samplers were left to equilibrate with pore water CEs for a period of 33 days taking into account of minimum equilibration times given by Devine and McCray (2004). Boreholes HBE and HBW were used as active controls (i.e., as comparison measurement locations) with triplicate diffusion sampler clusters suspended on a weighted line (Fig. 3.3.1B) at the base of screened interval of the borehole. An area of riverbed downstream of the LOCAR borehole array was also used as an additional blank control area for the remaining three samplers. At the end of the deployment period, the samplers were removed from the sediment, rinsed with deionised water and capped on site with PTFE-lined caps, before being transferred to a cool box at 4°C for transport to the laboratory.

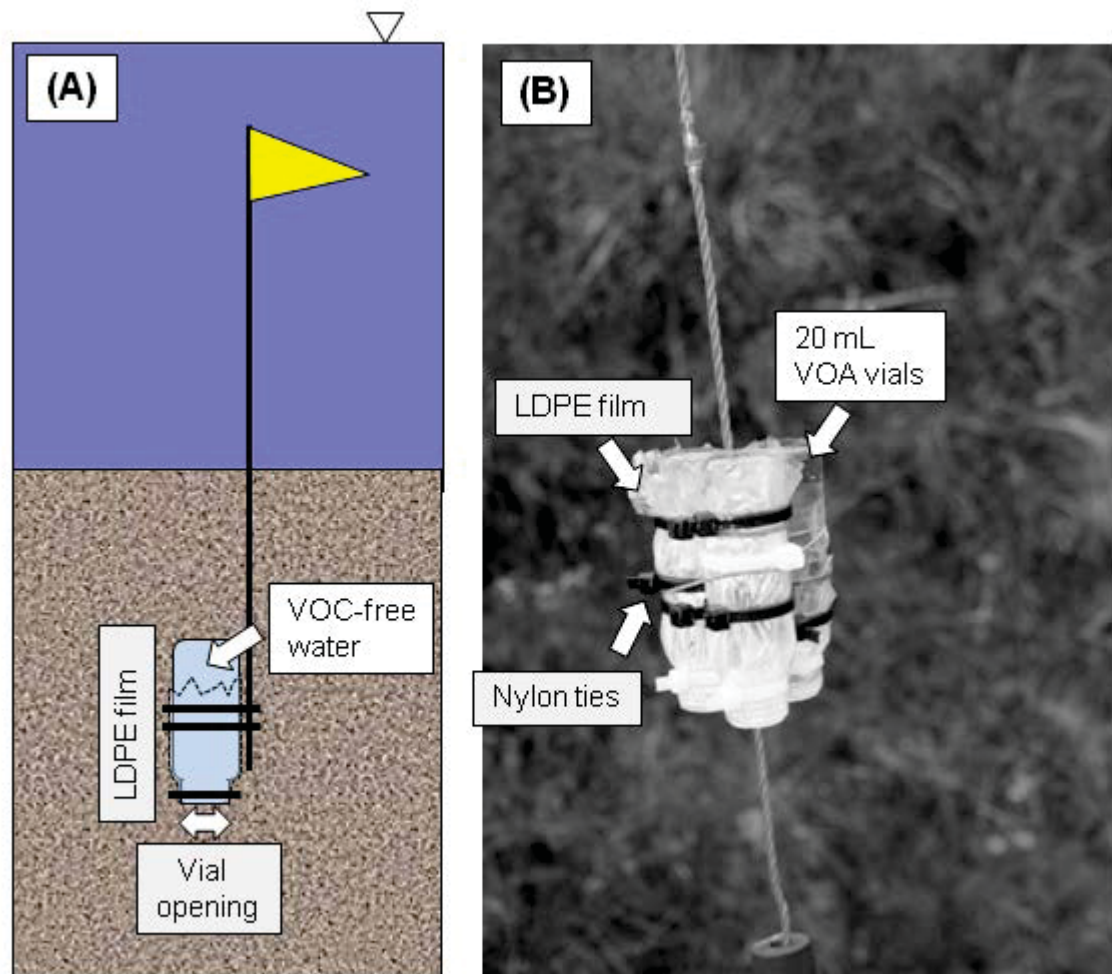


Fig. 3.3.1 (A) Riverbed diffusion sampler construction and (B) sampler clusters suspended in the boreholes as active controls.

3.3.2 Drive-point mini-piezometers

Drive-point mini-piezometers have been shown to be a robust and inexpensive approach for multi-level point sampling in riverbed sediments at sub-metre scales (Ellis and Rivett, 2007). The design used in this study was similar to those of Rivett et al. (2008) and Krause et al. (2013) and comprised a central rigid PEX (cross-linked polyethylene) tube with a 10 cm slotted section at the base, to which five Teflon sampling tubes (Grange Tubes, UK) were attached at 20 cm intervals (Fig. 3.3.2A). The sampling tubes were closed at the lower end by nylon micromesh to prevent sediment ingress during sample acquisition.

Each mini-piezometer was installed by advancing a steel drive tube, holding the prefabricated unit, to a depth of 1.2 m using a sledgehammer. To prevent invasion of sediment into the tube during installation, the lower end of the steel drive tube was closed with a sacrificial washer/nut assembly which was secured to the bottom of the piezometer tube (Fig. 3.3.2B). After the desired depth was reached, the drive tube was carefully removed from the riverbed with the piezometer held in place at the target depth. Surrounding riverbed deposits were allowed to re-collapse and fill the annular space around the piezometer and a minimum of three weeks were allowed to elapse before sampling took place. A total of 25 mini-piezometers were constructed (MP1–MP25) and installed along two cross-channel transects (TA and TB) which were joined by a 40 m channel-parallel transect (Transect D, Fig. 3.3.2C). An additional mini-piezometer was installed in the bed of the drainage ditch to the north of the study area (MP26). Completed mini-piezometer locations were surveyed in using a Total Station (Leica Geosystems) with an accuracy of ± 0.01 m. Further locational information for this network is included in Appendix A.

All mini-piezometers were sampled using 20 or 60 ml disposable polypropylene syringes interfaced with the sampling tubes after purging of 3 tube volumes (~ 15 mL). Chlorinated ethene samples were collected with 20 ml glass syringes which were used on a rotational basis, washed thoroughly with VOC-free water and allowed to air-dry between uses. To minimise potential disruption of in-situ solute gradients, sampling of each depth interval was ordered so that sampling of two adjacent levels in succession was avoided as far as possible.

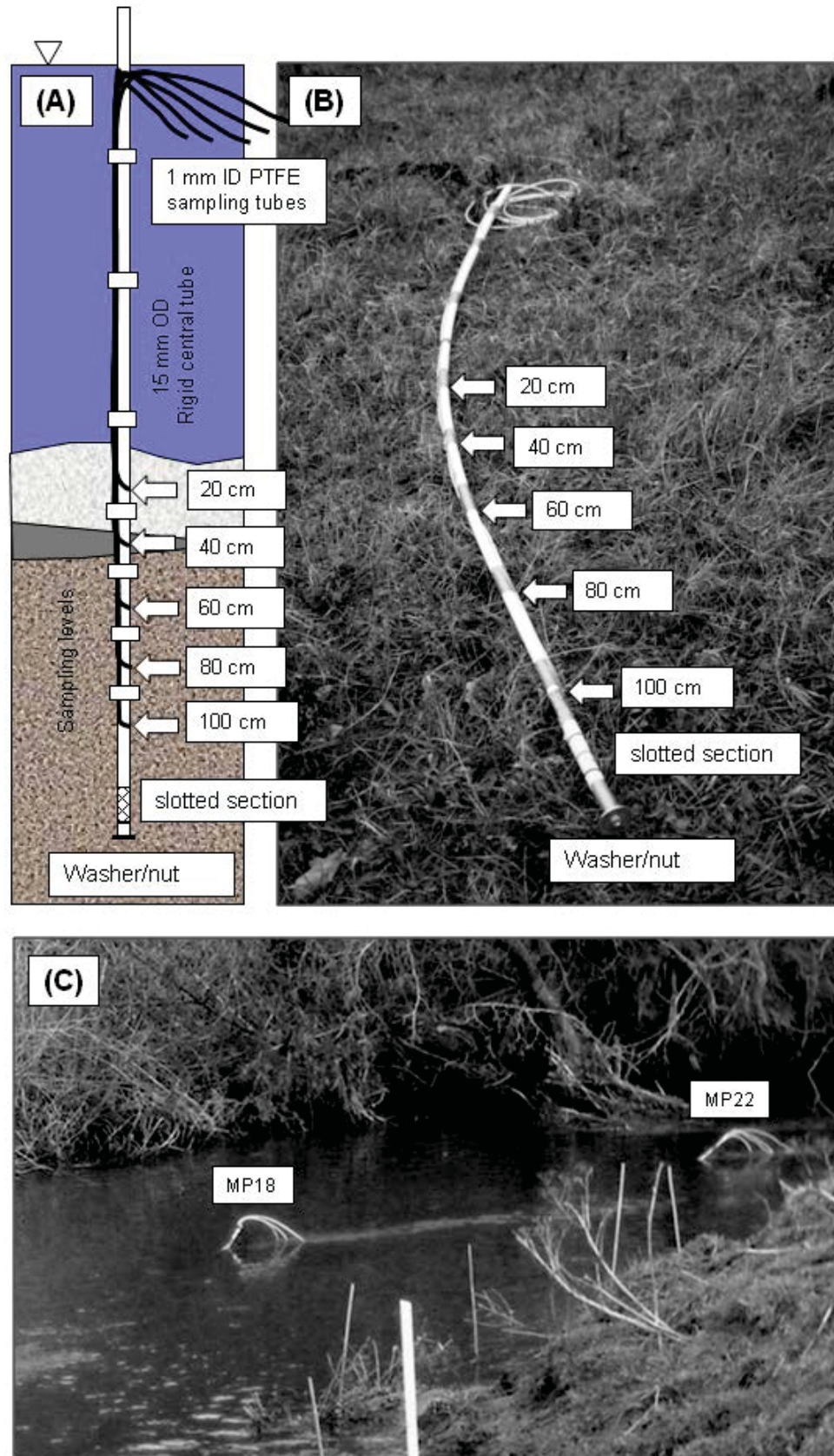


Fig 3.3.2 (A) Mini-piezometer construction details and a completed mini-piezometer (B) prior to installation and (C) MP18 and MP22 immediately after installation in the riverbed in November 2011.

3.3.3 Single-screen monitoring wells and piezometers

3.3.3.1 Alluvial monitoring wells

Shallow monitoring wells were installed in the floodplain alluvium (Chapter 4) to depths of between 2 and 4 m (Table 3.2) in auger holes created using an extendable Edelman hand-driven auger set (Eijkelkamp, The Netherlands). Construction was similar to the existing monitoring wells (Table 3.1) installed on the floodplain (Angermann et al., 2102; Krause et al., 2013). Instability of the auger hole walls generally prohibited installation to much greater than 1.5 m below the water table. Wells were constructed from a 32 mm OD uPVC tube which had a pre-drilled slotted section (slot diameter 8 mm) at the lower end to form the screened interval, which was wrapped in nylon mesh (with ~100 µm diameter openings) to prevent fine sediment ingress (Fig. 3.3.3A). The mesh was fixed around the tube with stainless steel wire and waterproof adhesive tape at the top and bottom of the screened interval (Fig. 3.3.3B). The base of the tube was left open and wrapped in the nylon mesh which was reinforced beneath with rigid HDPE mesh. Below the water table, natural deposits were allowed to re-collapse around the emplaced tube. Above it, fine sand was packed in to the annular space and capped with a layer of Portland cement to provide a water-tight seal at ground level (Fig. 3.3.3A). Wellhead elevations were surveyed in using a Total Station (Leica Geosystems).

To sample groundwater, monitoring wells were first purged using a peristaltic pump (Solinst Model 410, Waterra, UK) with dedicated Teflon tubing during which pH and electrical conductivity (EC) were monitored from the pump outlet (Fig. 3.3.3C). A low flow setting was used (usually 0.5 L min⁻¹) to minimise hydraulic stresses on the formation waters. Samples were collected after typically 3 well casings had been evacuated or when

pH and EC stabilised. However, where wells were slow to refill, a single volume was evacuated and a sample collected as soon as a sufficient volume was available. All samples were collected from the dedicated down-hole PTFE tubing (Papiernik et al., 2001) by reversing the flow direction to avoid potential adsorption or volatilisation losses (for VOCs) as well as potential sample carryover between locations.

Table 3.2 Details of alluvial monitoring wells completed during this study

Name	Easting	Northing	Z*	Total depth	Response zone
	(m)	(m)	(m AOD)	(m)	(m)
BH1	363329	328892	59.55	2.8	2.5-2.8
BH2	363322	328894	59.57	2.4	2.1-2.4
BH3	363318	328894	59.91	2.3	2.0-2.3
BH4	363311	328908	60.85	2.9	2.6-2.9
BH5	363313	328892	59.97	1.9	1.6-1.9
BH6	363308	328887	60.21	2.8	2.5-2.8
BH7	363305	328879	60.58	3.4	2.4-3.4
BH8	363267	328860	60.18	2.8	1.8-2.8
BH9	363311	328867	60.54	3	2.0-3.0
BH10	363319	328881	60.18	2.4	WT-2.4
BH10A	363319	328881	60.18	3.4	2.4-3.4
BH11	363326	328878	60.23	2.5	2.2-2.5
BH12	363328	328867	60.57	3.1	2.1-3.1
BH13	363320	328871	61.17	2.8	2.5-2.8
BH14	363317	328854	60.87	3.4	2.4-3.4

*Elevation measured at ground level beside the wellhead.

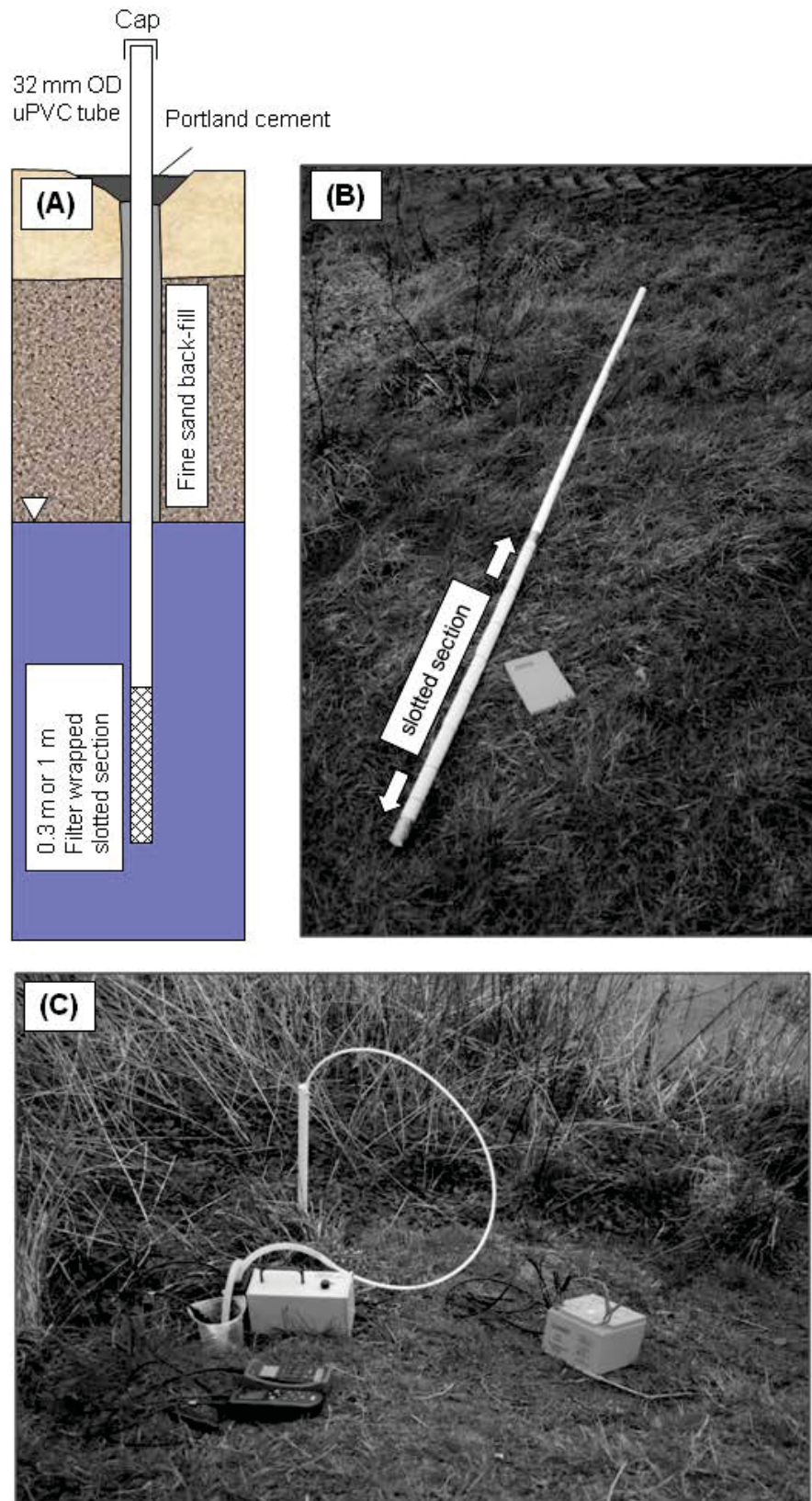


Fig. 3.3.3 (A) Single-screen monitoring well construction details (B) pre-fabricated well prior to installation (C) measuring in-situ parameters whilst purging BH1.

3.3.3.2 *Riverbed piezometers and stage recorder*

For the purpose of continuous monitoring of hydraulic head (using dataloggers), and to enable falling head tests to be carried out on the riverbed deposits, single-screened riverbed piezometers were constructed utilising the same design and materials as the alluvial monitoring wells (Fig. 3.3.3A). Initially, a single riverbed piezometer was installed (HZ) at the centre of the mini-piezometer network (Chapter 4). HZ was installed by slowly advancing a 1 m length (40 mm diameter) gouge corer (Eijkelkamp, The Netherlands) into the riverbed deposits. After the desired depth of 1 m was attained, the corer was carefully removed and the piezometer was rapidly inserted into the hole remaining before collapse of the surrounding sediment around the tube. Because the total length of the uPVC tubes was 3 m, a depth penetration of 1 m into the riverbed permitted hydraulic head observations under high river flow conditions. Adjacent to HZ, a stilling well was created for a datalogger to record river water levels using the same 32 mm OD uPVC tubing which had been perforated and tethered to a steel fence post driven into the riverbed. A further 10 riverbed piezometers were constructed and installed at 8 locations (Fig. 3.3.4) along a 72.5 m longitudinal transect (Transect S, Chapter 5). 5 of these locations consisted of a single piezometer with the remaining 3 comprising 2 piezometers at a shallow and deep depth in the sediment (Table 3.3). The pre-existing piezometer HZ was incorporated into this network (as SL5A) giving a total of 11 piezometers in the transect. Riverbed elevations beside the piezometers were surveyed in using a Total Station (Leica Geosystems).

The Transect S piezometers were sampled for CEs using a similar low-flow purge method as the alluvial monitoring wells. However, LDPE tubing was used for purging with the pump stationed on the river bank. Sampling was carried out using dedicated, 1 mm ID Teflon tubes interfaced with glass syringes.

Table 3.3 Details of the single-screen riverbed piezometers installed in this study

Name	Easting	Northing	Z*	Total depth	Response zone
	(m)	(m)	(m AOD)	(m)	(m)
SL1	363296	328869	57.99	0.74	0.44-0.74
SL2	363305	328871	57.98	0.63	0.33-0.63
SL3	363311	328878	58.14	0.94	0.64-0.94
SL4A	363318	328886	57.98	0.87	0.57-0.87
SL4B	363318	328886	57.98	0.59	0.29-0.59
SL5A/HZ	363328	328883	58.01	0.88	0.58-0.88
SL5B	363328	328883	58.01	0.56	0.26-0.56
SL6A	363331	328874	58.38	1.00	0.7-1
SL6B	363331	328874	58.38	0.57	0.27-0.57
SL7	363336	328865	58.16	0.98	0.68-98
SL8	363339	328853	58.16	0.60	0.3-0.6

*Elevation measured at riverbed level beside the piezometer.

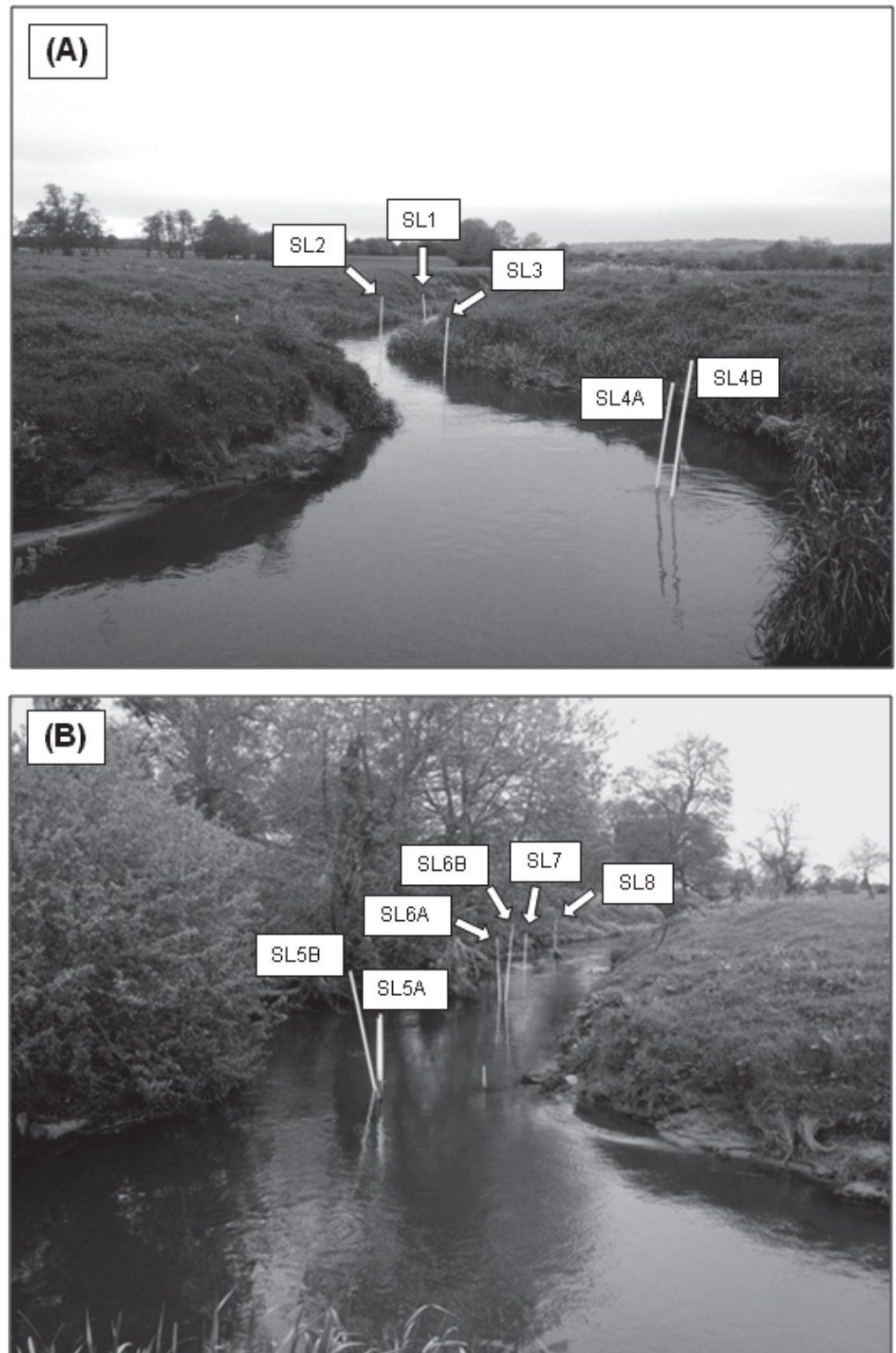


Fig. 3.3.4 (A) View upstream of the meander bend (looking north) showing completed single-screen piezometers (as annotated) of Transect S in May 2013. (B) View downstream from the same location (looking south) showing completed piezometers as annotated.

3.3.4 Direct-push methods

3.3.4.1 Pore water samplers

For the shallow investigation of solute gradients at sub-decimetre scales (see Chapter 6) a bespoke pore water sampler was designed that could be directly inserted into the sediment profile. Samplers were constructed from lengths of 10 mm OD copper pipes (Fig. 3.3.5A) where one end of the pipe was formed into a flat, tapered base by compressing the sides together in a vice. A small amount of cyanoacrylate adhesive was used to ensure a complete seal. 6 mm diameter holes were then drilled into the sides of the pipes through which 1 mm ID Teflon sampling tubes were threaded. These had a nylon micromesh point-screen at one end and were the same construction as those used in the drive-point piezometers described previously (Fig. 3.3.2). When the sampling tubes emerged from the top of the copper pipe, they were carefully pulled up to leave 5 cm of the lower end protruding from the drill hole (Fig. 3.3.5B). The hole was then sealed with a small amount of silicone sealant and the internal volume of the pipe was back-filled around the sampling tubes with expanding polyurethane foam. Initially, 4 samplers were constructed from 1 and 2 m lengths of pipe for field trial purposes (2 each). However, it was found that the 2 m samplers could not be inserted to much greater than 40 cm without the pipe bending. Therefore, only the 1 m design (with sampling depths of 5, 10, 20 and 30 cm, Fig. 3.3.6B) was actually used and could only be deployed in soft sandy sediments.

The initial samplers deployed were lost during flood events in July 2013 and never recovered. An additional 12 samplers were then constructed and deployed in a grid format as a 'plot scale' array to target shallow chemical gradients beneath the submerged macrophyte stand in the riverbed (Fig. 3.3.5C). The disturbance of natural chemical gradients in the sediment flow system arising from sample extraction was a concern. To

mitigate this, no samples were collected in succession from the same location. Instead, the sampling sequence proceeded by alternating between different depths and contrasting ends of the array. Furthermore, as part of the sampler design, the 5 cm and 10 cm depth intervals were installed on opposite sides of the copper pipe to maximise their distance from one another, whilst maintaining the same vertical distance from the riverbed surface (Fig. 3.3.6B). Sampling was carried out using disposable polyethylene or glass syringes as described in Section 3.3.2.

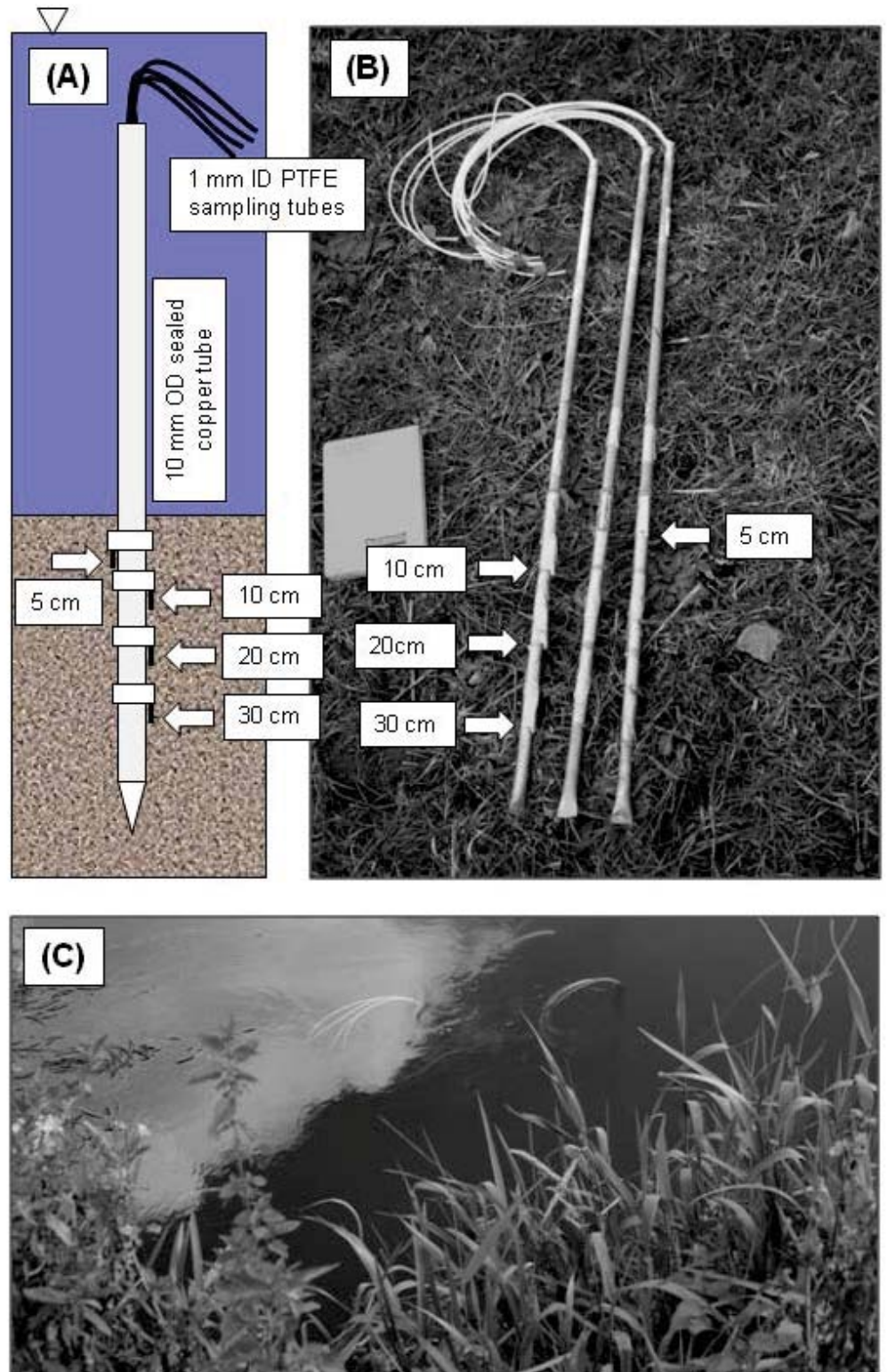


Fig. 3.3.5 (A) Details of pore water sampler construction (B) some completed samplers prior to installation and (C) grid of samplers installed under macrophyte stand (visible to the left) with samplers PW3 (top), PW4 (left) and PW5 (right) visible.

3.3.4.2 *Temporary piezometers nests*

To provide observations of depth-resolved hydraulic conductivity and hydraulic gradients in the riverbed (see Chapter 5), temporary piezometers were constructed from the same 10 mm copper tubing as used in the pore water samplers. A tapered base was formed by compression of the tubes (as described in the previous section), above which 10 mm slotted sections were drilled to form a short screen (Fig. 3.3.6A). Each section was wrapped in nylon mesh and secured with stainless steel wire. The piezometers were installed in the riverbed by gently advancing the tubes into the sediment (using a mallet) in a nested configuration (i.e., 3 single piezometers at different depths along a vertical profile) which was centred on the deeper single level piezometers of Transect S (Fig. 3.3.6B and Table 3.3). Tubes were marked with tape to ensure the top of the screens were at the correct depths of 10, 20 and 30 cm below the riverbed. 6 temporary piezometers were constructed to allow simultaneous investigation of two locations at once. Piezometer nests were left to equilibrate within the sediment flow regime for a period of 24 hours before hydraulic measurements were undertaken.

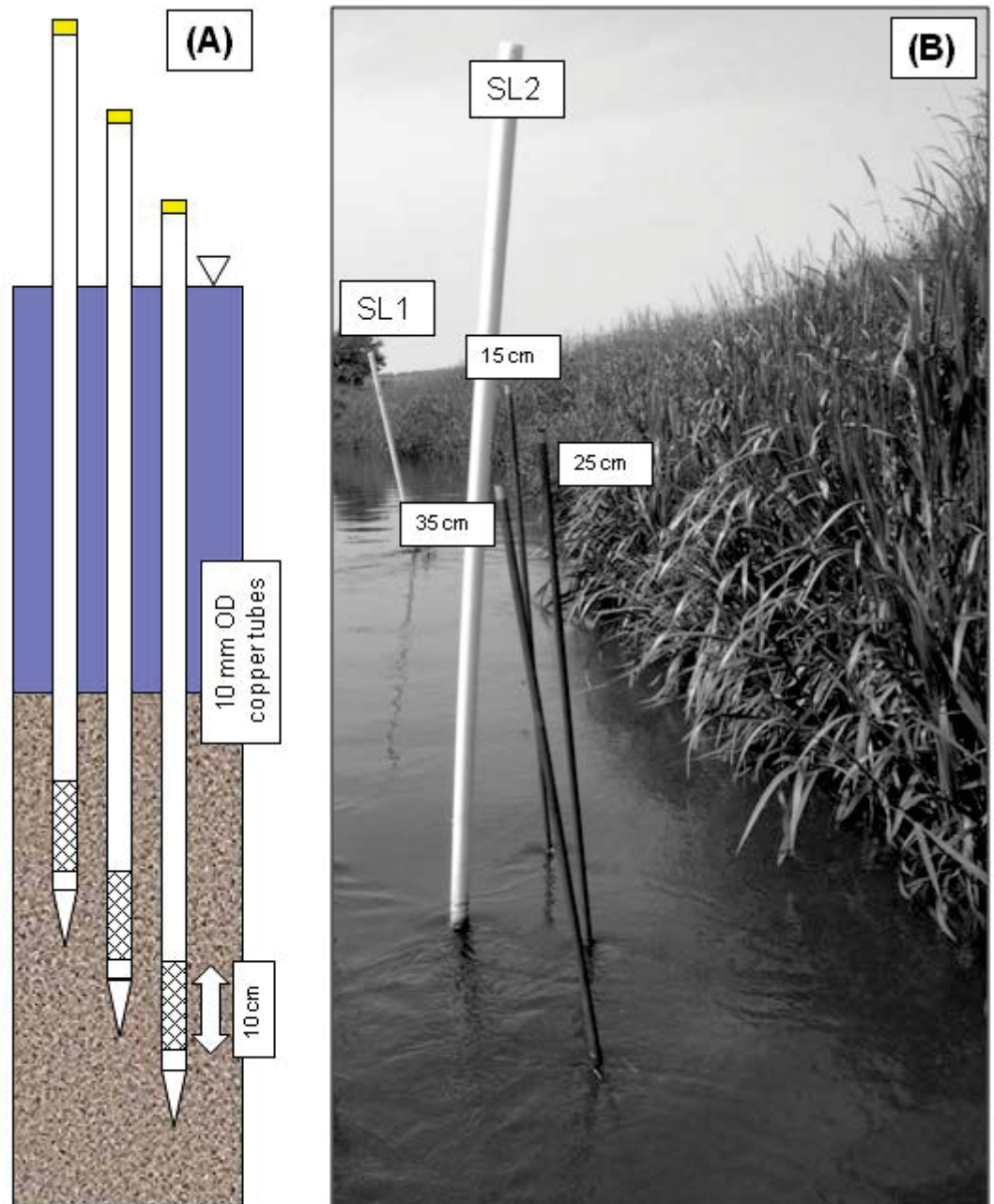


Fig. 3.3.6 (A) Construction and arrangement of the nested temporary piezometers and (B) piezometers installed in a nested configuration around SL2 prior to hydraulic testing.

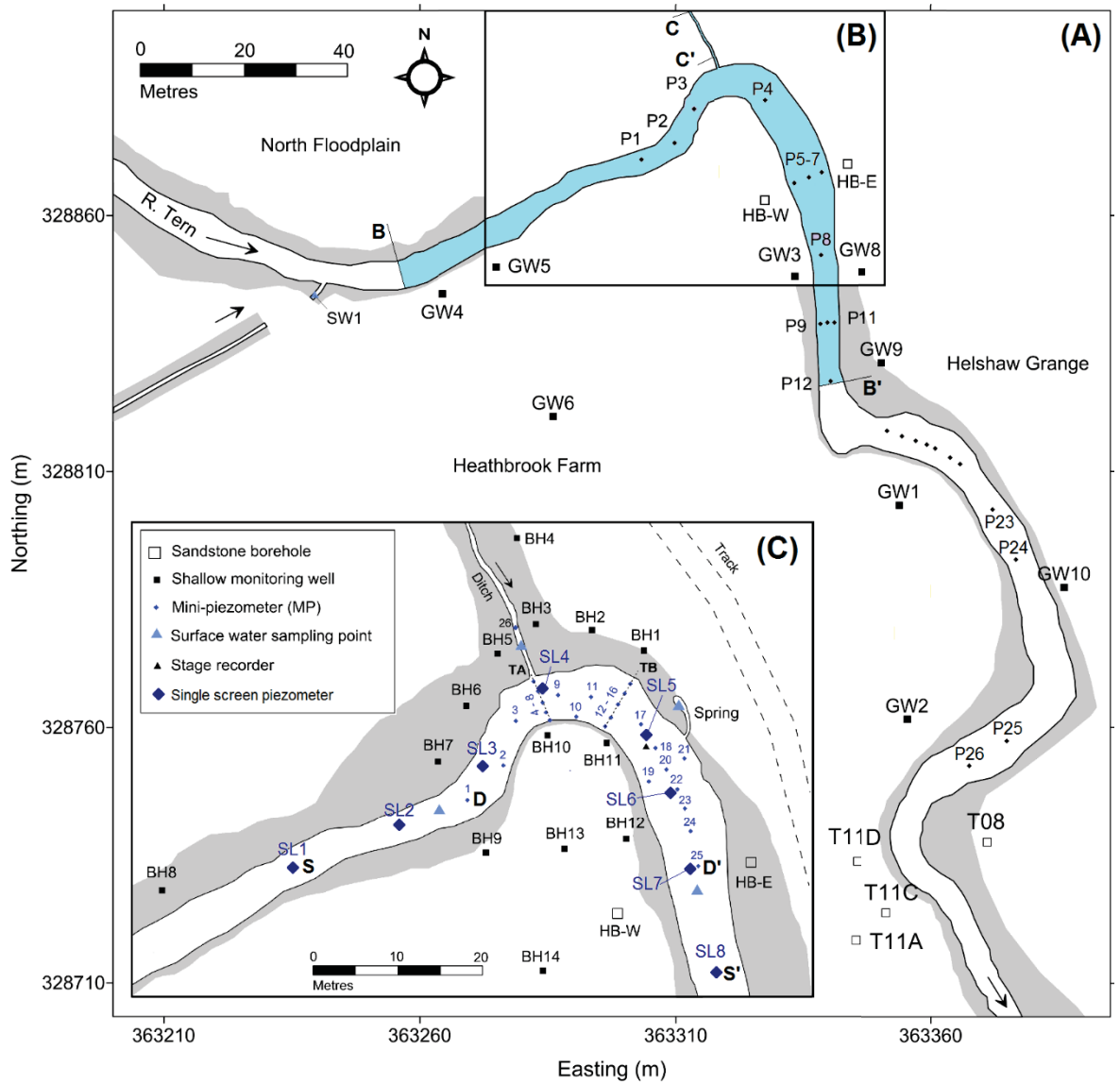


Fig. 3.3.7 Layout of all new and existing groundwater monitoring networks employed throughout this study at floodplain scale (A) with the diffusion sampler transects labelled B-B' (main channel) and C-C' (drainage ditch) highlighted in blue. (B) Denotes the area of interest within the context of the wider floodplain. (C) Details of the reach scale monitoring networks including drivepoint mini-piezometers (Fig. 3.3.2) alluvial monitoring wells (Fig. 3.3.3) single-screen piezometers (Fig. 3.3.4).

3.4 Physical characterisation methods

3.4.1 Sediment properties

3.4.1.1 Coring

A limited number of cores were collected from the riverbed immediately prior to installation of the drive-point mini-piezometers (Section 3.3.2). Core was collected using a 15 mm diameter 1 m long gouge corer (Eijkelkamp, The Netherlands). Core recovery from the riverbed was poor due to the loose and unconsolidated nature of the deposits which were washed from the corer before it could be removed from the river, particularly where sand was present. Where possible, sedimentary layer thicknesses (based on dominant grain size, Wentworth, 1922), colour and texture were logged. During installation of the monitoring wells in the floodplain (Section 3.3.3) a total of 20 auger holes were cored using the Edelman auger set (Eijkelkamp, The Netherlands). As the method does not produce a contiguous core, recovered sediment samples were removed from the auger blades were logged in sequence by placing samples in a graduated half pipe. A more detailed investigation of the riverbed stratigraphy was conducted during installation of the single-screen piezometers (Section 3.3.4). By using the larger diameter gouge (40 mm) and wrapping plastic sheeting around the corer underwater as it was being raised, core recovery was improved. Stratigraphy was logged as previously described with triplicate sediment samples collected in polythene bags from each stratigraphic horizon, which were transferred to a cool box (4°C) and frozen until analysis within 2 months of collection.

3.4.1.2 *Fraction organic carbon*

Fraction organic matter (f_{om}) [g g^{-1}] was determined gravimetrically using the loss-on-ignition (LOI) method (Heiri et al., 2001). Triplicate samples were homogenised by hand and then placed wet into pre-combusted ($550\text{ }^{\circ}\text{C}$) porcelain crucibles which had been previously weighed. Dry mass (DM) was calculated by subtracting the crucible mass from the sediment + crucible mass after the samples had been left overnight (>12 hours) in a drying oven at $105\text{ }^{\circ}\text{C}$. Dry samples were then combusted in a muffle furnace at $550\text{ }^{\circ}\text{C}$ for 3 hours and re-weighed after a cooling period of approximately 30 minutes. LOI_{550} (g g^{-1}) was then determined using Equation 3.1 (Heiri et al., 2001):

$$\text{Equation 3.1} \quad \text{LOI}_{550} = \frac{\text{DM}_{105} - \text{DM}_{550}}{\text{DM}_{105}} * 100$$

Where DM_{105} is the dry sediment mass (g) and DM_{550} (g) is the sediment mass after ignition and subtraction of the crucible mass. LOI_{550} has been shown to strongly correlate with both f_{om} and f_{oc} (Dean, 1974) where the loss in mass is attributed to oxidation of all the organic carbon present in the sample to CO_2 . In addition to organic carbon, inorganic carbon (present in carbonate species) is known to release CO_2 at temperatures exceeding $450\text{ }^{\circ}\text{C}$ (Pallaser et al., 2013). This may lead to an overestimate of the sedimentary organic carbon mass present. However, given the siliceous nature of sandstone and alluvial sediments, any solid carbonate material present is likely to be restricted to grain cements and represent an insignificant fraction of the overall CO_2 produced. Therefore, it was assumed that $\text{LOI}_{550} = f_{om}$. A conversion factor was then used to estimate f_{oc} from f_{om} where $f_{oc} = f_{om} \cdot (0.58)$ (Lyman, 1982). This assumes that a constant proportion of organic carbon is present in organic matter. However, it possible that this may not be the case in fluvial sediments which vary in age, provenance and degree of microbial degradation. The average coefficient of variation (CoV) for LOI_{550} between the triplicate samples was 18%.

3.4.1.3 Porosity and bulk density

Total porosity (n) [$v\ v^{-1}$] was determined for the same samples in the previous section. Using a 20 mL syringe of known and constant volume (with the front of the barrel removed), saturated sediment samples were carefully eased into the syringe by a combination of gentle pressing and displacement of the plunger. The 20 mL sediment sample was then extruded onto clean porcelain crucibles and left to oven dry overnight at 105°C. The sample was then re-weighed and n was calculated using Equation 3.2 (Freeze and Cherry, 1979).

$$\text{Equation 3.2} \quad n = \frac{V_v}{V_T} * 100$$

Where V_v [v] is void space estimated from the difference in mass between the dry and weight samples with the density of water taken to be 1 g cm⁻³ and V_T is the volume of the syringe (20 mL). Effective porosity is assumed to equal measured porosity for all calculations in this study.

Dry bulk density (ρ) [g cm⁻³] was calculated using Equation 3.3 (Freeze and Cherry, 1979).

$$\text{Equation 3.3} \quad \rho = \frac{DM_{105}}{V_T}$$

Where DM_{105} is the dry sample mass [g] of volume V_T (20 mL). The average CoV between the triplicate measurements of n and ρ were typically <5%.

3.4.2 Water level monitoring and hydraulic testing

3.4.2.1 Water level measurements

Water levels were measured in the alluvial monitoring wells and riverbed piezometer nests (Chapters 4 and 5) using a graduated electronic contact meter (Solinst Model 102; Waterra UK) using the top of the well casing as a reference point. The device makes an electrical circuit when in contact with the water surface and the depth to water [m] is read from the graduated tape. The accuracy of the method is considered to be ± 0.003 m (Käser et al., 2009). River water levels were also measured on the outside of the piezometers to permit calculations of vertical hydraulic gradients. Absolute elevation in metres above ordnance datum (m AOD) was determined using the Heathbrook West borehole as a benchmark to reference Total Station levels. Hydraulic head [m AOD] was then calculated by subtracting the depth to water level measurements from the reference point elevation. Riverbed piezometer hydraulic heads were calculated by adding the height of the piezometer tube above the riverbed to the surveyed elevation and then subtracting the depth to water level. Continuous monitoring of the hydraulic heads was conducted for the single-screen piezometers (Chapter 5) and alluvial monitoring wells (Chapter 6) using automatic pressure transducers (Solinst Levelogger Junior LT or LTC Model 3001, Waterra, UK) logging at 30 or 60 minute intervals with an accuracy of ± 0.01 m. Temperature was also recorded with water level which was used to automatically compensate the level readings. Pressure transducers were suspended in the piezometer or well casing at the screen midpoint using nylon cord and the distance between the sensor window and the top of the wellhead or piezometer tube was measured to calculate the hydraulic head. River stage [m AOD] was recorded with a pressure transducer with the logger suspended 20 cm above the bed level. Manual water level measurements were periodically taken using the contact

meter to check the consistency of logger readings. Barometric pressure fluctuations were removed from water level time series using a separate barologger recording at the same time intervals as recommended by the manufacturer. Loggers were programmed and interrogated on-site using an optical USB interface connected to a laptop.

3.4.2.2 *Hydraulic conductivity determinations*

Falling head tests were carried out on the alluvial monitoring wells, single-screen riverbed piezometers and the temporary piezometer nests (Chapter 5). Time-water level data were recorded with pressure transducers usually logging at 1 or 5 second intervals. A manual contact meter was used for the temporary piezometer testing due to the narrow pipe diameter. Tests were conducted by instantaneously releasing a slug of water from a 1 L bailer which typically raised the head by 80–150 cm in the monitoring wells and single-screen piezometers and by 50–80 cm in the temporary piezometers (or when overflow was observed). Rising head tests were needed in some alluvial wells where the static water levels were close to the ground surface. Rising head conditions were achieved using a peristaltic pump operating at the highest flow rate ($>3 \text{ L min}^{-1}$) which resulted in evacuation of the well casing within 30 seconds. Saturated hydraulic conductivity (K_s) [m d^{-1}] was derived from the water level recovery data using the Hvorslev solution (Hvorslev, 1951) for a partially penetrating well in the form of Equation 3.4 (Freeze and Cherry, 1979).

Equation 3.4
$$K_s = \frac{r^2 \cdot \ln(L/R)}{2 \cdot LT_0}$$

Where r^2 [m] is the radius of the well casing (0.16 or 0.5 cm), R [m] is the radius of the well screen (same as r^2), L [m] is the length of the well screen (10–100 cm), 2 is a ‘shape

factor' for $L/R = >8$, and T_0 [s] is the 'basic lag time' where water level recovery reaches 37% of pre-test conditions. T_0 was derived using the exponential regression function of the slope of H/H_0 (\log_{10} -scaled) [m] against time t [s] where H is the water level at time t , and H_0 is the level where $t = 0$. This estimate of K_s will have both horizontal and vertical components, with a bias towards horizontal permeability in an anisotropic system (Binley et al., 2013). Test data were not corrected for temperature, however, a constant and uniform groundwater temperature of 10°C was assumed for all measurements. All the variable head tests undertaken with pressure transducers were carried out in duplicate and occasionally in triplicate with the average coefficient of variation (CoV) for K_s between the tests being 13%. Approximately half the tests using the manual dip meter and temporary piezometer nests were carried out in duplicate with a mean CoV of 30%. Test data were rejected when only 2 or 3 head measurements could be made before return to static water levels (i.e., in some of the highly responsive sediments).

3.4.3 Electrical resistivity imaging

Electrical resistivity imaging (ERI) (alternatively known as electrical resistivity tomography), is a well-established method of geophysical investigation of the subsurface. It is increasingly employed for shallow hydrogeological applications at groundwater-surface water interfaces (e.g., Crook et al., 2008; Nyquist et al., 2009) and is often used as a 'proxy' indicator of relative moisture content in soils and sediments (Vereecken et al., 2006). The technique provides for a 2-D 'image' or 'tomogram' of apparent resistivity distribution arising from differences in the geoelectrical properties of subsurface materials, which may then be inverted to produce a 2-D section of the true bulk resistivity. This, in turn, may be correlated with actual hydrostratigraphic features (Reynolds, 2011).

3.4.3.1 *Survey design and data acquisition*

The ERI survey design was heavily constrained by the geometry and geomorphology of the area of interest on the floodplain of the river (see Chapter 4). Channel-crossing lines were not attempted due to complexities associated with the inversion of survey data (i.e., accounting for the effect of the river volume) as well as practical issues with ensuring electrode insulation from the low-resistance pathway presented by the surface water column. Instead, ERI profiles were acquired on bank-parallel traverses along the floodplain. As far as was practically possible, lines were co-located with locations of boreholes and auger holes to provide spatially-referenced, geological information to ‘ground-truth’ resistivity profiles. Each survey line used either 32 or 64 (Table 3.4) 30 cm long stainless steel electrodes placed ~15 cm into the soil which were connected to the resistivity system and 12 V DC battery source via a multi-core cable (Fig. 3.4.1). The relative elevation of each electrode was surveyed using a surveyor’s level where the topography of the line varied by greater than one metre (Table 3.4). Survey data were acquired using the constant separation Wenner array configuration (Fig. 3.4.1) using a Campus Tigre automated resistivity system (Campus International Products Ltd., Dunstable, UK) with data acquisition using ImagerPro 2000 software (Media Cybernetics Inc., Bethesda, MD). Contact resistances were checked for anomalously high resistance values using three electrodes as reference points before multiple readings were acquired in accordance with standard procedures (Milsom, 2004). Where significant variation in contact resistances were found, electrodes were re-seated or re-positioned until approximate equivalence along the line was observed. DC current was sequentially increased every three levels from 0.5 mA at the surface level ($n = 1$) to 8 mA at the deepest levels of the profile for optimal signal-to-noise ratio. Each measured resistance was averaged over 3 readings to produce a value with an error of less than 1%, where the error

was greater, readings were repeated with increasing current levels until errors reduced to below 1%.

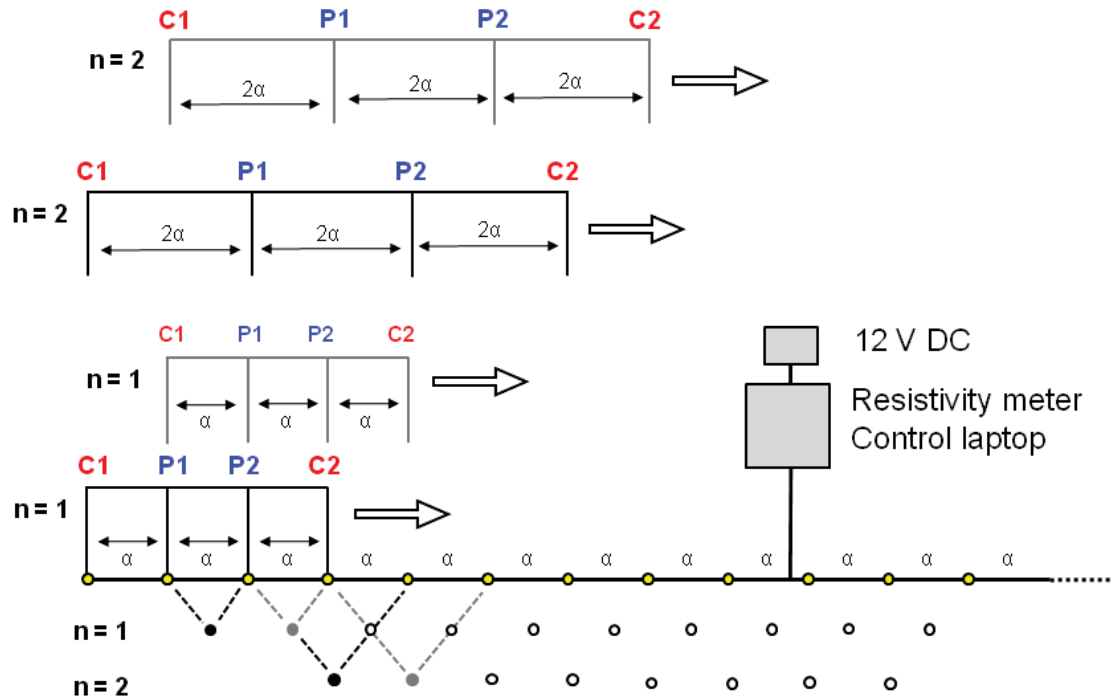


Fig. 3.4.1 Schematic of the ERI survey design using the Wenner Array configuration with expanding constant offset (α). Current electrodes are C1 and C2 with the potential difference measured by P1 and P2 where the offset is increased sequentially between levels (n).

3.4.3.2 Data processing and inversion

Raw ERI data were processed to remove anomalous values (e.g., where measurement errors were $>1\%$) which typically comprised less than 3% of measured resistivity values per section. Using Excel, a linear interpolation function was used to fill blank values left by removal of rejected data points. Before the inversion was performed, relative elevation values for each electrode location were added to the input data file to allow topographic corrections to be included in the model outputs. Inversions were completed individually using the ordinary least-squares approach based on the work of Loke and Barker (1995)

using Geotomo Res2Dinv (v.355) package (Geotomo Software; Penang, Malaysia). Damping factors were applied to all inversions in order to reduce noise using an initial factor of 0.160 and a minimum of 0.03. Model refinement using half-cell spacings was performed on all sections to help reduce the possible impacts of near-surface effects (cf. Ritz et al., 1999). Final models converged after 5 iterations for all profiles with root mean square (rms) errors less than 5% for all profiles other than for ER7, which had an error of 7% rms (Table 3.4). This particular line bisects the drainage ditch and is heavily corrected for topography due to the steep gradient present at its eastern edge. Therefore, it can be expected that a significant error may be introduced as a result of these geometric influences. Raw ERI data collected in 2002 (Table 3.4) as part of the LOCAR program (Blackwell, 2002) were inverted using the same processing steps as the data collected as in this study in order to provide additional coverage in the Heathbrook Farm floodplain area. These lines used a 2 m electrode spacing using a Campus Geopulse resistivity system (Blackwell, 2002).

Table 3.4 ERI data acquisition and survey configuration

Line	Acquisition date	No of electrodes	Max depth	Topographic correction	Model error
			(m)		(%)
ER01	05/11/2012	64	9	No	2.2
ER02	06/11/2012	64	9	Yes	1.8
ER03	19/04/2013	64	9	Yes	1.7
ER04	26/06/2013	64	9	Yes	4.7
ER05	01/07/2012	64	9	Yes	3.9
ER06	06/12/2012	32	5	Yes	7
ER07	04/12/2012	32	5	No	3.7
ER08	04/12/2012	32	5	No	3.4
ER09	06/12/2012	32	5	No	3.6
ER10*	20/05/2002	50	18	No	0.81
ER11*	20/05/2002	50	18	No	1.11

**ERI lines collected in Heathbrook Farm as part of the LOCAR program and included in this study (Blackwell, 2002).*

3.4.3 Riverbed temperature mapping

A custom temperature probing system was designed in order to investigate temperature gradients in the riverbed sediment (see Chapter 5). The sediment probe was constructed from a 2 m length of 10 mm OD copper pipe where a short (2 cm) perforated section was drilled at one end (Fig. 3.4.2A). A temperature probe (HOBO, UK) was then threaded through the pipe from a hole drilled near its top until the sensor was at the same level as the perforated section. A small amount of silicone sealant was used to retain the sensor in place as well as provide thermal insulation from the surrounding copper. The bottom of the pipe was then very carefully compressed to form a flat tapered point (Fig. 3.4.2B), to facilitate easy insertion into the bed sediments. Extreme care was taken to avoid crushing the sensor. After this was completed, the entire internal volume of the tube was back-filled with expanding polyurethane foam to provide additional thermal insulation and reduce the effect of unwanted temperature signals migrating down from the surface environment (Krause et al., 2011b). In order to measure river water temperature simultaneously, a second probe was constructed using a 1 m steel strut which could be embedded in the sediment. The wire of the sensor was wrapped around the strut with the sensor itself suspended several cm away in the water column. Both probes were graduated with insulation tape to ensure accurate and consistent depth measurements. The temperature sensors were connected to a 4-channel logger unit using the internal thermistor with an accuracy of ± 0.2 °C. The surface water probe was kept at a constant depth of 10 cm above the bed level with care taken to keep the probe shaded from direct sunlight. The stabilisation of the temperature readings was achieved within 3 minutes and the data read out from a laptop connected to the logging unit.

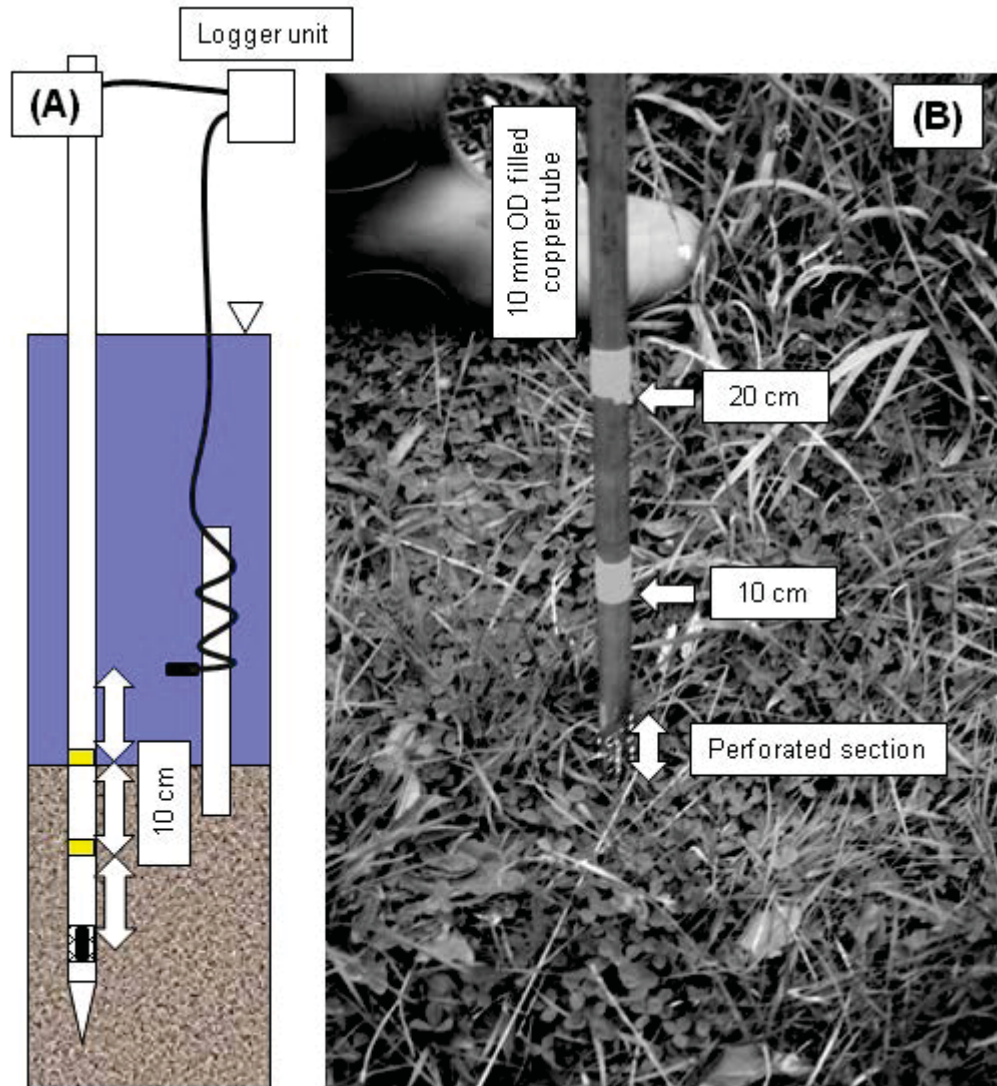


Fig. 3.4.2 Details of the probe used to map riverbed temperatures as a schematic (A) and in close up (B).

3.5 Sampling and chemical analysis

3.5.1 In-situ measurements

3.5.1.1 Dissolved oxygen

Dissolved oxygen (DO) was determined using an optical luminescence (LDO) probe attached to a Hach-Lange (Hach Company, Germany) hand-held unit (HQ30D). All DO measurements were carried out on site by first completely filling a 20 mL syringe with a sample then carefully removing the plunger and promptly inserting the DO sensor, which displaced about half of the syringe volume. Because the technique is sensitive to ambient light levels, the sampling syringes were modified so that the barrel was rendered opaque using insulation tape, thereby allowing DO determinations to be carried out in darkness. The technology offers advantages over traditional polarographic electrodes in that no time is needed for membrane polarisation and the time required for the stabilisation of readings is typically shortened to <1 min. Daily calibration checks were performed using 100% saturated water solutions. The manufacturer-specified detection limit was 0.01 mg L⁻¹ with an accuracy of ± 0.1 mg L⁻¹ (www.hach.com). Repeat measurements were carried out on around 20% of samples where the mean relative error was determined to be 8%.

3.5.1.2 pH and electrical conductivity

pH was determined on site using for groundwater samples using a pH electrode connected to the HQ30D unit with a millivolt accuracy of ± 0.1. Daily calibrations were performed with certified pH 7 and pH 10 buffer solutions (Fisher Scientific, UK). Electrical conductivity (EC) was also determined on groundwater samples using a TetraCon 325 EC probe connected to a WTW P4 meter (WTW, Germany) with an accuracy of ±1 µS cm⁻¹.

EC was automatically temperature adjusted and daily calibration checks were performed using a certified 1413 $\mu\text{S cm}^{-1}$ stock solution (VWR, UK).

3.5.2 Volatile organic compounds

3.5.2.1 Chlorinated ethenes

HydraSleeve samples for chlorinated ethenes (CEs) were collected in 125 mL PET bottles leaving no air spaces and closed PTFE-lined caps. These were sent to the Environment Agency's laboratories in Exeter where samples were analysed for a wide range of volatile organic compounds (VOCs) using qualitative, purge-and-trap gas chromatography-mass spectrometry (GC-MS). Quantitative determinations on chlorinated species were carried using gas chromatography with electron capture detection (GC-ECD) after extraction using pentane (Andrew Pearson, EA; personal communication).

All other CE samples in this study were analysed using headspace GC-MS (GC: Agilent 6890 series; MS: Agilent 5973 MSD) at Keele University Forensic Science laboratories. Samples were collected in 20 mL clear glass VOA vials (Fisher Scientific, UK) leaving no air spaces which were closed with precision-thread, PTFE-lined screw caps. All samples were immediately transferred to a cool box at 4°C before transfer to the laboratory where they were refrigerated at 3°C. Because of the potential for degradation of the more labile CEs (i.e., vinyl chloride), samples were prepared for analysis within 48 hours of collection and analysed within 2 weeks. A GC-MS analysis method was developed specifically for the investigation based generally on USEPA Method 524.2 (USEPA, 1992) but using static headspace equilibration (Agilent Technologies, 2008) for quantitative determination of dissolved CEs including; TCE and its chlorinated metabolites *cis*-1,2 dichloroethene,

(cDCE), *trans*-1,2-dichloroethene (tDCE), 1,1-dichloroethene (1,1-DCE) and vinyl chloride (VC). Samples were prepared by removing a 10 mL aliquot of the refrigerated unfiltered sample using glass pipettes of which 500 μ L was retained for anion analysis (or the whole 10 mL used for duplicate analysis). 7 grams of pesticide-grade anhydrous sodium sulphate (Pestnorm; VWR, UK) was immediately added to the vials as a matrix modifier to improve method sensitivity (Agilent Technologies, 2008) which were re-closed with PTFE-lined centre hole screw caps to allow for syringe extraction. Initially, samples were equilibrated in a water bath for 20 minutes at 75°C after which a 1 ml aliquot of the vapour phase was transferred to the GC split/splitless injector using a gas-tight syringe (SGE Analytical Science, Australia). The sensitivity of the method was improved by extending the equilibration period to 40 minutes with a final 30 seconds of vigorous manual shaking. To minimise the possibility of sample carryover, the gas-tight syringe was kept at a constant 90°C inside a heated unit between runs. Chromatography was performed using a DB-624 capillary column (25 m x 180 μ m x 1 μ m) (J&W Scientific) using a CP-grade helium carrier with a flow rate of 0.4 mL min⁻¹. An optimal peak shape for all analytes was obtained using a split ratio of 50:1 in constant pressure mode set at 95 kPa. A single temperature ramp was used with an initial hold of 5 minutes at 40°C rising to 100°C at 8°C min⁻¹, giving a total run time of 12.5 minutes. Mass spectrometry was performed using electron impact ionisation with data acquired by selective ion monitoring (SIM) where only two ions are recorded within a time window around compound elution. Table 3.5 provides details of the retention times and quantitation ions for the chlorinated compounds investigated.

Table 3.5 Mass spectrometer SIM ions and retention times for specific CEs.

Analyte	Retention time	Target ion	Qualifier ion
	minutes	m z ⁻¹	m z ⁻¹
Vinyl Chloride	1.43	62	64
1,1-Dichloroethene	2.54	96	61
<i>trans</i> -1,2-Dichloroethene	3.08	61	96
<i>cis</i> -1,2-Dichloroethene	3.44	61	96
Trichloroethene	7.97	132	95

It was not possible to detect ethene (the final product of reductive dechlorination of TCE) due to the poor chromatographic resolution for high-volatility VOCs with the type of capillary column used. Calibration standards were prepared using serial dilutions of certified reference materials (Restek Corporation, USA) dissolved in HPLC-grade methanol (VWR, UK). These were used to spike VOC-free water in the 20 mL vials with the same liquid:headspace ratio and matrix modifier as the samples. 6-point calibration curves were used to determine the unknown concentrations with R² values (coefficient of determination) >0.99 for all compounds. Typically, 10% of samples were analysed in duplicate and laboratory blanks were run at the start and end of each analysis session as well as once every 15–20 samples (to determine if any contamination was present). The limit of detection (LoD) for each compound was determined by replicate analyses of a 1 or 0.5 µg L⁻¹ standard (USEPA, 1992). For the initial method, the LoD was approximately 1 µg L⁻¹ for all compounds with a relative error of <10%. This was later improved with the longer sample equilibration 0.1 µg L⁻¹ for TCE and the DCE isomers and ~0.2 µg L⁻¹ for VC with a typical relative error of <5%.

3.5.2.2 *Methane*

Samples for dissolved methane (CH₄) were collected in 12 mL soda glass Exetainer (Labco, UK) vials from the groundwater and mini-piezometers and 6 mL vials for samples from the pore water samplers. Vials were slowly bottomed-filled and allowed to over flow for 1–2 volumes before the addition of either a 100 µL (12 mL sample) or 50 µL (6 mL sample) of a 50 molar zinc chloride solution to inhibit biological activity (Trimmer et al., 2010). Vials were then capped tightly with no air bubbles using thick butyl rubber septated caps with centre holes and transferred to a cool box at 4°C. Vials were refrigerated at 3°C and analysed within one month of collection. CH₄ was determined using gas chromatography with flame ionisation detection (GC-FID; Agilent GC7890A series) which was custom designed for CH₄, carbon dioxide and nitrous oxide measurements at atmospheric concentrations (Agilent Technologies, 2010). Prior to analysis, samples were allowed to warm to room temperature (20°C). A 10 or 20 mL gas-tight polypropylene syringe was used to withdraw 5 or 10 mL of sample from the vial through the centre hole into the syringe which was locked using a 3-way stopcock. A 5 or 10 mL inert headspace was created by displacing oxygen-free nitrogen gas (OFN) (BOC, UK) into the syringe from a Tedlar (Sigma Aldrich, UK) gas sampling bag. Samples were equilibrated by vigorous manual shaking for 3 minutes after which a second syringe was interfaced to the equilibration syringe via another 3-way stopcock, into which the headspace gas was displaced. The equilibrated gas sample was then injected via a splitless injector interfaced to a 1 mL sample loop. OFN was used as a makeup gas with a flow rate of 2 mL min⁻¹ and chromatographic separation was achieved using a 1/8 inch stainless-steel packed column (HayeSep Q 80/100) (J&W Scientific) under isothermal conditions (60°C) with a 48 and 500 mL min⁻¹ hydrogen/air flow mix for the FID. The FID was allowed to ‘warm up’ for at least 3 hours prior to analysis to ensure a stable baseline. Calibrations were performed

using certified reference gases (BOC, UK) with which serial dilutions were made using OFN. 5 point calibration curves were used to determine the unknown samples with a typical R^2 of >0.99 . Laboratory air blanks were analysed at the start and end of each analytical session as well as every 20–30 runs. 10% of the samples were analysed in duplicate. Although the column and detector would have been suitable to detect ethene, the GC hardware was specifically customised for analysis of the three aforementioned gases only, and a modification of the method was not possible.

The aqueous mass concentration of CH_4 [μg or mg L^{-1}] was calculated retrospectively from the headspace volume concentrations [ppm v^{-1}] (determined from calibrations) using an approach based on Henry's Law of ideal gas concept (Equation 3.5) (Kampbell and Vandegrift, 1998):

$$\text{Equation 3.5} \quad \text{TC} = C_{\text{H}} + C_{\text{Aq}}$$

Where TC is the original sample mass concentration [mg L^{-1}] C_{H} is the concentration in the headspace [mg L^{-1}] and C_{Aq} is the concentration in the liquid phase [mg L^{-1}]. First, the density factor (ρ) for CH_4 is calculated from the following properties:

$$\text{Equation 3.6} \quad \rho = \frac{\text{MW} \cdot T}{22.4 \cdot T_s}$$

Where MW is the molecular mass of CH_4 (16.04 g mol^{-1}), T is standard temperature (273 K), 22.4 is the volume [L mol^{-1}] of any gas at standard temperature and pressure (according to the ideal gas laws) and T_s is the temperature at which the equilibration was carried out (293 K).

The headspace concentration (C_H) is then determined using Equation 3.7.

$$\text{Equation 3.7} \quad C_H = \frac{C_v \cdot \rho \cdot V_h}{V_a \cdot 1000}$$

Where C_v is the concentration of CH_4 [ppm v^{-1}], ρ is the density factor, V_h is the volume of the headspace (5 or 10 mL) and V_a is the volume of the liquid phase (5 or 10 mL).

Similarly, the aqueous concentration (C_{Aq}) is calculated from Equation 3.8.

$$\text{Equation 3.8} \quad C_{Aq} = \frac{C_v \cdot 55.5 \cdot MW}{H \cdot 1000}$$

Where C_v and MW are already given, 55.5 is the molarity of pure water [mol L^{-1}] and H is Henry's law constant [atm mol^{-1}] for CH_4 at 20°C (37600) which was estimated from solubility coefficients (USEPA, 2004). The detection limit for CH_4 using this approach was $0.1 \mu\text{g L}^{-1}$ based on an analysis of replicate standards (USEPA, 2004) with high precision indicated by a typical relative error of $<1\%$. The average of all laboratory air blanks were used to calculate an approximate atmospheric saturation of CH_4 ($1.38 \mu\text{g L}^{-1}$) by substituting a representative groundwater temperature of 10°C into the previous calculations.

3.5.3 Anions

Samples for anions, including nitrate (NO_3^-), sulphate (SO_4^{2-}) and chloride (Cl^-), were collected unfiltered as part of the CE sampling process or separately in 30 mL HDPE bottles (Fisher Scientific, UK), which were used from new and factory clean. Samples were either refrigerated at 3°C and analysed within 48 hours of collection or frozen and analysed within 3 months. Anions were determined by ion chromatography on a Dionex ICS1000 (Dionex Corporation, UK) equipped with an anion exchange column and an

autosampler. A carbonate/bicarbonate eluent was used with a flow rate of 1 ml min⁻¹ and a suppression system to remove background conductivity. 10% of samples were analysed in duplicate and 4 point calibration curve were generated for serial dilutions of a certified mixed stock solution (Sigma Aldrich, UK) to determine the unknowns. Laboratory blanks were included in the samples batches every 10–20 samples as well as at the start and end. Detection limits were 0.2 mg L⁻¹ for NO₃⁻, 0.05 mg L⁻¹ for Cl⁻ and 0.1 mg L⁻¹ for SO₄²⁻ based on a replicate analysis of a 1 mg L⁻¹ standard with an average relative error of <4%.

3.5.4 Iron and manganese

The metals iron (Fe) and manganese (Mn) were sampled in 30 mL HDPE bottles which were used from new and factory clean. To fix samples and prevent adsorption to the container surfaces, 200 µL of 15% ACS grade nitric acid (Aristar; VWR, UK) was added immediately before sampling to reduce the pH to <4. Samples were filtered inline using disposable 0.45 µm cellulose acetate membrane syringe filters (Whatman, UK) and transferred immediately to a cool box at 4 °C. Because the samples were preserved, analysis was typically carried out between 3 and 6 months after sampling. Fe and Mn were determined using inductively coupled argon plasma optical emission spectroscopy (ICP–OES) (Varian Vista Pro MPX) equipped with an autosampler. Typically 3 or 4 emission wavelengths were scanned simultaneously (in radial view) with 238.2 and 257.6 nm providing the best sensitivity and reproducibility for Fe and Mn, respectively. 4 point calibration curves, derived from serial dilutions of a certified multi-component standard (Sigma Aldrich, UK), were used for quantitation from the mean of 3 injections. 10% of the samples were analysed in duplicate with acidified laboratory blanks analysed every 10–20 samples. Limits of detection were calculated using replicate analysis of acid-spiked

laboratory blanks (Armbruster and Pry, 2008) and were established as 0.07 mg L^{-1} for Fe and 0.05 mg L^{-1} for Mn, with an average relative error of $<5\%$.

3.5.5 Dissolved organic carbon

Samples for dissolved organic carbon (DOC) were collected in 20 mL amber glass vials which had been pre-combusted at 550°C in a muffle furnace for a minimum of 3 hours (in order to remove any trace organic contamination, despite being used from new). Samples were filtered on site using $0.7 \mu\text{m}$ Whatman glass-fibre membrane filters (GF/C) (Fisher Scientific, UK) which had also been pre-combusted at 550°C for 3 hours. Samples were acidified and preserved on site by the addition of $200 \mu\text{L}$ of 30% reagent-grade hydrochloric acid (Aristar; VWR, UK) after which vials were closed with screw caps containing PTFE-lined caps. Samples were then transferred to a cool box at 4°C and refrigerated in the laboratory at 3°C . Because the solubility of high molecular weight DOC (such as humic acids) is pH-sensitive (Neirop et al., 2002), it is conceivable that some of this fraction may have precipitated from solution after sample acidification, possibly leading to an underestimation of the DOC present. However, the source of uncertainty associated with this preservation method was deemed acceptable given that (1) sample analysis within 24 hours of acquisition was not practical and (2) freezing zero-headspace glass vials would have been impossible. DOC samples were analysed within one month of collection at the University of Birmingham School of Geography, Earth and Environmental Science laboratories. Determination of DOC was made as non-purgeable organic carbon (NPOC) on a Shimadzu TOC-Vcpn analyser (Shimadzu Corporation, Japan). Acidified samples were sparged for 20 minutes with oxygen to remove inorganic carbon followed by high temperature combustion with infrared detection of NPOC as carbon dioxide from the mean of 3–5 injections (Baker et al., 2008). In-line dilutions of a total organic carbon

reference standard (Sigma Aldrich, UK) were used for quantitation over 5 calibration levels with laboratory blanks included every 10 samples. The limit of detection was 0.2 mg C L⁻¹, based on a replicate analysis of the 1 mg L⁻¹ calibration level, with an average relative error of 3%.

3.6 Statistical analysis

All statistical analyses of the hydraulic and hydrochemical variables were performed in SPSS v19 (IBM, USA). Before any comparisons of datasets were attempted, distributions were checked using the Shapiro-Wilk test of normality to determine whether parametric or non-parametric tests were appropriate using a significance level of 0.05 (Schuenemeyer and Drew, 2011). The Shapiro-Wilk test is considered to have the superior power for a chosen alpha level in comparison to other normality tests such as Anderson-Darling or Lilliefors (Razali and Wah, 2011).

3.6.1 Parametric tests

Most datasets had significant skewness and kurtosis but were able to satisfy the normality criterion after application of a log transformation (base 10). In these cases, differences in means between two groups were analysed using paired T-tests or one-way analysis of variance (ANOVA) for three or more groups with a 0.05 significance level. All means reported were back-transformed from their logarithms in order to provide meaningful values. The null hypothesis of these tests states that the means are equal and therefore the samples are drawn from the same population (Field, 2005). Although a significant ANOVA result ($p = <0.05$) indicates that the differences between groups are greater than within-group differences, it cannot specify which groups differ from one another (Pallant,

2005). This was accomplished by using exploratory post-hoc testing using either Scheffe's method, where homogeneity of variance, is assumed or the Games-Howell method where homogeneity of variances cannot be assumed. Homogeneity of variances were investigated using Levene's test where a non-significant result ($p = >0.05$) indicates homogeneity of variances can be assumed (Field, 2005). Pearson's correlations were used to describe the strength and direction of relationships between variables (Pallant, 2005) although a causal relationship is not necessarily implied by correlated variables as a third unseen variable may influence both (Field, 2005). Only significant correlations are reported ($p = <0.05$).

3.6.2 Non-parametric tests

Where it was not possible to satisfy the normality criterion for parametric analyses, non-parametric tests were used. Mann-Whitney U-tests were used as a non-parametric alternative to T-tests where differences in medians are examined rather than means. Spearman's rank order correlation (ρ) was used as the non-parametric alternative to the Pearson's correlation where data are ranked before the Pearson equation can then be applied (Pallant, 2005). Only significant results are reported at a 0.05 significance level.

4. Plume discharge zone characterisation

4.1 Chapter introduction

Prior to this stage of the investigation, the TCE plume was already known to have migrated from its (presumably) deep source area in the up-gradient aquifer to a relatively shallow depth in the sandstone, as intercepted by the boreholes Heathbrook East and West, situated adjacent to the River Tern (Figs. 3.2.6 and 3.2.9, Chapter 3). However, no other information on its down-gradient geometry or configuration was known or whether the contamination front had reached the alluvial deposits, riverbed sediments or the river itself. This chapter aims to delineate and characterise the potential riparian discharge zone of the TCE plume. This aim is achieved through a multi-scale investigative approach utilising (1) the existing groundwater monitoring network, (2) a riverbed diffusion sampler survey (3) installation of multi-level, mini-piezometer transects and (4) installation of bank-side alluvial monitoring wells. The hydrogeological properties, structure and thickness of the floodplain drift deposits along the potential discharge zone are also investigated using augerhole observations and 2-D electrical resistivity imaging (ERI).

4.2 Delineation of the plume discharge zone

4.2.1 Sampling of pre-existing monitoring networks

4.2.1.1 Permo-Triassic sandstone boreholes

Prior to any sampling in the down-gradient area of the plume, depth-discrete groundwater

samples were retrieved from the sandstone aquifer in May 2011 (Figs. 3.2.5 and 3.2.9, Chapter 3) using the passive HydraSleeve method (ITRC, 2006). Substantial increases in TCE concentrations were revealed in samples from the Helshaw Grange abstraction borehole (HGA) (Table 4.1). Maximum concentrations of 135–139 $\mu\text{g L}^{-1}$ were observed at a depth range of 60–80 m with an average increase of 53 $\mu\text{g L}^{-1}$ (or 112%) for the whole borehole over the two years since previous sampling. The Helshaw Grange observation (HGO) borehole showed only slight increases in TCE with an average change of just 4 $\mu\text{g L}^{-1}$ (Table 4.1). At the floodplain, TCE was below the GC-MS limit of detection (LoD) of 1 $\mu\text{g L}^{-1}$ in all piezometers of the LOCAR borehole array in the southern part of the research area. This also included the 45 m deep T11A abstraction borehole open over a substantial vertical thickness of the Permo-Triassic aquifer (Table 4.1). TCE was detected in the boreholes Heathbrook East (HBE) at 6.8 $\mu\text{g L}^{-1}$ and Heathbrook West (HBW) at 17.8 $\mu\text{g L}^{-1}$ (where the plume was previously known to be present), representing an average concentration increase of 70% since 2009. No TCE dechlorination daughter products (cDCE and VC) were detectable in any of the sandstone groundwater samples.

Table 4.1 Dissolved TCE determinations from multi-level HydraSleeve samples for the up-gradient groundwater monitoring boreholes in comparison with prior sampling by the Environment Agency (EA, 2010; unpublished data).

Sample depth	TCE Mean 2009	TCE May 2011	Increase	Percent
(m)	($\mu\text{g L}^{-1}$)	($\mu\text{g L}^{-1}$)	($\mu\text{g L}^{-1}$)	(%)
<i>Helshaw Grange abstraction borehole</i>				
20	20	44	24	118
35	38	65	27	70
50	55	89	34	62
60	58	139	81	138
70	47	135	88	187
80	71	139	68	95
<i>Helshaw Grange observation borehole</i>				
20	28	32	4	14
40	41	44	3	8

4.2.1.2 Floodplain boreholes and riverbed piezometer network

The pre-existing network of in-stream piezometers installed along a 250 m reach of the river (Krause et al., 2013) were sampled during a baseflow period in late May 2011 (Fig. 4.2.1). Of this network, 22 piezometers were sampled at depths of between 1 and 1.5 m below the riverbed surface. The presence of TCE was revealed in the northern part of this transect where concentrations were at (or just above) the LoD of $1 \mu\text{g L}^{-1}$ at P12 to a maximum of $29 \mu\text{g L}^{-1}$ at in P4 (Fig. 4.2.2) (Weatherill et al., 2014). TCE was detectable in the outflow from a drainage ditch in the northern floodplain at $3.5 \mu\text{g L}^{-1}$ (Fig. 4.2.2) but not in any other surface water samples. No dechlorination products (e.g., cDCE or VC) were detectable in any of piezometer samples from the riverbed. TCE was also not found in any of the shallow monitoring wells (Krause et al., 2013) previously installed in the floodplain alluvium deposits (Fig. 4.2.2).

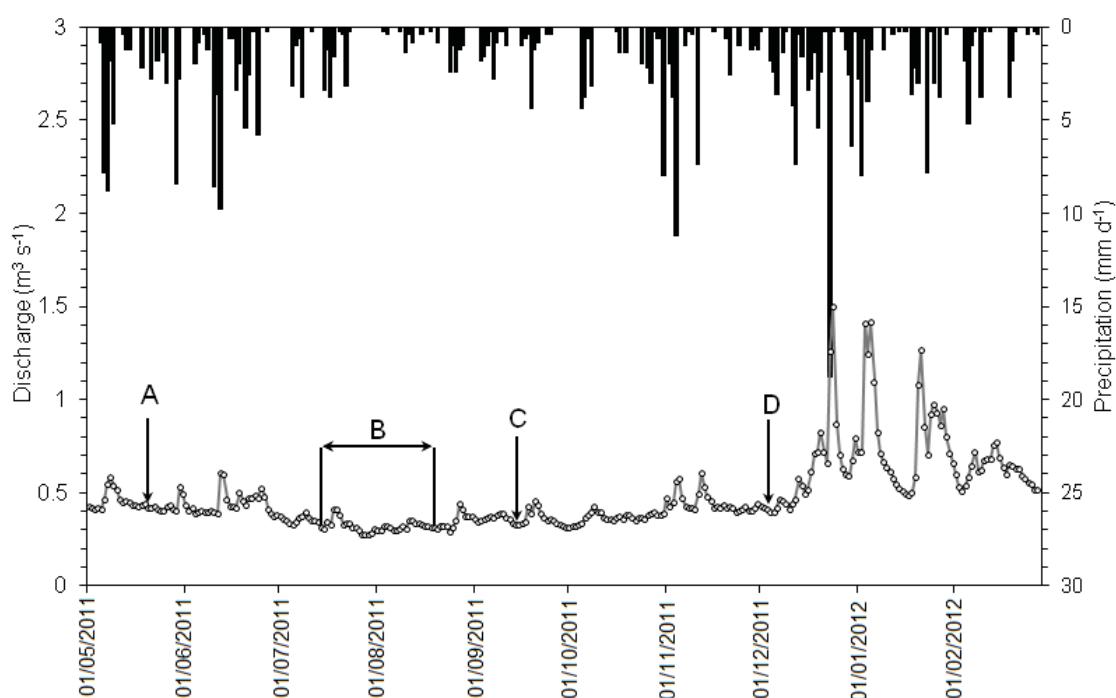


Fig. 4.2.1 Daily rainfall for Childs Ercall station 5 km southwest of the site (Met Office ID 431325) and river discharge for Ternhill hydrometric station (see Chapter 3) for the sampling campaigns in this chapter (EA, 2010, unpublished data). Time periods labelled include (A) initial sampling of riverbed piezometers, (B) diffusion sampler deployment period (C) September 2011 sampling snapshot and (D) December 2012 sampling snapshot (modified from Weatherill et al., 2014).

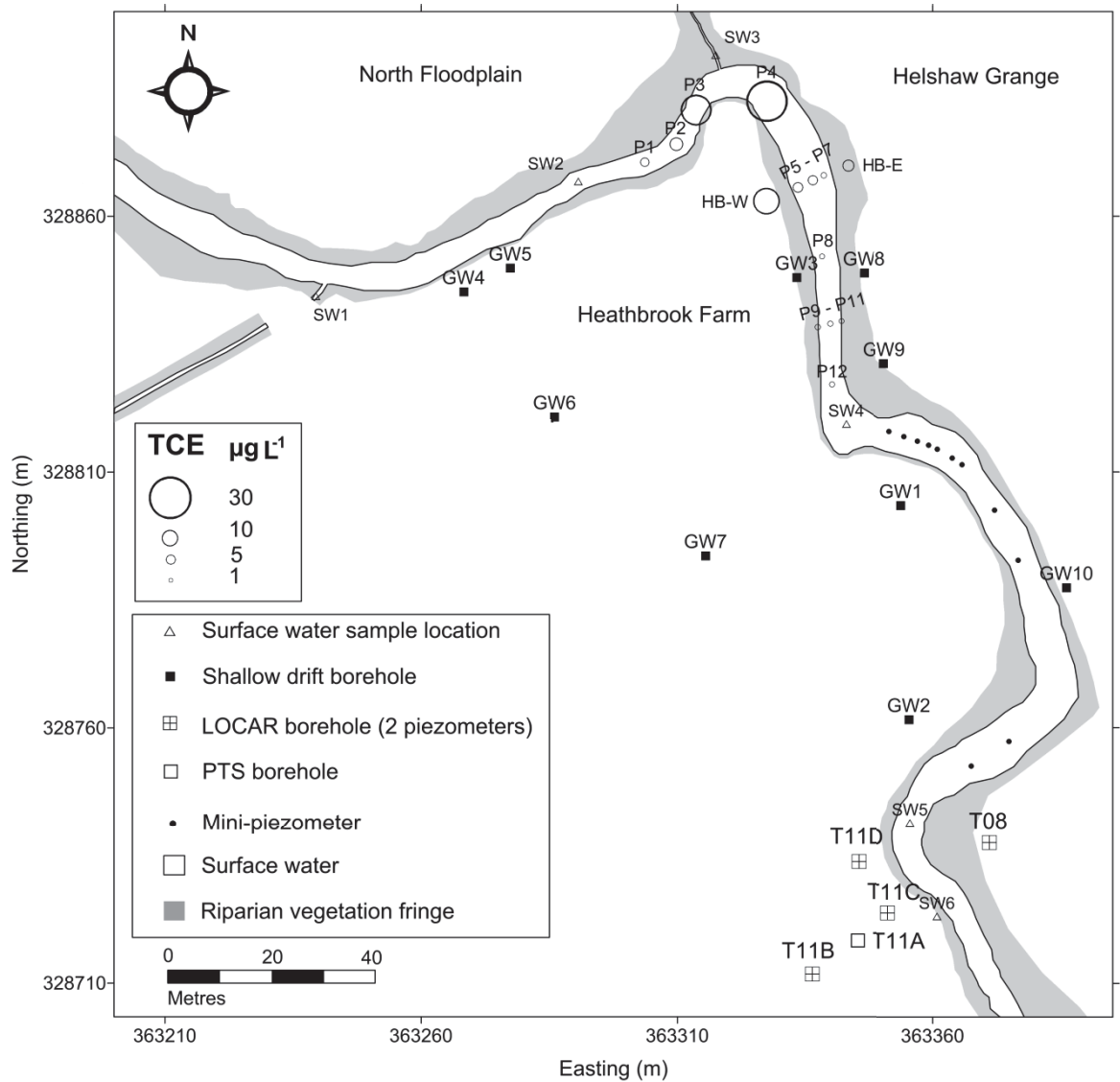


Fig. 4.2.2 Pre-existing floodplain groundwater and riverbed monitoring network sampled during the initial campaign. TCE concentrations from May 2011 are represented by scaled circles. Surface water sampling locations are also included (modified from Weatherill et al., 2014).

4.2.2 Passive diffusion sampling campaign

The diffusion sampler campaign provided an opportunity to define the upstream boundary of the upwelling zone of the plume west of piezometer P1 where no prior monitoring points were available in the riverbed (Fig. 4.2.2). Samplers were deployed in two transects (A and B) stationed along 5 m intervals of the main channel with two samplers per station of Transect B and one per station of Transect C in the drainage ditch. TCE was detectable in at least one sampler at each location of the 120 m long transect (B-B', Fig. 4.2.3A), with

a median concentration of $2.1 \mu\text{g L}^{-1}$. Daughter products cDCE and VC were not detectable at any location in the main channel survey area (Fig. 4.2.3B). At the upstream section of the survey, riverbed TCE concentrations ranged from the LoD of $1 \mu\text{g L}^{-1}$ at the 0 m position to $5.8 \mu\text{g L}^{-1}$ at 20 m and $7 \mu\text{g L}^{-1}$ at 40 m (Fig. 4.2.3A). It was impossible to relocate the samplers deployed at the 45 m position due to excessive *Ranunculus* growth in the channel. Samplers located at the 65 and 70 m positions of the transect were rejected due to perforation of the LDPE membranes, which presumably occurred during their installation. Between 50 and 75 m, median TCE concentrations increased to $9.5 \mu\text{g L}^{-1}$ reaching a maximum of $21 \mu\text{g L}^{-1}$ at 70 m (Fig. 4.2.2A). This area coincides with a meander bend in the floodplain where the river flow direction changes from approximately east-west to north-south and also where the eastern bank forms a terrace rising over 10 m above the surrounding floodplain. This area is also approximately co-located with the in-stream piezometers P1–P7 where TCE was detected in the preceding sampling campaign (Fig. 4.2.2). Cross-channel concentration gradients were apparent at some of the paired sampler locations. The median TCE concentration of the 20 m long transect (C–C') installed in the ditch channel (Fig. 4.2.3A) was $2 \mu\text{g L}^{-1}$ with a maximum of $4.1 \mu\text{g L}^{-1}$. In contrast to the previous sampling campaigns, the daughter product cDCE was observed at all five locations reaching a maximum of $17 \mu\text{g L}^{-1}$ at the 10 m position (Fig. 4.2.3B). TCE concentrations obtained from the triplicate sampler clusters suspended at the base of the screened sections of the sandstone boreholes (used as quality control measures) were $5 (\pm 0.7) \mu\text{g L}^{-1}$ at Heathbrook East and $14.2 (\pm 2.4) \mu\text{g L}^{-1}$ at Heathbrook West. These concentrations lie within approximately 20% of those obtained with the HydraSleeve method (6.8 and $17.8 \mu\text{g L}^{-1}$, respectively for each well) collected in May 2011 (Weatherill et al., 2014).

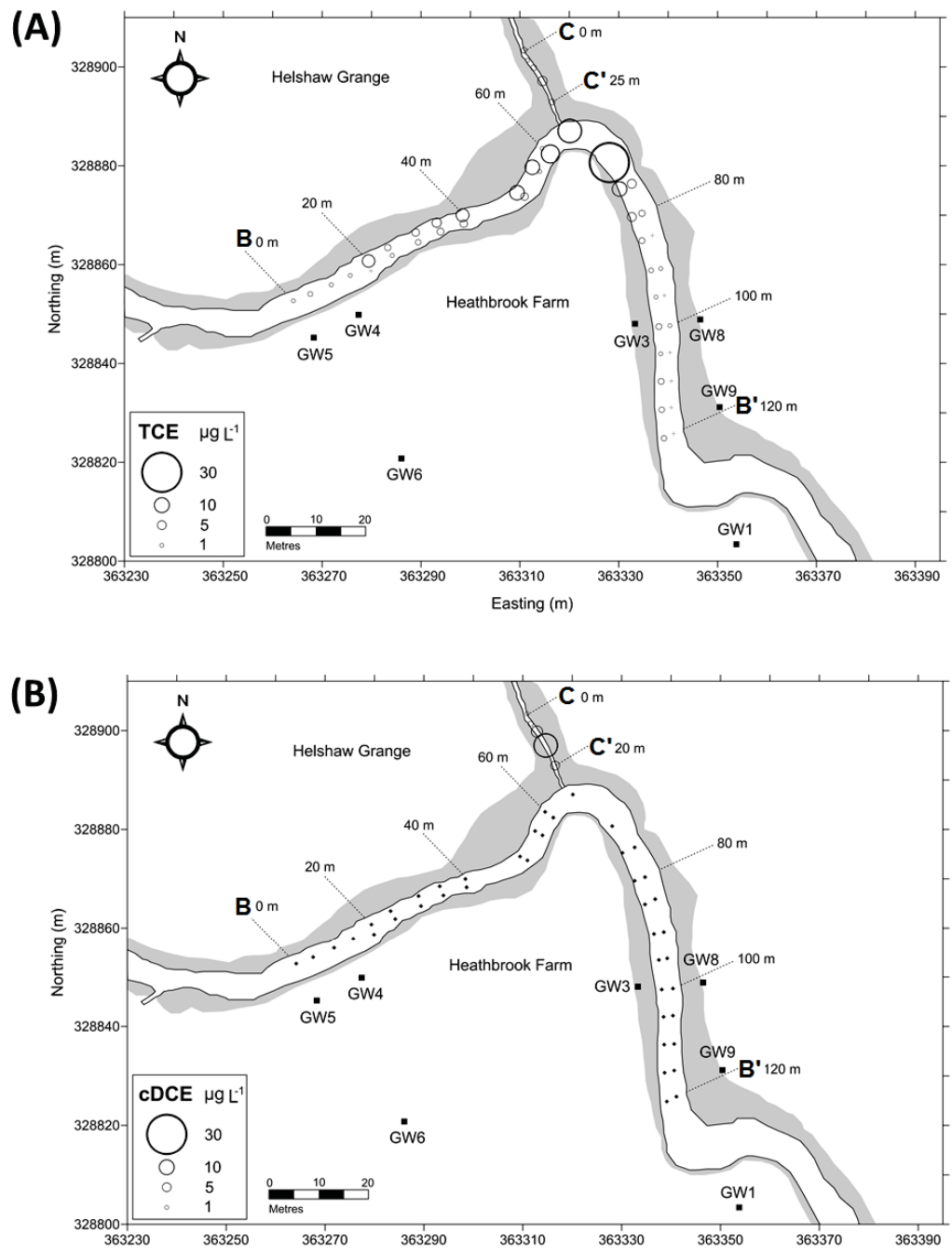


Fig. 4.2.3 (A) Diffusion sampler TCE concentrations are 33 days equilibration with the sediment pore water and (B) results for cDCE. Note the higher concentration zone centred round the meander bend (cf. Fig. 4.2.2) (modified from Weatherill et al., 2014).

4.2.3 Riverbed mini-piezometer investigation

The previous sampling campaign's observation of relatively elevated TCE concentrations along the reach located around the head of the meander bend provided a focus for multi-level sampling to characterise depth-discrete longitudinal and cross-channel spatial variability of the plume in this area of the riverbed (Fig. 4.2.2).

4.2.3.1 September 2011 snapshot

The first sampling campaign in September 2011 revealed TCE levels in excess of those originally sampled in May 2011 at HBE and HBW in the sandstone aquifer. TCE exceeded $30 \mu\text{g L}^{-1}$ at the mini-piezometers MP7, MP8, MP13 and MP23 (Fig. 4.2.4) with a median of $13.6 \mu\text{g L}^{-1}$. A cross-channel concentration gradient was apparent at TA piezometers MP5 to MP8 immediately upstream of the meander head. With a general increase from the southern bank (at Heathbrook Farm) to north a maximum of $36 \mu\text{g L}^{-1}$ was obtained at MP8 at a depth of 100 cm below the riverbed adjacent to the northern bank. At the downstream transect, TB, this spatial pattern was reversed with a significant cross-channel concentration gradient ranging from a maximum concentration of $35 \mu\text{g L}^{-1}$ at 60 cm depth (MP13) on the Heathbrook Farm bank side, decreasing to just $8.3 \mu\text{g L}^{-1}$ at MP16 (100 cm below the sediment-water interface) on the opposite bank (Fig. 4.2.4) (Weatherill et al., 2014).

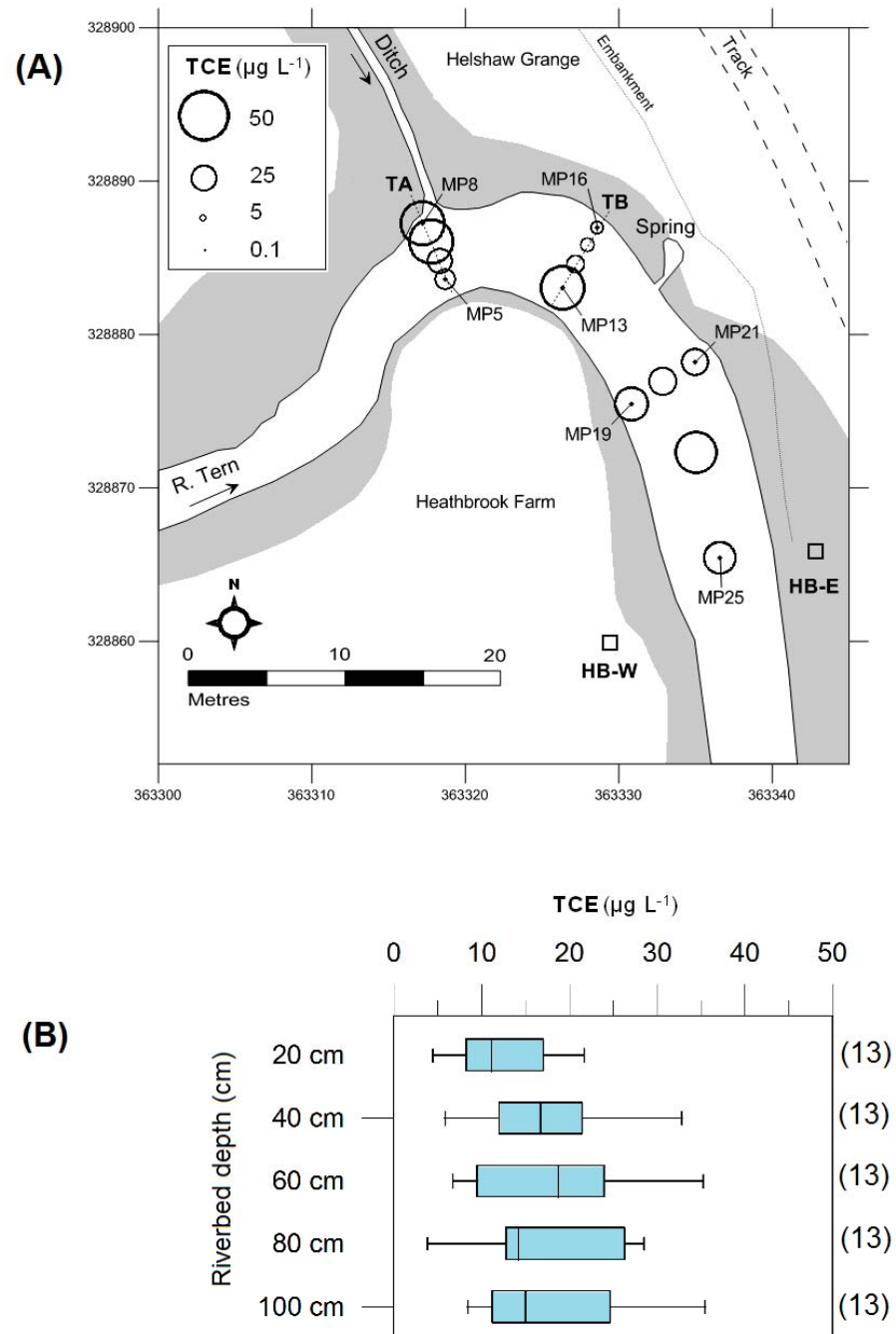


Fig. 4.2.4 (A) Spatial variation in maximum TCE concentrations determined from mini-piezometer investigation in September 2011. (B) Box plots summarising the variation of TCE concentrations with piezometer sampling level. Box-plots present a non-parametric summary of data as quartiles with the median represented by a vertical line. The ‘whiskers’ represent maximum and minimum values. Sample size (n) given in parentheses on the right (modified from Weatherill et al., 2014).

4.2.3.2 *December 2011 snapshot*

The mini-piezometer network was considerably expanded for the December 2011 sampling campaign (Fig. 4.2.5) in order to provide a greater density of monitoring points (see Appendix A). The presence of clay and peat deposits underlying parts of the riverbed to the north of transects TA prevented collection of pore water samples from some of the sampling levels of MP1, MP2 and MP3. The spatial patterns of TCE concentrations were generally consistent with those observed during the September campaign with a median riverbed concentration of $17 \mu\text{g L}^{-1}$, although the cross-channel concentration gradient at TA was less well defined. Plume concentrations of $<10 \mu\text{g L}^{-1}$ were observed in an area near the northern bank between the outlet of the ditch and the spring seepage area (at MP11, MP14, MP15 and MP16, Fig. 4.2.5). Downstream of MP19–MP21, TCE concentrations appeared to be more homogeneous with concentrations in the region of $20 \mu\text{g L}^{-1}$. Plume concentrations in excess of $35 \mu\text{g L}^{-1}$ were observed at MP3 and MP12 reaching a maximum of $40 \mu\text{g L}^{-1}$ at MP18. These higher plume concentrations were observed at depths of 80–100 cm below the riverbed surface with the exception of MP3 where the high level was observed at 20 cm (Fig. 4.2.5). Fig. 4.2.6 visualises the longitudinal spatial variability of TCE concentrations with depth in the top metre of the riverbed. As can be seen, a clear zone of plume concentrations in excess of $30 \mu\text{g L}^{-1}$ can be observed between MP17 and MP16 with the majority of higher concentrations occurring below the 60 cm sampling level, suggesting a potential ‘hotspot’ of TCE contamination in this section of the reach. In addition, zones of reduced TCE concentrations can be made out between MP9 and MP14, juxtaposed by a higher concentration area immediately downstream (Weatherill et al., 2014).

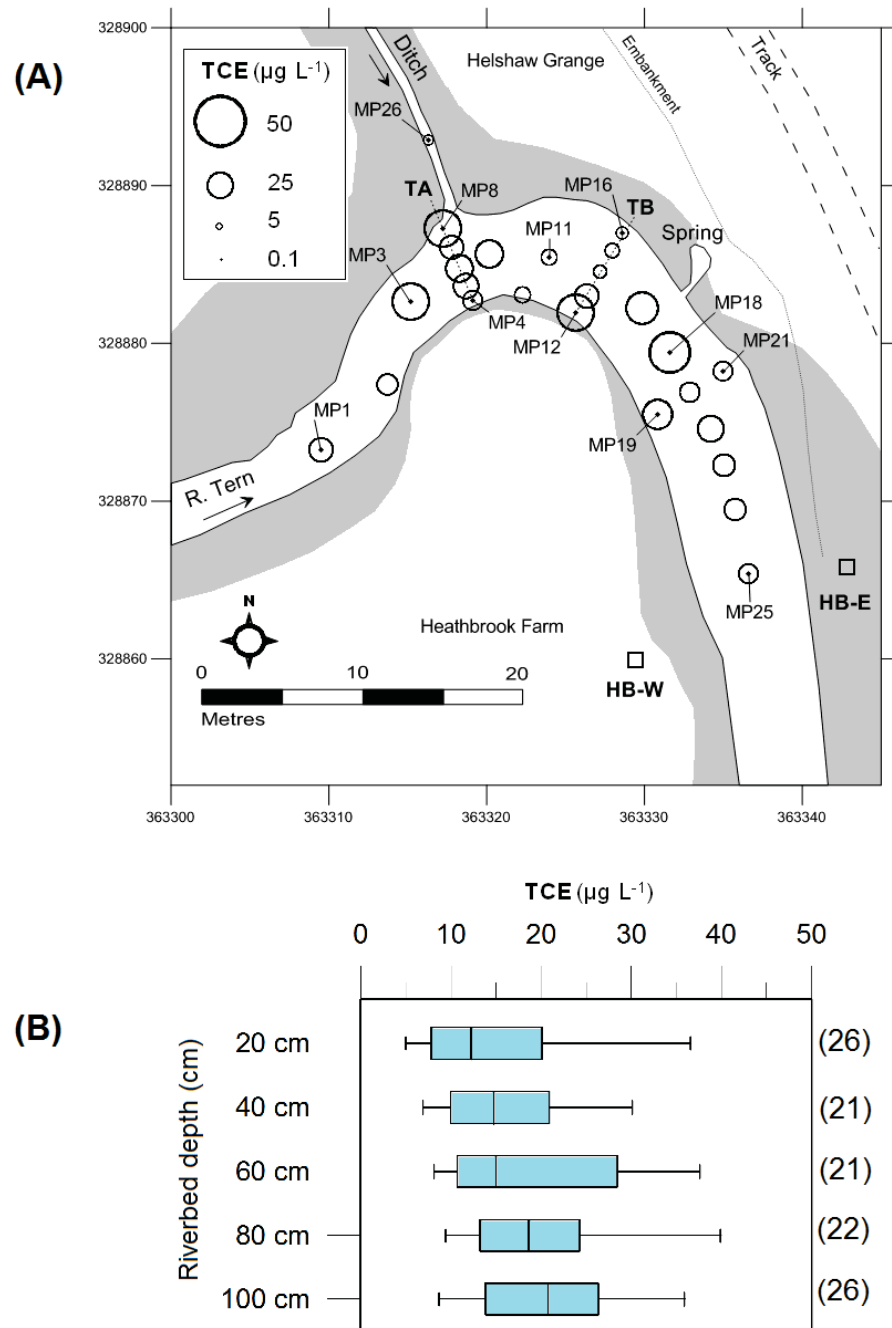


Fig. 4.2.5 (A) Spatial variation in maximum TCE concentrations determined for mini-piezometer snapshot in December 2011. (B) Box-plots summarising the variation of TCE concentrations with piezometer sampling level. Box-plots present a non-parametric summary of data as quartiles with the median represented by a vertical line. Sample size (n) given in parentheses on the right (modified from Weatherill et al., 2014).

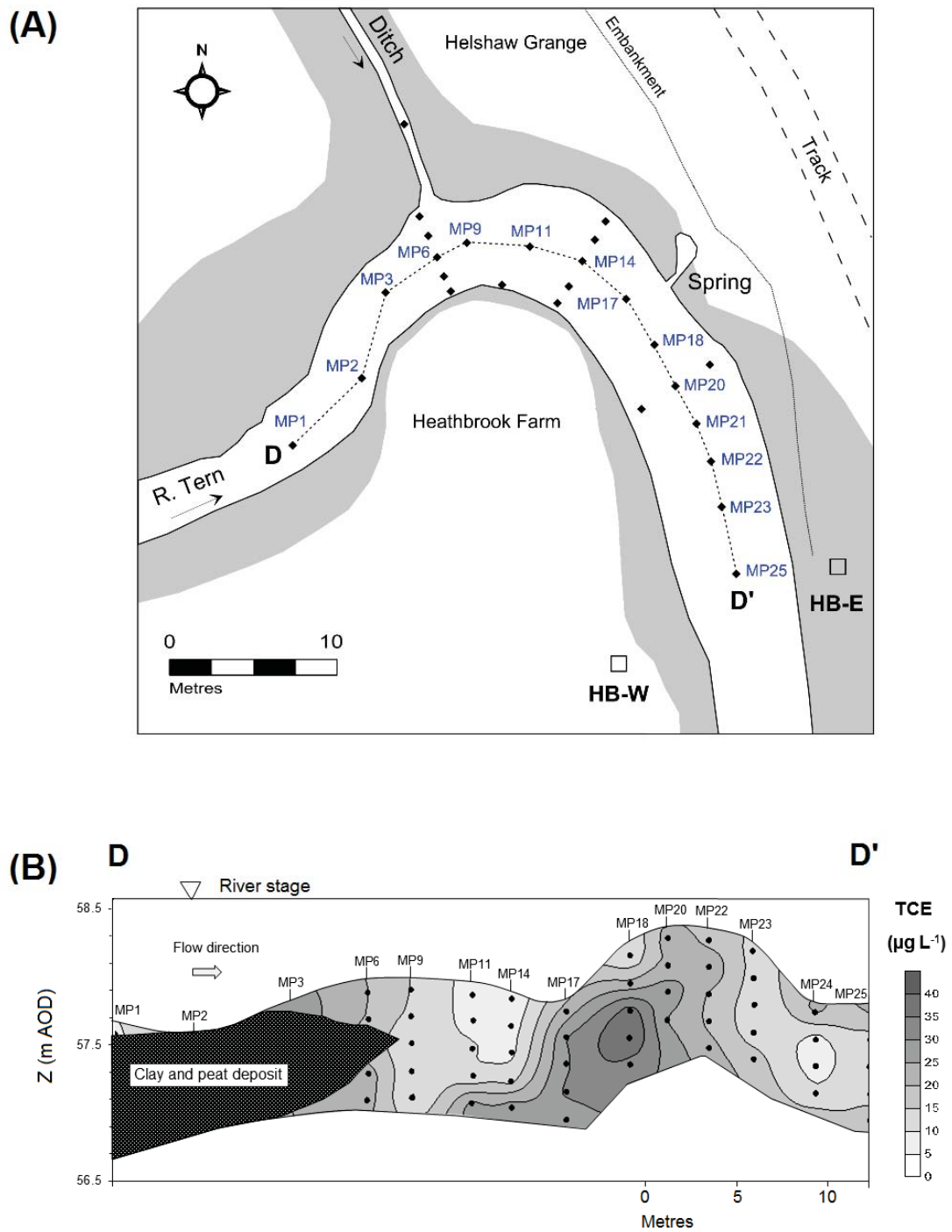


Fig. 4.2.6 (A) Location of the longitudinal transect of piezometers (Transect D) in the study area. (B) Longitudinal spatial variability of TCE with depth over Transect D piezometers interpolated using Kriging. Grey area indicates clay/peat area where it was not possible to retrieve samples. Individual sampling depths indicated by black dots (modified from Weatherill et al., 2014).

4.2.3.3 *Daughter product detections in the riverbed*

In contrast to the previous sampling campaigns in the main channel of the river, daughter products were observed in the vertical profiles from the September sampling campaign. Approximately 11% of the pore water samples exhibited dechlorination products in the shallow (e.g., 20 cm) sampling level with cDCE being the most common transformation product (Fig. 4.2.7). The TA transect showed a higher number of daughter products than in the downstream transect, TB, although the maximum cDCE concentration of $5.4 \mu\text{g L}^{-1}$ was found at MP13 (of TB). VC was also detected in pore water from monitoring points MP7, MP8 and MP13 at a depth of 20 cm during the September campaign with a maximum concentration of $1.9 \mu\text{g L}^{-1}$ at MP7. For the December campaign (Fig. 4.2.8), approximately 12% of the 110 pore water samples contained reductive dechlorination products with cDCE again as the primary transformation product. VC was detected in just 6% of the samples, reaching a maximum of $3.1 \mu\text{g L}^{-1}$ at MP18. A maximum cDCE concentration of $8.3 \mu\text{g L}^{-1}$ was observed at the 20 cm level of MP18. This is located in the central channel area (downstream of TB) at the base of a topographic rise in the channel forming the head of a riffle sequence (Fig. 4.2.6). The installation of mini-piezometers MP4, MP10 and MP12 around the head of the meander revealed a comparatively reactive area of the riverbed at depths of 20 and 40 cm showing cDCE concentrations of $2.1\text{--}6.6 \mu\text{g L}^{-1}$ (Fig. 4.2.8). This area is located along the channel margin where river water velocities are typically quite low, resulting in fine sediment accumulation as well as abundant macrophyte growth during the summer months (Weatherill et al., 2014).

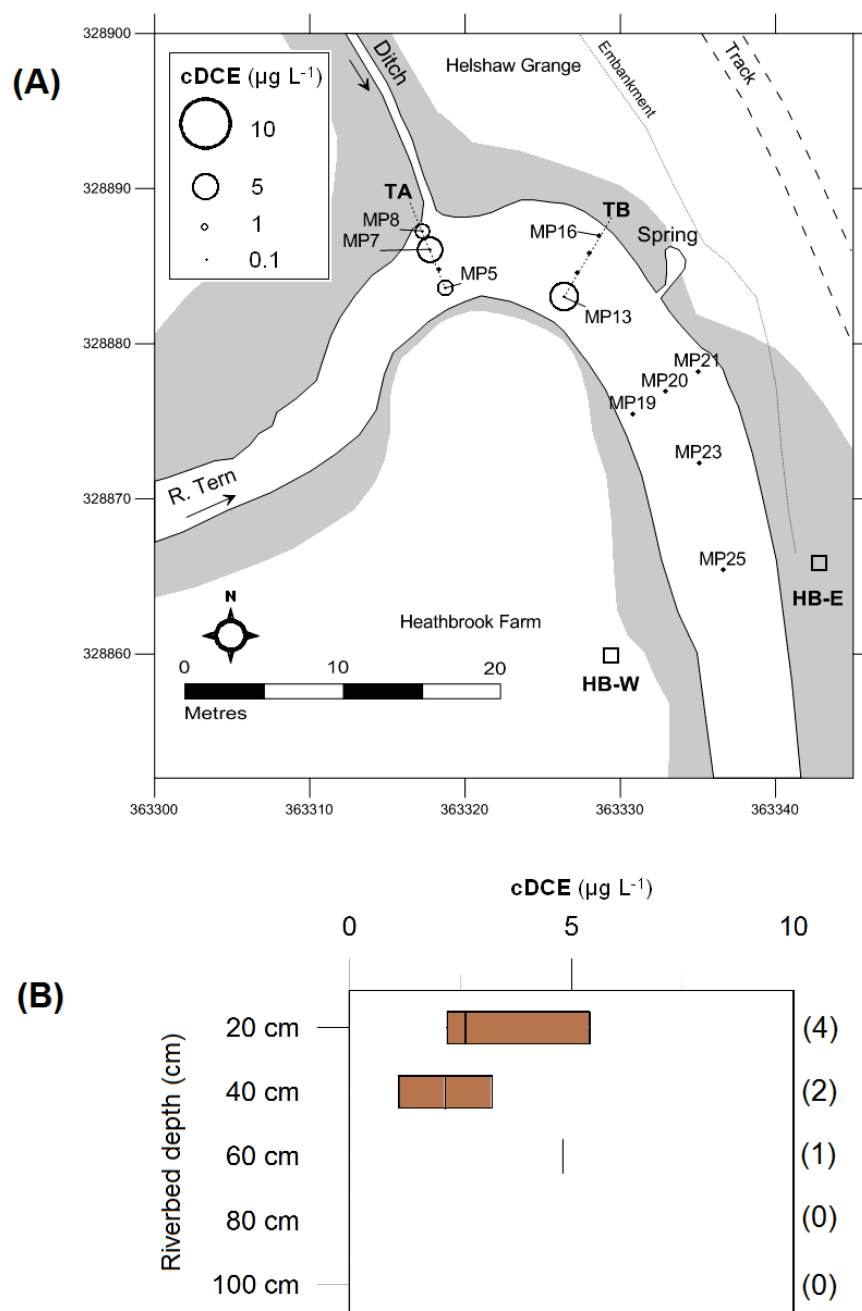


Fig. 4.2.7 (A) Spatial variation in cDCE concentrations determined from mini-piezometer investigation in September 2011. (B) Box-plots summarising the variation of cDCE concentrations with piezometer sampling level where possible. Box-plots present a non-parametric summary of data as quartiles with the median represented by a vertical. Sample size (n =) given in parentheses on the right (modified after Weatherill et al., 2014).

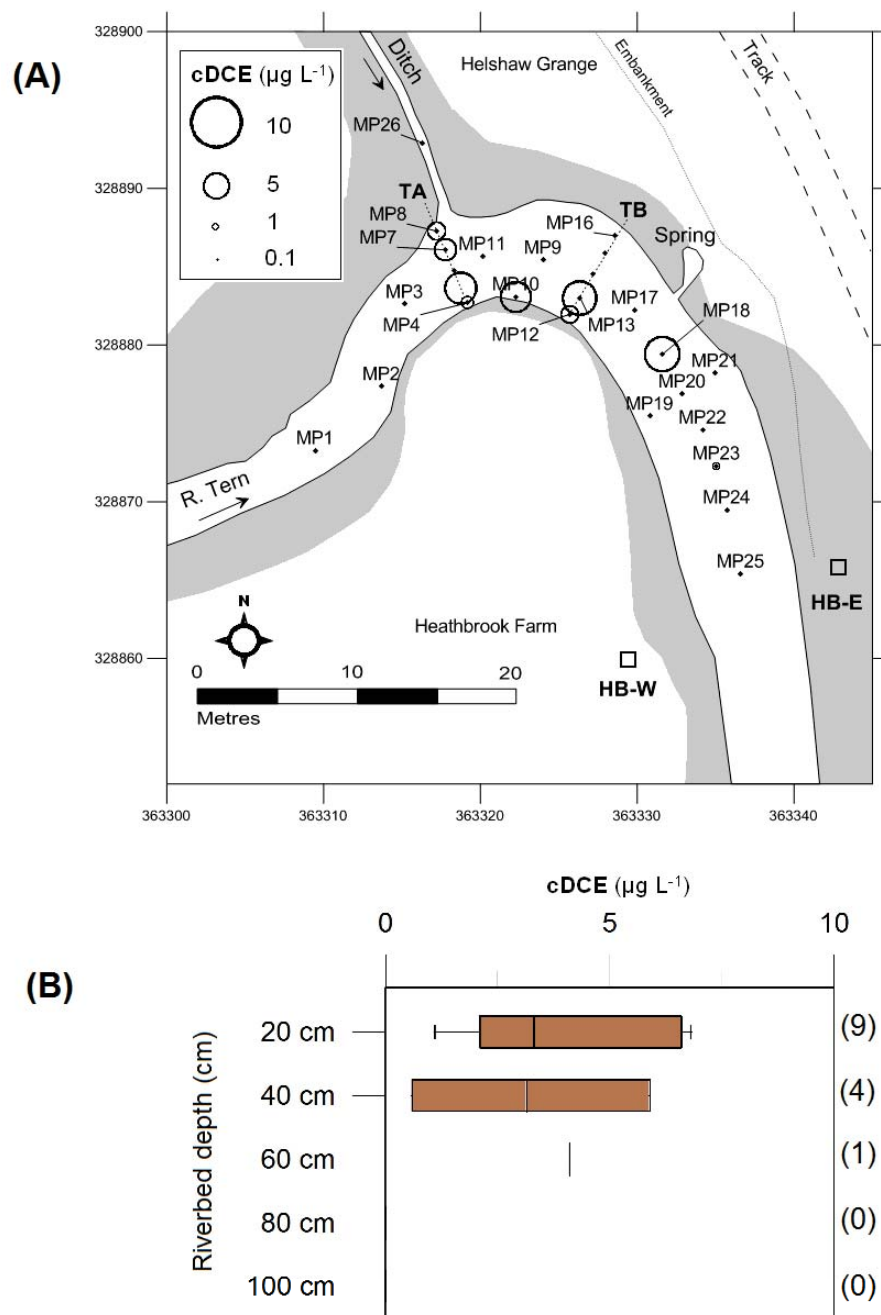


Fig. 4.2.8 (A) Spatial variation in cDCE concentrations determined from mini-piezometer investigation in December 2011. (B) Box-plots summarising the variation of cDCE concentrations with piezometer sampling level where possible. Box-plots present a non-parametric summary of data as quartiles with the median represented by a vertical. Sample size (n) given in parentheses on the right (modified after Weatherill et al., 2014).

4.3 Floodplain hydrogeological investigation

4.3.1 Characterisation of the alluvium deposits

4.3.1.1 Geological observations from augering at Helshaw Grange

The installation of monitoring wells in the floodplain provided an opportunity to observe the composition of the alluvial drift deposits which underlie the river corridor along the reach where TCE was detected (Fig. 4.3.1A). In the eastern edge of the site (e.g., BH1, BH2 and BH4) the upper metre of the alluvium was found to be dominated by homogeneous medium-coarse, grey-to-brown sand with thin, sandy topsoil (Fig. 4.3.1B) according to the Udden-Wentworth grain size classification scheme (Wentworth, 1922). Below this, more heterogeneous grey-to-brown sandy silt and rising water levels were noted in BH1 and BH2 during coring. The clay content of the sediment profile below ~1 m was observed to increase at BH3 on the bank of the drainage ditch (Fig. 4.3.1B) whereas more granular sediments were observed (clean sands) at comparable depths on the opposite bank of the ditch at BH5 (Fig. 4.3.1B). A considerable thickness (e.g., >1.5 m) of medium brown sands with occasional organic fragments was observed in BH6 and BH7 on the northern bank of the river (Fig. 4.3.1A), which was found to be unsaturated to a depth of approximately 1.7 m. Below this, the underlying silt-dominated unit was observed to be bounded by a thin horizon of sandy peat in BH7 (at 2.6 m depth) but was not found at BH6. No groundwater ingress was observed in AH1 or AH2 at depths of >2.6m and these holes were not completed as monitoring wells. Grey-to-blue soft clay was laterally extensive under the northern floodplain with only BH8 having significant ingress of groundwater. Weathered sandstone (at ~2.8 m depth) in the form of coarse orange sand was also encountered at the base of AH5 and BH8.

4.3.1.2 *Geological observations from augering at Heathbrook Farm*

At Heathbrook Farm, the stratigraphy of the alluvial overburden was found to be more heterogeneous. At BH9 (Fig. 4.3.1A), a medium brown sand horizon was encountered in the top 1.6 m of the drift along the riverbank which was underlain by soft grey clay. This was observed to be underlain by a layer of soft black peat approximately 0.6 m thick which was further underlain by competent orange sand, interpreted as weathered sandstone (Fig. 4.3.1B). Clay was again observed at AH3 to a depth of 2.6 m with outcrops noted above the water line on the riverbank. The thickness of the upper sand horizon reduced to 0.2 m in BH10 at the apex of the meander bend with heterogeneous clayey sand and peat below. No evidence of bedrock was observed below 3 m deep (despite its proximity in nearby BH9, Fig. 4.3.1B). Gravel and cobble (supported within a clayey matrix), was encountered to a depth of 1.2 m at BH11 (Fig. 4.3.1B), also located at the head of the meander bend (Fig. 4.3.1A). No gravels were found along the riverbank to the south of BH11 where the stratigraphy contained an upper unit of relatively clean sand (1.4 m in thickness) underlain by silty or clayey sand. BH13 and BH14 were located in the centre of the meander bend, away from the banks of the river (Fig. 4.3.1A) and had contrasting drift compositions. At BH13, grey-to-blue clay loam was observed from the surface to a depth of 1 m which was underlain by relatively pure clay as well as silt (similar to that observed at BH9 and AH3, Fig. 4.3.1B). At BH14, a similar clay loam layer was observed to a depth of 2.2 m which was bounded below by saturated, fine-to-medium sand (Fig 4.3.1B). This sand presented difficulties during the insertion of the pre-fabricated monitoring well due to rapid collapse of the auger hole walls. No evidence of sandstone bedrock was encountered at BH14 at a depth of ~3 m in the floodplain.

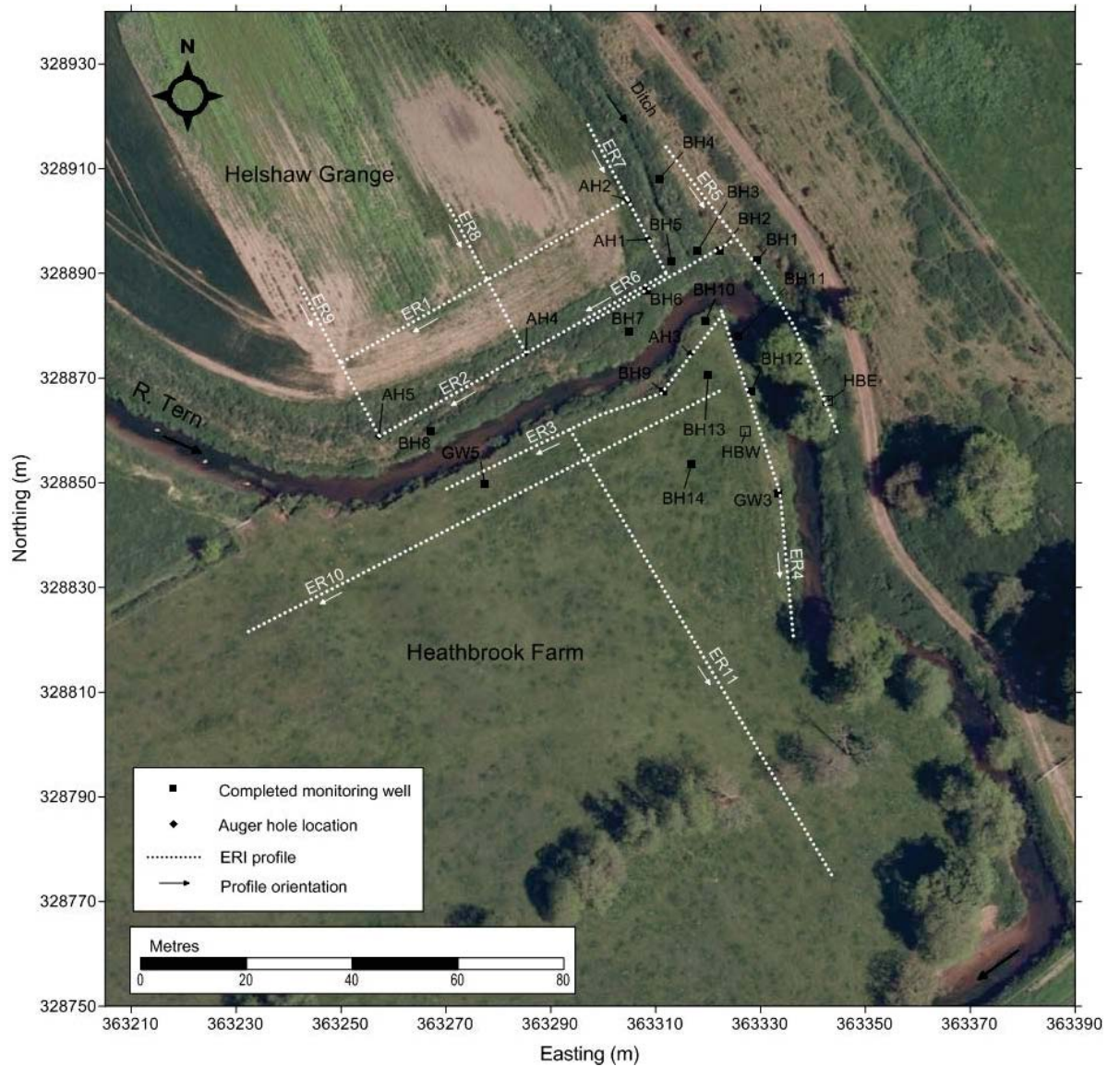


Fig. 4.3.1 (A) Overview of floodplain investigation area with borehole and auger hole locations and electrical resistivity imaging profile locations. Arrows indicate the orientation of the resistivity profiles presented later in this chapter. Ortho-rectified aerial photography from GetMapping Plc. (copyright, 2009).

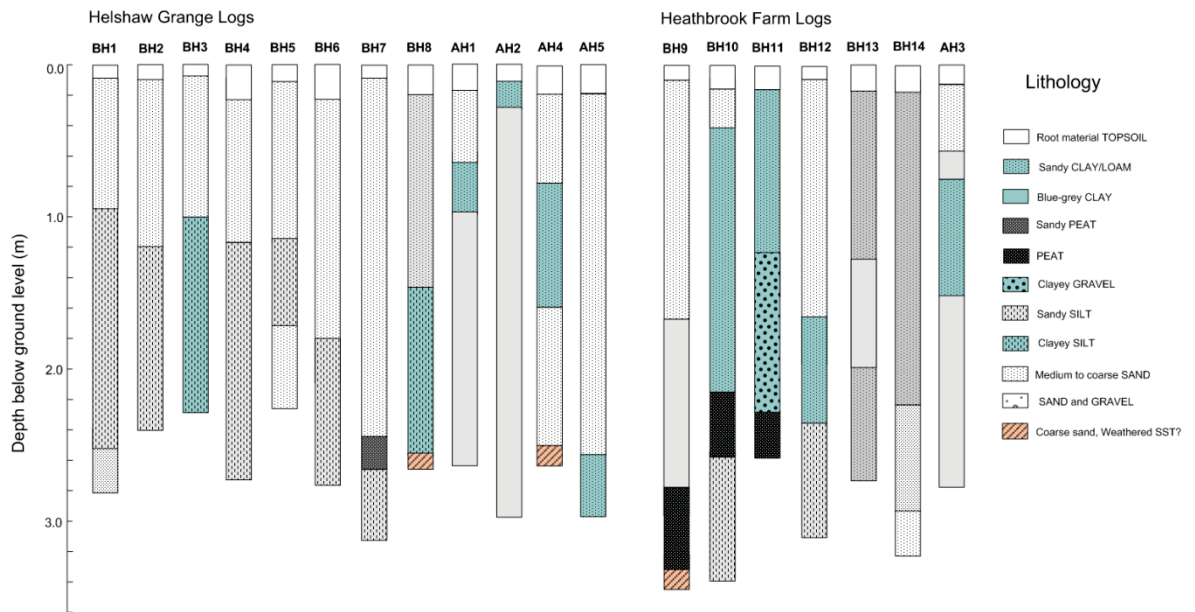


Fig. 4.3.1 (B) Geological logs for monitoring wells and auger holes retrieved from the floodplain during the intrusive investigation (see part A for coring locations).

4.3.1.3 Hydraulic conductivity and head distribution in the floodplain.

Variable head tests were conducted on monitoring wells after the December 2011 snapshot to derive saturated hydraulic conductivities (K_s). Overall, the K_s of the floodplain alluvium ranged over two orders of magnitude from just 0.001 m d^{-1} at BH11 to 0.74 m d^{-1} at BH9 with a site geometric mean of 0.03 m d^{-1} . Both of these wells are situated in the inner meander bend at Heathbrook Farm (Fig. 4.3.2). BH1, BH5, BH9 and BH14 had K_s ranges of $0.32\text{--}0.74 \text{ m d}^{-1}$ with all other alluvial groundwater monitoring wells having a K_s value two orders of magnitude lower than this and one order lower than the site geometric mean. Groundwater level measurements in the drift (taken at the time of the December sampling campaign), indicated that the potentiometric surface of the alluvial groundwater system was significantly above the river stage at all monitoring well locations (Fig. 4.3.2). This

illustrates that ‘gaining’ conditions were present at the time of sampling which is in accordance with previous observations of the river-aquifer configuration at the site (Krause et al., 2011b; 2012). Maximum hydraulic head in the alluvial aquifer was observed in the area of BH1 at 59.55 m AOD with minimum heads observed in BH6, BH7 and BH8 (not shown in Fig. 4.3.2). A maximum head difference of 0.76 m was observed between BH1 and the single-screen piezometer HZ installed directly in the riverbed at the centre of the mini-piezometer Transect D (Fig. 4.3.2). This implies the presence of a significant lateral hydraulic gradient of 0.076 m m^{-1} with a groundwater flow direction from northeast to southwest towards the floodplain from the west of the river valley towards the plume source area. Sub-artesian conditions were observed in the area of BH1 and BH2 with the potentiometric surface lying at, or just above, ground level at the eastern edge of the floodplain (Fig. 4.3.2). An area of groundwater seepage near BH1 is indicative of elevated groundwater upwelling pressure in this area. Groundwater upwelling below the central area of the meander bend is also suggested in Fig 4.3.2 with relatively constant head along the axis of the meander between BH14 and BH13 and lateral flow indicated to the NW and NE from the central area. Given the significant head difference between the east and west banks of the drainage ditch (0.44 m between BH3 and BH5), groundwater inflow to the ditch can be expected from the eastern side along an axis from BH4 to BH1 (Fig. 4.3.2). Hydraulic head in the mini-piezometer MP26 (Fig. 4.2.1) was approximately the same as the water level in the ditch, suggesting that the ditch level approximates that of the local water table with water inflow likely to be originating from the northwest.

4.3.1.4 *Plume distribution in the alluvium*

During the September 2011 snapshot, the concentrations of TCE in the alluvial monitoring wells (Fig. 4.3.1) were all less than $10 \mu\text{g L}^{-1}$ (but still above the LoD), apart from BH4 and BH6 (Fig. 4.3.3A). A maximum TCE concentration of $4.5 \mu\text{g L}^{-1}$ was observed at BH1 with a median concentration of $0.3 \mu\text{g L}^{-1}$ over all well locations. The screened sections of BH3, BH4, BH6 and BH13 were deployed within the low-permeability drift material of the area and hence, refilled very slowly (typically more than 8 hours) after purging. The effect of volatilisation losses during the slow recharge period cannot be excluded for these boreholes and may introduce a negative bias to the results. TCE was again detected from the drainage ditch and seepage area close to BH1 with concentrations of 3.8 and $5.1 \mu\text{g L}^{-1}$ respectively. TCE was at, or close to the LoD, at all three drift well locations in Heathbrook Farm. BH11 was the only monitoring well of the September 2011 sampling campaign to show traces of daughter products with just $0.6 \mu\text{g L}^{-1}$ of cDCE detectable. The median TCE concentration for the monitoring borehole network was $1.1 \mu\text{g L}^{-1}$ for the December 2011 snapshot sampling with a maximum of $5.9 \mu\text{g L}^{-1}$ detected in the surface water of the ditch (Fig. 4.3.3B). BH9 and BH10 in Heathbrook Farm showed significant levels of TCE at 4.3 and $3.1 \mu\text{g L}^{-1}$, respectively. No VC was detected in any samples with cDCE being the only daughter product observed at trace levels in three locations (Fig. 4.3.3B) (Weatherill et al., 2014).

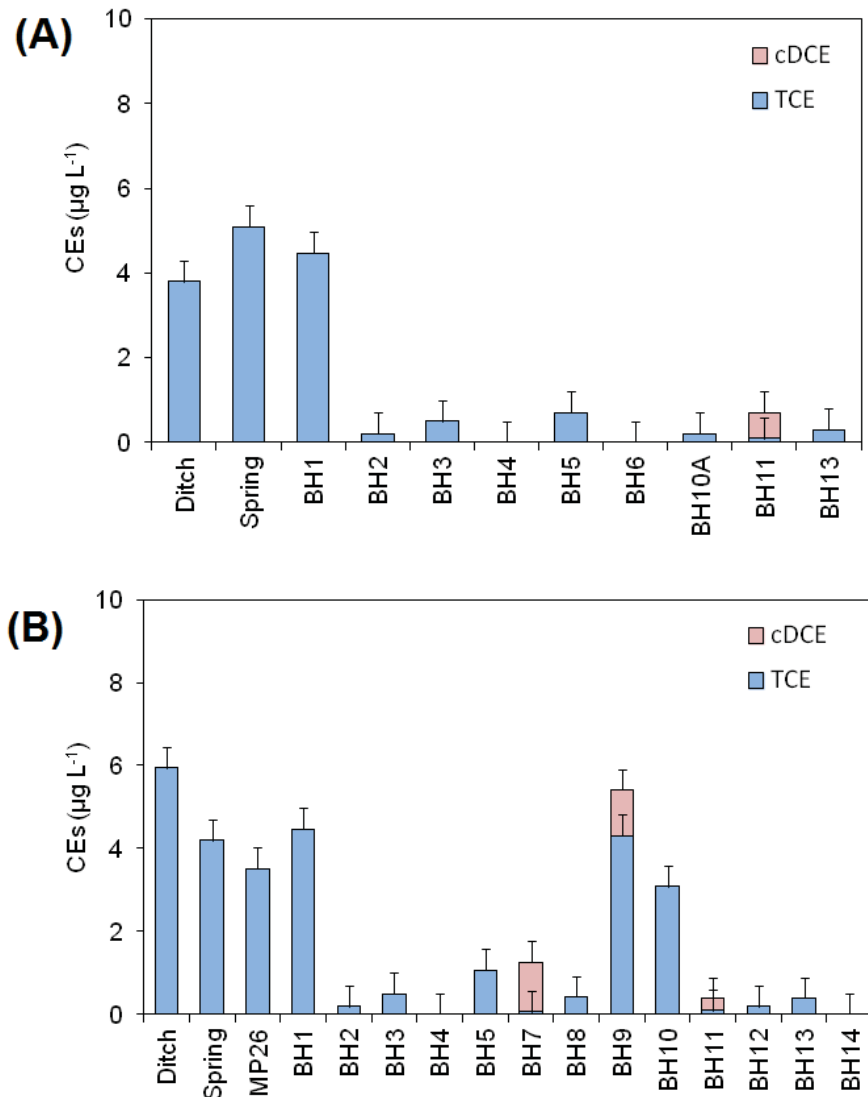


Fig. 4.3.3 Chlorinated ethene concentrations determined from alluvial borehole samples and surface water flows in **(A)** September 2011 and **(B)** December 2011. cDCE was the sole daughter product detected in the alluvial groundwater system (modified after Weatherill et al., 2014).

4.3.2 Electrical resistivity imaging surveys

4.3.2.1 64 m resistivity profiles

Electrical resistivity imaging (ERI) profiles ER1 (Fig. 4.3.1A) and ER2 (Fig. 4.3.1B) were collected along SW-NE orientated traverses running parallel to the river. Inversion results for line ER1 reveal two distinctive ‘geolectric’ units (i.e., with contrasting resistivity

values) with a gradational contact that undulates but is approximately planar across the profile (Fig. 4.3.4A). The upper, ~4 m thick layer is dominated by low resistivity values in the range of 25 to ~50 ohm meters (Ω m), particularly at the NE end of the line where it reaches a maximum observed depth of approximately 5 m. The resistivity of this layer increases to >60 Ω m around the centre of the profile where the spatial distribution of resistivity becomes more heterogeneous. This upper layer is bounded at depth by a high resistivity unit (range ~100–340 Ω m) which is considerably more heterogeneous than the upper layer with several local zones of higher resistivity. However, close to the base of the profile (approximately 9 m below ground level), the resistivity of this layer reduces to <100 Ω m.

Line ER2 was acquired along the northern bank of the River Tern (Fig. 4.3.1A) where it was necessary to correct for topography along the profile. Model results (Fig. 4.3.4B), reveal three distinctive geoelectric units with a relatively complex geometry. A discontinuous, high resistivity layer (340–700 Ω m) is apparent in the 0–16 m position of the pseudosection which reappears between 38–64 m in the profile. This layer has an approximate thickness range of 0.5–2 m and is bounded by a sharp contact. A lower resistivity layer is observed below this (range 40–80 Ω m) which extends to the ground surface along the 16–38 m section of the traverse. The resistivity of this layer increases at the 42 m position to ~80–100 Ω m. The thickness of this unit varies significantly and ranges from approximately 2–4 m with a distinct ‘step’ in the depth at ~20m along the profile. Beneath this, a higher resistivity layer is present with resistivity values in the range of 140–280 Ω m. This layer is characterised by a strongly inclined interface with the bounding layer from the 16–20 m section of the profile. This unit has similar spatial

patterns of higher resistivity with a drop to $<100 \Omega \text{ m}$ at the base of the profile similar to ER1 (Fig. 4.3.4A).

ER3 was collected in riverbank at Heathbrook Farm (Fig. 4.3.1) along SW-NE orientation (parallel to ER1 and ER2) and was corrected for the significant changes in electrode elevation along the survey line (Fig. 4.3.4C). Three geoelectrical units can be distinguished in the pseudosection. The first unit occupies the upper 0.5–2 m of the section and is characterised by high resistivity values (160–800 $\Omega \text{ m}$) which are bounded by a sharp contact with the underlying layers. This feature is comparable to the high resistivity layer evident on ER2 (Fig. 4.3.4B). This layer increases in thickness to 2.5 m from 51–59 m along the profile line. Below this layer, a lower resistivity unit (40–80 $\Omega \text{ m}$) is evident which extends from 6–36 m along the section with an approximate thickness of 3 m. This unit is absent from the rest of the section after 36 m along the profile. This layer is bounded at its base and truncated on its SW extent by a higher resistivity zone (120–180 $\Omega \text{ m}$) which has a more gradational contact with the upper high resistivity layer in the SW section of the profile. Similar to ER1 and ER2, this unit contains localised zones of lower resistivity (e.g., $<100 \Omega \text{ m}$) close to the base of the section.

ER4 (Fig. 4.3.4D) was collected long the eastern riverbank of Heathbrook Farm (Fig. 4.3.1A) in a NW-SE orientation and was corrected for geometric distortion due to the differences in elevation along the 64 m survey line. Two geoelectrical units are distinguishable in the profile. Similar to ER2 and ER3, a high resistivity layer (300–1000 $\Omega \text{ m}$) is present in the top 2 m of the section which is laterally continuous throughout the profile. The thickness of this layer varies considerably and thins to less than 1 m thickness after 40 m towards the SW end of the profile. Unlike the other profiles where this feature is

present, the contact with the underlying layer is considerably more gradational. Below this layer, an extensive lower resistivity zone is present with a resistivity range 40–120 Ω m. Line ER5 was also collected in a NW-SE orientation along the eastern margin of the floodplain at Helshaw Grange, parallel to the river downstream of the meander bend (Fig. 4.3.1A). The inversion results (Fig. 4.3.4E) show less distinctive geoelectrical layers than ER1, ER2 or ER3. The uppermost 1–1.5 m of the profile displays a large degree of variability in modelled resistivity with a high-resistivity layer (\sim 300–800 Ω m) present from 0–24 m of the traverse which has an approximate thickness of 1 m. After 24 m, the resistivity of the top 1 m of the profile decreases to 100–140 Ω m and rises again as the topography increases after the 40 m position. This high resistivity layer has a sharp contact with the underlying low resistivity unit that is comparable in form to that observed in ER2 (Fig. 4.3.4B). Below this layer (at \sim 2 m), distinguishing between differing geoelectrical units becomes problematic as much of the profile is characterised by low resistivity values with a narrow range (40–80 Ω m) which are relatively homogeneous with depth. This low resistivity zone reaches the surface between 33 and 39 m which coincides with the lowest topographic part of the survey line. However, a zone of increased resistivity (100–180 Ω m) is apparent from 15–26 m of the profile at a minimum depth of approximately 4 m.

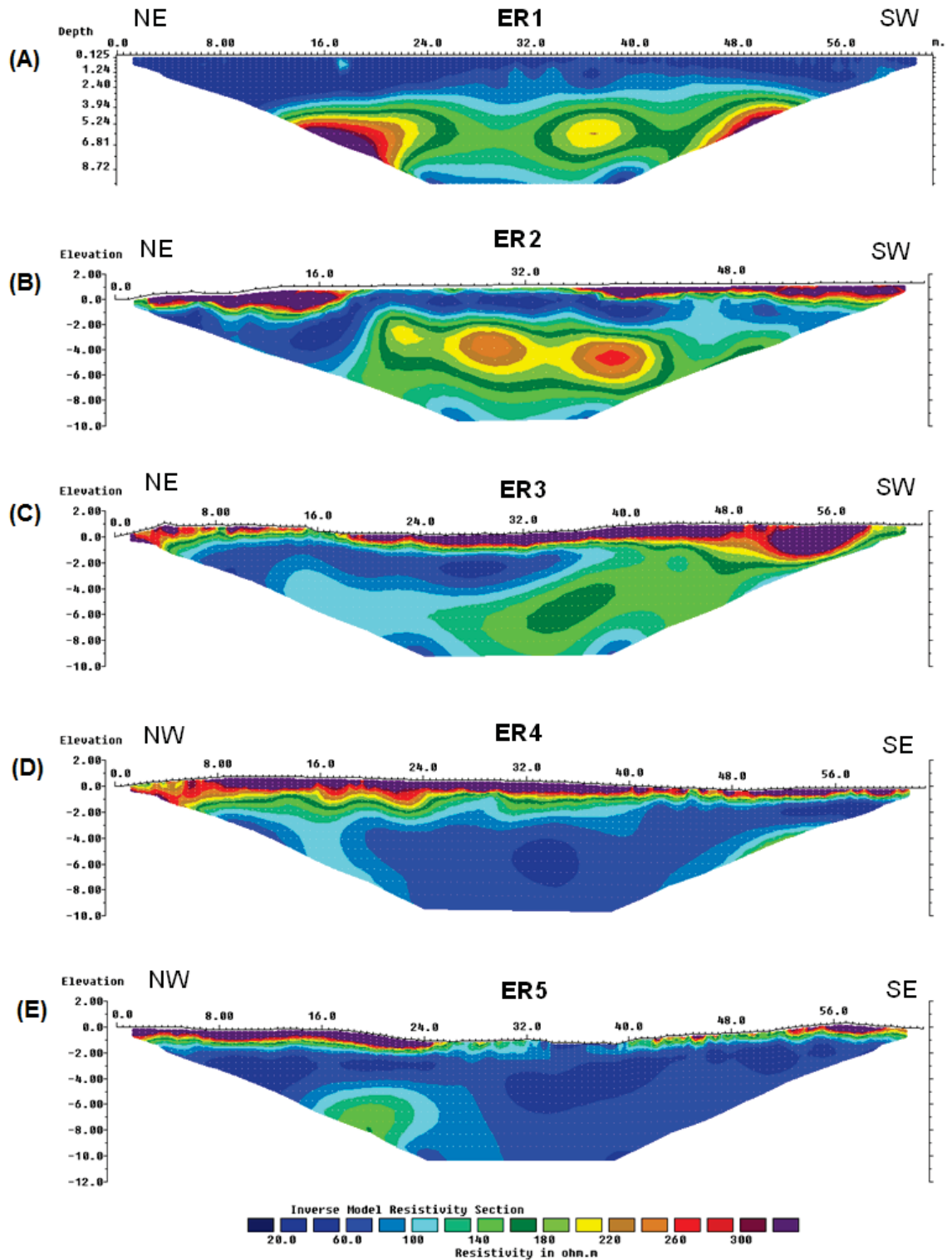


Fig. 4.3.4 (A–E) Inversion results for the 64 m electrical resistivity imaging profiles illustrating the inversely modelled ‘true’ resistivity of the subsurface. Refer to Fig. 4.3.1A for location of each profile in the study area.

4.3.2.2 32 m resistivity profiles

ER6 (Fig. 4.3.5A) required significant correction due to the large topographic gradient at the NE end of the traverse as well as the channel of the drainage ditch (located at ~9 m on the survey line). It is possible to distinguish between two geoelectric units in ER6. The first unit is discontinuous and heterogeneous and characterised by a high variability in the calculated resistivity with a contact which varies from relatively sharp at the NE end of the line to gradational at the SW end. At 1–5 m position along the line, this layer has high resistivity values (300–650 Ω m) and a thickness of approximately 1 m. This zone has a comparable thickness and resistivity to the high valued layer observed in ER5 at the same location on the floodplain (Fig. 4.3.4D). This layer is thin or absent in the area of the drainage ditch. The resistivity of the top 1 m of the profile increases again SW of the drainage channel with a range of 160–280 Ω m as far as the 20 m position where it drops to ~100 Ω m and the thickness increases to approximately 2 m. A higher resistivity feature is present between 25–31 m with a range of 140–240 Ω m. Beneath this layer, a relatively homogeneous zone of lower resistivity (~40–80 Ω m) is observed throughout most of the section which reaches the surface at the base of the drainage channel. ER7, ER8 and ER9 (Fig. 4.3.5 B–D) were collected along traverses orthogonal to ER1 and ER2 in order to provide information on subsurface geoelectrical properties as they vary with distance away from the channel of the river. ER7 (Fig. 4.3.5B) was collected approximately parallel to the NE 32 m long section of ER5. It reveals a relatively homogenous single geoelectrical unit characterised by low resistivity (~20–60 Ω m) which is laterally continuous throughout the section. However, from 24–32 m the resistivity of the upper 1 m of the section increases to >100 Ω m with an increase of >80 Ω m also evident at depths of approximately 4 m on the profile. ER8 (Fig. 4.3.5C) was collected at the centre points of ER1 and ER2 (Fig 4.3.1A). Two geoelectrical units can be distinguished in this section. The first has similar low

resistivity values to ER7 (~40–60 Ω m) which has a gradational contact with the underlying higher resistivity layer which ranges from 80–160 Ω m. ER9 (Fig. 4.3.5D) was the most westerly line collected at the site (Fig. 4.3.1A). This section displays more heterogeneity in geoelectrical properties than either ER7 or ER8 with a discontinuous layer of lower resistivity (40–80 Ω m) in the top 2–3 m of the profile. The base of this layer is bounded by an undulating higher resistivity layer (>100 Ω m). From 24–30 m, the calculated resistivity shows a marked gradient where resistivity from 100 to >300 Ω m at the SW end of the profile (Fig. 4.3.5D).

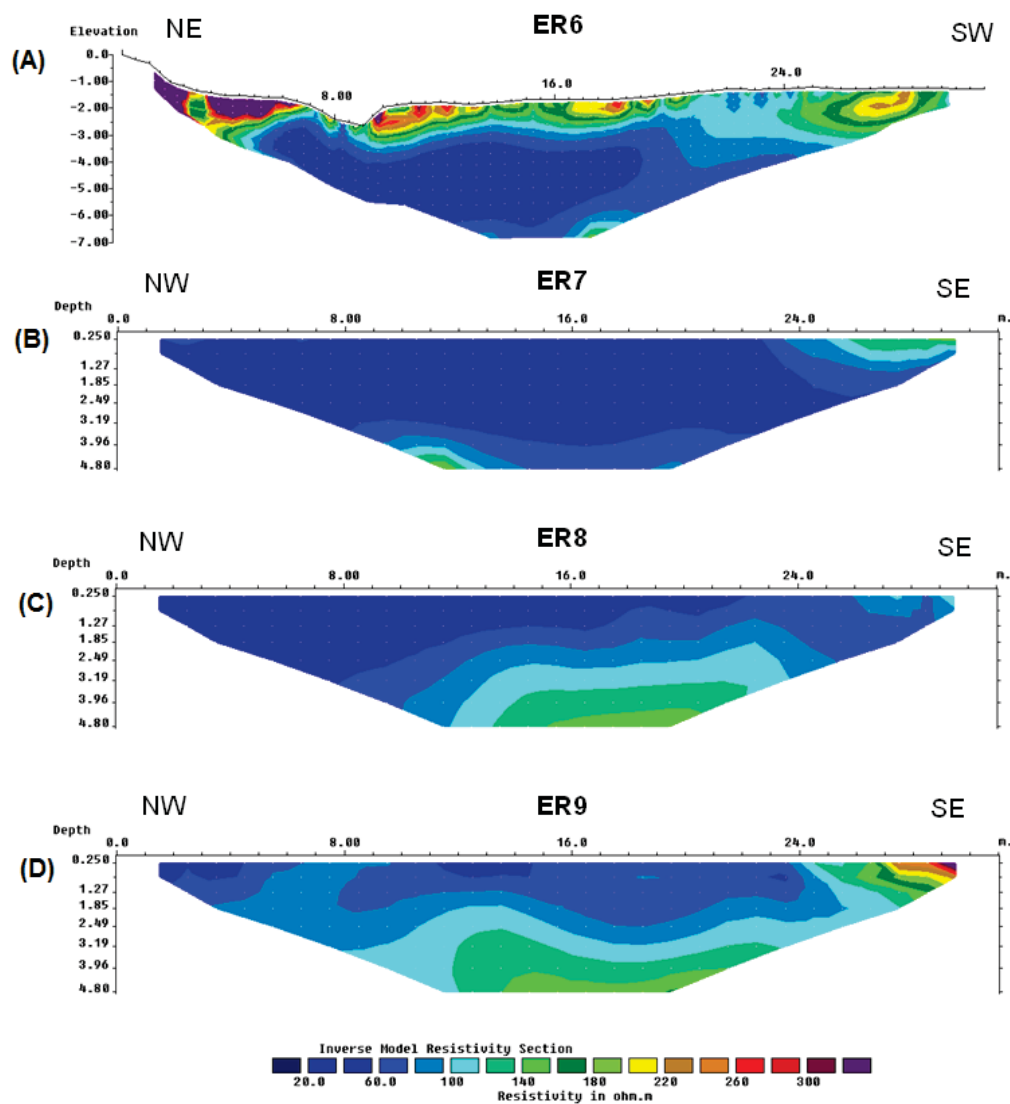


Fig. 4.3.5 (A–D) Inversion results for the 32 m electrical resistivity imaging profiles. Refer to Fig. 4.3.1A for location of each profile in the study area.

4.3.2.3 *LOCAR resistivity profiles in Heathbrook Farm*

ER10 (Fig. 4.3.6A) is 100 m in length and was collected along the northern section of Heathbrook Farm, approximately parallel to ER3 (Fig. 4.3.1A). Two principal geoelectrical units are apparent in this section. The upper unit is characterised by resistivities in the range of 40–120 Ω m which is generally laterally continuous across the section, with an apparent thickness range of 2–4 m. A small high resistivity feature (160–600 Ω m) with lenticular geometry is notable at the SW end of the line from 0–10 m. Below the upper layer, a zone of higher resistivity (120–220 Ω m) is observable throughout the section with an approximately planar contact with the overlying layer. Comparable to ER1, ER2 and ER3 (Fig. 4.3.4), the lower higher resistivity layer contains localised zones of lower resistivity. This is particularly notable close to the centre of the section (50 m position) at approximately 18 m depth where the calculated resistivity drops to below 80 Ω m. ER11 (Fig. 4.3.6B) was acquired orthogonally to ER10 and extends 100 m in length and provides coverage of the inner floodplain area, to the SW of Heathbrook Farm. Two distinctive geoelectrical units can be observed in this profile. The upper layer is characterised by low resistivity values (40–80 Ω m) which are relatively homogeneous with a thickness of approximately 4–5 m. Below this layer, a higher resistivity unit (120–280 Ω m) is apparent with an approximately planar surface topography. The base of this unit (~16 m depth) also shows an area of lower resistivity (<100 Ω m) located close to the centre point of the profile.

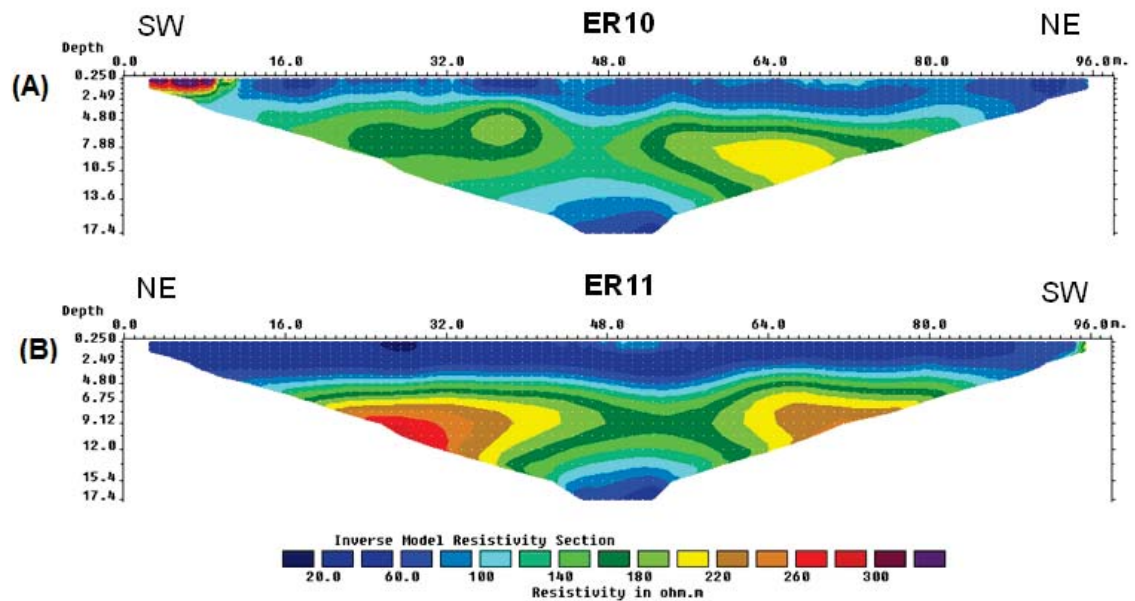


Fig. 4.3.6 (A–B) Inversion results for the 100 m electrical resistivity imaging profiles originally collected as part of the LOCAR programme in 2002 (Blackwell, 2002). Refer to Fig. 4.3.1A for location of each profile in the study area.

4.3.3 Hydrogeological interpretation of ERI profiles

4.3.3.1 Interpretation approach

Table 4.2 provides the nominal values and representative resistivity ranges for different sediment lithologies likely to be present in the alluvial deposits as well as the sandstone bedrock. This includes the most frequently encountered resistivity values for the UK Permo-Triassic sandstone recorded by the National Resistivity Sounding Database, which is based on 256 surveys (Cuthbert et al., 2009). As can be seen from Table 4.2, there is significant overlap in resistivity ranges for the different geological materials. Therefore, lithological information from the previously collected auger holes on the floodplain (Fig. 4.3.1B) are used to provide qualitative ‘ground-truth’ information on the likely composition of the observed resistivity layers where they are co-located on the ERI

profiles (Fig. 4.3.1A). As the purpose of this geophysical investigation was to provide laterally continuous information on the thickness and composition of the alluvial deposits covering the bedrock aquifer, ERI profiles are interpreted as a simple 2 or 3 layer cases (A, B, C) where layer C is interpreted as the sandstone bedrock. The depth of the bedrock interface is interpolated between known bedrock depths from the well installations. The confidence of this interpretation is rated as 'high' or 'low' where high confidence is given to areas on the profile adjacent to a known bedrock depth and where there is a significant contrast between geoelectrical units which approximately correlates with this depth. Low confidence is attributed to pseudosections with weak contrast between geoelectrical units and should be considered as tentative boundaries. As can be seen from Table 4.2, the degree of water saturation can have a major influence on measured resistivity values. Therefore, to aid in interpretation, representative piezometric levels for the alluvial aquifer (Fig. 4.3.2) recorded during baseflow conditions in December 2011 (Fig. 4.3.1) are interpolated across ERI interpretations for ER2 (Fig. 4.3.7B), ER3 (Fig. 4.3.7C), ER4 (Fig. 4.3.7D), ER5 (Fig. 4.3.7E) and ER6 (Fig. 4.3.8A). It is important to note that groundwater levels were not measured during each ERI profile acquisition and only average levels representative of low flow conditions are presented. In addition, as all monitoring wells are screened below the water table, a direct correlation between observed resistivity gradients and piezometric levels is not expected. Finally, saturated hydraulic conductivities (K_s) derived from the variable head tests are included to characterise permeability distribution within the alluvial cover.

Table 4.2 Published representative resistivity values of subsurface materials likely to be encountered in the study area.

Lithology	Nominal resistivity (Ω m)	Reference
Topsoil	250–1700	Reynolds, 2011
Soil (20% clay)	33	Reynolds, 2011
Soil (40% clay)	8	Reynolds, 2011
Clay	1–100	Reynolds, 2011
Clay (unsaturated)	50–150	Reynolds, 2011
Boulder clay	15–35	Reynolds, 2011
Alluvium and sand	10–800	Reynolds, 2011
Quaternary/recent sand	50–100	Reynolds, 2011
Gravel	100	Reynolds, 2011
Gravel (unsaturated)	1400	Reynolds, 2011
Sherwood Sandstone	100–400	Reynolds, 2011
UK Permo-Triassic sandstone (saturated)	60–145	Cuthbert et al., 2009

4.3.3.2 *ER2 interpretation*

ER2 (Fig. 4.3.7B) is interpreted on a 3-layer basis where three geoelectrical units are readily distinguishable. Layer A is characterised by high resistivity values (340–700 Ω m) and correlates with a sandy topsoil and a medium sand horizon, which is generally free of fine material, identified in the cores from BH6 and BH7. These reach a depth of over 2.4 m at BH7. This is interpreted as a recent unsaturated overbank deposit comprising sandy material from the riverbed, most likely deposited during flood flows. The measured resistivity of this unit will be heavily influenced by antecedent soil moisture conditions as well as stage fluctuations in the river. At AH4, the thickness of this horizon reduces to 0.6 m and the high resistivity layer is thin or absent. At BH8, the sand horizon has significant clay content, however, higher resistivity values are observed at this location than at AH4. Layer B has lower resistivity values (40–80 Ω m) and correlates with the deeper alluvial cover which is generally characterised by fine sediments in the NE section of the profile

including sandy silt with peat horizons in BH6 and BH7. At AH4, a sand unit is also noted in this layer, indicating that the clay content of the alluvium is varied. At BH8, the resistivity values of Layer B increase to $>100 \Omega \text{ m}$ which correlates with the sandy silt encountered at this depth in BH8. The three monitoring wells screened within layer B had a K_s range of $0.0018\text{--}0.0041 \text{ m d}^{-1}$ with a geometric mean of 0.003 m d^{-1} , suggesting that the low resistivity values observed for this horizon were indicative of clay content rather than saturated granular material. Bedrock was encountered at depths of approximately 2.5 m in AH4 and BH8. This correlates with the interface of Layer B and C, with C characterised by a marked rise in resistivity values ($140\text{--}280 \Omega \text{ m}$) and is well defined as far as 42 m along the profile. After 42 m, the interpretation becomes more uncertain due to the lower contrast in geoelectrical properties for the alluvial cover in this area of the section. As can be seen from Fig. 4.3.7B, the potentiometric surface is at, or close to, the interpreted bedrock interface for much of the profile. This profile also corresponds with the area of lowest hydraulic head (average $\sim 59 \text{ m AOD}$) in the alluvial groundwater system (Fig. 4.3.2). An interesting feature of the interpreted bedrock interface (Fig. 4.3.7B) is the apparently steep inclination of this layer from 16–20 m along the profile. This is interpreted as an inclined surface of the sandstone bedrock where the difference in geoelectrical properties between the bedrock and alluvial cover are relatively strong. However, geometric distortion associated with the modelling/inversion process cannot be ruled out as a factor influencing the apparent shape of this interpreted feature.

4.3.3.3 *ER3 interpretation*

BH10, BH9 and AH3 provide ground truth lithological information for line ER3 (Fig. 4.3.7C). The generally high resistivity layer forming the uppermost 1–4 m of the profile is interpreted as Layer A which is interpreted geologically as an overbank deposit similar to

that observed at ER2. This layer is heterogeneous between BH10 and AH3 having both silt-rich as well as sand-dominated horizons evident in the cores. At BH9, the stratigraphy is sand-dominated for the top 1.6 m of the sediment profile; however, this does not correlate with a high resistivity zone as observed in ER2, possibly due to the impact of antecedent moisture conditions at the time of the survey. SW of BH9, this high resistivity zone is present for the rest of the section. From 50–57 m along the profile the top ~2 m of this high resistivity area is partially exposed due to bank erosion along the channel of the river which is characterised by massive or planar-bedded, medium-coarse sand with organic fragments and an absence of clay. There is no evidence of bedrock outcrop along the exposed section. The lower resistivity layer underlying Layer A in the NE half of the profile is interpreted as Layer B which correlates with soft clay horizons present in AH3 and at BH9 (where it is bounded by a thin horizon of peat at its base). The clay observed in these cores is similar to that observed in AH1 and AH2 (Fig. 4.3.1B). Bedrock was present at the base of BH9 at a depth of 3.2 m but was not encountered at AH1 or BH10. BH9 has a measured K_s of 0.75 m d^{-1} in comparison to 0.002 m d^{-1} for BH10. Given that BH9 is screened directly above the sandstone bedrock, where a thin weathered layer was encountered during coring, it is possible that this small weathered zone is contributing to the elevated K_s observed in this monitoring well. Therefore, the K_s value of 0.002 m d^{-1} at BH10 may be more representative of the alluvial cover in this section. This known bedrock depth provides the basis for the interpreted interface between Layer B and Layer C which is interpreted as the sandstone bedrock. This interface becomes less clear along the SW half of the profile where Layer B is absent. NE of BH9 the interface exhibits an apparent steep inclination, similar to that of ER2 on the opposite bank (Fig. 4.3.4B). It is unclear as to whether this is an artefact of the inversion process or a real feature of the bedrock topography, given that bedrock was not encountered in either BH10 or AH3. As can be

seen in Fig. 4.3.7C, piezometric levels lie approximately at the interface of Layers A and B and A and C after Layer B is truncated with GW5 (Angermann et al., 2012) providing an additional groundwater level monitoring point for this profile.

4.3.3.4 *ER4 interpretation*

ER4 (Fig. 4.3.7D) is co-located with BH11, BH12, HBW (EA, 2010; unpublished data) and GW3 (stratigraphy from Angerman et al., 2012). Layer A in this profile is defined by the high resistivity zone present over much of the top 0.5–1.5 m of the section. Similar to other profiles, this zone correlates with near-surface sand and topsoil horizons identified in cores from BH12 and GW3, which is likely to be unsaturated given the depth of the piezometric surface along the profile. Below this zone, (as already noted) the interpretation of the resistivity layers becomes difficult due to the lack of a significant contrast in the geoelectrical properties. The observed K_s values of 0.001–0.004 m d⁻¹ are assumed to be indicative of the upper 2–3 m of the alluvium in this area. Bedrock was encountered at a depth of 6.5 m in borehole HBW (Fig. 4.3.1), however there are no significant changes in resistivity evident at this depth in the profile. Given that the stratigraphy is dominated by sand and gravel, it can be expected that the porosity, moisture content and sediment composition are similar for both the bedrock and the unconsolidated material which would not present any significant variation in bulk resistivity with depth. Therefore, the interpreted depth of the bedrock interface (Layers B and C) for this profile is poorly constrained.

4.3.3.5 *ER5 interpretation*

Resistivity line ER5 (Fig. 4.3.7E) has ground truth information available from BH4, BH1 and Heathbrook East. The thin (<1 m), high resistivity layer (~300–800 Ω m) in this profile

is interpreted as Layer A and correlates with the topsoil and medium sand horizon identified in BH4. At BH1 this sand layer is also present, however, resistivity values in this area of the profile reduce to $<300 \Omega \text{ m}$. At the SE end of the profile, this high resistivity layer re-appears and correlates with a 1 m thick sand horizon identified in the driller's log for HBE (EA, 2010; unpublished data). Differentiation between the sandstone bedrock and alluvial cover using ERI is problematic due to lack of resistivity contrasts with depth along most of the line. Bedrock was met at 1 m in HBE but was not encountered at BH1 or BH4 at depths of 2.8 and 2.9 m, respectively. It is clear that the geoelectrical properties of the alluvial cover below BH4 and BH1 are not significantly contrasting. Therefore, the interpreted bedrock interface (Layers B and C) is less well-defined along this particular section. The area of ER5 forms the zone of maximum hydraulic head (59.5 m AOD) in the alluvial groundwater system (Fig. 4.3.2) which manifests itself as sub-artesian conditions in the area of BH1, as well as an area of groundwater seepage where the piezometric surface is above ground level. The thin, high resistivity layer in this profile is probably indicative of unsaturated granular material similar to that seen in the other ERI profiles. BH1 had significantly elevated K_s (0.33 m d^{-1}), relative to most other alluvial monitoring wells, and is two orders of magnitude greater than BH4 (0.002 m d^{-1}). Although silty deposits were noted in the cores from BH1 and BH4, an extensive confining layer (such as the thick clay to the west of these boreholes) was not evident in the alluvium in this area.

4.3.3.6 *ER6 interpretation*

ER6 (Fig. 4.3.8A) has ground-truth information available from BH2, BH5, BH6 and BH7 (Fig. 4.3.1A) and is interpreted as a 2 layer case. Similar to the other ERI profiles, Layer A shows considerable variability in resistivity above the piezometric surface and is characterised by higher resistivity values ($>100 \Omega \text{ m}$). These are correlated to the topsoil

and sand horizons identified in all borehole cores, which range in thickness from 1 m in BH3 to 2.4 m in BH7. Given that a high resistivity zone is observed at the NE edge of the profile (interpreted as unsaturated sands observed in BH2), it is likely that the observed resistivity variability in the rest of Layer A is due to variability in the sediment clay content. Layer B is defined by the low resistivity values (40–80 Ω m) encountered below the high resistivity surface layer and appears to be relatively homogeneous with depth. This layer correlates with the sandy-silt to sandy-clay deposits observed in all boreholes, although a sand horizon is also located in this layer at BH5 indicating heterogeneous distribution of fine materials within the alluvial sediments in this section. Although there was no evidence for the presence of bedrock in any of the auger holes, the hydrostratigraphy in this area of the floodplain appears to be relatively complex due to the distinct variability in piezometric levels. As already indicated in Fig. 4.3.3, a substantial lateral hydraulic gradient of 0.017 m m⁻¹ is present, as calculated along the axis of the profile from BH2 to BH7. BH2, BH3, BH6 and BH7 were found to have K_s values typical of most other well screened in the low conductivity alluvium with a geometric mean of 0.0035 m d⁻¹ and a range of 0.0018–0.0058 m d⁻¹. However, the K_s value at BH5 was two orders of magnitude higher at 0.543 m d⁻¹ indicating that permeable zones are present in the alluvial cover, although it has not been possible to distinguish differences in geoelectrical properties in the area of BH5.

4.3.3.7 *ER7 interpretation*

ER7 (Fig. 4.3.8B) is co-located with two auger holes (AH1 and AH2) (Fig. 4.3.1A). This profile is dominated by a single layer (B) characterised by low resistivity values (~20–60 Ω m) which is laterally continuous. This zone corresponds to the homogenous soft grey-to-blue clay encountered in both auger holes in this location of the floodplain. The higher

resistivity values (Layer A) at the SE end of the section adjacent to ER2 are interpreted as an zone of sediment with reduced clay/greater sand content closer to the River Tern, similar to that observed in ER2 and ER6 at comparable depths (Figs. 4.3.7B, 4.3.8A). These are, again, interpreted as overbank deposits originating from the modern River which is consistent with the findings from ER2 and ER6.

4.3.3.8 *Profiles without ground-truth information*

ERI profiles lacking any directly co-located auger hole stratigraphy (i.e., ER1, ER8, ER9 and ER10) are interpreted in the context of adjacent lines where ground-truth data are available. ER1 (Fig 4.3.7A) was collected at the midpoint of ER07, ER08 and ER09 (Fig. 4.3.1A). This profile illustrates the lateral extent of the low resistivity horizon (Layer B) which dominates the floodplain stratigraphy in this area. From adjacent core data, this horizon is interpreted as a laterally extensive clay deposit. The higher resistivity zone ($>100 \Omega \text{ m}$) below this layer is interpreted as the Permo-Triassic bedrock due to the comparable depth ($<5 \text{ m}$) and resistivity ranges observed in ER2 where the bedrock was encountered at BH8 and AH4. However, given the lack of ground-truth points on this profile, the depth of this interface is approximate only.

ER8 (Fig. 4.3.8C) does not have any ground truth locations, however, given its proximity to ER7 and ER2 the low resistivity layer (B) is interpreted as a lateral extension of the clay deposit identified at AH1 and AH2. The higher resistivity zone ($>100 \Omega \text{ m}$) at the base of the profile (Layer C) is interpreted as a possible bedrock interface, given the relatively shallow known bedrock depths noted in ER2 ($<3 \text{ m}$). ER9 (Fig. 4.3.8D) was the westernmost ERI profile collected in the area which also displays a low resistivity zone ($20\text{--}60 \Omega \text{ m}$) at comparable depths ($0\text{--}3 \text{ m}$) to ER7 and ER8. This is interpreted as further lateral continuity of the clay horizon noted from previous profiles in the north Helshaw

Grange floodplain. However, a significant high resistivity zone ($>100 \Omega \text{ m}$) is present at the SE edge of the profile, proximal to the river channel. Similar to ER7, this is interpreted as a sand-dominated zone associated with the riverbank which is evident in the cores of BH7 and AH5.

Lines ER10 and ER11 (Fig. 4.2.9 A–B) are interpreted via the ground-truth information derived from the ERI and core data collected from ER3 (Fig. 4.3.7C) and ER4 (Fig. 4.3.7D) in Heathbrook Farm (Fig. 4.3.1A). Both profiles are interpreted as 2 layer cases with the upper layer (B) comprising low resistivity values ($40\text{--}120 \Omega \text{ m}$) which are interpreted as alluvial cover containing a major fraction of fine-grained, conductive material. At the SW end of ER10 a high resistivity feature is present (denoted as Layer A with values of $160\text{--}600 \Omega \text{ m}$ and a maximum thickness of 3 m) which is interpreted as having a much greater proportion of granular material, in contrast to the rest of the alluvial stratigraphy along the section. This feature was previously interpreted as a palaeochannel of the either the River Tern itself or a distributary channel which has since become in-filled with coarse material (Blackwell, 2002). The high resistivity layer (C) below Layer B is interpreted as the Permo-Triassic bedrock, given the similar resistivity ranges to ER2 and ER3 ($120\text{--}280 \Omega \text{ m}$) where bedrock was encountered. However, the exact depth to the formation cannot be determined accurately as no borehole cores are available in this area of Heathbrook Farm.

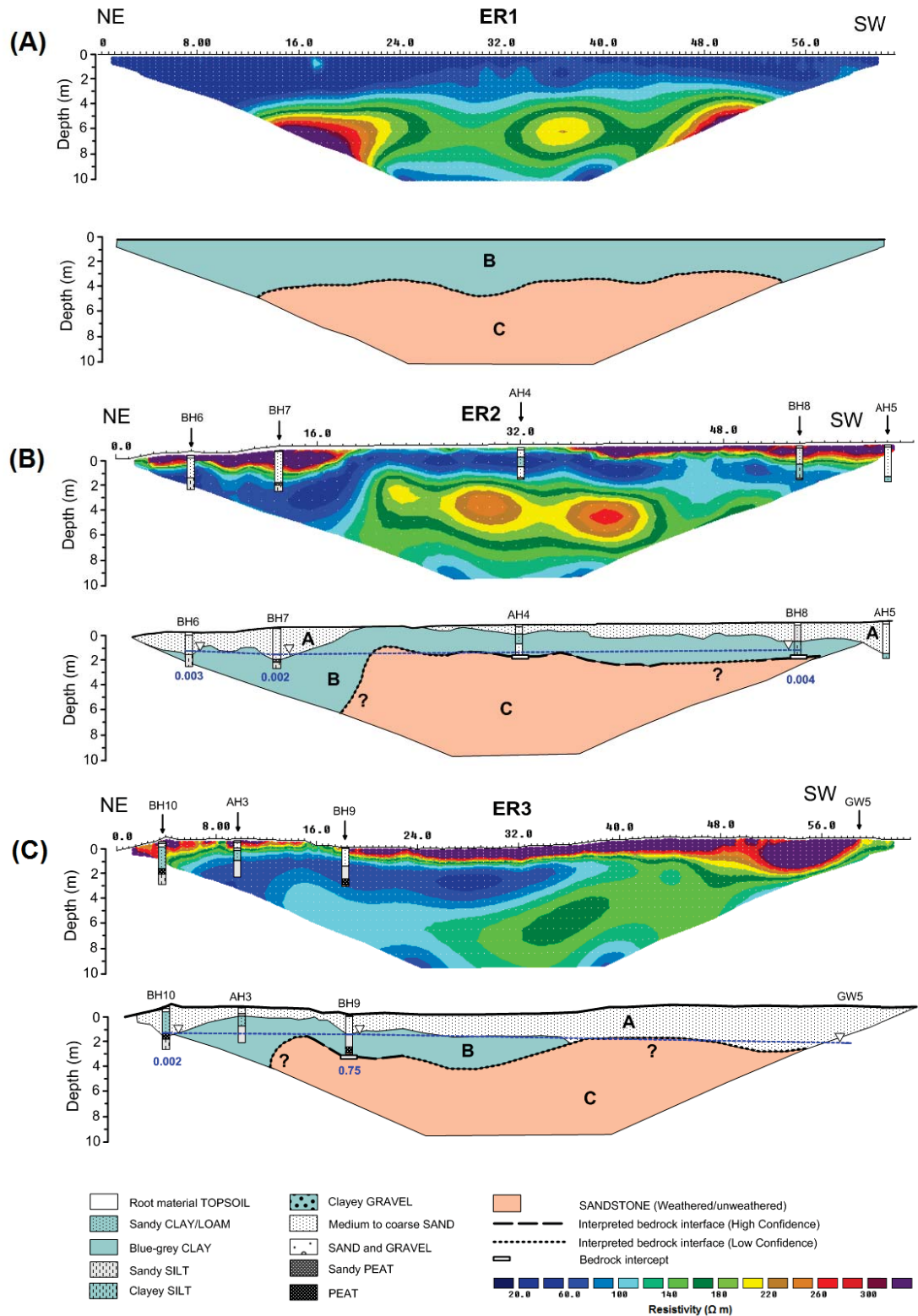


Fig. 4.3.7 (A–C) Geological and hydrogeological interpretation of 64 m long Electrical resistivity imaging profiles ER1–ER3 with stratigraphic from Section 4.3.1 (where available). Interpolated piezometric surface indicated by dashed blue line. Hydraulic conductivity values (in m d^{-1}) are annotated in blue under the relevant well locations. Question marks denotes areas of uncertainty in the interpretation.

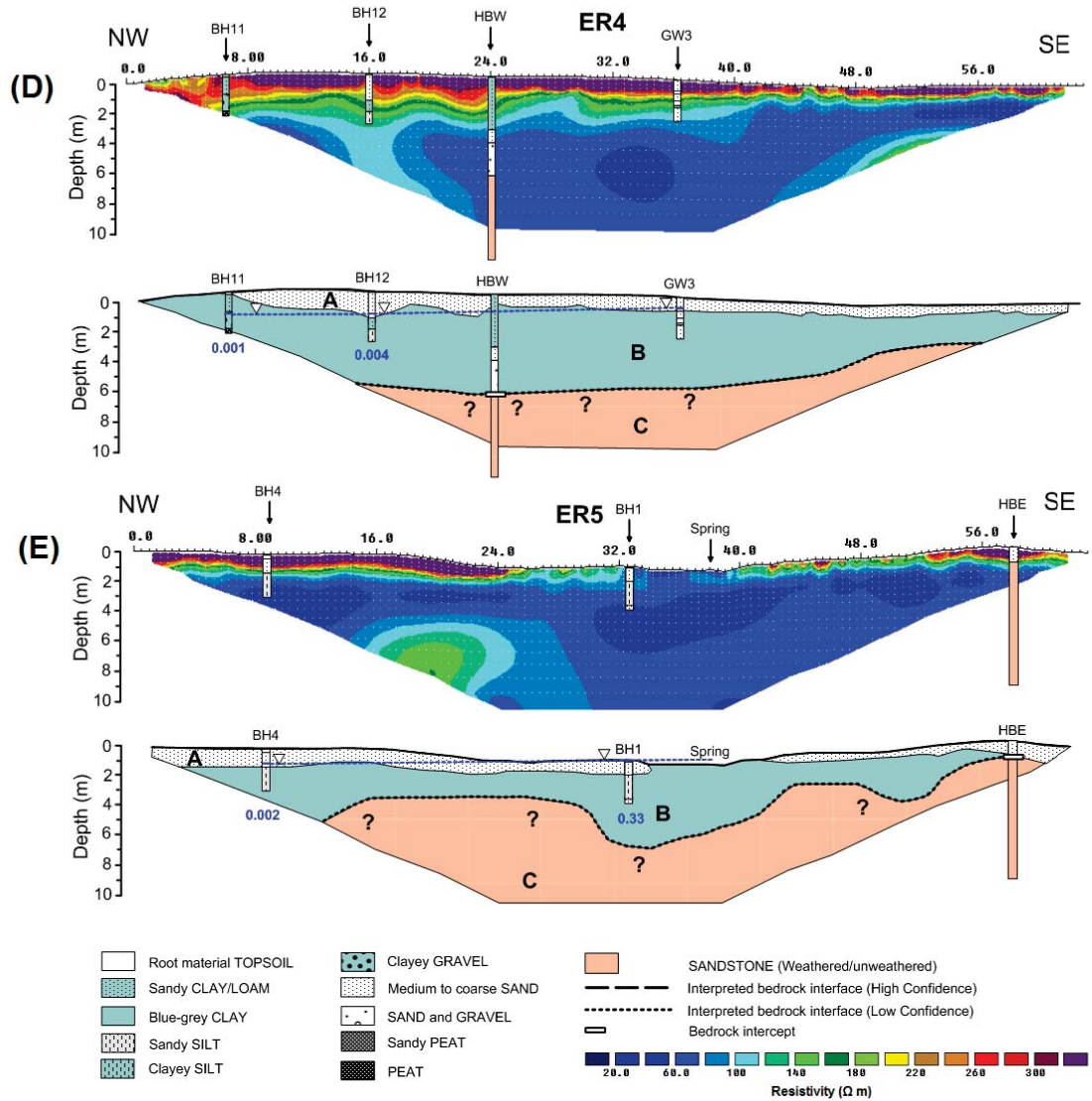


Fig. 4.3.7 Geological and hydrogeological interpretation of 64 m imaging profiles ER4 (D) ER5 (E) with stratigraphic information from Section 4.3.1. Interpolated piezometric level is indicated by the dashed blue line. Hydraulic conductivity ($m d^{-1}$) is annotated in blue under well location where possible. Refer to Fig. 4.3.1A for location of profiles and well/auger hole locations. Question marks denotes areas of uncertainty in the interpretation.

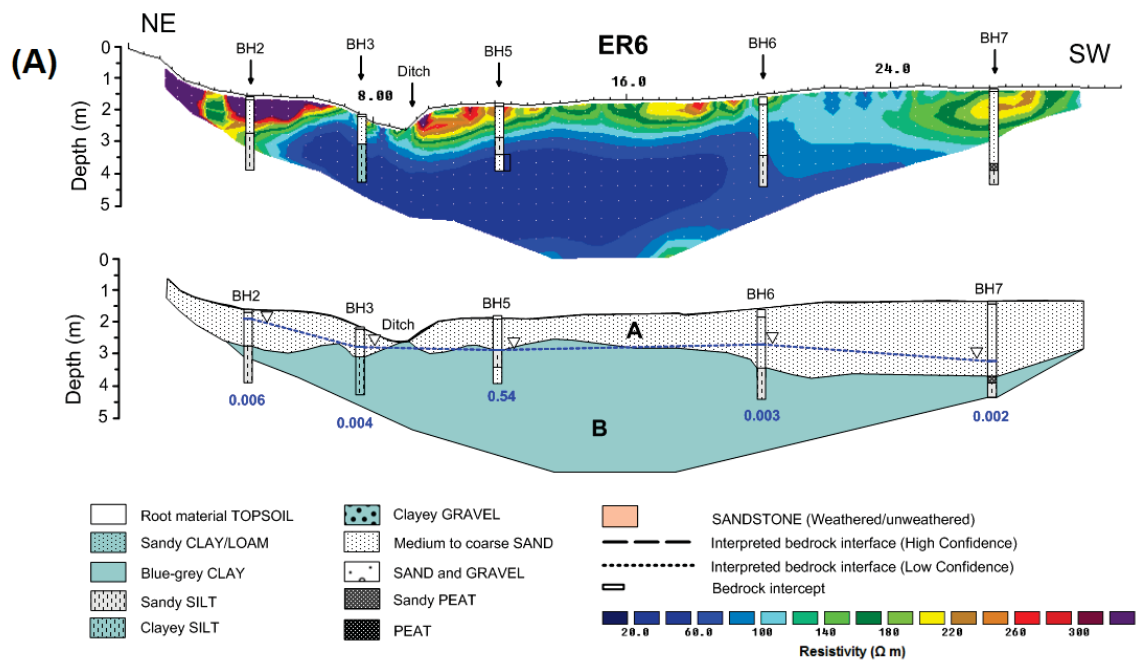


Fig. 4.3.8 (A) Geological and hydrogeological interpretation of 32 m imaging profiles ER6 with stratigraphic information from Section 4.3.1. Interpolated piezometric level is indicated by the dashed blue line. Hydraulic conductivity (m d^{-1}) is annotated in blue under well location. Refer to Fig. 4.3.1A for location of profiles and well/auger hole locations. Note that ER6 is partially co-located with ER2 (Figs. 4.3.4B, 4.3.7B).

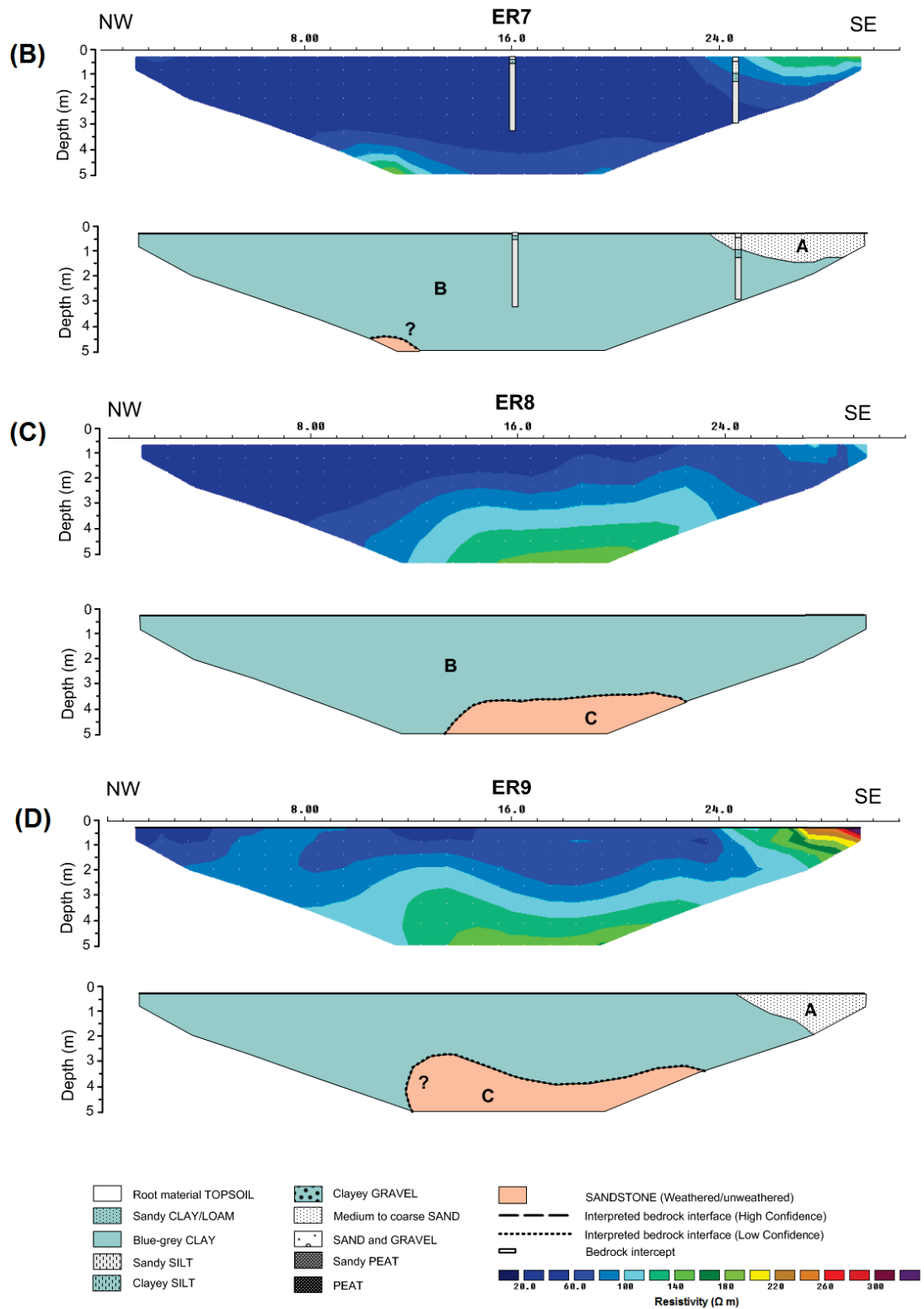


Fig. 4.3.8 Interpretation of 32 m ERI profiles acquired in Helshaw Grange for **(B)** ER7 which has some stratigraphic data from auger holes (Section 4.3.1) and **(C)** ER8 and **(D)** ER9 which do not have ground-truth information. Refer to Fig. 4.3.1A for the position of these profiles. Question marks denotes areas of uncertainty in the interpretation.

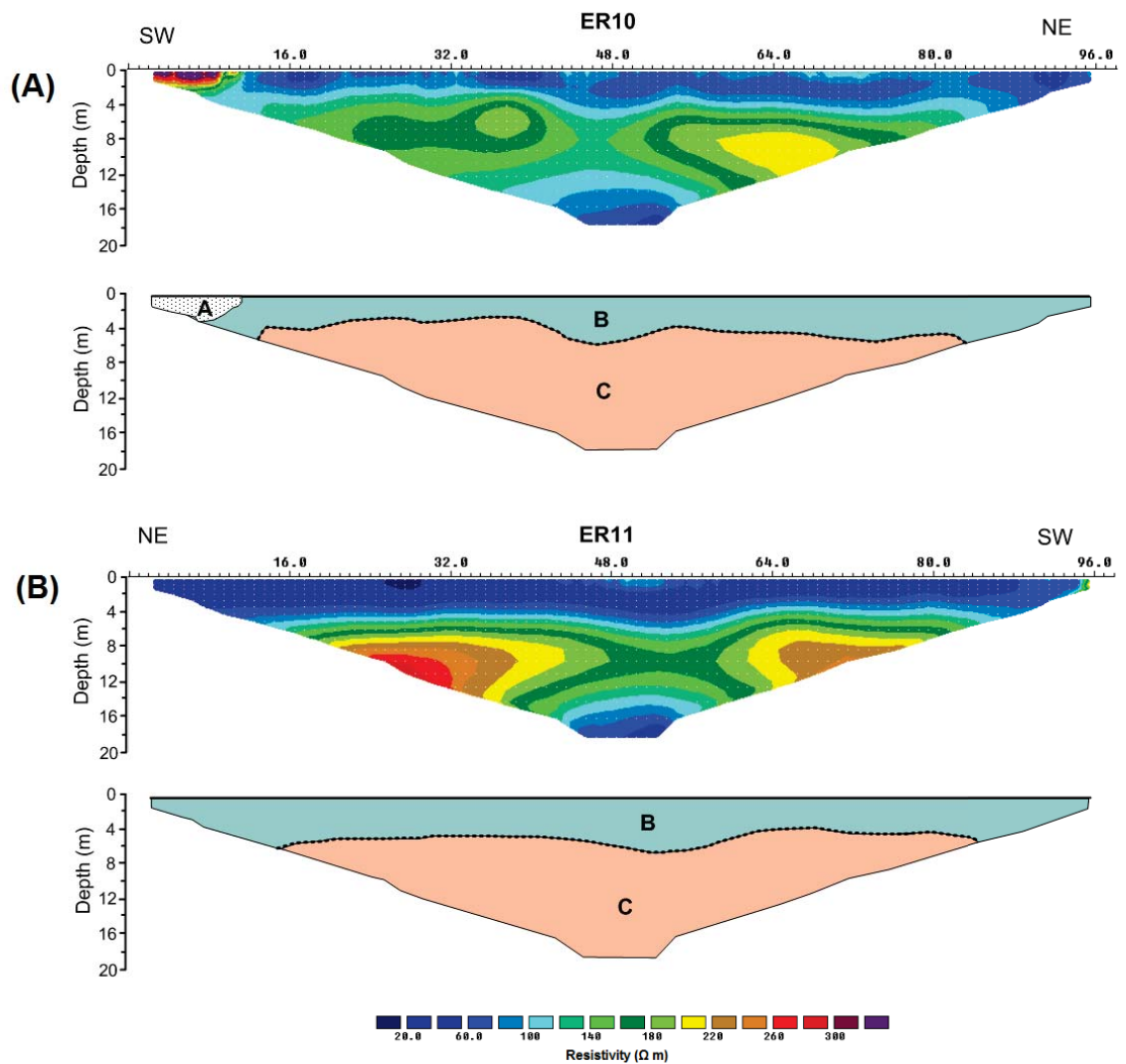


Fig. 4.3.9 Interpretation of 100 m ERI profiles ER10 (A) and ER11 (B) acquired as part of the LOCAR program located in Heathbrook Farm which do not have associated ground-truth information. See Fig. 4.3.1A for the geographic location of these profiles in the study area.

4.4 Discussion

4.4.1 Delineation of the plume discharge zone in the riverbed

By applying a multi-scale approach it has been possible to reveal the potential discharge zone of the dissolved-phase TCE plume where it extends along a river reach of approximately 120 m in length, upwelling from a depth of probably 80 m in the underlying Permo-Triassic sandstone aquifer. This reach has been identified by (1) the diffusion samplers at 0–50 m of transect B–B' (Fig. 4.2.3A) and (2) the pre-existing piezometers P1–P12 (Fig. 4.2.2) where TCE concentrations were observed to be at, or above, $1 \mu\text{g L}^{-1}$. Both of these investigations clearly identify a sub-reach centred on a meander bend in the floodplain where TCE concentrations were $\geq 10 \mu\text{g L}^{-1}$ at both 1.5 m (sampling depth of the existing piezometers) and ~ 0.15 m (depth of the diffusion sampler openings) which reached a maximum around P4/70 m station of B–B' (Figs. 4.2.2 and 4.2.3A). It is expected that the majority of the contaminant mass from the groundwater plume will discharge through this 'core' zone (Cherry, 1997). Downstream of P4, concentrations declined similarly in both the diffusion samplers and the existing piezometers. With this information, the reduced TCE concentrations ($1\text{--}4 \mu\text{g L}^{-1}$) observed both up and down stream of the meander bend (e.g., 0–50 and 80–120 m of B–B' and P5–P12) are interpreted as a 'fringe' zone (Cherry, 1997) of the plume where dispersion is likely to be spreading the plume out along the axis of the river channel. TCE concentrations in the mini-piezometers significantly exceeded those in the (1) shallow sandstone boreholes (HBE and HBW), (2) alluvial monitoring wells (BH1–14) and (3) diffusion samplers, reaching a maximum of $\sim 40 \mu\text{g L}^{-1}$ at MP18 (Fig. 4.2.5). The high-resolution, 2D longitudinal section given in Fig 4.2.6 visualises the intricate vertical variability of the plume at decimetre scales in the top metre of the riverbed deposits. One 'hotspot' of contamination evident

between monitoring points MP17 and MP22, suggests a locally focussed pathway of TCE discharge through the riverbed in an otherwise more diffuse flow system. This area is located at the head of a riffle-sequence where an armouring layer of coarse sand, gravel and cobbles dominates the substrate. This section may represent a zone of relatively high permeability forming a 'geological window' where the hydraulic connectivity with the underlying TCE-contaminated sandstone aquifer is enhanced (Lyford et al., 1999; Fryar et al., 2000; LaSage et al., 2008). No CEs were detectable in the surface water samples collected from within the main channel of the River Tern during any of the sampling campaigns. This is presumably due to the large dilution potential available in the river itself (Weatherill et al., 2014).

4.4.2 Characteristics of the floodplain groundwater system

An investigation of the floodplain alluvial groundwater system using single-screened monitoring wells indicated generally low levels (e.g., $<6 \mu\text{g L}^{-1}$), or a complete absence of, CEs detectable in the shallow groundwater in drift deposits (Fig. 4.3.3 & Fig. 4.2.1). This suggests that the plume is not dispersing significantly within the shallow alluvium deposits of the floodplain and is confined mostly to the riverbanks. Observations of hydraulic head distribution in the alluvial groundwater system during baseflow conditions (Fig. 4.3.2) suggests that the lateral groundwater flow approximately reflects a subdued version of the local surface topography with a significant lateral gradient from NE to SW, which is approximately parallel to the regional hydraulic gradient in the Permo-Triassic aquifer within the wider drainage basin (Fig. 3.2.5, Chapter 3). Additional, weaker hydraulic gradients were apparent from the centre of the meander bend with flow directions to NW and NE which is suggestive of groundwater upwelling below the meander bend (Fig. 4.3.2). Discrete observations of hydraulic conductivity from slug tests together with the

slow refill characteristics of many of the monitoring wells observed during sampling campaigns suggest the alluvial cover may act as a local aquitard at reach-scale forming a low-permeability cap. This cap confines the underlying highly permeable bedrock flow system over the flat, low-lying area of the floodplain to the west of the terrace marking the eastern edge of the river corridor (Fig. 4.3.2). Evidence for this comes from the majority of observation wells which partially penetrate the upper ~1.5 m of the saturated alluvium which is mostly characterised by silt or clay-dominated material (with a geometric mean hydraulic conductivity of 0.0035 m d^{-1} and a narrow range of $0.001\text{--}0.006 \text{ m d}^{-1}$). This value is three orders of magnitude lower than the 3 m d^{-1} geometric mean K_s of the Bridgnorth sandstone (Streetley and Shepley, 2005) which underlies the study area, on a regional scale (Chapter 3). However, the distribution of low-permeability material cannot be considered as entirely homogeneous where approximately 30% of wells (BH1, BH5, BH9 and BH14) exhibit hydraulic conductivities two orders of magnitude greater than the rest with a geometric mean of 0.54 m d^{-1} . Although the permeability of BH9 may be partly ascribed to the influence of weathered sandstone, no evidence of bedrock was observed in cores from the remainder of the wells (Fig. 4.3.1B). This suggests that the local aquitard underlying the floodplain may be considered as ‘leaky’ with permeable zones present within the stratigraphy. These conditions may provide potential preferential pathways for rapid transport of the plume to the river where riparian flow paths are hydrologically connected with the underlying contaminated groundwater. For instance, detection of TCE in the surface water of the drainage ditch and seepage area is indicative of preferential flow, resulting in TCE concentrations in the order of $5 \mu\text{g L}^{-1}$ that discharge directly to the river (as of May 2011). These features represent point impacts from the plume that ‘short circuit’ more diffuse pathways in the alluvial sediments (Fryar et al., 2000; Conant, 2004).

The unconsolidated alluvial valley deposits of lowland rivers are known to form important controls on groundwater-surface water interactions at river corridor scale (Woessner et al., 2000; Wheeler and Peach, 2004; Grapes et al., 2006; Byrne et al., 2013). For example, in the chalk catchment of the Pang-Lambourn rivers (Berkshire, UK), an extensive alluvial gravel system is known to form an important high-permeability pathway for lateral groundwater-surface water mixing and hyporheic exchange as well as a providing an potential pathway for pollutant exchange (Abesser et al., 2008; Allen et al., 2010). Furthermore, meander bends have been shown to enhance hyporheic mixing in streams via bypass flow through alluvial deposits (Peterson and Sickbert, 2006). However, at the River Tern site, the low-permeability of the alluvium throughout much of the plume upwelling zone is likely to prohibit significant lateral exchange of river water with floodplain groundwater, as well as focus flow lines of the plume towards the interface of permeable zones in the riverbed. For example, TCE concentrations in excess of $35 \mu\text{g L}^{-1}$ were observed in discrete sampling levels of MP3, MP8, MP12 and MP13 (Fig. 4.2.5). From these observations, it is possible that the plume is discharging laterally to the riverbed from beneath alluvium mantle from the northern bank at piezometer Transect TA and also from the Heathbrook Farm bank at Transect TB. As shown by previous studies at this site (e.g., Krause et al., 2012b; 2013) and other CE plume sites (Conant et al., 2004), aquitard materials in the riverbed and banks may be exerting significant, local-scale geological controls on the location and magnitude of groundwater contaminant discharges across the aquifer-aquifer interface. This interpretation is depicted in Fig. 4.4.1 which presents a conceptual model of the plume discharge zone along a cross-section centred on the mini-piezometers MP17 and MP18 (Fig. 4.3.6) where the highest concentration of TCE was discovered.

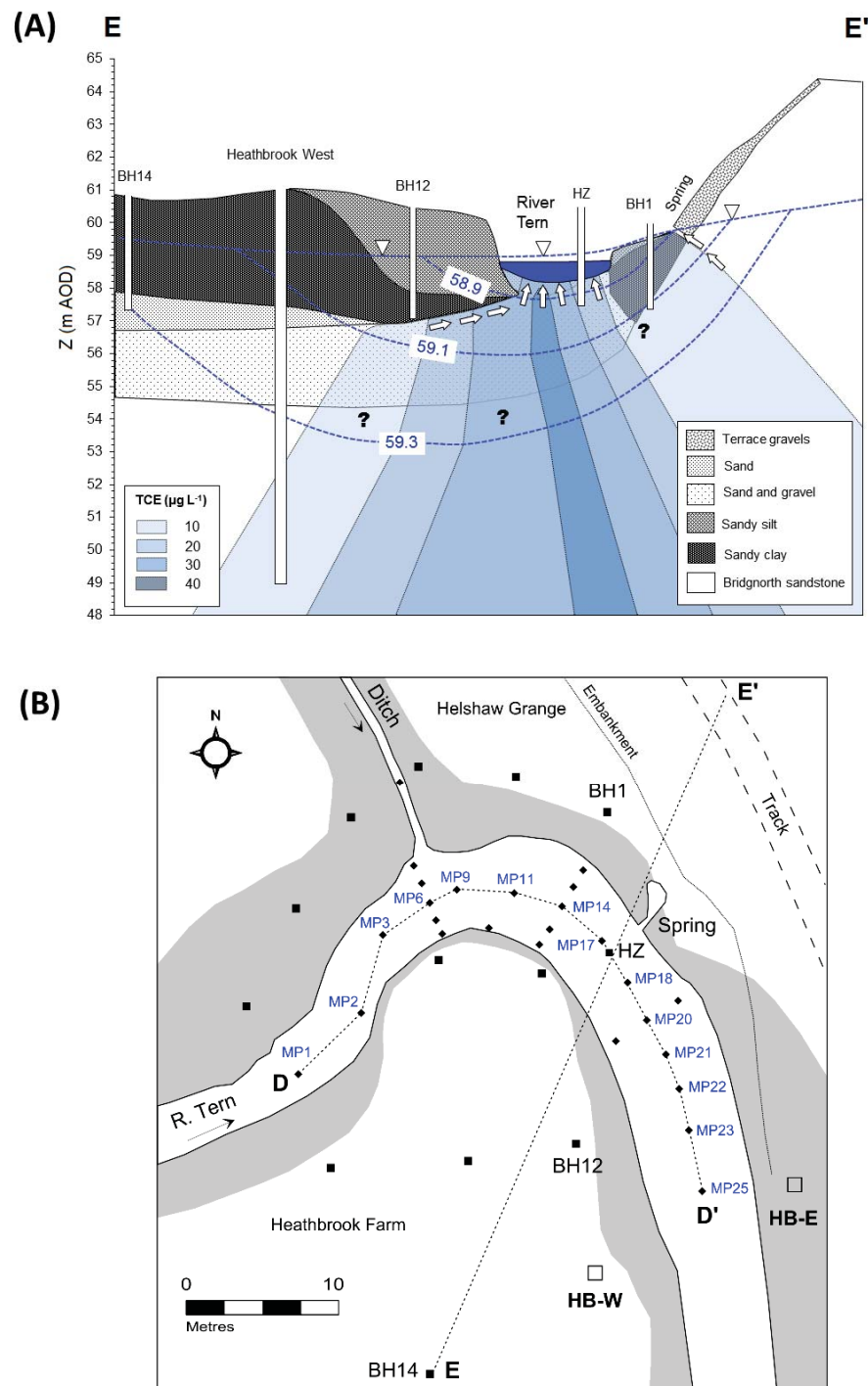


Fig. 4.4.1 (A) Hydrogeological cross-section (E-E') through the floodplain along the same axis as Fig. 3.2.6 (See Chapter 3). Hydraulic head contours and TCE concentrations are interpolated from measurements (at the boreholes labelled) in December 2011. Arrows represent interpreted advective transport pathways for the plume influenced by (1) low permeability alluvium deposits in the floodplain and (2) bypass flow through the spring/seepage zone. Question marks denote areas of uncertainty (modified after Weatherill et al., 2014). (B) Location of cross-section E-E' (see Fig. 4.3.1A for location in study area).

4.4.3 Insights from electrical resistivity imaging

With the use of 2-D electrical resistivity imaging (ERI) as non-invasive characterisation tool, in combination with a relatively limited number of point observations of local stratigraphy from auger holes, it is possible to observe the lateral continuity of hydrostratigraphic units floodplain-scale with measurement densities considered impractical with intrusive investigation methods alone (Binley, 2010). However, successful ERI-related characterisation relies on there being sufficient lateral and vertical contrasts in the bulk geoelectrical properties arising from differences in porosity, clay content, water content, pore water dissolved solutes and temperature in order to successfully discriminate between true stratigraphic boundaries (Crook et al., 2008; Clifford and Binley, 2010). For imaging the spatial extent and geometry of the alluvial aquitard, which caps the Permo-Triassic sandstone at the site, the electrically conductive clays present in the Holocene alluvial sequence provide an important contrast with (1) the underlying, clay-free sandstone bedrock and (2) the overlying and unsaturated clean sand (interpreted as overbank fluvial deposits). For the majority of the ERI profiles acquired, a three-layer interpretation was possible based on these distinguishing properties. At lines ER1, ER2 and ER3 (Figs. 4.3.4 and 4.3.7), orientated along bank-parallel NE-SW traverses (Fig. 4.3.1A), it is possible to visualise the lateral extent of the aquitard as well as the topography of the bedrock interface. ER7, ER8 and ER9 (Figs. 4.3.5, 4.3.8) provided additional supporting observations in an orthogonal orientation. It is clear from these imaging profiles that the alluvial aquitard is laterally continuous throughout the northern floodplain with an approximate average thickness of 4 m. The topography of the bedrock interface beneath appears somewhat heterogeneous with a decrease in the alluvial cover thickness toward the riverbank from ER1 to ER2. At ER2 the bedrock interface appears to be steeply inclined at 0–18 m along the profile (Fig. 4.3.7A) which is supported by an absence of bedrock

interception in either BH7 or BH6 at a depth of ~3 m. As already indicated, this may be an artefact of the inversion process. However, at ER6 (which is partially co-located with ER2, Fig. 4.3.1A), no evidence of bedrock is observed at a maximum depth of 5 m below the survey centre point (Fig. 4.3.8A). On the opposite bank at ER3 (Fig. 4.3.7C) the alluvial aquitard appears to 'pinch out' between 32 and 40 m along the profile with a possibly inclined bedrock interface at the NE end of the profile. These imaging results suggest that a significant feature in the bedrock topography may be present underlying the area close to the head of the meander bend resulting in thickening of the alluvium cover, through which the core of the plume discharges. Given the meandering nature of the lowland River Tern in this area of the catchment, it is not inconceivable that these observations are indicative of the presence of an in-filled palaeochannel structure with a putative NW-SE orientation. Such features have been documented using ERI approaches in lowland sedimentary settings elsewhere (e.g., Baines et al., 2002) as well as elsewhere on the floodplain at ER10 (Blackwell, 2002). However, without directly co-located ground-truth information on the actual bedrock depth, this interpretation (based on the geophysical evidence alone) is somewhat speculative. Nevertheless, the overburden thickness is known to reach 6.5 m at Heathbrook West (Fig. 4.3.7D) which is considerably greater than ~3 m at BH9 located approximately 20 m ENE in Heathbrook Farm (Fig. 4.3.1A). However, the poorly contrasting geoelectrical properties of the subsurface at ER4 (Fig. 4.3.7D) which is co-located with Heathbrook West as well as at ER5 (Fig. 4.3.7E) on the eastern bank of Helshaw Grange limit the delineation of the eastern extent of this possible structural feature. It is also interesting to note that the boreholes located within this interpreted channel-fill deposit (e.g., BH6 and BH7, Fig. 4.3.1A) coincide with the area of lowest hydraulic head in the floodplain groundwater system (Fig. 4.3.2). A possible interpretation of this head pattern is that the groundwater which these wells intercept is hydraulically

isolated by the in-fill deposits from the regional upwelling pressure exerted by the bedrock system elsewhere in the floodplain.

4.4.4 Preliminary evidence of in-situ transformation of the plume

This phase of the investigation was primarily designed to identify the discharge zone of the TCE plume with the detection of any daughter products taken as evidence of in-situ degradation of the single-component plume. The complete absence of daughter products in any of the sandstone bedrock boreholes suggests that destructive attenuation within the sandstone aquifer is probably negligible. Additionally, the lack of any daughter products detected by the diffusion samplers in the main channel suggests that the plume is not being actively degraded in the riverbed sediments. However, it is possible that reverse diffusion of dissolved oxygen from the aerobic sampler medium may have led to removal of these daughter products from the local pore water if anaerobic conditions were present (given that cDCE and VC are capable of being oxidised aerobically even in low-oxygen conditions, Bradley and Chapelle, 2000a; Abe et al., 2009; Gosset et al., 2010). Interestingly, the highest levels of cDCE were recorded from diffusion samplers deployed in the organic silts in-filling the drainage ditch (Fig. 4.2.3B) where TCE was also present in the water column. Consistent with this, Abe et al. (2009) noted that cDCE oxidation was insignificant in aerobic microcosms prepared from riverbed sediments and incubated over a period of 1.5 years. However, later sampling of the ditch outflow water did not reveal any further cDCE (or VC) detections in this area. Some monitoring wells in the alluvium displayed trace levels of cDCE (e.g., BH7 and BH10) (Fig. 4.3.2). These boreholes are associated with the low permeability alluvial silt, clay and occasional peat which comprise much of the floodplain material of the meander bend area (Fig. 4.3.1B). Given the low hydraulic conductivity (e.g., $<0.005 \text{ m d}^{-1}$) and slow recovery of many wells in this area, a

greater residence time can be expected in these deposits and, therefore, a greater opportunity for chemical reactions to occur (Damgaard et al., 2013). With the benefit of the multi-level vertical profiles provided by the mini-piezometers, some evidence of in-situ reductive dechlorination has been identified (Fig. 4.2.6, 4.2.7) which appears to be spatially restricted to certain parts of the channel and concentrated in the top 20-40 cm of the riverbed sediment profile. Dechlorination of the plume appears to be generally limited to cDCE production with no significant quantities of the 1,1-DCE or *trans*-1,2-DCE isomers detected on the chromatograms, suggesting that cDCE production is occurring primarily as a result of microbial transformation of TCE (Bouwer, 1994). However, the application of compound-specific stable isotope analysis and the characterisation of the microbial consortia would be required in order to discriminate between specific biotic and abiotic degradation pathways (Abe et al., 2009; Hunkeler et al., 2011; Hamonts et al., 2012; Damgaard et al., 2013). Nonetheless, the spatial variability and the biogeochemical controls on these localised transformation zones in the riverbed will be investigated in detail in Chapter 6.

4.5 Chapter summary

This chapter has shown the plume to be present in the shallow riverbed sediments with a ‘footprint’ of contamination defined by TCE detectable at $\geq 1 \mu\text{g L}^{-1}$ in (1) the riverbed diffusion samplers from 0–50 m of Transect B (2) the pre-existing mini-piezometers from P1–P12. These two sampling campaigns identified a sub-reach approximately 40 m in length centred around a meander bend where TCE concentrations were in excess of $10 \mu\text{g L}^{-1}$. This sub-reach is most likely where the ‘core’ of the groundwater plume intercepts the aquifer-river interface surrounded by a ‘fringe’ zone arising from dispersive transport. Two sampling campaigns using mini-piezometers revealed multi-level patterns of TCE contamination in the riverbed were persistent with both cross-channel and longitudinal concentration gradients within the core of the plume. Low level detections of cDCE (and occasionally VC) in some of the piezometer profiles indicated in-situ transformation of TCE was occurring in shallow levels of the riverbed sediment profile. The plume does not appear to be dispersing significantly within the floodplain sediments with only low-level contamination ($< 6 \mu\text{g L}^{-1}$) present in some bank-side monitoring wells with traces of cDCE. Hydrostratigraphic units in the floodplain could be delineated with ERI surveys and point sampling from augering. High-resistivity, unsaturated sands observed at the top of most ERI profiles and auger holes along the river banks have been interpreted as overbank deposits originating from the modern river. Interbedded silt, clay and occasional peat horizons mostly dominate the saturated zone along the banks. These deposits form an aquitard characterised by very low K_s values (e.g., $< 0.005 \text{ m d}^{-1}$), however some more permeable zones exist that suggest a ‘leaky’ aquitard with evidence of preferential flow occurring through a seepage area and drainage ditch where TCE was detected. This low-permeability alluvium cap over the sandstone aquifer is likely to influence groundwater discharge patterns along the river corridor where the plume discharges.

5. Controls and drivers of contaminant discharge through the riverbed

5.1 Chapter introduction

This chapter aims to investigate the controls and drivers of the contaminant flux through the riverbed, which forms the main pathway through which the plume discharges to the river. In order to achieve this, a detailed knowledge of the geological framework of this pathway is required. To this end, detailed mapping of the substrate is undertaken and sediment cores are retrieved to investigate the shallow stratigraphy and retardation potential. Because the mass flux from the plume is driven by rates of groundwater discharge, an understanding of the drivers (hydraulic gradients) and controls (hydraulic conductivity) of groundwater flow through the riverbed is important. The spatial variability of hydraulic conductivity and vertical hydraulic gradients is investigated over a 72.5 m longitudinal transect of nested piezometers which encompasses both the core of the plume and part of the surrounding fringe area. The significance of hyporheic exchange along this transect is investigated through the continuous monitoring of hydraulic heads and river stage. Heterogeneity in the spatial variability of groundwater discharge rates is investigated using high-resolution temperature mapping. Point-observations of hydraulic conductivity and hydraulic gradients are used to estimate 1-D vertical groundwater fluxes which are ‘up-scaled’ to provide estimates of groundwater baseflow along the reach, from which TCE mass fluxes are determined. The impact of the riverbed stratigraphy on TCE migration rates and residence times is quantified from the properties determined on sediment cores and the estimated rates of vertical groundwater discharge.

5.2 Flow controls and properties

5.2.1 Physical properties of the riverbed

5.2.1.1 Surficial sediment mapping

Riverbed sediment cover was mapped by visual inspection during the temperature survey campaign (Section 5.3.2) in early September 2013 where the dominant sediment type of the top 10 cm of the riverbed was recorded at 1 m intervals along transects across the river channel (Fig. 5.2.1). Approximately 60% of the surficial riverbed sediment at the site was dominated by loose, medium sand deposited mainly in 1–5 m diameter lenses, often in association with submerged macrophyte stands. These grey-to-light-brown lenses represented the dominant sediments type along the reach from SL1 to SL5 with small scale (e.g., 5–10 cm) ripple marks superimposed over the larger bedforms. This sand closely resembles the upper 1–2 m of the floodplain alluvium deposits from previous core samples (Chapter 4), in both grain size and mineralogy (e.g., quartz-rich). This sand layer had variable organic matter content with small-scale detrital organic matter deposition evident on the lee slopes of ripple structures as well as more widespread deposition in areas of reduced current velocities around the channel periphery. Consolidated organic matter was recorded along the bank at Helshaw Grange from SL1 to SL4 which typically comprised organic-rich silt and mud with a variable fraction of medium sand, often in association with emergent macrophyte growth along the channel margin. A patch of gravel set within a clayey matrix was present to the north of SL5 along the Helshaw Grange bank, towards the area of BH1. Downstream of SL5, the topographic high in the riverbed (Fig. 4.2.6, Chapter 4) was composed of ‘armoured’ grits, gravel, cobbles and occasional boulders, covering approximately 14% of the riverbed area (Fig. 5.2.1). Similar armouring layers have been

described at other lowland river sites in the UK (e.g., Ellis and Rivett, 2008; Krause et al., 2009). Loose, medium sand was observed to drape the downstream end of this feature as far as SL7. Outcrops of grey-to-blue clay with peat layers were present along the bank of Heathbrook Farm in the area of SL3 (Fig. 5.2.1). These clayey silt layers were also encountered during the installation of mini-piezometers MP1–MP3 in Chapter 4. This clay and peat in the riverbed was texturally similar to that observed in the floodplain auger samples from AH1 and AH2 (Helshaw Grange) as well as BH9 and AH3 (Heathbrook Farm) (Fig. 4.3.1B, Chapter 4).

5.2.1.2 *Shallow riverbed stratigraphy*

Riverbed cores (Fig. 5.2.2) were recovered in late May 2013 between SL1 and SL4 (Fig. 5.2.1) during installation of the Transect S piezometers (see Chapter 3). The uppermost loose sand layer was found to extend down to a depth of ~20 cm in the fluvial sediment sequence. Core recovery of this layer was poor and it was necessary to take grab samples from coring locations to provide representative samples. Below this surficial layer, the stratigraphy was more heterogeneous. Grey-to-brown organic silt was encountered from 20–70 cm in SL1 and from ~20–80 cm in SL2, which was underlain by grey-to-blue clayey sand or sandy clay. The main silt horizon had coarse sand stringers with a typical thickness of ~1–3 cm. Permo-Triassic sandstone was reached at the base of SL1 at approximately 96 cm below bed level. The sandstone was relatively competent and characterised by red-to-orange coarse sand. A further organic horizon was encountered in SL3 (Fig. 5.3.1) from ~20–90 cm which comprised brown peat with a significant sand component underlain by fine, light grey sand and clay. At SL4 (Fig. 5.2.2) a similar peat horizon was observed at approximately 20 cm depth which was soft and generally free of sand, as well as appearing dry in places. This ‘dry’ peat phenomenon was also noted by Krause et al. (2013) along the

same reach of the river. Downstream of the head of the meander bend (Fig. 5.3.1), this organic horizon was absent in the area of SL5. At this location, the stratigraphy was dominated by fine-to-coarse, grey-to-brown sand with a thin silt horizon at 60 cm. Downstream of the ‘armoured’ section (SL6 and SL7), a laterally continuous soft brown-to-black peat horizon was observed underlying the surficial sand at depths of ~20–35 cm, sometimes containing occasional intercalations of coarse or medium sand. At SL6, the base of the peat sequence was not encountered (Fig. 5.3.2). The surficial material of the riverbed at SL8 was dominated by coarser sediment (similar to the armoured area upstream) with large cobbles and boulders mixed with coarse sand and gravel. Intact core recovery was not possible with the gouge corer at this location. It was necessary to use Edelman auger to install the piezometer at SL8. However, coarse sand/gravel/cobble material was presumed to be present below ~10 cm of sand.

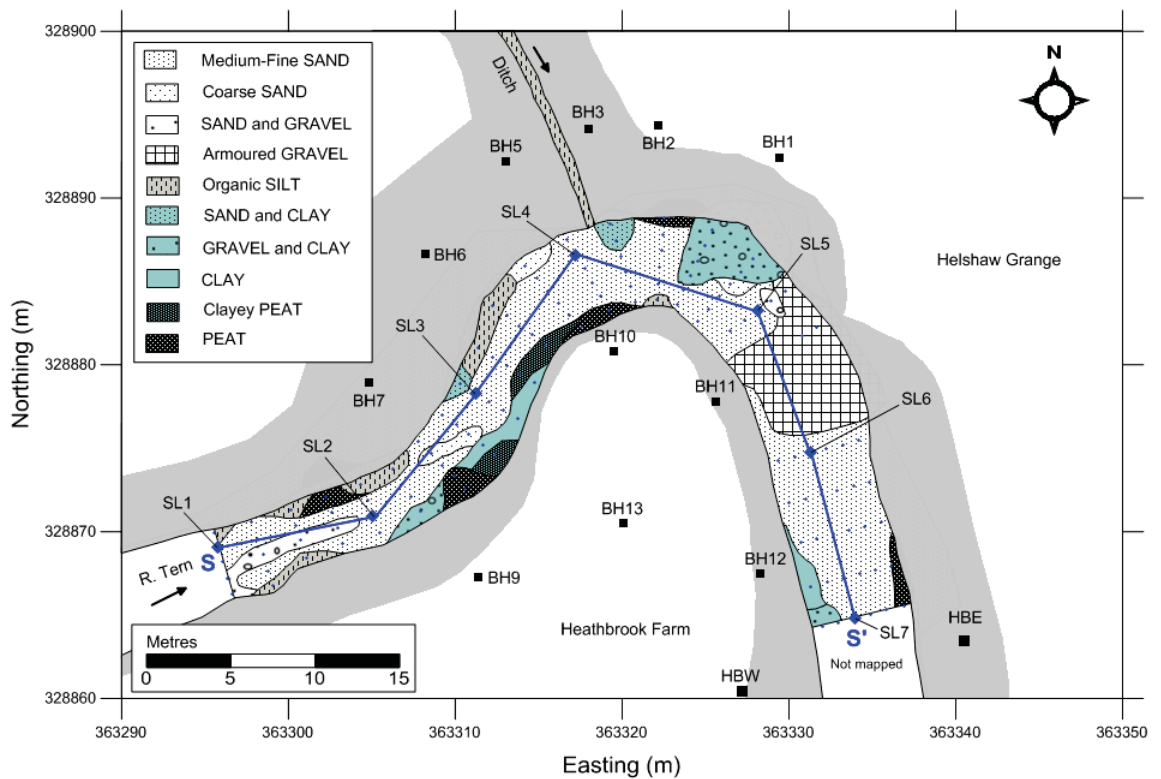


Fig. 5.2.1 Surficial sediment composition of the River Tern bed in the investigated reach (SL8 not shown). The location of the Transect S piezometers/coring locations is highlighted in blue with the small blue dots denoting points where the sediment composition was recorded.

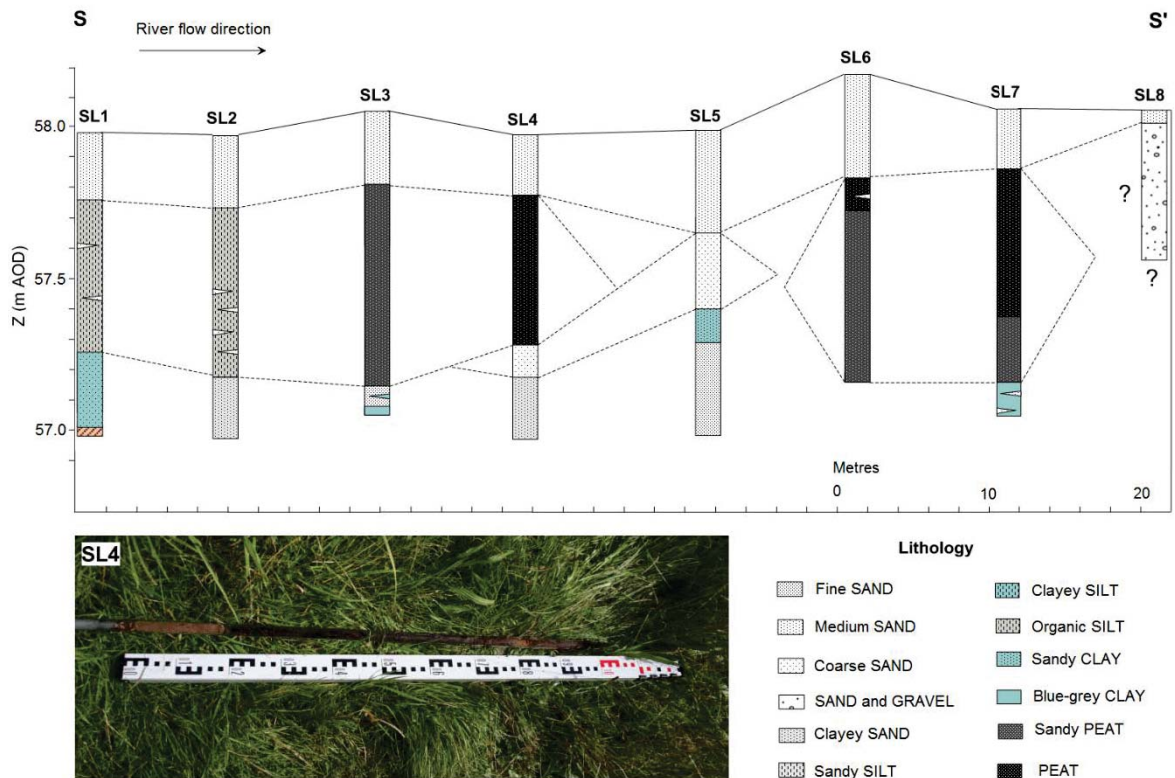


Fig. 5.2.2 Riverbed stratigraphy determined from the core sampling along the reach. A photograph of the core from SL4 shows the prominent organic horizon which is representative of the sedimentary conditions across much of the reach.

5.2.1.3 Organic carbon content of the riverbed deposits

To quantify the adsorption potential of TCE in the riverbed sediment sequence, the mass fraction of organic carbon (f_{oc}) [g g^{-1}], porosity (n) [v v^{-1}], and bulk density (ρ) [g cm^{-3}] were determined on triplicate sediment samples taken from the formations logged in the cores of Fig. 5.2.2. Because f_{oc} is the most important sediment property controlling hydrophobic sorption (Weidemeier et al., 1998), mean values for the triplicate samples are presented as step plots in Fig. 5.2.3. Over the whole reach, f_{oc} varied by three orders of magnitude with a geometric mean of 0.05 (5% g g^{-1}). The most carbon-poor sediments were associated with the surficial sand sequence with an average f_{oc} of 0.0106 (over all coring locations), reaching a maximum of 0.029 at SL4 and a minimum of 0.0014 at SL7

(Fig. 5.2.9). The lack of organic horizons at SL5 (Fig. 5.2.2) produced the lowest average f_{oc} for an individual core at 0.00983 (0.9% $g\ g^{-1}$). This carbon-poor zone in the stratigraphy can be seen clearly in Fig. 5.2.3. The peat deposits between SL6 and SL7, as well as SL2, SL3 and SL4 (Fig. 5.2.2) all had an f_{oc} greater than 0.2 (20% $g\ g^{-1}$) which is approximately 20-fold greater than the overlying sand. The site maximum f_{oc} of 0.39 occurred in the peat formation at a depth of 20–70 cm at SL7 (Fig. 5.2.2).

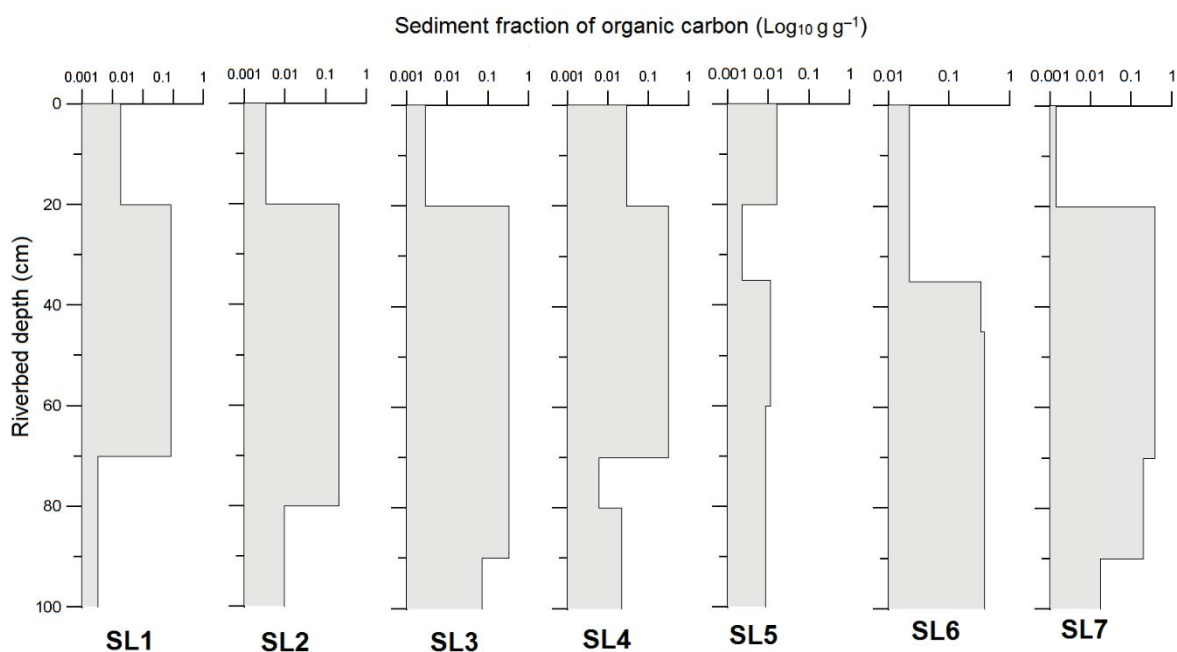


Fig. 5.2.3 Log_{10} -scaled mass fraction of organic carbon determined on core samples for the different sediment units, scaled by their measured thicknesses. Note the relatively carbon-poor zone at SL5. Refer to Fig. 5.2.1 for a comparison with the geological logs and Fig. 5.2.1 for the coring locations along the reach.

To provide a context for the sorption potential of the riverbed, it is useful to compare it with that of the underlying Permo-Triassic sandstone (PTS). In core samples from the LOCAR borehole array to the south of the investigated reach (Fig. 3.2.9, Chapter 3), Smith and Lerner (2008) determined an average f_{oc} of just 0.00035 (0.03% g g^{-1}) on ‘fresh’ core samples from the Bridgnorth Sandstone. This carbon content over two orders of magnitude less than the mean f_{oc} determined from the riverbed of the River Tern. For the relatively high energy fluvial sediments of the River Tame in Birmingham, Ellis and Rivett (2007) observed an f_{oc} range of 0.0008–0.092 from 15 core samples. The maximum f_{oc} observed in their investigation is still an order of magnitude lower than the maximum f_{oc} of the riverbed in this study.

5.2.1.4 *Retardation potential of the riverbed*

Using the equilibrium hydrophobic partitioning theory discussed in Section 2.3.2 of Chapter 2, it was possible to estimate a bulk coefficient of retardation (R) affecting TCE migration rates through the riverbed. The distribution coefficient (K_d) was calculated using Equation 2.3 (Chapter 2) with the f_{oc} values from the previous section and a literature estimate for K_{oc} of 94 ml g^{-1} for TCE. This is the geometric mean derived from a literature review provided in USEPA (1996) and used by Ellis and Rivett (2007) in their retardation calculations for TCE adsorption by the River Tame sediments in Birmingham. R could then be estimated with n and ρ values determined on the samples using Equation 2.4 (Chapter 2). To provide bulk estimates for each core taken from the riverbed, means were calculated for f_{oc} , n and ρ that were weighted by the thickness of the individual sediment units (Figs. 5.2.2 and 5.2.3). These weighted means and calculated R values are presented in Table 5.1. As a means of comparison, R was also calculated for the Bridgnorth Sandstone using the aforementioned f_{oc} measurements of Smith and Lerner (2008) with mean values for n and ρ collated from Streetly and Shepley (2005) which have previously

been used for modelling purposes. As can be seen from Table 5.1, the average retardation potential of the top metre of the riverbed is approximately 40-fold greater than that of the bedrock groundwater system beneath. The retardation capacity reaches up to 85 times that of the bedrock in the organic-rich sediment profile at SL3 (Fig. 5.2.2). This exceeds the ~50-fold greater retardation capacity of the bed sediments of the River Tame in comparison to the Birmingham PTS (based on the maximum R value of 66) derived by Ellis and Rivett (2007). This retardation capacity is similar to what Conant et al. (2004) determined for semi-confining deposits of silt and peat (R range of 22–88) at the Pine River site (Ontario, CA) where a PCE plume was discharging. However, PCE is more hydrophobic and more competitive for adsorption sites than TCE (Li and Werth, 2004).

As discussed in Chapter 2 (Section 2.3), a single value of K_{oc} for TCE is unlikely to be truly representative of actual sorption capacity, given the varying organic matter ages, provenances and molecular weights present along the plume flow paths. For example, the carbon present in the sandstone is of Permian age and will have undergone significant diagenesis since its original burial. In its unweathered form, this ‘hard’ carbon is likely to be kerogen-dominated and of a high molecular weight with the lowest oxygen/carbon ratios relative to the other organic matter types present. It is expected to be largely insoluble. Experimental evidence suggests this carbon will have the greatest sorption affinity (Grathwol, 1990; Huang and Peng, 2003) however, retardation by the sandstone will be negligible given its extremely low f_{oc} (Smith and Lerner, 2008). In contrast, the peat lenses are likely to be composed of ‘softer’ carbon characterised by greater oxygen/carbon and hydrogen/carbon ratios and a wider range of molecular weights. However, some microbially-mediated diagenetic changes may have taken place at certain locations since burial in the Holocene which may lead to significant spatial variability of

K_{oc} within the peat sequence. This organic carbon is likely to have a greater tendency to undergo solvation than the sandstone bedrock. The recent organic matter is most likely to be dominated by soft carbon characterised by amorphous humic substances where equilibration onset is rapid and isotherms are generally linear over wide concentration ranges (Allen-King et al., 2002). This carbon will be derived from allochthonous sources within the surface water catchment (such as the soil zone) and is likely to contain a large soluble fraction including low molecular weight labile species (Baker et al., 2000).

Table 5.1: Bulk sediment properties and calculated retardation coefficients for TCE in the top metre of the fluvial sediment sequence. The number of samples (n=) used for weighted mean calculations is given in parentheses

Location	Sediment lithology	f_{oc}	n	ρ	R
		(g g ⁻¹)	(v v ⁻¹)	(g cm ⁻³)	(-)
SL1	Sand, organic silt, sandy clay (3)	0.0593	0.28	1.38	28.6
SL2	Sand, organic silt, clayey sand (3)	0.144	0.24	1.51	85.9
SL3	Sand, peat, clay/sand (3)	0.2619	0.3	1.29	106
SL4	Sand, peat, coarse sand, silt (4)	0.1845	0.51	0.99	34.8
SL5	Sand, coarse sand, sandy clay, fine sand (4)	0.0104	0.2	1.72	9.3
SL6	Sand, peat, sandy peat (3)	0.2564	0.51	0.89	43.6
SL7	Sand, peat, sandy peat, clay (4)	0.2444	0.2	0.77	88.6
SL8	Sand (1)	0.007	0.2	1.88	7.2
Bridgnorth SST	<i>Unweathered Permo-Triassic sandstone</i>	0.0003 ^a	0.25 ^b	1.80 ^b	1.24

^a Sourced from Smith and Lerner (2008)

^b Sourced from Streetley and Shepley (2005)

5.2.2 Discrete observations of groundwater flow

Falling head tests were conducted to determine saturated hydraulic conductivity (K_s) in the riverbed piezometers of Transect S (Fig. 5.3.1 and Table 3.3, Chapter 3) around which temporary piezometers were installed in a nested configuration (see Section 3.3.4, Chapter 3). These temporary piezometers were deployed within a one metre radius of the Transect S piezometer with screened intervals open at depths of 10–20, 20–30 and 30–40 cm below the riverbed surface. The depths quoted in this section refer to the depth of the screen midpoint below the sediment-water interface. These tests were carried out from the 13th–16th of June 2013 during a baseflow period in which steady-state conditions were assumed. Average river stage, measured by the stage recorder at SL5 during this week was 58.67 m AOD with a gradual decline of 5 cm over the week from 58.71 to 58.66 m AOD.

5.2.2.1 Hydraulic conductivity variation

For the shallowest temporary piezometer level (15 cm), water levels responded too quickly in all but three of the locations (SL1, SL4 and SL7) to be accurately measure K_s . In most cases, this depth corresponded to the loose medium sand which drapes the underlying sediment sequence over much of the site (Figs. 5.2.1 and 5.2.2). Overall, K_s approached a log-normal distribution in the riverbed, according to the Shapiro-Wilk test of normality ($p = 0.03$), which is in accordance with that reported for other fluvial sediment sequences (e.g., Ellis, 2003; Ryan and Boufadel, 2007; Binley et al., 2013). The geometric mean ($n = 29$) K_s of the riverbed was 0.84 m d^{-1} with an overall observed range of $0.016\text{--}8.7 \text{ m d}^{-1}$. The frequency distribution of all riverbed K_s observations is given in Fig. 5.2.4A. The pattern of this distribution suggests a large degree of heterogeneity in hydraulic conductivity was present with approximately 45% values lying below the geometric mean. The depth distribution of the measured K_s is summarised in Fig. 5.2.4B. The shallower

observation levels displayed the greatest variation in K_s with a ranges of 0.03–2.25 m d^{-1} at 25 cm and 0.016–5.46 m d^{-1} at 35 cm. K_s increased below these depths but with a narrower range of values at 45 cm (2.5–8.7 m d^{-1}) and at 70 cm (0.54–3.15 m d^{-1}). Comparison of the log-transformed means of each depth interval using single-factor analysis of variance (ANOVA) revealed statistically significant differences ($p = <0.05$), as might be suspected from 5.2.4B. Post-hoc testing was completed using the Games-Howell method where unequal variances are assumed (Field 2006), based on a significant result for the Levene's test ($p = <0.05$). Pairings of depth interval means which showed statistically significant differences ($p = <0.05$) from one another included K_s between 25 cm (0.39 m d^{-1}) and 45 cm (5.05 m d^{-1}) as well as between 45 cm and 70 cm (1.19 m d^{-1}). These results indicate significant changes in riverbed hydraulic conductivity occur with depth with low but variable conductivity materials occurring in the shallower deposits which are underlain by generally more homogeneous and more conductive sediments beneath.

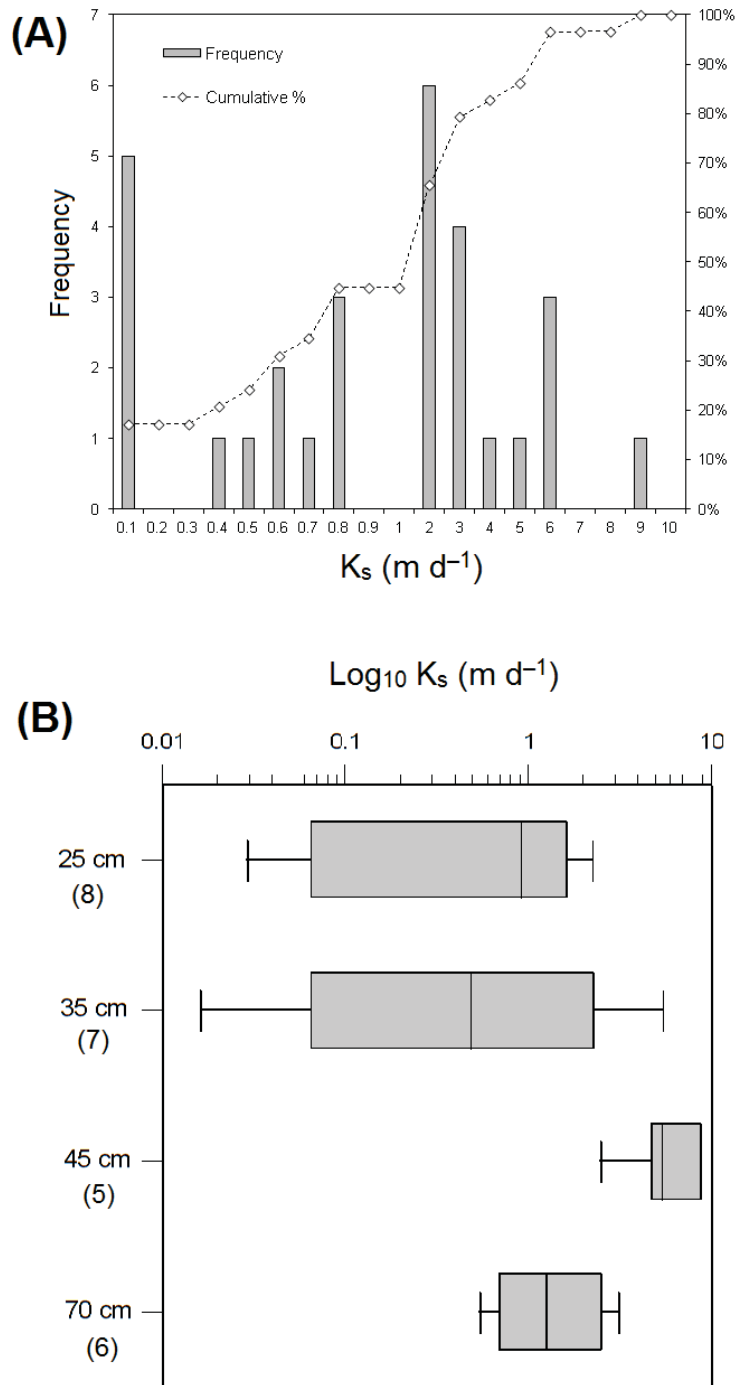


Fig. 5.2.4 (A) Cumulative frequency histogram of all hydraulic conductivity measurements in the riverbed ($n = 29$). (B) Box-plot summarising the \log_{10} -scaled hydraulic conductivity variation with depth in the riverbed. Note that the box-plots present a non-parametric summary of the data as quartiles with the max and min represented by the short vertical lines at each end, the interquartile range denoted by the shaded area and the median by the vertical line.

5.2.2.2 *Vertical hydraulic gradient observations*

Before falling head tests were carried out, static water levels were measured inside the piezometers with river levels measured on the outside of the tubes in order to compute the vertical hydraulic gradient (VHG) [m m^{-1}]. The VHG quantifies the pressure gradient between a river and a specific depth in the sediment sequence below (Kalbus et al., 2006) and is defined by Equation 5.1.

Equation 5.1
$$\text{VHG} = \frac{dh}{dl}$$

Where dh [m] is the difference between the river level outside the piezometer and the water level within the piezometer and dl [m] is the linear distance between the screened interval mid-point and the sediment-water interface. The VHG provides an indicator of the direction and magnitude of water flow through the riverbeds where a positive value indicates (potentially) groundwater upwelling conditions and negative values suggest downwelling of river water is likely. If no gradient is present, hydrostatic conditions exist where the relative intensities of upwelling groundwater pressure is balanced by that of infiltrating river water (Kalbus et al., 2006; Krause et al., 2012b). However, as Rosenberry and Pitlick (2009) point out, a positive (or negative) VHG does not necessarily indicate a hydrological connection is present as a confining layer may exist between the screened interval of the piezometer and the sediment-water interface.

All measured VHGs were positive in the riverbed indicating that potential groundwater upwelling conditions were present throughout the reach over all depths at the time of measurement. VHGs were found to be log-normally distributed based on the Shapiro-Wilk test of normality ($p = 0.46$) and the frequency distribution is given in Fig. 5.2.6A. As can be seen, the majority (60%) of VHGs observations were less than 0.3 with the lowest value of 0.01 recorded at SL6 at a depth of 25 cm which rose to just 0.07 at 85 cm depth at this

location in the riverbed. The depth-discrete variation of measured VHGs are summarised in Fig. 5.2.5B. The shallowest depth intervals (25 and 35 cm) displayed the narrowest range of pressure gradients (0.01–0.26 and 0.02–0.22 m m^{-1} , respectively). From Fig. 5.2.5B, a clear ‘stepped’ increase in VHG magnitudes was apparent from between 35 cm and 45–70 cm where the range substantially increased to 0.04–0.62 m m^{-1} (over the two depths intervals). A comparison of means from the different depth ranges using one-way ANOVA (after log-transformations) indicated statistically significant differences were present ($p = <0.05$). Post-hoc testing, this time using Scheffe’s method (Levene’s test $p = >0.05$), revealed that only the differences in mean VHGs measured at a depth of 25 (0.08 m m^{-1}) and 75 cm (0.3 m m^{-1}) were statistically significant ($p = <0.05$). These results indicate that, for much of the reach, a significant pressure gradient exists between the base of the riverbed and the river, which decreases substantially closer to the surface. At all locations, VHGs were observed to increase with depth; however, at SL3 a VHG of 0.26 was measured at 25 cm, which decreased to 0.2 at 35 cm (note that this exceeds the measurement uncertainty of ± 0.3 cm). The reason for this behaviour is unclear; however, it may be due to small-scale heterogeneity in sediment composition within the measurement radius of the temporary piezometers at this particular location.

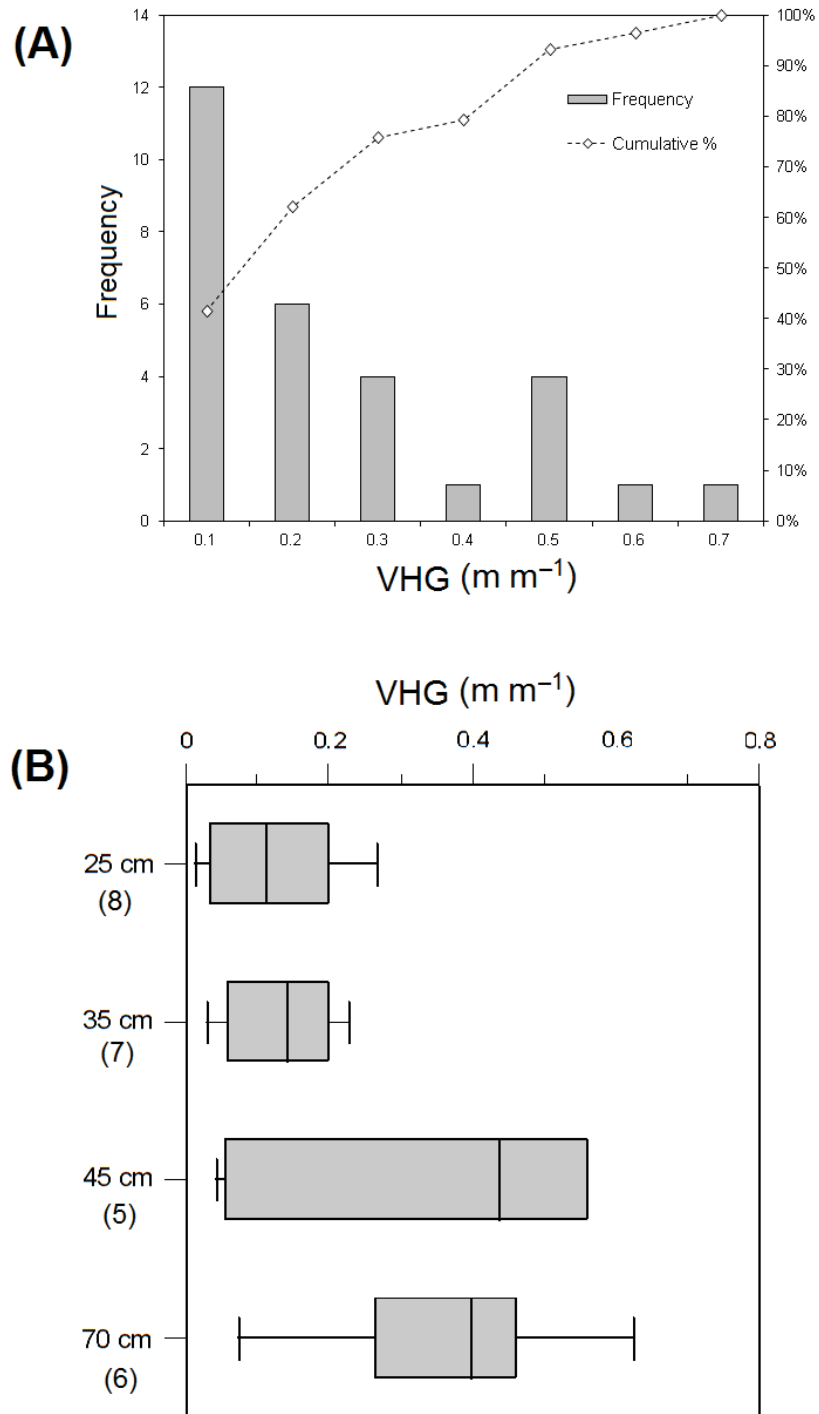


Fig. 5.2.5 (A) Cumulative frequency histogram of all vertical hydraulic gradient observations measured in the riverbed (n = 29). (B) Box-plot summarising the VHG variation with depth in the riverbed. Box-plots present a non-parametric summary of data as quartiles with the median represented by a vertical line. Note the significant increase in the vertical gradient below 35 cm.

5.2.2.3 *Spatial variability of hydraulic conductivity and pressure gradients*

Both the observed hydraulic conductivities and VHGs showed substantial longitudinal spatial variability within the top metre of the riverbed over the investigated reach (Fig. 5.2.6). A discontinuous, semi-confining horizon is suggested by the low K_s values at depths of 25 and 35 cm for the upstream part of the reach. For example, K_s at 35 cm (SL1 and SL4), and 25 cm (SL3), is $<0.1 \text{ m d}^{-1}$ with a range of 0.029–0.098 m d^{-1} . The prevailing pressure gradient appears to be modified by these low- K layers which probably gives rise to the stepped depth-distribution of VHG magnitudes. Other than the anomalous shallow variations at SL3 (as previously discussed), the other VHG depth profiles show a marked increase from 25 to 75 cm, suggesting local groundwater upwelling flow confinement resulting in steeper pressure gradients driven by regional groundwater discharge from the underlying PTS aquifer. A comparison with the riverbed stratigraphy (Fig. 5.2.1) recorded at these shallow depths indicates that these depths are associated with the upper ~ 20 cm of the organic/peat horizon just below the interface with the overlying medium sands. At SL5 and SL6, the hydraulic conductivity of the riverbed exceeds 0.5 m d^{-1} for all depths. From Fig. 5.3.5, it can be seen that the intensity of the vertical pressure gradient is markedly decreased in this area (e.g., <0.1) suggesting the semi-confining layer is absent. A comparison with the stratigraphy at this location (Fig. 5.2.1) supports this, given the absence of a significant horizon of organic material which correlates spatially with low K_s observations upstream. However, the stratigraphy at SL6 is dominated by peat and sandy peat, which is an order of magnitude more permeable than the upstream organic horizons (0.50–5.8 m d^{-1}). This indicates that the presence of peat in the stratigraphy does not guarantee decreased riverbed permeability. This location also had the lowest observed VHGs (<0.1) throughout the whole reach together with little apparent change with depth. This indicates an absence of a confining layer in the substratum in this area with relatively

permeable peat deposits. This is in marked contrast to the adjacent downstream piezometer at SL7 where the hydraulic conductivity of the peat drops to 0.065–0.16 m d⁻¹ (from 25 to 35 cm) with a linear increase in the VHG with depth from 0.09 at 15 cm to the site maximum of 0.63 at 83 cm. As is clear from Fig. 5.2.6, this produces a substantial longitudinal hydraulic gradient which suggest upwelling groundwater flow in the opposite direction to surface water flow direction. This pattern also suggests the presence of a confining layer from 25–35 cm in the streambed stratigraphy, similar to that in the upstream reach. Hydraulic conductivity was greater than 1 m d⁻¹ in the area of SL8 suggesting an area of potentially enhanced groundwater discharge given the substantial VHG in this area (0.2 at 25 cm and 0.56 at 45 cm). However, in the absence of detailed stratigraphic information for this piezometer, the presence of a local confining layer present between sampling depths cannot be ruled out.

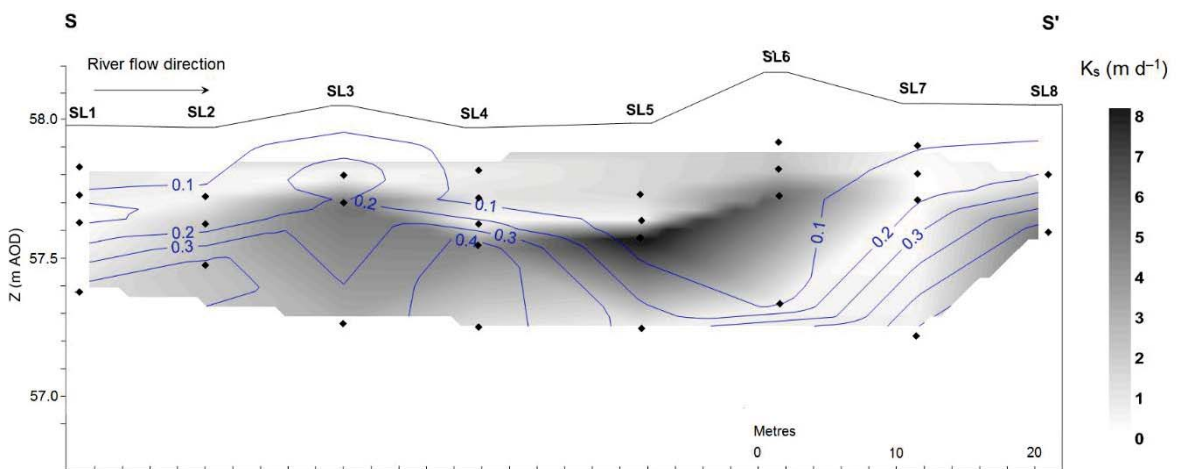


Fig. 5.2.6 Longitudinal spatial variability of hydraulic conductivity and vertical hydraulic gradients (blue lines) interpolated using triangulated linear interpolation. Black dots indicate the discrete depth measurement locations. Note the areas of reduced hydraulic conductivity at SL7 and from 57.6–57.8 m AOD from SL1 to SL4. Also note the area of reduced vertical head gradient centred below SL5 and SL6 which approximately coincides with the increased hydraulic conductivities at ~57.6 m AOD.

5.2.3 Continuous monitoring of riverbed pressure gradients

5.2.3.1 Temporal variability of hydraulic heads and river stage

River stage and riverbed hydraulic head time series were measured automatically at 30 minute intervals at the 8 locations of Transect S (Fig. 5.2.1) over a 62-day period from the 21st of May 2013 through to the 21st of July 2013 (Fig. 5.2.7). SL4, SL5 and SL6 were dual installations with deep and shallow level piezometers (Table 3.3, Chapter 3). Daily rainfall was measured at Child's Ercall synoptic station (5 km SW of the site, Met Office ID 431325) and mean daily flow in the River Tern (Environment Agency, 2013; unpublished data) was measured at Ternhill gauging station situated approximately 5 km upstream of the study reach (see Fig. 3.2.1, Chapter 3). The average daily mean flow in the River Tern over the 62 day monitoring period was gauged at $0.635 \text{ m}^3 \text{ s}^{-1}$ with a peak flow of $1.33 \text{ m}^3 \text{ s}^{-1}$ occurring on the 29th of May and a minimum flow of $0.451 \text{ m}^3 \text{ s}^{-1}$ recorded on the 20th of July 2013 (Fig. 5.2.7A). A total of 63 mm of rainfall fell during the observation period with a significant event notable on the 28th of May where a total of 15 mm fell within 24 hours (Fig. 5.2.7A). Several additional rainfall events were also recorded in July, however, these did not produce major discharge responses (Fig. 5.3.3A). These flow conditions are representative of the typical spring/summer baseflow recession period in the River Tern (Hannah et al., 2009; Krause et al., 2011b) interspersed with some short-duration rainfall events. Mean daily flow in the river was generally below the long-term average for the Ternhill station ($0.9 \text{ m}^3 \text{ s}^{-1}$) and approached the Q₉₅ of $0.4 \text{ m}^3 \text{ s}^{-1}$ (Marsh and Hannaford, 2009) at the end of the observation period.

Hydraulic heads, measured in the deep piezometers for the upstream reach (SL1–SL4A) (Fig. 5.2.7B) were all consistently above the river stage which was indicative of

continuous, groundwater upwelling conditions with heads showing similar patterns of temporal variability to river water levels. A relatively narrow range of head distribution was observed over the 4 upstream piezometers with an average difference of 12 cm maximum of 55 cm. SL4A showed the greatest hydraulic head in this section of the riverbed reaching a maximum of 59.35 m AOD with an average head difference of 31 cm between the river stage and the fluvial sediments at 72 cm (screen mid-point). SL2 displayed the lowest hydraulic head in the upstream reach with a minimum of 58.7 m AOD and an average head difference of 19 cm between the river level elevation and 48 cm depth in the sediment sequence. The hydrograph for SL1 showed some anomalous temporal patterns such as a gradual rise in head in the days after immediately after installation together with some short and rapid fluctuations in mid-June. The reason for this behaviour is not known. The late-May rainfall event produced a rise in river stage of ~38 cm over a period of approximately 12 hours with river level returning to pre-event levels after 3 days. This event produced a corresponding rise in piezometer heads ranging from 24 cm for SL4A to 27 cm at SL3. Although there is no evidence of any potential surface water infiltration to the deep riverbed zone in any of the hydrographs for the late May rainfall event, it is clear that head differences were reduced to a minimum of approximately 5 cm on the rising limb of the flow event for the 12 hour period preceding the peak flow.

In the downstream reach, a significantly greater range in hydraulic heads was observed between the piezometers (Fig. 5.2.7C). A minimum head level was observed at piezometer SL6A (58.65 m AOD) at a depth of 85 cm in the riverbed with a maximum head observed in the adjacent piezometer, SL7, (59.54 m AOD) at 83 cm depth, forming the area of maximum hydraulic head observed in all piezometers. The maximum range of observed heads for the downstream reach was 89 cm with an average range between piezometers of

44 cm over the 62-day period. For most locations, groundwater heads were above river stage with an average difference of 25 cm. However at SL6A, for approximately 3 days surrounding the late May rainfall event, the head difference between the piezometer and river level ranged from ~1–0 cm indicating that groundwater pressure and surface water hydrostatic pressure were in near balance as far as 85 cm into the riverbed sediments. Given that the uncertainty in the pressure transducer measurements is ± 1 cm, the possibility of potential surface water downwelling is not excluded to this depth in the riverbed. The inclusion of an additional shallow piezometer at SL4, SL5 and SL6 (Fig. 5.2.7D–F) permitted the simultaneous observation of hydraulic heads at two depths around the meander bend area (Fig. 5.2.1). SL4A and SL4B showed that the hydraulic head at a depth of 42 cm in the sediment sequence (SL4B) was significantly greater than river stage with an average difference of 17 cm with no evidence of flow reversal during the rainfall event in May. This contrasts with SL5B where river stage exceeded the hydraulic head in the piezometer by several cm for approximately 3 days surrounding the flow event. This is indirect evidence of potential river water downwelling to a depth of 41 cm (screen mid-point) into the sediment profile at this area. The hydraulic head at SL6B was markedly similar to that of SL5B with groundwater head and river stage very closely aligned with, typically, only 1–3 cm greater head difference at 44 cm deep in the riverbed. A similar pattern of pressure gradient reversal was observed at this piezometer location as at SL5B during the event flow. Given the weak pressure gradient observed at the deeper piezometer level, SL6A (as already discussed), potential infiltration of river water to a depth of 85 cm into the riverbed was possible at this part of the reach. Cuthbert et al. (2010) observed similar transient gradient reversals of comparable duration during storm flows in the River Tame in Birmingham.

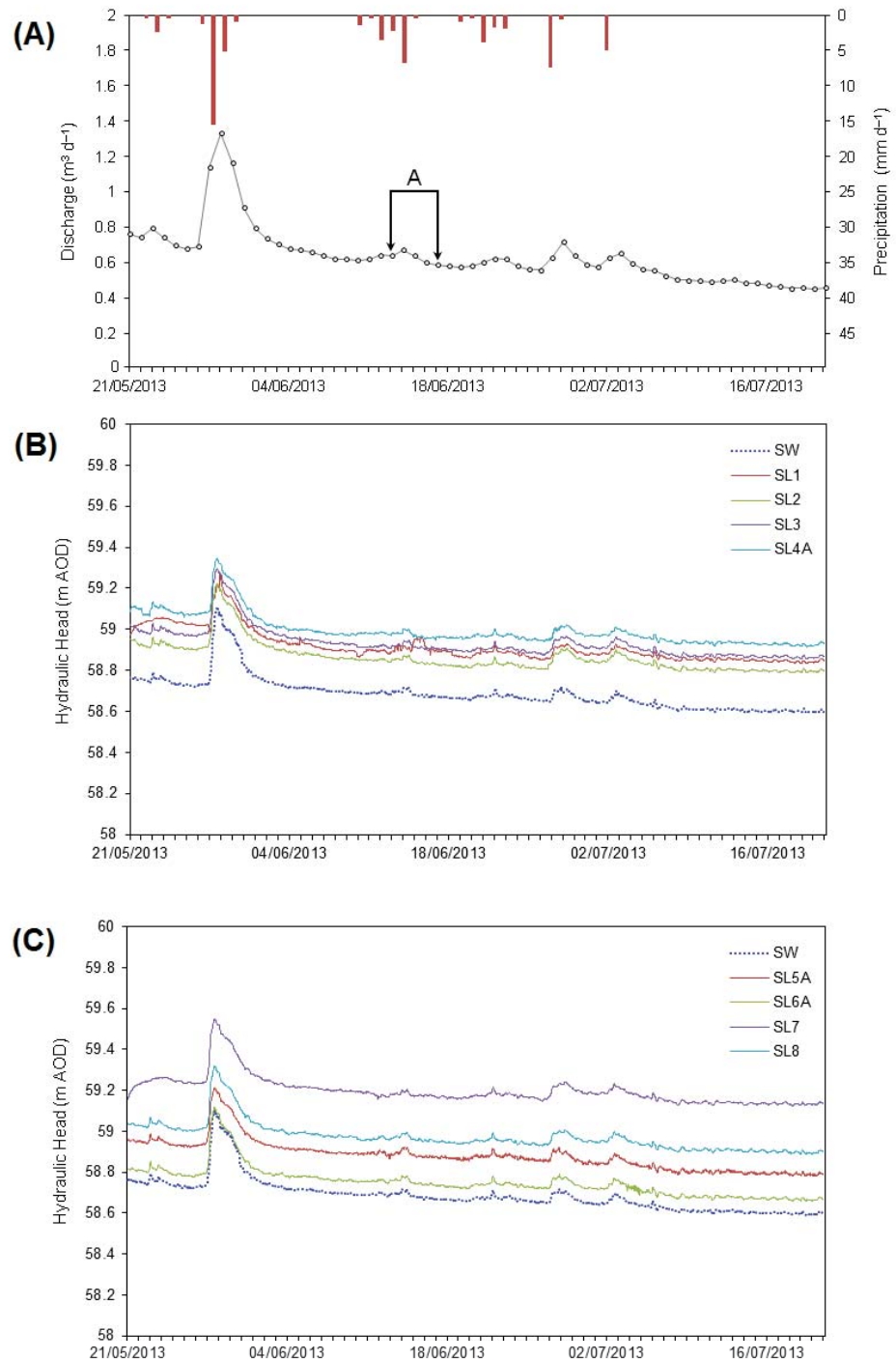


Fig. 5.2.7 Temporal variability of hydraulic head and river stage over the 62-day monitoring period. See Fig. 5.2.1 for location of the piezometers. **(A)** Mean daily flow for the River Tern at Ternhill and the daily total precipitation for the Child's Ercall rainfall station. **(B)** Upstream piezometer hydrographs and surface water stage (measured at SL5) **(C)** Downstream piezometer hydrographs in comparison to the river water levels (SW). Heads corrected for average river stage gradient along the transect upstream and downstream of SW. Error bars omitted from data points for clarity. Time period labelled 'A' marks the week where the discrete measurements were carried out in Section 5.2.2

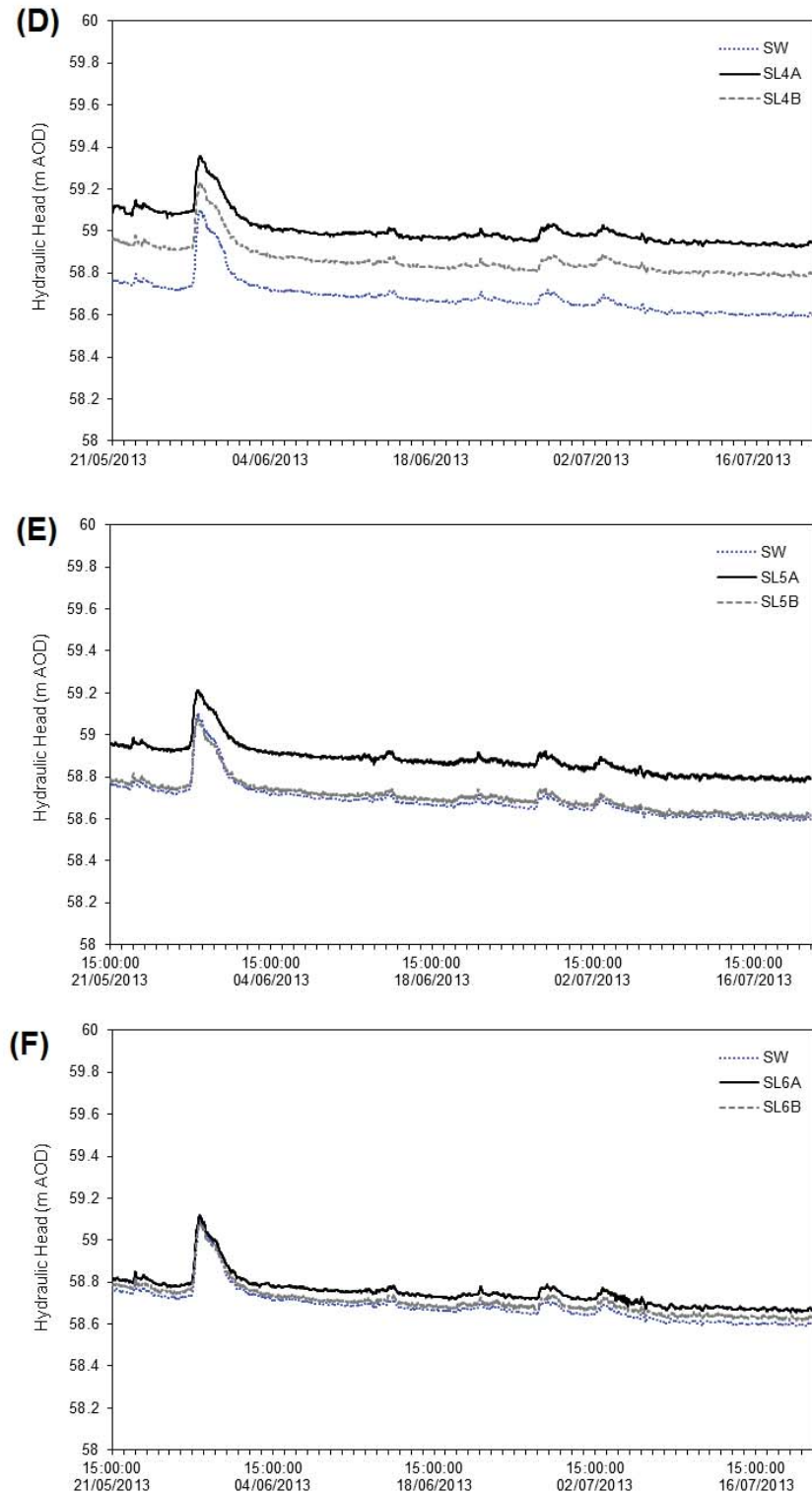


Fig. 5.2.7

Contd. Dual level piezometer hydrographs and river stage (SW) at (D) SL4, (E) SL5 and (F) SL6. Error bars omitted from all figures for clarity. Deep piezometer levels are labelled 'A' with corresponding shallow levels identified as 'B' for each location. Heads corrected for average river stage gradient along the transect upstream and downstream of SW. See Fig. 5.2.1 for location of the piezometers along the reach.

5.2.3.2 *Temporal variability of the VHG in the riverbed*

The continuous monitoring of both river stage and subsurface hydraulic heads allowed the variability of the VHG to be determined in high temporal resolution which represents the primary driver of contaminant discharge along the plume-impacted reach. Fig. 5.2.8 summarises the observed variability of VHG measurements for each piezometer location, illustrating the predominant direction and magnitude of the pressure gradient along the reach. As indicated by the discussion in the previous section, the upstream reach (SL1–SL4) was characterised by strong, positive VHGs at a depth range of 48 cm (SL2) to 80 cm (SL3) where the minimum VHG did not drop below 0.2 (m m^{-1}) apart from at SL1 where the highest range of 0.38 was observed. Median VHGs were approximately similar (~ 0.4) for SL1, SL2 and SL4, however, at SL3 the median VHG was reduced to 0.34 and the interquartile range around the median reduced to 0.02. This suggests that upwelling groundwater pressure was relatively constant in the area of SL3. At SL4, the shallow and deep piezometer levels displayed similar VHG variations, suggesting that groundwater upwelling pressure was relatively uniform over the two depths. A different pattern was observed at SL5, however. The interquartile range was extremely narrow (< 0.01) for the deep level (SL5A) with a median value comparable to that of the minimum VHG seen between SL2 and SL4. The gradient reversal suggested by the hydraulic head time series could be quantified with a maximum negative VHG of -0.06 recorded at 42 cm depth at SL5B, suggesting downwelling conditions were likely. Both the shallow and deep piezometers at SL6 showed comparable median VHGs of < 0.1 with a similar maximum negative VHG of -0.07 recorded at SL6B. It can be seen that the interquartile range of SL5A to SL6B is greatly restricted when compared to the other locations. This is likely to be due to the close coupling of surface water stage and groundwater hydraulic heads in this section of the reach as evident in the time-series plots (Fig. 5.2.7). It is clear from these

observations at SL5 and SL6 that groundwater upwelling pressure is weaker than the rest of the reach and a relatively modest flow event in the river capable of overcoming groundwater discharge resulting in a gradient reversal. At SL7 and SL8, the VHG variability is comparable to that observed at SL1–SL3 but with stronger upwelling pressure conditions indicated by the higher median values (~ 0.58) for each location.

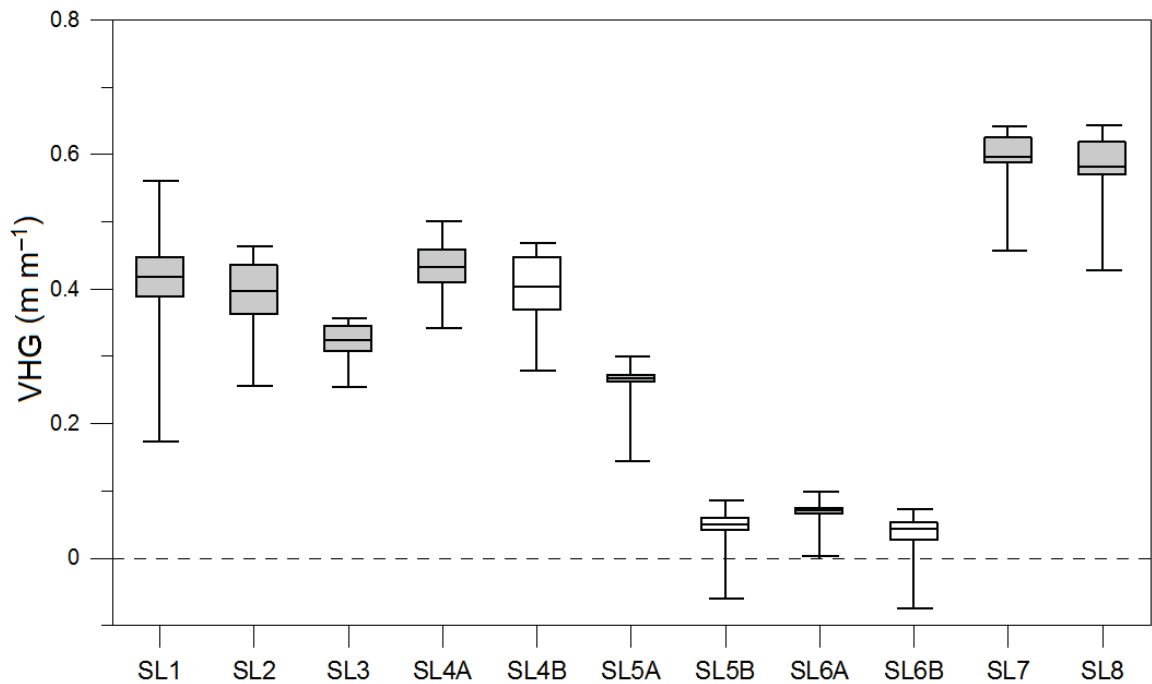


Fig. 5.2.8 Box-plots summarising the observed variability of the VHG measured for all piezometers over the 62-day monitoring period ($n = 2,929$). Box-plots present a non-parametric summary of data as quartiles with the median represented by a vertical line. The grey boxes represent interquartile ranges for the deeper piezometer levels and the white boxes show the interquartile ranges of shallow levels. The dashed line indicates where the VHG is zero and hydrostatic conditions are present where no pressure gradient exists in either direction. Most VHG signals are strongly positive indicating a strong groundwater upwelling potential. However, negative gradients are observed for SL5B and SL6B indicating the potential for flow reversal (cf. Fig. 5.2.7).

5.3 Groundwater and contaminant fluxes through the riverbed

5.3.1 Groundwater flux based on Darcian flow

5.3.1.1 Darcy flux approach

From the discrete measurements of K_s (Fig. 5.2.4B) and the VHG (Fig. 5.2.5B) presented in Section 5.2.2, it is possible to estimate the 1-D vertical groundwater flux (q_z) [$L d^{-1} m^{-2}$] (also known as the specific discharge) through the riverbed at each piezometer location using Equation 5.2 (Blume et al., 2013) based on Darcy's law (Darcy, 1856).

Equation 5.2
$$q_z = -K_s \cdot VHG \cdot 1000$$

However, because the total volumetric groundwater discharge (Q_z) [$L d^{-1}$] along the reach drives the mass flux from the groundwater plume to the river, an area term must be added to Equation 5.2. This was accomplished by field measurement of the riverbed seepage area (A) along the 72.5 m reach covered by the Transect S piezometers (Fig. 5.3.1), completed during the temperature mapping (discussed in later sections). The Transect S piezometers were installed along the reach at 10 m stations. Using the northern riverbank as a reference bank, the river channel width (y) [m] was measured along 2.5 m increments (x) [m] from SL1 to SL8, thereby subdividing the groundwater seepage area of the riverbed (total measured area 332.5 m²) into 30 discrete sections (with areas of 7.5–12.5 m²). This allowed Q_z to be calculated using the Equation 5.3.

Equation 5.3
$$Q_z = \sum q_z \cdot (x \cdot y)$$

However, because q_z was measured at 8 locations along the reach (which have been subdivided into 30 sections), a linear interpolation of K_s and VHG between measurement points was undertaken in order to ‘up-scale’ the flow term (Blume et al., 2013) for the whole reach (see Appendix B for full calculations). In addition, because both K_s and the VHG were measured at multiple depths (Section 5.2.1), it was possible estimate Q_z from the perspectives of shallow and deep seepage areas in the riverbed (Appendices B1 and B2). The input parameters for these two depth perspectives are given in Table 5.2.

Table 5.2 Input parameters for the Darcy flux estimates from the perspectives of a shallow and deep seepage area. ‘n’ is the number of values used in the calculation (see Appendix B for full calculations).

Parameter	Unit	n	Range
<i>Shallow seepage area</i>			
Flux depth	cm	–	25
K_s	m d ⁻¹	11	0.1–2.5
VHG	m m ⁻¹	8	0.13–0.26
<i>Deep seepage area</i>			
Flux depth	cm	–	44-85
K_s	m d ⁻¹	29	0.05–3.36
VHG	m m ⁻¹	8	0.07–0.63

For the shallow flux estimate, K_s and the VHG measured at the 25 cm depth interval of the temporary piezometers were used. For the deeper flux, these parameters measured at the deepest piezometers of Transect S were applied. The harmonic mean of K_s was used to average multiple observations of K_s along the vertical distance to the sediment/water interface. The harmonic mean is often seen as a better measure of central tendency for hydraulic conductivity in riverbeds where vertical flow is dominant (Binley et al., 2013). In order to compute the flux, two assumptions were made about the boundary conditions of riverbed flow regime. (1) Groundwater flow was vertical and no exchange occurred with

the river water or riparian groundwater, (2) K_s and VHG were distributed uniformly over the sub-divided seepage area. Fig. 5.3.1 provides a conceptual schematic of this approach.

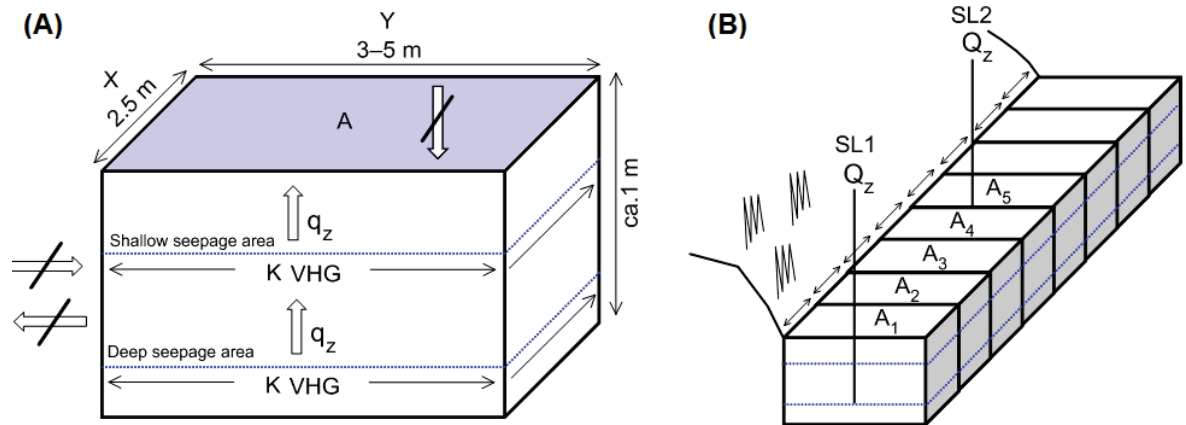


Fig. 5.3.1 Conceptual schematic illustrating how Q_z was interpolated over the reach. (A) Individual groundwater seepage area measured in the field (x, y) with assumptions about the boundary conditions of the flow regime. (B) Illustration of how up-scaling of measured fluxes was achieved over the whole reach.

5.3.1.2 Potential groundwater fluxes

For the shallow seepage area with a uniform depth of 25 cm (the piezometer screened interval mid-point), the spatial average q_z was calculated at $70 \text{ L d}^{-1} \text{ m}^{-2}$ with a standard deviation of $40 \text{ L d}^{-1} \text{ m}^{-2}$. The maximum observed flux of $214 \text{ L d}^{-1} \text{ m}^{-2}$ was calculated for the most downstream piezometer, SL8. Over the whole reach, the daily total groundwater baseflow discharge (Q_z) was calculated to be in the region of $23,230 \text{ L d}^{-1}$ ($23.2 \text{ m}^3 \text{ d}^{-1}$) or approximately 270 mL s^{-1} . For the deep seepage area with a variable depth (Table 5.2), the calculated spatial average q_z increased by a factor of 4 to $260 \text{ L d}^{-1} \text{ m}^{-2}$ with a standard deviation of $210 \text{ L d}^{-1} \text{ m}^{-2}$ with a very high maximum flux of $1,000 \text{ L d}^{-1} \text{ m}^{-2}$ calculated for SL8. The resultant total daily Q_z from the perspective of the Transect S deep piezometers was estimated to be $86,440 \text{ L d}^{-1}$ ($86.4 \text{ m}^3 \text{ d}^{-1}$), giving an instantaneous flow rate of approximately 1 L s^{-1} over the 72.5 m reach investigated. Fig. 5.3.2 presents these

fluxes as they were interpolated over the reach between SL1 and SL7. Comparison with Fig 5.2.6 illustrates the controls on groundwater discharge over the reach. From Fig. 5.3.2, It can be seen that SL8 dominates the groundwater discharge to the river at both depths where both the hydraulic conductivity ($>1 \text{ m d}^{-1}$) and pressure gradient ($0.2\text{--}0.55 \text{ m m}^{-1}$) are elevated. Conversely, at SL1, although the pressure gradient is significant (0.45 m m^{-1}), the effective hydraulic conductivity is low (0.17 m d^{-1}) and the resulting flux is reduced. It is important to note that these estimates represent potential fluxes and the true groundwater discharge may not reflect the potential flux. Unseen heterogeneities (such as confining layers) may be present which restrict actual discharge rates (Rosenberry and Pitlick, 2009; Kaser et al., 2009).

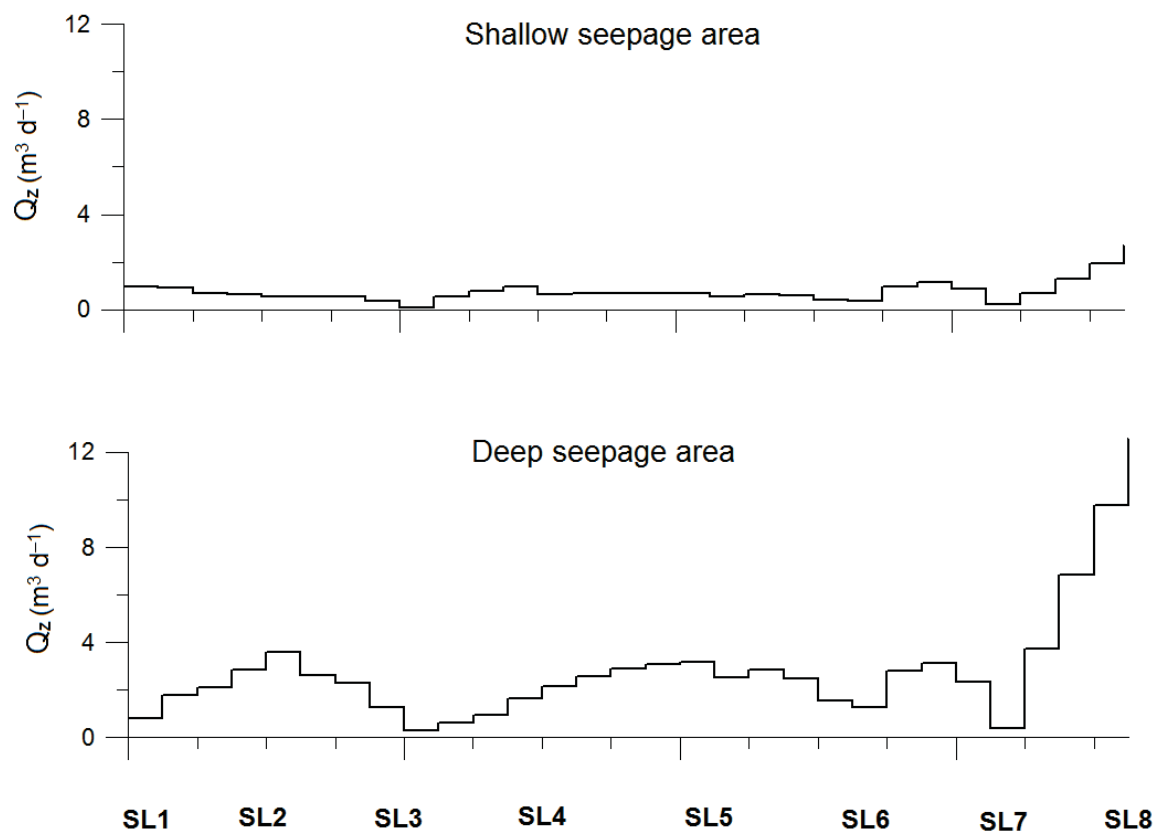


Fig. 5.3.2 Calculated Q_z (expressed in $\text{m}^3 \text{d}^{-1}$), distributed spatially along the 72.5 m reach using the interpolation procedure outlined, from the perspectives of hydraulic conductivity and pressure gradients measured at shallow and deep points in the top metre of the riverbed.

5.3.2 Groundwater flux based on temperature profiling

5.3.2.1 Depth-distribution of temperature

Riverbed temperature mapping was completed over the 3rd (12:00–19:00) and 4th (10:00–12:30) of September 2013 during a period of low flow in the river. Air temperature (measured at the well head of Heathbrook East) ranged from 13.6–14.4°C over the survey period. River water temperatures fluctuated diurnally with a total range of 1 °C (a low of 14.5 °C and high of 15.5 °C with an average of 15.9 °C). Fig. 5.3.3 provides a summary of the observed temperature gradients in the riverbed, in comparison to the groundwater and surface water end-members. Groundwater temperatures were measured at the start of the campaign (12:00 on the 3rd of September) in SL1–SL8 at depths of 60–100 cm (base of the piezometer screens) and at Heathbrook West (12 m depth) showed a narrow range in variability from 9.8 °C (at Heathbrook West) to 10.4 °C (at SL5). Repeat temperature measurements at end of the survey (13:00 on the 4th of September) showed no significant differences to the previous day (e.g., $<\pm 5\%$). Riverbed pore water temperatures measured at 10 and 20 cm depth at 122 individual locations in the riverbed exhibited ranges intermediate to that of the surface water and groundwater values (Fig. 5.3.3). At 10 cm, riverbed temperatures ranged from 11.6–15.0 °C with a median of 13.9 °C. At 20 cm, the observed temperature range was comparable to that at 10 cm with minimum of 10.8 °C and maximum of 14.7 °C. However median temperatures were lower by approximately 0.5 °C at 13.4 °C and 13.2 °C, respectively. From these data, the maximum temperature difference between groundwater and surface water end-members, throughout the survey period, was 5.7 °C as measured from groundwater at a depth of ~12 m in the Permo-Triassic aquifer (Heathbrook West). A similar difference (5.4 °C) is observed from the 87 cm depth of SL4 indicating that near-isothermal conditions exists in the aquifer at greater

than ~1 m depth. Therefore, at the time of measurement, it is apparent that cold patches of the riverbed indicated areas of groundwater discharge where river-aquifer connectivity is locally enhanced, together with potential for TCE discharge. Conversely, where little or no temperature gradient was present, a disconnection between river and aquifer was likely.

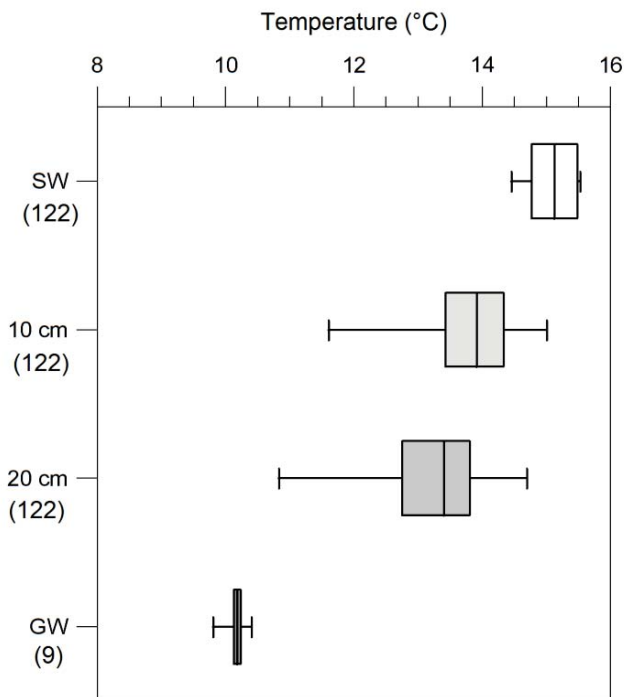


Fig. 5.3.3 Box-plots summarising the observed temperature distribution between the river water and groundwater. Note that box-plots present a non-parametric summary of the data as quartiles with the median represented by a vertical line. Groundwater temperatures are those of the Transect S piezometers (deep levels only) and the Heathbrook West observation borehole screened within the bedrock aquifer.

5.3.2.2 *Spatial patterns of pore water temperature*

High-resolution riverbed temperature mapping was conducted along 23 cross-channel transects (T1–T23) where temperatures were measured at 1 m intervals across the channel. Each temperature traverse was collected perpendicular to the bank with readings every 2.5 m along the length of the channel, as measured from the outside bank (Helshaw Grange).

The armoured gravel/cobble section between SL5 and SL6 and downstream of SL7 (Fig. 5.2.1) prevented the insertion of the probe to more than ~8 cm into the sediment and these data were excluded.

Fig. 5.3.4 visualises the plan-view spatial variability of measured riverbed temperature at (A) 10 cm and (B) 20 cm depth within the survey reach. For both depths, spatial patterns of temperature distribution were consistent and were observed to decrease with depth from 10 cm to 20 cm at all locations. A discrete cold area of the riverbed (approximately 10 m in length and 1–2 m wide) was observed between SL1 and SL2 in a bank-parallel orientation. From transects T2–T4 at 10 cm and T1–T5 at 20 cm, temperatures dropped to <11.5 °C in this area. From SL2/T5 this thermal pattern was observed in reverse with a distinct cold area located along the northern bank (Helshaw Grange) extending approximately 10 m downstream as far as SL3/T9. The coldest part of this section was located at T7 and T8 with minimum temperatures of <11.5 °C, observed at 20 cm depth. The opposite (southern) bank along this section (T7–T9) was characterised by relatively warm pore water temperatures with a range of 13.5–14.5 °C observed at 20 cm. A relatively homogeneous area of riverbed temperature was observed over the 10 m reach between SL3 and SL4 with a continuation of the relatively warm zone along the southern bank at Heathbrook Farm, evident as far downstream as T15. Two cold areas (<12.5 °C) were observed at the head of the meander bend between SL4 and SL5 at T13–T14 and T16–T17. These two zones were located at comparable positions just south of the channel mid-point in this section of the reach. A significant lateral thermal gradient was observed at the Heathbrook Farm end of T14 where temperatures dropped 2 °C over a distance of 1 m along the transect. In the area of T16–T18, the north-eastern half of the channel (0–3 m transect positions) showed a relatively homogeneous spatial distribution of temperatures

with a range of 13.5–14 °C over both depths. Between SL6 and SL7, considerable spatially heterogeneity in the pore water temperature distribution was observed with several discrete cold zones located at T20/T21 along the eastern bank and at T22 on the western side of the channel.

The riverbed thermal anomaly (ΔT) allows the magnitude of temperature differences to be examined and is calculated as the difference in average surface water temperature from pore water temperature (at 20 cm). ΔT is interpolated spatially over the reach in Fig. 5.3.4C. The spatial patterns are similar to that of Fig. 5.3.4B with distinct longitudinal zones with a ΔT of >3 °C associated with margins of the riverbed between SL1 and SL3, parallel to the banks. These are juxtaposed by a distinct area with a very low ΔT (<0.5 °C) which is approximately continuous along the Heathbrook Farm bank from T7 as far downstream as T15. Additional areas with a weak temperature gradient (<1 °C), which cover comparatively large areas of the riverbed, are identifiable between SL3 and SL4 as well as to the north west of SL5. The riverbed thermal anomaly becomes more complex in the area between SL6 and SL7 with several discrete anomalies (>2.5 °C) observable on the scale of metres together with weak gradient zones (<1 °C) associated with T22 and T23 adjacent to the Heathbrook Farm bank.

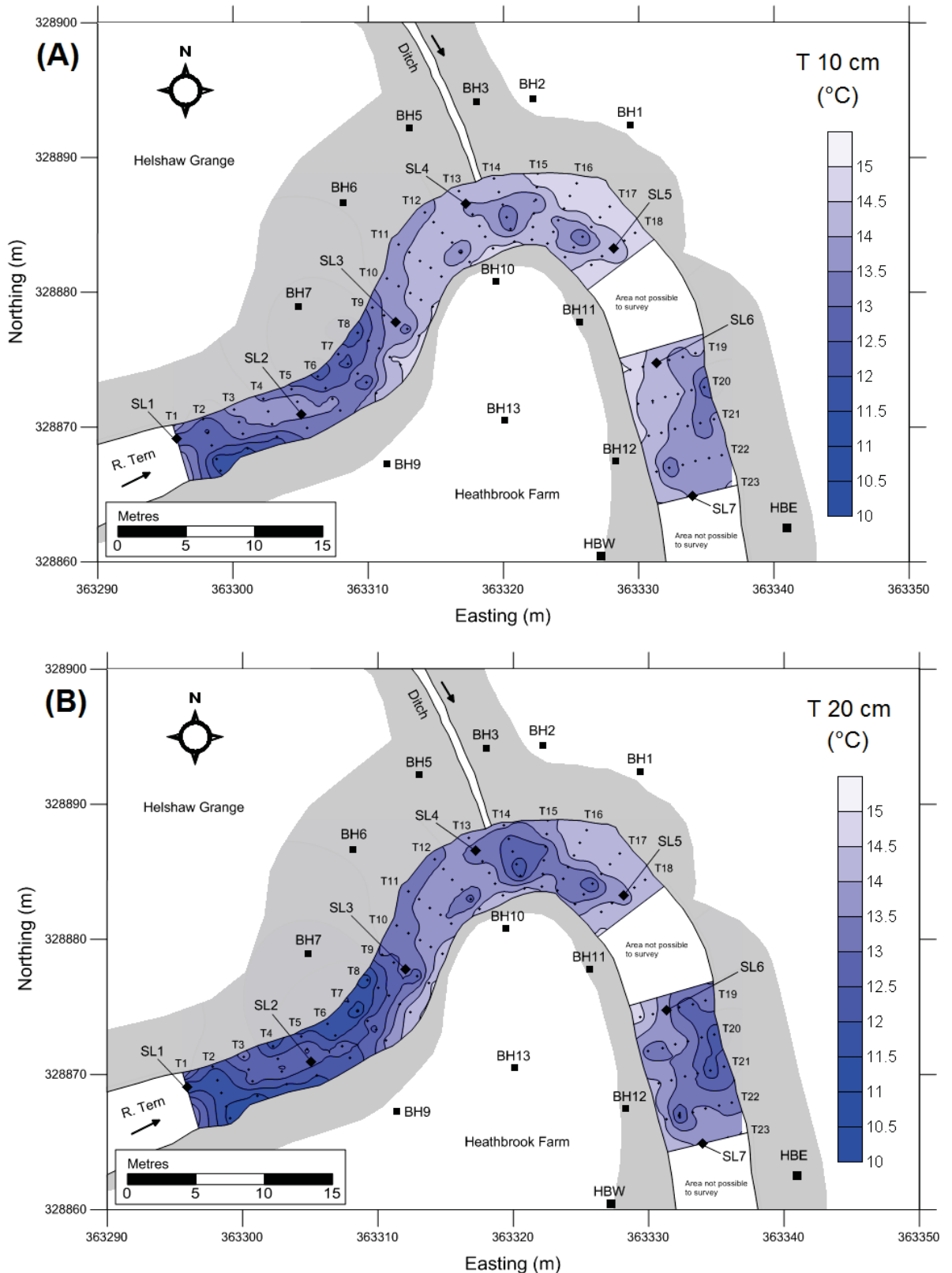


Fig. 5.3.4 Spatial variability of pore water temperature distribution (interpolated using Kriging) at a depth of (A) 10 cm and (B) 20 cm in the riverbed. Measurement locations are denoted by the black dots. Note the significant cold patches which are indicative of groundwater discharge areas (during summer conditions), concentrated between SL1 and SL3.

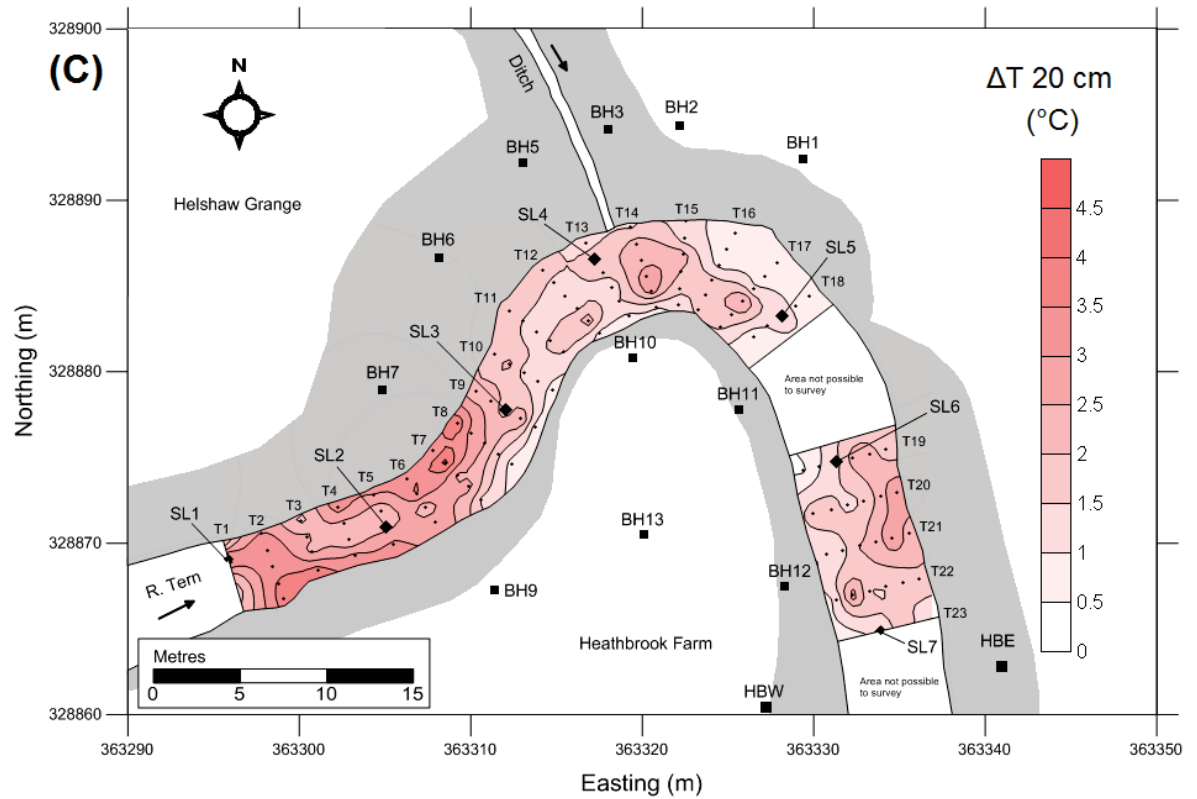


Fig. 5.3.4 Contd. (C) Spatial variability of the riverbed temperature anomaly (interpolated using Kriging) at 20 cm depth. Measurement locations are denoted by the black dots. The magnitude of the temperature differences can be visualised where a greater difference indicates stronger groundwater discharge through the riverbed.

5.3.2.3 Calculated groundwater flux

An estimate of the vertical Darcy flux (q_z) [$L\ d^{-1}\ m^{-2}$] may be derived from temperature gradient profiling through the application of an analytical solution (Stallman, 1965; Tuncotte and Schubert, 1982) to the 1-D steady-state heat transport equation for advection and diffusion (Schmidt et al., 2006; 2007). Equation 5.4 is provided by Schmidt et al. (2007) with full calculations included in Appendix C1.

$$\text{Equation 5.4} \quad q_z = \frac{K_{fs}}{\rho_f c_f z} \cdot \ln \frac{T_z - T_L}{T_0 - T_L} \cdot 1000$$

Where K_{fs} is the saturated thermal conductivity [$J\ s^{-1}\ m^{-1}\ K^{-1}$] of the riverbed, $\rho_f c_f$ is the volumetric heat capacity of water ($4.19 \times 10^6\ J\ m^{-3}\ K^{-1}$, Schmidt et al., 2007), T_z is the

temperature at depth z [$^{\circ}\text{C}$], T_L is the lower boundary condition (where temperature is constant) and T_0 is the upper condition (river water temperature). Schmidt et al. (2007) stipulates two assumptions for the use of Equation 5.4. (1) Quasi-steady-state temperature conditions exist at depth z , (2) the Darcy flux is vertical. Diurnal temperature oscillations have been shown to not significantly influence riverbed temperatures at depths much greater than 15 cm for gaining streams (Conant, 2004; Schmidt et al., 2006; Kalbus et al., 2007). Therefore, the 20 cm mapping depth was selected as T_z with the temperature at Heathbrook West ($9.9\text{ }^{\circ}\text{C}$) used for the lower boundary condition (T_L) and T_0 represented by the average surface water temperature ($15.1\text{ }^{\circ}\text{C}$) measured throughout the campaign. A constant value of $1.45\text{ J s}^{-1}\text{ m}^{-1}\text{ K}^{-1}$ was utilised for K_{fs} . This value was used in a previous riverbed flux estimation at a site with comparable sediment type (medium sand), clast mineralogy (predominantly quartz) and total porosity (~ 0.3) (Conant, 2004; Schmidt et al., 2007; Abe et al., 2009). In addition, the range of values of K_{fs} for saturated sediments is known to be small (Stonestrom and Constantz, 2003) with published estimates considered to be satisfactory for flux estimation purposes (Schmidt et al., 2006).

Calculated q_z at 20 cm is presented in Fig. 5.3.5 with all fluxes shown together with the observed groundwater and surface water temperature ranges. Upper and lower boundary conditions are represented by the solid lines. For the majority of data points, the calculated fluxes are less than $100\text{ L d}^{-1}\text{ m}^{-2}$. As might be expected from Equation 5.4, the calculated fluxes plot on a second-order polynomial curve which becomes asymptotic as temperatures approach either the groundwater or surface water boundary condition.

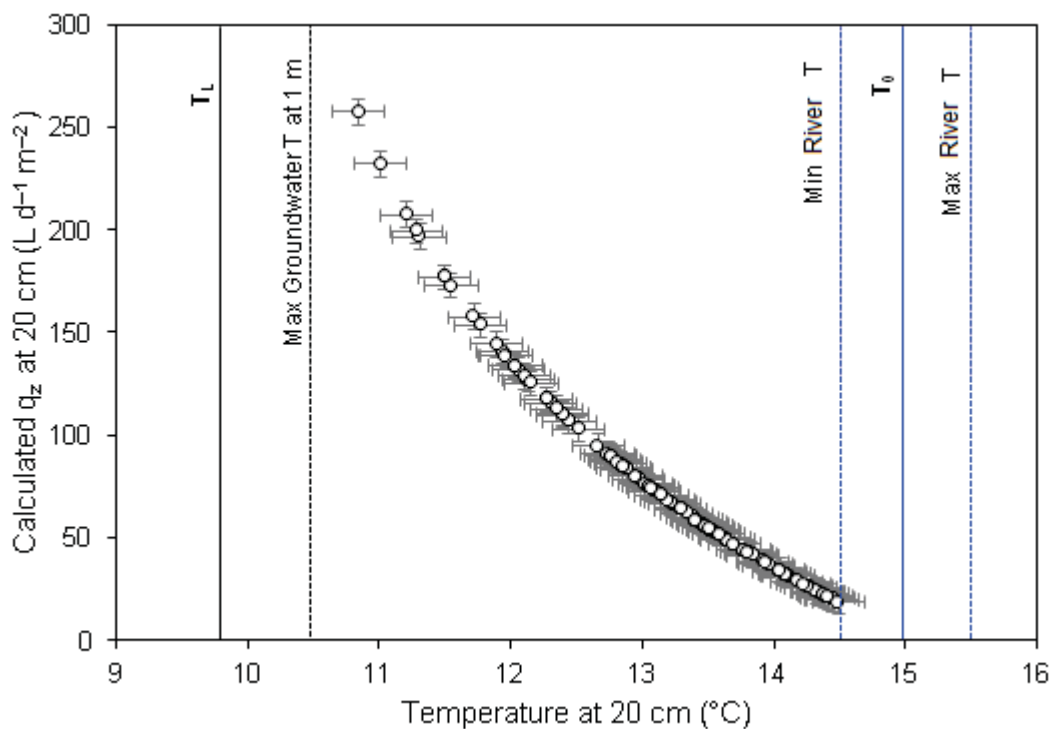


Fig. 5.3.5 Calculated vertical Darcy flux derived from 122 temperature profiles collected throughout the reach. Boundary conditions are denoted by the solid lines with dashed lines indicating the ranges observed in both end-members.

The spatial variability of q_z over the surveyed reach is presented in Fig. 5.3.6. It is clear from this figure that groundwater discharge through the riverbed shows considerable spatial heterogeneity over the plume-impacted reach. The spatial average q_z was calculated at $75 \text{ L d}^{-1} \text{ m}^{-2}$ with a maximum flux of $260 \text{ L d}^{-1} \text{ m}^{-2}$ observed at the 1 m position of transect T7. As indicated from the temperature mapping (Fig. 5.3.5B–C), the previously identified cold zones, located between (SL1 and SL3) represent zones of locally enhanced groundwater discharge with calculated fluxes in excess of $150 \text{ L d}^{-1} \text{ m}^{-2}$ over riverbed areas in the order of 5 m^2 . Relatively low flow rates ($<100 \text{ L d}^{-1} \text{ m}^{-2}$) were obtained for large areas of the riverbed between SL3 and SL4 with minimal or no flow areas (e.g., $<50 \text{ L d}^{-1} \text{ m}^{-2}$) identified along the channel margin on the Heathbrook Farm bank (from T7 to T14) where pore water temperatures were within $\sim 0.5 \text{ }^\circ\text{C}$ of river temperatures (Fig. 5.3.4C).

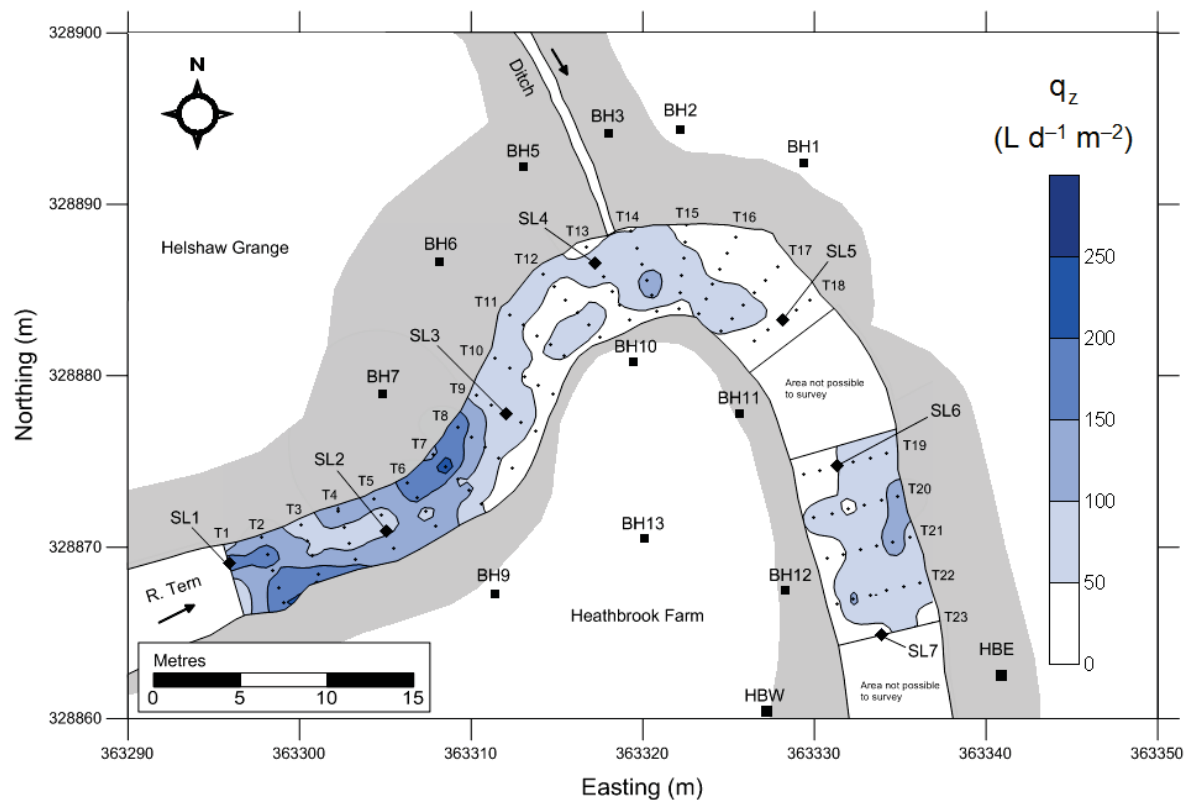


Fig. 5.3.6 Spatial variability of vertical groundwater discharge derived from the temperature profiles at 20 cm, interpolated using Kriging. Profile measurement locations are indicated by black dots. Zones of high groundwater fluxes can be identified at the cold spots located between SL1 and SL3 with low or no flow zones located on the adjacent to the Heathbrook Farm bank between BH9 and BH10 as well as on the Helshaw Grange bank north of SL5 towards BH1.

By applying Equation 5.3 to the calculated fluxes, it was possible to estimate Q_z for the mapped riverbed area of $247.5\ m^2$ (see Appendix C2). A constant value of $2.5\ m^2$ was used for area term in the equation (x.y) which was an arbitrary division of the total area by the number of measurement points. Using this approach, the total potential groundwater baseflow contribution from the entire survey reach was estimated to be in the region of $22,880\ L\ d^{-1}$ or $23\ m^3\ d^{-1}$ ($265\ mL\ s^{-1}$) giving an average discharge of $93\ L\ d^{-1}$ over the reach, when normalised to the total seepage area.

5.3.3 Contaminant flux assessment

5.3.3.1 TCE concentrations in the riverbed

All the Transect S piezometers (including the shallow levels at SL4, SL5 and SL6), were sampled on the 17th of July 2013 during a low flow period where the average daily river discharge was recorded at $0.463 \text{ m}^3 \text{ s}^{-1}$ at the Ternhill gauging station (Fig. 5.2.7A). Given that the discharge and river stage were lower on the sampling day than that observed during the discrete measurement campaign (Fig. 5.2.7A), dilution of the plume at SL5 and SL6 by infiltration of surface water is probably unlikely. TCE was above the limit of detection for all piezometer locations with an average concentration of $22.4 \text{ } \mu\text{g L}^{-1}$. The ‘core’ of the plume, determined from the nested monitoring approach in Chapter 4, was clearly apparent with concentrations in excess of $10 \text{ } \mu\text{g L}^{-1}$ as observed in SL3 to SL5 close to the head of the meander bend. The highest concentrations were observed at SL3 ($48 \text{ } \mu\text{g L}^{-1}$) and SL4A ($47 \text{ } \mu\text{g L}^{-1}$) with most dual-level piezometers showing a modest decrease in concentration from the deepest to the shallowest level. However, at SL5, the shallow piezometer had a significantly greater ($45 \text{ } \mu\text{g L}^{-1}$) concentration than the deep level ($31 \text{ } \mu\text{g L}^{-1}$). Downstream of SL5, TCE concentrations ranged from $9.4 \text{ } \mu\text{g L}^{-1}$ at SL6A to $7.3 \text{ } \mu\text{g L}^{-1}$ at SL8. The reductive dechlorination products of TCE (cDCE and VC) were undetectable in all but one location (SL5B) where a trace of cDCE ($0.3 \text{ } \mu\text{g L}^{-1}$) was detected on the chromatogram.

Because groundwater discharge through the riverbed drives the contaminant flux from the groundwater plume to the river, it is possible to estimate the potential mass discharge rates from the groundwater plume to the river through the application of a flow-concentration product approach (Kalbus et al., 2007; Ellis and Rivett, 2007; Schmidt et al., 2008). The 1-D vertical TCE flux (q_c) [$\mu\text{g m}^{-2} \text{d}^{-1}$] was calculated using Equation 5.5

$$\text{Equation 5.5} \quad q_c = q_z \cdot c$$

Where q_z is the vertical Darcy flux [$\text{L d}^{-1} \text{m}^{-2}$] and c is the concentration [$\mu\text{g L}^{-1}$]. By applying an area term, it was possible to estimate the mass discharge (Q_c) [mg d^{-1}] from the whole reach using Equation 5.6, where q_z , x and y are already known.

$$\text{Equation 5.6} \quad Q_c = \frac{\sum q_z \cdot (x \cdot y) \cdot c}{1000}$$

As already discussed for the up-scaling of groundwater fluxes in Section 5.3.1 (see Fig. 5.3.1), it was necessary to apply a similar linear interpolation to TCE concentrations over the reach in order to spatially distribute the concentration term (see Appendix B). The results of this interpolation are presented in Fig. 5.3.7.

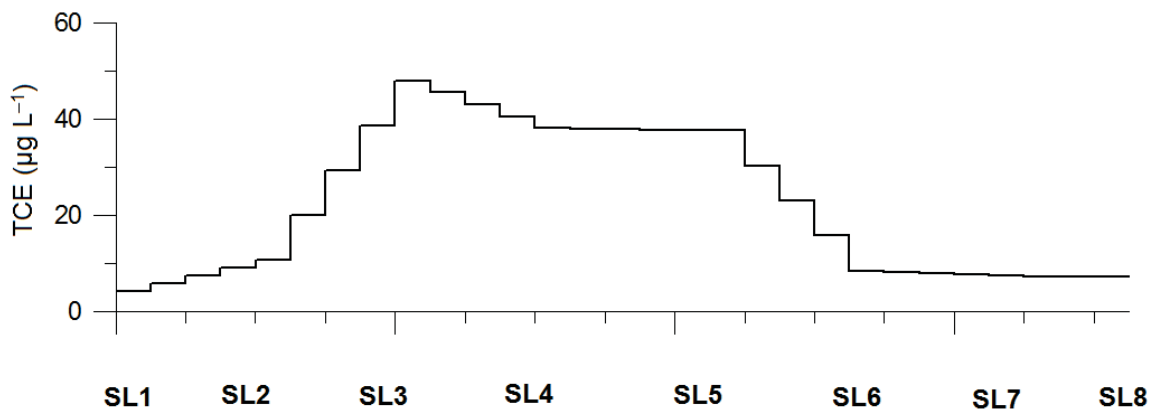


Fig. 5.3.7 Linear interpolation of plume concentrations over the 72.5 m reach based on concentrations obtained from the Transect S piezometers. The ‘core’ of the plume can clearly be made around SL3 to SL5 (see Appendix B).

The fluxes calculated in the following sections only estimate the advective component of the plume and do not consider, dispersion, sorption (discussed later in this section) or transformation during vertical transport.

5.3.3.2 *Potential TCE flux based on Darcian flow*

For the perspective of the shallow groundwater seepage area (Table 5.2), the spatial average q_c was estimated to be $1288 \mu\text{g d}^{-1} \text{m}^{-2}$ ($0.01 \mu\text{g s}^{-1} \text{m}^{-2}$) with a standard deviation of $860 \mu\text{g d}^{-1} \text{m}^{-2}$. A maximum potential TCE flux of $2043 \mu\text{g d}^{-1} \text{m}^{-2}$ was calculated for SL5, close to the head of the meander bend and situated within the core of the plume (Fig. 5.3.7). The total mass discharge rate (Q_c) from the plume across the shallow groundwater seepage area was estimated at $433 \text{ mg TCE d}^{-1}$ ($5 \mu\text{g s}^{-1}$) or approximately 157 g y^{-1} for the advective baseflow contaminant contribution from the plume-impacted reach. For the deeper seepage area, where pressure gradients were stronger (Table 5.2), the spatial average 1-D TCE flux was estimated at $4486 \mu\text{g d}^{-1} \text{m}^{-2}$ or $0.05 \mu\text{g s}^{-1} \text{m}^{-2}$ with a standard deviation of $2910 \mu\text{g d}^{-1} \text{m}^{-2}$. The maximum q_c calculated was $9393 \mu\text{g d}^{-1} \text{m}^{-2}$ and again, located at SL5. This single-level piezometer approximately coincides with the ‘geological window’, inferred from the elevated TCE concentrations (e.g., $>30 \mu\text{g L}^{-1}$) in the multi-level profiles of MP17 and MP18 (see Fig. 4.2.6, Chapter 4).

Up-scaled over the entire 72.5 m reach, Q_c was estimated to be in the order of $1,500 \text{ mg d}^{-1}$ ($18 \mu\text{g s}^{-1}$) or 0.552 kg y^{-1} for the vertical advective component of the plume. Fig 5.3.8 presents the longitudinal variability of Q_c as it was interpolated along the reach in order to estimate the total mass fluxes (see Figs. 5.3.1 and 5.3.2). Although SL8 dominated the groundwater flux along the reach (Fig. 5.3.2) it does not dominate the plume flux because TCE concentrations were $<10 \mu\text{g L}^{-1}$ (Fig. 5.3.7) in that area, which is considered to be the

fringe zone of the plume (Chapter 4). Instead, the majority of plume mass discharges through the ‘core’ zone between SL3 and SL6 (Chapter 4), centred around SL5 where pressure gradients were weaker ($<0.2 \text{ m m}^{-1}$) than the rest of the reach but hydraulic conductivity was enhanced ($\geq 1 \text{ m d}^{-1}$) (Fig. 5.2.6). From the up-scaled assessment approach, the reach between SL3 and SL6 accounts for $>60\%$ of the total mass discharge from the groundwater plume for the perspectives of both the shallow and deep seepage areas (see Appendix B).

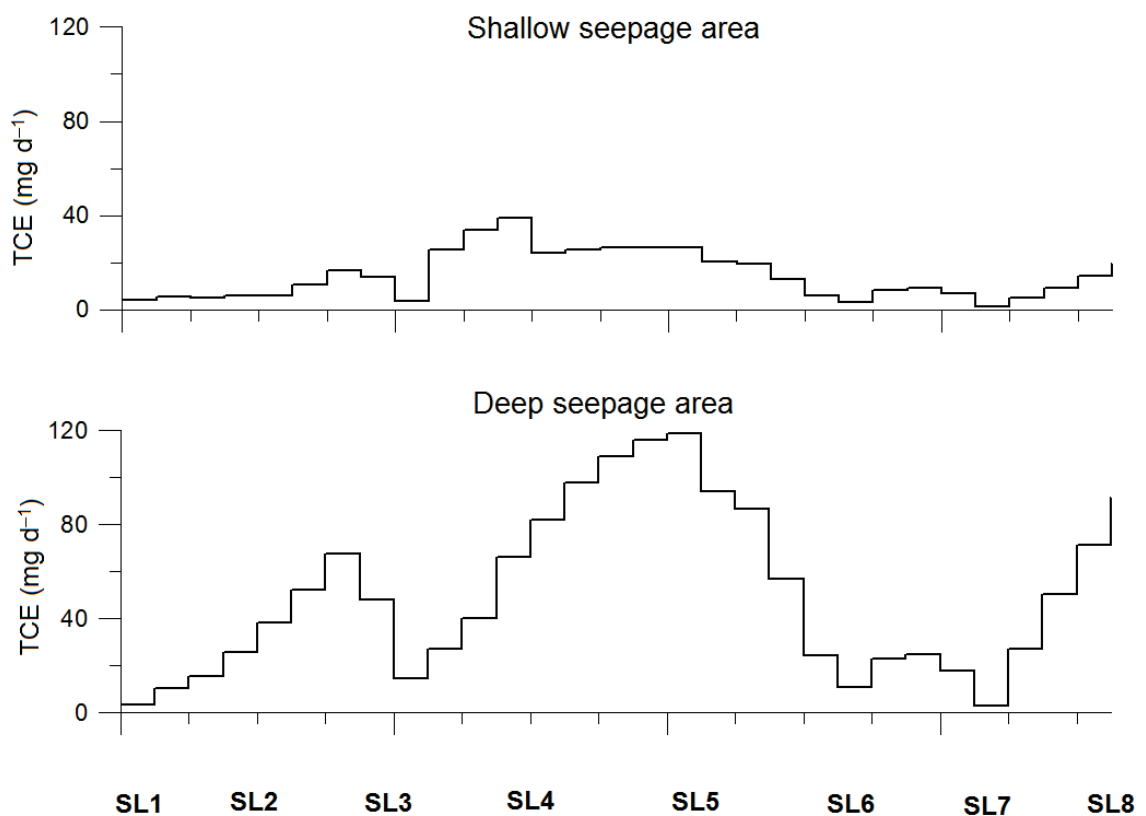


Fig. 5.3.8 Linear interpolation of Q_c derived from Equation 5.6 and the concentration term interpolated in Fig. 5.3.7 for both seepage depths. Note the dominance of the plume core area which contributes $>60\%$ of the contaminant mass to the river based on this up-scaled assessment.

5.3.3.3 *Theoretical dilution within the surface water column*

Using the preceding estimates of Q_z and Q_c , it was possible to estimate theoretical TCE concentrations in the river, at the time of measurement (Fig. 5.2.7A) using flow data from the Ternhill gauging (EA, 2013; unpublished data). Two assumptions were made about this estimate: (1) the water column of the river is fully mixed, (2) all the mass present in the riverbed discharges instantaneously, with no sorption, transformation or dispersion. In addition, volatilisation through river-atmosphere partitioning was not considered. For the shallow groundwater seepage area, the calculated total Q_z of 0.27 L s^{-1} represents the baseflow accretion from the reach into an average river flow of 655 L s^{-1} where it is a diluted by approximately 2400-fold. This produces a river water concentration of TCE in the order of just $0.002 \mu\text{g L}^{-1}$. The total groundwater baseflow accretion Q_z from the deeper seepage area (where pressure gradients were higher) was calculated at approximately 1 L s^{-1} , giving a dilution factor of approximately 650-fold (for an instantaneous Q_c of $18 \mu\text{g s}^{-1}$) using the same river average flow. This produces a dissolved concentration in the water column of the River Tern of just $0.03 \mu\text{g L}^{-1}$ at the downstream end of the discharge zone at SL8.

5.3.3.4 *Potential TCE flux based on temperature mapping*

Equation 5.5 was applied to q_z calculated from the 122 temperature profiles using the linear interpolation of the concentration term (see Appendix C3) and is visualised in Fig. 5.3.9. With the benefit of temperature mapping, the spatial resolution of the flow term measurement was improved by a factor of 15 along the reach with cross-channel, lateral spatial variability also captured. However, because the concentration term was measured at a much lower resolution, unobserved spatial heterogeneity in this term may introduce significant uncertainties in determining the actual distribution of plume fluxes through the

reach. Nonetheless, it was still possible to use q_c to estimate both the probable location and likely rates of potential TCE upwelling through the riverbed. Over the whole reach, the spatial average of q_c was $1668 \mu\text{g m}^{-2} \text{d}^{-1}$ with a standard deviation of $1422 \mu\text{g m}^{-2} \text{d}^{-1}$. Fig. 5.3.9 presents a spatial interpolation of q_c over the reach. Although the temperature-derived q_z was relatively elevated in discrete zones in the western part of the reach near SL1 and SL2 (Fig. 5.3.6), these piezometers were located within the fringe zone of the plume where TCE concentrations were less than $10 \mu\text{g L}^{-1}$ (Fig. 5.3.7). Therefore, these locally-enhanced groundwater discharge pathways are probably unlikely to represent 'hotspots' of contaminant input to the river. However, the elevated TCE concentrations at SL3 ($48 \mu\text{g L}^{-1}$), coupled with the high indicated groundwater flux immediately upstream of this area (centred on northern half of temperature transects T6–T9, Fig. 5.3.6), indicate a high probability for potentially focussed contaminant input to the river in this part of the reach. A flux in excess of $7,000 \mu\text{g m}^{-2} \text{d}^{-1}$ could be possible through this pathway. However, much of the core of the plume is present in the riverbed where the groundwater flux was relatively low and more diffuse, such as the area between SL3 and SL4 (Fig. 5.3.9).

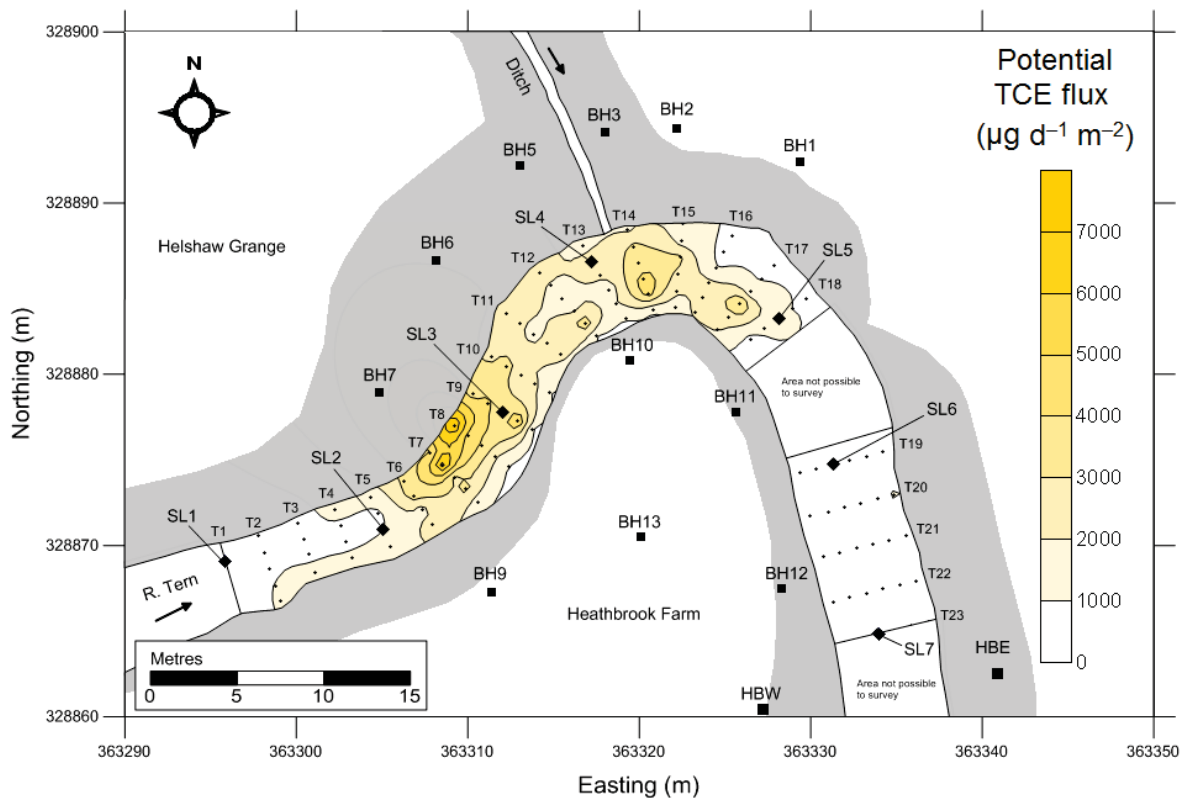


Fig. 5.3.9 Spatial variability of q_c derived from temperature fluxes and interpolated Transect S piezometer TCE concentrations. Temperature profile measurement locations are indicated by black dots. High potential flux zones are indicated where the interpolated core of the plume intercepts enhanced groundwater discharge areas; for example, in the area between SL2 and SL3.

5.3.3.5 Comparison of fluxes

Due to equipment availability, it was not possible to conduct the temperature mapping at the same time as discrete measurements in Section 5.2.2. However, as can be seen from Figs. 5.3.4, 5.3.6 and 5.3.9, temperature transects T1, T5, T9, T13, T18, T19 and T23 were intentionally co-located with the Transect S piezometers SL1–SL7 (see Section 5.2.2). Temperature profiles along these transects were collected within a 1 m radius of the single-screen piezometer where measurements of K_s and VHG were made at 25 cm. This allowed a comparison between the two independent estimates of q_z which drives the contaminant flux to be made. Fig. 5.3.10 compares the two estimates of q_z as a bivariate scatter plot. The distribution of the VHG-derived q_z followed a normal distribution (Shapiro-Wilk $p =$

0.73) whilst the temperature-derived q_z was log-normally distributed ($p = 0.09$). Therefore, Spearman's rank correlation was used on the untransformed datasets and a strong positive correlation was ($\rho = 0.82$, $p = 0.02$) was obtained between the fluxes (with two-tailed significance). Reasonable agreement can be seen from Fig. 5.3.10 for fluxes of $<100 \text{ L d}^{-1} \text{ m}^{-2}$. However, the temperature-derived q_z for SL1 ($232 \text{ L d}^{-1} \text{ m}^{-2}$) is over twice that of the corresponding VHG-derived q_z ($96 \text{ L d}^{-1} \text{ m}^{-2}$). The reason for this deviation is not certain. However, because the measurements were not precisely co-located in the riverbed sediment, it was probably due to sub-metre scale heterogeneity in the distribution of K_s where a permeable zone was intercepted by the temperature probe but not by the temporary piezometer. Conant (2004) was only able to produce a satisfactory empirical relationship from temperatures and Darcy fluxes after rejection of extreme values which could be subsequently validated by heat flow modelling (Schmidt et al., 2007).

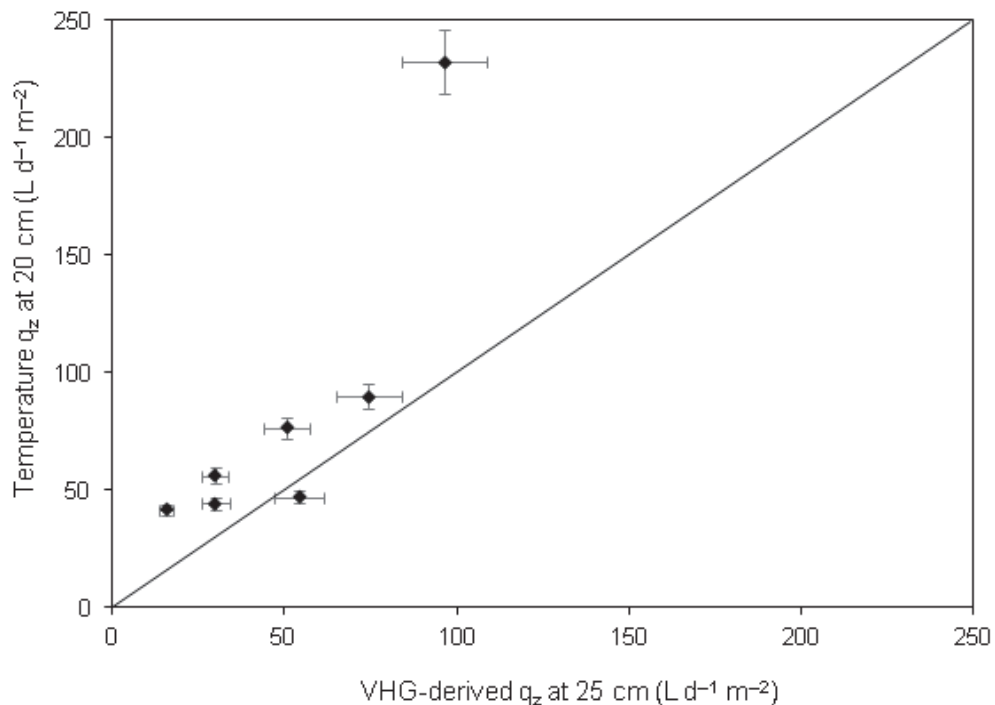


Fig. 5.3.10 Comparison of the two independent estimates of the vertical Darcy flux through the riverbed. The solid diagonal line plots where the fluxes are equal.

Table 5.3 summarises the antecedent conditions present during both campaigns and compares calculated Q_z for both methods, which drives the total mass discharge from the plume (Q_c). The riverbed area where temperature could not be measured is omitted from the comparison (leaving a seepage area of 247.5 m²). The average river stage differed by 10 cm between the campaigns with the lower river stage/flow conditions present for the temperature campaign. As indicated by the time series data presented in Fig. 5.2.7 (and discussed in Section 5.2.3), the pressure gradient between groundwater in the riverbed and river stage was relatively constant other than for up to several days around storm flows. Therefore, fluxes measured at different positions along the reach during baseflow recessions can be assumed to be relatively constant with time. Both estimates of Q_z (and Q_c) agree to within an order of magnitude. The spatial heterogeneity of q_z revealed by the high-resolution temperature mapping produced a greater total Q_z than the lower spatial resolution, VHG-derived Q_z . This illustrates the importance of metre-scale variability of groundwater discharge when attempting to up-scale from sparse point measurements..

Table 5.3 Summary of antecedent conditions and comparisons of whole-reach groundwater and TCE flux estimates.

Parameter	Unit	VHG flux	Temperature flux
Seepage area depth	cm	20	25
Average daily river flow	m ³ s ⁻¹	0.61	0.5
Average river stage	m AOD	58.68	58.57
Spatial average q_z	L d ⁻¹ m ⁻²	62	75
Total baseflow (Q_z)	L d ⁻¹	15,076	22,881
Spatial average q_c	µg d ⁻¹ m ⁻²	1375	1423
Plume flux (Q_c)	mg d ⁻¹	347	484

5.3.3.6 *Influence of the sediment matrix contaminant transport*

The timeframe over which the preceding estimates of Q_c reach the surface water column will be influenced by the retardation capacity (Table 5.1) of the riverbed (Figs. 5.2.2 and 5.2.3). By applying Equation 2.1 (see Chapter 2) to the K_s and VHG observations for the Transect S piezometers (Table 5.2) and n determinations from their cores (Table 5.1), the vertical advective velocity (V_a) [cm d^{-1}] was estimated through the top metre of the riverbed. Using Equation 2.5 (Chapter 2) and the R estimates for TCE in Table 5.1, it was possible to quantify the sorption-modified contaminant velocity (V_r) [cm d^{-1}]. Finally, by calculating the reciprocal of these velocities, the advective (T_a) and sorption-modified residence times (T_r) [d m^{-1}], respectively, were estimated. These estimates are presented in Table 5.4. As a comparative measure, a hypothetical 1 m section of riverbed composed of pure Bridgnorth sandstone with a porosity of 0.25 (Streetly and Shepley, 2005) was conceived, where a value for q_z was calculated from (1) the product of the average VHG of SL1–SL8 (Section 5.2.2) and (2) the published geometric mean K_s (3 m d^{-1}) for the regional aquifer (Streetley and Shepley, 2005).

Table 5.4 Estimated velocities and residence times for advective and sorption-modified TCE transport through the top metre of the riverbed at the Transect S piezometer locations.

Location	V_a	V_r	T_a	T_r
	(cm d^{-1})	(cm d^{-1})	(d m^{-1})	(d m^{-1})
SL1	34.9	1.22	2.87	82
SL2	198	2.31	0.51	43
SL3	9.8	0.09	10.2	1081
SL4	34	0.98	2.94	102
SL5	123	13.2	0.82	7.55
SL6	20	0.46	4.98	217
SL7	15.3	0.17	6.53	578
SL8	1508	209	0.07	0.47
Bridgnorth SST	482	389	0.21	0.26

From a comparison of Table 5.4 and Fig. 5.2.2, it can be seen that the peat lenses in the stratigraphy have a dramatic impact on TCE velocities with migration rates reduced to <1 cm d^{-1} at SL3, SL4, SL6 and SL7. This is particularly so where both f_{oc} is high (e.g., >0.2 g g^{-1}) and K_s is low (e.g., <0.1 m d^{-1}), such as at SL3 (Figs. 5.2.3 and 5.2.6). From Table 5.4, the average T_a in the riverbed for a conservative (non-sorbing) solute would be approximately 3.6 days, as compared to approximately 5 hours for an equivalent metre of the sandstone bedrock. However, the range over the whole reach is considerable with just 1.6 hours for location SL8 to approximately 10 days for SL3. From Table 5.4, it can be seen that hydrophobic sorption would greatly increase the bulk residence time of the plume in the riverbed with an average T_r of 264 days and reaching as long as approximately 3 years at SL3. T_r is, on average, 1000-fold greater in the top metre of the riverbed, in comparison to a discharge zone composed of pure Permo-Triassic sandstone. However, this retention potential is highly variable spatially with ‘windows’ clearly apparent in the stratigraphy which are carbon-poor (Fig. 5.2.3). For example, the T_r at SL5 is just 7.5 days and as little as 6 hours for SL8. However, at SL8 only a single grab sample of sediment was possible for f_{oc} determination and the stratigraphy below ~ 10 cm was unknown. In addition, as already discussed, the area of SL8 lies within the fringe of the plume and this ‘window’ is unlikely to form a major pathway. However, SL5 does present a significant zone for preferential TCE input to the river, as it is situated within the core of the plume with concentrations currently approaching $50 \mu\text{g L}^{-1}$ (Fig. 5.3.7).

5.4 Discussion

5.4.1 Flow regime of the riverbed

At the scale of the plume discharge zone along the reach, groundwater discharge rates, which drive the contaminant mass flux from the aquifer to the river, are controlled by the spatial variability of K_s and the magnitude of the VHG. In comparison to the floodplain (characterised in Chapter 4), the riverbed fluvial deposits are more stratified and heterogeneous (Figs. 5.2.2 and 5.2.6) with an intermediate range of K_s (0.03–8.6 m d⁻¹), between the floodplain alluvium (0.001–0.74 m d⁻¹) and underlying sandstone bedrock (0.1–26 m d⁻¹, Streetly and Shepley, 2005). At reach scale, Angermann et al. (2012) and Krause et al. (2012) investigated the spatial patterns of riverbed VHGs in the 250 m long pre-existing piezometer network (Fig. 3.2.9, Chapter 3). Their work incorporated part of the reach investigated here (P1–P8, Fig. 3.2.9). They were able to conceptualise two contrasting modes of groundwater-surface water interaction, based on the spatial and temporal variability of the pressure gradient with knowledge of riverbed stratigraphic heterogeneity. Where clay and peat lenses were present in the stratigraphy, they observed large VHG magnitudes (up to 0.8 m m⁻¹) characterised by significant temporal variability. This confined or semi-confined mode was contrasted by an unconfined mode, where a weaker pressure gradient (0.1–0.4 m m⁻¹) and less temporal variability was observed. They interpreted this mode as indicative of ‘free’ groundwater upwelling from the bedrock aquifer where flow-confining structures were absent in the fluvial sediment sequence. This conceptual model can be validated by the observations of this study. It is clear from Fig. 5.2.8 (with reference to Fig. 5.2.6) that the magnitudes of riverbed pressure gradients are both greater and more temporally variable beneath the interpreted semi-confining horizons along the reach around SL1–SL4 and SL7. This also accounts for the ‘stepped’ depth

distribution of VHGs along the reach (Fig. 5.2.5B), discussed previously. The weaker pressure gradients observed around SL5 and SL6 with less temporal variability than the rest of the reach (Figs. 5.2.6 and 5.2.8), suggested more unconfined conditions. However, median VHGs at SL6 were less than 0.1 which is weaker than would be expected for free groundwater upwelling conditions (e.g., 0.1–0.4), according to the previous conceptual model proposed for the site. This suggests the piezometers at SL6 did not fully penetrate the semi-confining layer, whereas at SL5 (where the median VHG was ~ 0.28 for the deeper piezometer), free upwelling through this ‘geological window’ was more likely, based on the piezometric and stratigraphic evidence. These observations illustrate the importance of local-scale structural heterogeneity in riverbed sediment sequences in controlling rates and spatial patterns of groundwater discharge.

With continuous monitoring of the hydraulic heads in the riverbed over a storm flow event (Fig. 5.2.7), it was possible to observe the transient behaviour of the riverbed pressure gradient over the reach. It was clear that the gradient significantly reduced at all piezometer locations on the rising limb of the event flow, lasting in the region of 12 hours. These observations are supported by insights from numerical simulations of transient conditions on a lowland reach of the River Leith in Cumbria, U.K (Munz et al., 2011). That study showed that head distributions in the riverbed were modified by the onset of peak flows so that the probability of surface water infiltration to the bed sediments was greatly increased. At both depths of SL6 (and SL5B), the weaker groundwater pressure gradient was overcome for a short period by the river flow response which produced a gradient reversal, resulting in possible surface water infiltration (hyporheic exchange) to the riverbed by at least as much as 50 cm (Figs. 5.2.7 and 5.2.8). Therefore, based on the indirect piezometric evidence, the ‘classic’ hyporheic zone (e.g., White, 1993; Brunke and

Gonser, 1997) where groundwater and surface water may readily interact may be extended in the area of SL5 and SL6. However, additional direct evidence (such as geochemical tracers) would be required to confirm this. For example, Byrne et al. (2012) and Binley et al. (2013) were able to validate piezometric indications of surface water infiltration on the aforementioned River Leith site by using surface water chloride as a conservative solute tracer. They were able to observe the shallow (e.g., 20 cm) penetration of river water to bed sediments in certain sections of the river. A similar tracer approach could be applied at the River Tern. As discussed in Chapter 2, hyporheic exchange can have important implications for microbial respiration and biogeochemical turnover in riverbeds; through the introduction of carbon sources and electron donors (Baker and Vervier, 2004; Byrne et al., 2013).

5.4.2 Spatial variability and controls on groundwater fluxes

Darcy fluxes are thought to provide the best indicator of actual groundwater discharge rates to rivers (Kaser et al., 2009; Binley et al., 2013), in the absence of direct measurements of fluxes using seepage meters (Kalbus et al., 2006; Rosenberry, 2008). However, practical constraints and cost considerations limit the measurement density achievable with piezometers. Up-scaling from a limited number of point measurements may fail to capture small-scale heterogeneity and risks introducing large uncertainties when attempting to integrate flux assessments over larger scales (Blume et al., 2013). However, temperature mapping and the application of heat flux models, can provide a rapid ‘multi-one-dimensional’ (Schmidt et al., 2007) flux assessment, which, in this study, could exceed the shallow VHG/piezometer measurements density by 15-fold. Comparison of these two independently-derived estimates (Fig. 5.3.10) indicates a good correlation exists for an intermediate range of fluxes (e.g., 50–100 L d⁻¹ m⁻²). However, other than at

SL1, the shallow temporary piezometers of Transect S did not directly intersect either the high or low-flux zones, situated along the channel margins (Fig. 5.3.7) which exert a major control on the how the baseflow accretion is distributed along the reach. For example, the high-flux zones where discharge rates exceeded $200 \text{ L d}^{-1} \text{ m}^{-2}$ (Fig. 5.3.7) supplied approximately 60% of the baseflow from 42% of the seepage area. Most of these zones were concentrated in the west of the reach between SL1 and SL3 and accounted for ~50% of the total Q_z . From the electrical resistivity profiles in Chapter 4 which were acquired along the riverbank in this area (ER2 and ER3; Fig 4.3.7), it can be seen that the interpreted bedrock interface lies approximately 1 m below the riverbed surface in the west, which was validated by contact with the sandstone at SL1 (Fig. 5.2.2). However, the most concentrated area of groundwater discharge on the northern bank between SL2 and SL3 (Fig. 5.3.7) does not coincide where the bedrock is close to the surface in nearest ERI profile (ER2). Instead this area is located where the alluvium is locally thickened and the bedrock topography dips downwards (Fig. 4.3.7B). However, as noted in Chapter 4, a ‘ground-truthing’ of bedrock depth in this area would be necessary to confirm this. This zone contributes approximately 10% of the groundwater discharge from only 5% of the seepage area. The importance of cross-channel variability in groundwater discharge can be seen at this location. For example, at transect T8, the calculated flux ranges from $207 \text{ L d}^{-1} \text{ m}^{-2}$ at 0 m (on the northern bank) down to $24 \text{ L d}^{-1} \text{ m}^{-2}$ at the opposite bank (at 4 m along the transect).

This lateral variability in groundwater discharge is likely to be controlled by the cross-channel continuity of the semi-confining deposits within the riverbed stratigraphy. From SL3 to SL4, the low to moderate discharge regime probably reflects a greater lateral continuity of the semi-confining silt and peat deposits in this area. A comparison of Figs.

5.2.1 and Fig. 5.3.6 provides insights into the geological controls which affect the spatial distribution of groundwater discharge through the surficial sediments. The mapped clay deposits, which outcrop on the bank at Heathbrook Farm between BH9 and BH10, coincide with the low or no flow zones in the riverbed which were also encountered during the mini-piezometer installation around MP1–MP3 (Fig. 4.2.6, Chapter 4). This is likely to be the riverward extension of the alluvial aquitard cap underlying the floodplain across the river channel around the head of the meander bend. However, the K_s of the semi-confining deposits of the riverbed were two orders of magnitude greater than floodplain alluvium. Previous FO-DTS surveys over the wider 250 m reach of the River Tern (Angermann et al., 2012; Krause et al., 2012, 2013) revealed spatially-localised cold and warm riverbed locations (in summer and winter surveys, respectively) which are approximately co-located with the significant groundwater flux zones between SL1 and SL3. However, due to signal averaging, difficulties arise in precisely determining the location and amplitude of the thermal anomalies on fibre-optic cables (e.g., Rose et al., 2013). Nevertheless, the looped-cable format of the survey approach revealed comparable cross-channel spatial variability patterns of temperature with parallel cables sampling either side of the same channel reach. This indicates that these mapped high flux zones are persistent over annual time scales and therefore, most likely arise from relatively deep flow-controlling structures which are not sensitive to the effects of seasonal erosion and deposition cycles.

5.4.3 Plume flux assessment

Using a flow-concentration product approach to estimate advective TCE mass flux (Q_c) at the River Tern, Q_c to the river from the 72.5 m discharge zone was estimated to be in the region of 0.43–1.5 g TCE d⁻¹ for July 2013 concentrations, under typical summer baseflow conditions. As discussed in Section 5.3.3 and the preceding section, the accuracy of this flux assessment is limited by uncertainty in the spatial variability of both flow and concentration terms, during their up-scaling to the whole reach. Although the temperature mapping provided highly refined information on the spatial distribution of the flow term (e.g., 122 data points), the concentration term was observed at a much lower resolution (e.g., 8 data points). Because interpolation was used to up-scale, uncertainty in the concentration term is likely to be greatest at the margins of the core of the plume where differences in concentration are highest between adjacent piezometers (e.g., SL2–SL3 and SL5–SL6, Fig. 5.3.7). Given the concentration patterns already observed in the multilevel profiles (e.g., Fig. 4.2.6, Chapter 4), it is clear that even within the core, small-scale heterogeneity in the concentration term exists. TCE obtained from single-screen Transect S piezometers represents the concentration present in the formation at a radius of just ~10 cm from the piezometer screen (assuming an average porosity of 0.3 with a total purge volume of approximately 5 L). Simultaneous sampling of the whole piezometer transect to obtain average riverbed concentrations where the radius of influence of each encompasses the entire discharge zone could be used to overcome this uncertainty (e.g., Kalbus et al., 2007). However, if flow and concentration terms can be assumed to be linearly related, then Fig. 5.3.7 suggests that approximately 25% of the mass of the plume may potentially be discharging from only 12% of the survey area between SL2 and SL3. However, previous work has shown that plume flow lines do not necessarily coincide with groundwater discharge flow lines due the natural convergence of different flow paths as well as

complications introduced by sorption (e.g., Conant et al., 2004). Nevertheless, temperature transects T13 and T17 were co-located with multilevel mini-piezometer transects TA and TB, respectively (Fig. 4.2.5, Chapter 4). Fig. 5.4.1 provides a spatial comparison between temperature-derived groundwater fluxes and TCE concentrations observed at 20 cm in mini-piezometer profiles (See Fig. 4.2.5, Chapter 4). A comparison of Figs. 5.3.7 and 5.4.1 reveals an approximately comparable spatial pattern of TCE concentrations with potential TCE fluxes obtained from temperature mapping. This is particularly evident at the cross-channel transects where high fluxes coincide with increased TCE concentrations at the channel margins. Therefore, the flux assessment based on temperature may be valid for certain areas of the plume discharge zone where the magnitude of contaminant and groundwater discharge are linearly related. For these areas of the discharge zone, TCE can be considered to behave as a quasi-conservative tracer of groundwater discharge from the deeper aquifer along the reach.

In Chapter 4, it was noted that TCE was not found to be detectable in any samples taken from the water column of the river from approximately 20 cm above the bed surface. By estimating Q_c , it was possible to provide a ‘worst case scenario’ for river contamination during periods of low river flow in the summer when the dilution potential will naturally be at its lowest. For the July 2013 summer flow of $0.65 \text{ m}^3 \text{ s}^{-1}$, the likely surface water TCE concentrations are estimated to be somewhere in the region of $0.002\text{--}0.03 \text{ } \mu\text{g L}^{-1}$. This concentration is 1–2 orders of magnitude less than the limit of detection for the GC-MS method employed in this study and 2–3 orders of magnitude less than the regulatory limit of $10 \text{ } \mu\text{g L}^{-1}$ (see Chapter 1). For the 7 day minimum flow of $0.27 \text{ m}^3 \text{ s}^{-1}$ (recorded at the Ternhill gauging station, Marsh and Hannaford, 2008), the highest river water concentrations expected would be in the order of just $0.06 \text{ } \mu\text{g L}^{-1}$. In addition to dilution,

volatilisation would be expected to rapidly attenuate this groundwater contamination signal and prevent any off-site migration in the surface water (McKnight et al., 2010).

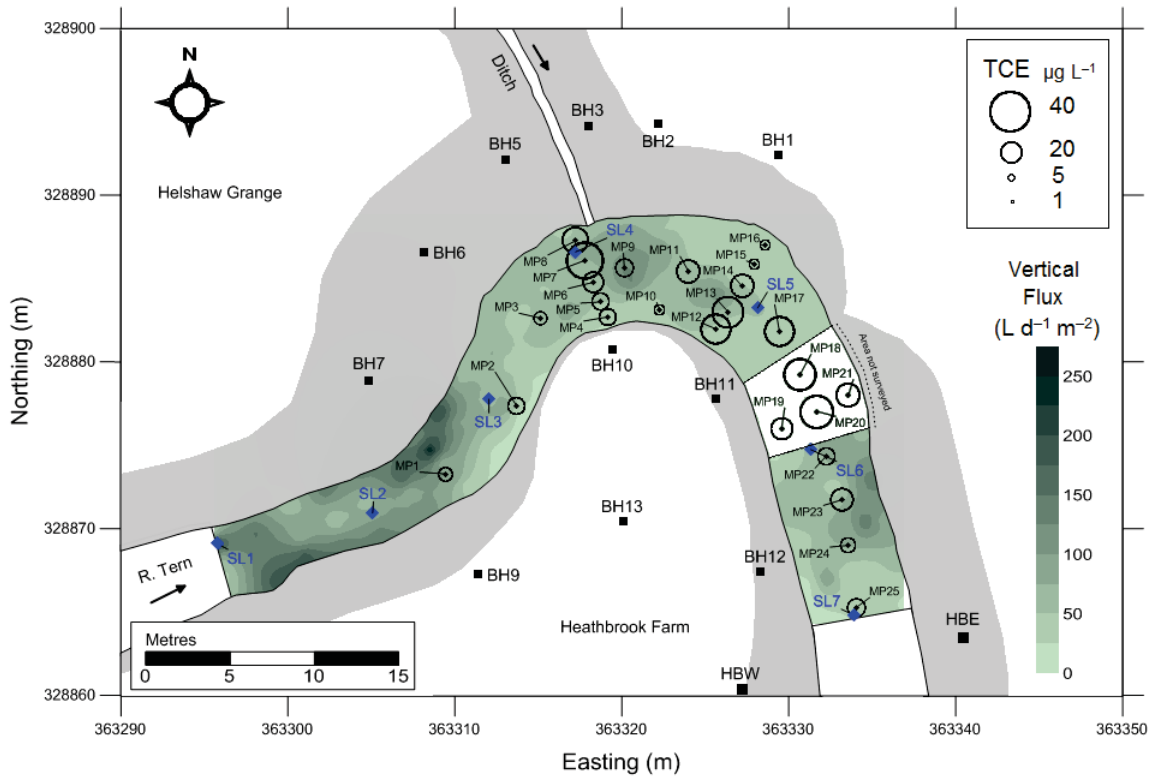


Fig. 5.4.1 Spatial comparison of temperature-derived riverbed groundwater fluxes with TCE concentrations observed at 20 cm during the December 2011 mini-piezometer campaign (See Section 4.2, Chapter 4). Location of Transect S piezometers and mini-piezometers also included. See Fig. 3.3.7 (Chapter 3) for wider context within the study area.

5.4.4 Plume transport through the riverbed

A generalised conceptual model, which integrates the observations of the hydrophysical controls affecting the vertical transport of the plume in the top metre of the riverbed, is proposed in Fig. 5.4.2. In this model, the discharge regime is dominated by diffuse pathways and TCE concentrations within the core of the plume are clearly identifiable. Temperature observations of groundwater discharge are incorporated where the interpreted breach in the confining layer is visualised between SL2 and SL3. Integration of the calculated retardation factors for the different coring and piezometer locations allows for estimates of the sorption-modified migration velocities and residence times to be made for the top metre of the riverbed sediment profile. Based on the observation of stratigraphic and hydraulic controls, two extreme cases (A and B) for vertical transport are presented which exemplify the observed range of transport behaviour in the riverbed. Case (A) is representative of the semi-confining deposits containing peat which contain up to 20-30% (g g^{-1}) carbon. The vertical migration rate of the plume through this type of sediment may be as low as 1 mm d^{-1} . Case (B), which is representative of a ‘geological window’ has largely unrestricted upwelling where migrations rates may exceed 10 cm d^{-1} . These transport parameters are based on the bulk properties of the top metre of the riverbed deposits and do not consider the full saturated thickness of the Holocene deposits overlying the bedrock. For example, bedrock was only confirmed at SL1 at a depth of approximately $\sim 1 \text{ m}$ (Fig. 5.2.1) therefore, a vertical residence time of approximately 80 days is likely to be representative of the entire upwelling pathway through the fluvial sequence here. However, the thickness of the unconsolidated deposits overlying the bedrock is known to reach up to 6.5 m at Heathbrook West (Fig. 4.3.7) with the average elevation of the riverbed situated approximately 2.5 m below this level (Fig. 4.2.6). Extrapolation of the bulk physical properties and the hydraulic gradient over a 4 m vertical flow path in the

sediment indicates that the actual residence times for the plume may be exceed a decade for the Case A-type conditions. Therefore, it is clear that the high carbon content evident in some parts of the sediment profile (Fig. 5.3.9) is likely to significantly prolong the lifetime of the plume in the riverbed, through adsorption-desorption interactions with the solid phase. These residence times will place constraints on reaction half-lives in order for in-situ transformation to take place (Ellis and Rivett, 2007).

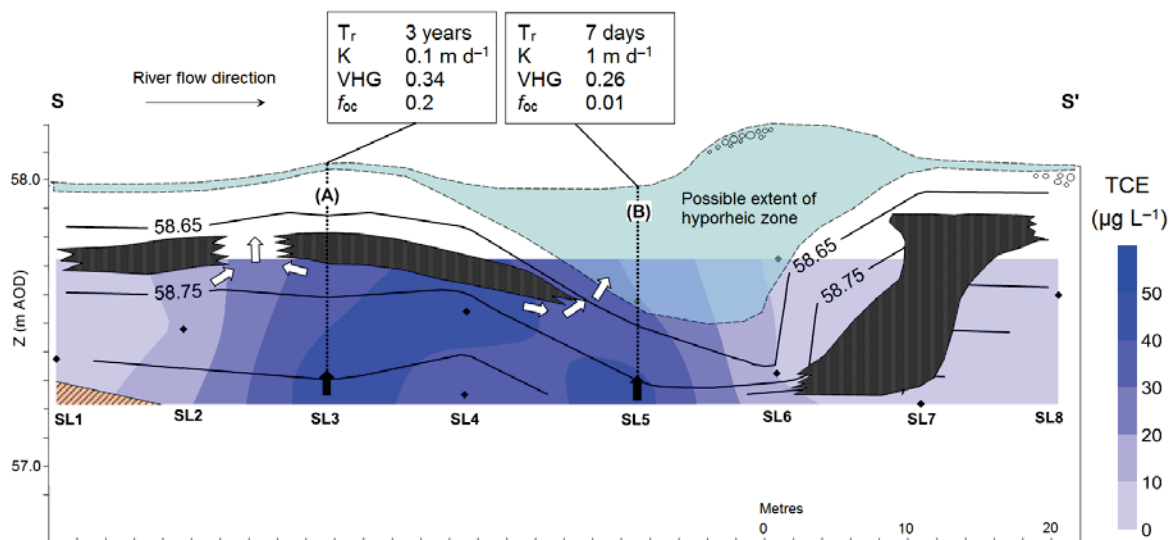


Fig. 5.4.2 Generalised model of plume transport through the riverbed along the investigated reach. TCE concentrations are interpolated from 11 discrete observations with measurement points denoted by black dots. Hydraulic head contours are plotted for baseflow conditions measured at the same locations as TCE concentrations. ‘A’ and ‘B’ denote vertical 1 m flow paths where contrasting transport behaviour is characterised. The principal advective flow lines for the plume are indicated by white arrows. Grey shaded areas approximate the inferred locations of semi-confining horizons along the reach.

5.5 Chapter summary

This chapter has characterised the hydrogeological framework of the riverbed through which the plume discharges. Discontinuous peat/silt horizons exhibited the widest range of K_s (0.02–6 m d⁻¹), centred around 40 cm depth in stratigraphy, which are probably an extension of the alluvial aquitard in the floodplain. Where present, peat lenses present a retardation capacity for TCE of up to 80 times that of the sandstone aquifer. These stratified deposits form an important reach-scale control on aquifer-river connectivity and create semi-confined, groundwater upwelling conditions. A ‘stepped’ increase of VHG magnitudes with depth was consistent with semi-confined conditions. However, one ‘geological window’ was found at SL5 where an absence of the semi-confining deposits resulted in a lower pressure gradient with an increased potential for surface water exchange with the riverbed during high flows. High-resolution temperature mapping revealed heterogeneity in groundwater discharge with most baseflow accretion originating from the channel margins along the reach to the west of the plume core where the sandstone bedrock is close to the riverbed surface. Cross-channel variation in temperature-derived groundwater fluxes approximately corresponded to the TCE concentration gradients observed at the TA and TB mini-piezometer transects in Chapter 4. Up-scaling of VHG-derived vertical Darcy fluxes at two depths for the whole plume-impacted reach indicated rates of groundwater baseflow ranged between 23.2 and 86.4 m³ d⁻¹ with a corresponding TCE mass flux of 0.43–1.5 g d⁻¹ for the dissolved-phase plume. Final dilution of the plume in the river was likely to reduce contaminant concentrations by 2–3 orders of magnitude below the regulatory limit for TCE. Groundwater fluxes based on the temperature mapping agreed reasonably well with the shallow VHG-derived fluxes for co-located measurements. Total baseflow estimates for the reach from these two approaches also agreed to within one order of magnitude.

6. Redox conditions and controls on in-situ transformation.

6.1 Chapter introduction

The detection of both cDCE and VC in the riverbed and cDCE in the alluvial monitoring wells indicated that in-situ reductive dechlorination of the plume was occurring in the discharge zone. This chapter aims to characterise the spatial variability of the redox conditions and controls on reductive dechlorination in these reactive zones. The ‘background’ conditions prevalent in the up-gradient aquifer and the unreactive parts of the discharge zone are also considered. This is achieved through two seasonal ‘snapshot’ sampling campaigns of the riverbed mini-piezometer and alluvial monitoring well networks (see Chapter 4) as well as a HydraSleeve investigation (ITRC, 2006) of the Permo-Triassic sandstone groundwater. A high-resolution grid of pore water samplers is also applied to investigate fine-scale redox and transformation patterns in the shallow riverbed sediments. The extent of dechlorination of the plume in reactive zones is quantified using a ‘chlorine number’ metric (Weaver et al., 1997) which allows the interaction between TCE dechlorination and other hydrochemical variables to be examined.

Redox conditions are assessed, along with chlorinated ethene concentrations, using a redox-sensitive solute approach (Chapelle and McMahon, 1995; Abe et al., 2008). Although direct measurements of E_h can be used to assess redox conditions (Wiedemeier et al., 1998), difficulties have been reported in the interpretation of platinum electrode measurements. For example, the solution redox potential for a particular active reaction can encompass a wide range of measured Eh values with large overlaps frequently described (e.g., Lovely and Goodwin, 1988). This is interpreted to result from (1) a lack of redox equilibrium conditions being present in most environments (Lovely et al., 1994) and the unresponsiveness of platinum electrodes to certain redox couples (Darling and Goody, 2006). Therefore, the decline, or disappearance, of soluble terminal electron acceptors (TEAs), dissolved oxygen (DO), nitrate (NO_3^-), and sulphate (SO_4^{2-}), coupled with the appearance or increase of reduced metabolites including soluble Mn (assumed to be predominantly Mn^{2+}), soluble Fe (also assumed to be mostly Fe^{2+}) and dissolved methane (CH_4), are used to ascribe the predominant terminal electron accepting processes (TEAPS) present (see Fig. 2.5.2, Chapter 2). Dissolved organic carbon (DOC), as the principal microbial substrate (Baker and Vervier, 2004), is also determined for the HydraSleeve and summer snapshot campaigns. Although the speciation and solubility of Fe and Mn phases are pH dependent, the pH range observed in groundwater at the site of 6.96–7.94 was approximately circumneutral (see Appendix D1). As such, dissolved Fe and Mn are most likely to arise from microbially-mediated reductive dissolution processes. This pH range also lies within the optimum range for microbial reductive dechlorination reactions (Wiedemeier et al., 1998).

The site-specific criteria used to assess TEAP conditions is presented in Table 6.1. Although strictly anaerobic conditions were never observed at any location, e.g., DO <0.5 mg L⁻¹ (Baker et al., 2000), evidence of anaerobic TEAPs operating at DO concentrations <2 mg L⁻¹ were regularly observed. Therefore, a DO threshold of 2 mg L⁻¹ was applied in order to define the transition between the predominantly aerobic and anaerobic conditions.

Table 6.1 Criteria for the assessment of predominant TEAPs based on the disappearance of terminal electron acceptors (TEAs) or the appearance of reduced species. See Section 2.5 of Chapter 2 for a discussion of the significance of these microbial processes in the transformation of TCE.

TEAP	DO	NO ₃	Mn	Fe	SO ₄	CH ₄
	(mg L ⁻¹)					
Aerobic respiration	>2	>5	<1	<1	>5	<1
Denitrification	<2	>5	<1	<1	>5	<1
Mn⁴⁺ reduction	<2	<5	>1	<1	>5	<1
Fe³⁺ reduction	<2	<5	>1	>1	>5	<1
Sulphate reduction	<2	<5	>1	>1	>5	<1
Methanogenesis	<2	<5	>1	>1	<5	>1

6.2 Chlorinated ethene observations

6.2.1 River flow conditions during sampling campaigns

Sampling of the riverbed mini-piezometers and alluvial monitoring wells (installed as part of Chapter 4) was carried out in the Spring of 2012 over the week of Monday 12th to Friday 16th of March 2012 during a baseflow period in the river (Fig. 6.2.1A–B). The HydraSleeve sampling campaign was also carried out during this week. The mean vertical hydraulic gradient (VHG) measured at HZ (Fig. 6.3.1B) over the sampling week was 0.23 m m⁻¹ indicating that groundwater discharge conditions were present. A second snapshot of this network took place between 6th and 10th of August 2012 during a period of relative low flow, which was preceded by a protracted period of wet weather and high river flows in the previous month (Fig. 6.2.1A). The mean VHG at HZ for this week was 0.17 m m⁻¹ indicating, again, that ‘gaining’ conditions were likely to be present. A high resolution, ‘plot-scale’ snapshot, using a grid of shallow pore water samplers (Fig. 6.2.1C) was carried out one week after the second snapshot (12th of August 2012). Sediment deposition beneath a submerged macrophyte stand (*Ranunculus* spp.) was specifically targeted for this campaign and its approximate outline over the riverbed is indicated on Fig. 6.2.1C. Samples from this network were grouped by head and tail sections (Fig. 6.2.1C) to determine whether any significant depth-dependant or longitudinal changes were present in the distribution of solute concentrations. River flow conditions and the VHG measured at HZ did not change appreciably from the preceding week during this campaign (Fig. 6.2.1A).

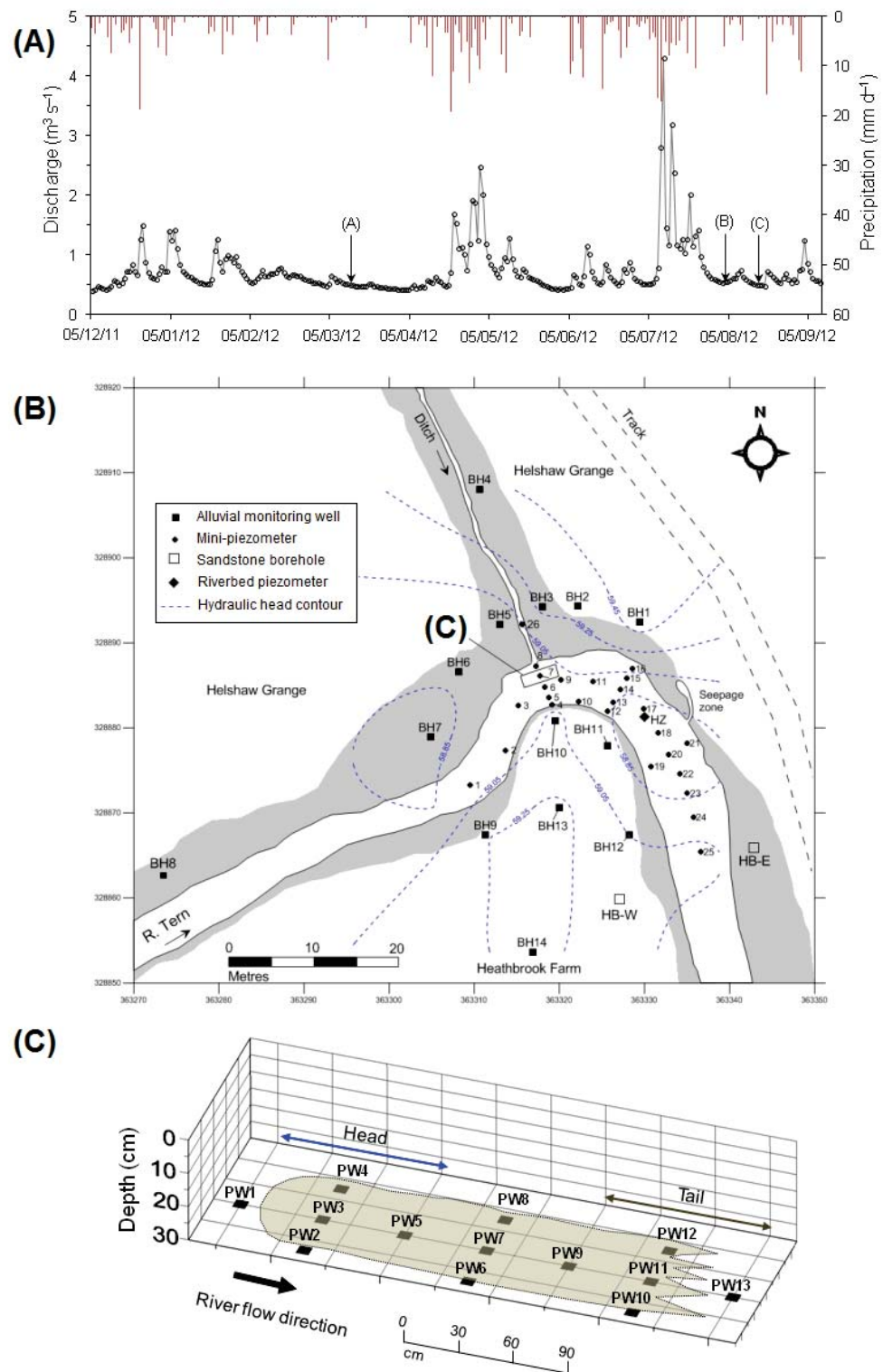


Fig. 6.2.1 (A) Mean daily river flow (Ternhill station) and rainfall (Child’s Ercall station) (EA, 2013; Unpublished data). Sampling campaigns labelled ‘A’ spring snapshot, ‘B’ summer snapshot and ‘C’ ‘plot-scale’ snapshot. (B) Layout of monitoring network with plot-scale array location marked by ‘C’. Representative groundwater levels measured during sampling are included. (C) Layout of plot-scale pore water sampler grid deployed below macrophyte stand (indicated by green-shaded area). The depth on the z-axis indicates the approximate water depth.

6.2.2 Variation in groundwater chlorinated ethene concentrations

6.2.2.1 Permo-Triassic sandstone

Locations of the Environment Agency sandstone boreholes in the wider study area sampled using the HydraSleeve method are given in Fig. 3.2.5 and Table 3.1 of Chapter 3. TCE concentrations were found to have increased from the previous sampling in May 2011 (Chapter 4) by an average of 23% for the Helshaw Grange abstraction borehole (HGA, 89–162 $\mu\text{g L}^{-1}$ at 35–80 m, respectively) and 60% for the observation borehole (HGO, 48.8–74.4 $\mu\text{g L}^{-1}$ at 20–40 m, respectively). On the floodplain, plume concentrations at the Heathbrook East (HBE) borehole increased by 40% to 9.4 $\mu\text{g L}^{-1}$ with a 50% rise to 26.9 $\mu\text{g L}^{-1}$ at Heathbrook West (HBW), over the preceding 10 months.

6.2.2.2 Alluvial groundwater monitoring network

Groundwater samples from the alluvial monitoring network (Fig. 6.2.2A) in Spring 2012 were log-normally distributed (Shapiro-Wilk $p = 0.11$) with a mean concentration of 1.8 $\mu\text{g L}^{-1}$. The spatial distribution of chlorinated ethenes (CEs) over the reach showed generally similar spatial patterns to the December 2011 campaign (Fig. 4.3.3, Chapter 4) and no CEs were detectable in BH4, BH6, BH11 or BH14 (Fig. 6.2.2A). BH1 was the only location where CE concentrations had reduced from 4.5 $\mu\text{g L}^{-1}$ (in December 2011) to 2.5 $\mu\text{g L}^{-1}$. Significant increases were observed at BH8 (from 0.5 $\mu\text{g L}^{-1}$ to 3.2 $\mu\text{g L}^{-1}$) and BH9 where the plume levels approximately doubled to 8.1 $\mu\text{g L}^{-1}$. The drainage ditch and seepage zone retained similar TCE concentrations at 6 and 3.1 $\mu\text{g L}^{-1}$, respectively with TCE only detectable in the 20 cm sampling level of MP26 at 5.1 $\mu\text{g L}^{-1}$. cDCE was the only daughter product found to be present (at trace levels) in the alluvial groundwater and

only in three locations with a maximum of $0.45 \mu\text{g L}^{-1}$ in the shallow sampling level of MP26 (Fig. 6.2.1B).

For the second snapshot in Summer 2012, the spatial distribution of the TCE in the bank side wells was found to be consistent with previous campaigns (Fig. 6.2.2B). TCE was again log-normally distributed ($p = 0.41$) with a mean of $1.9 \mu\text{g L}^{-1}$. The highest TCE concentration was again observed at BH9 ($8.3 \mu\text{g L}^{-1}$) with minimum concentrations ($\sim 0.1 \mu\text{g L}^{-1}$) found at BH7 and BH11 (Fig. 6.2.2B) whilst BH10 showed an increase to $7.2 \mu\text{g L}^{-1}$, representing almost a doubling of concentrations since March. Concentrations of TCE in the seepage zone ($5.1 \mu\text{g L}^{-1}$), drainage ditch ($4 \mu\text{g L}^{-1}$) and MP26 ($6.1 \mu\text{g L}^{-1}$) were all similar to the previous campaign. cDCE was the only daughter product found in the floodplain groundwater with considerably more detections than the Spring snapshot with a maximum of $1.2 \mu\text{g L}^{-1}$ in the surface water of the drainage ditch (Fig. 6.2.6B). BH5 also had a relatively high cDCE concentration ($1.1 \mu\text{g L}^{-1}$) where no previous sampling of this borehole showed any evidence of TCE dechlorination. The mean TCE concentration for this snapshot was not statistically different ($p = >0.05$) to the spring mean (based on a paired, two sample T-test) suggesting the overall distribution of plume in the alluvium had not changed appreciably between campaigns.

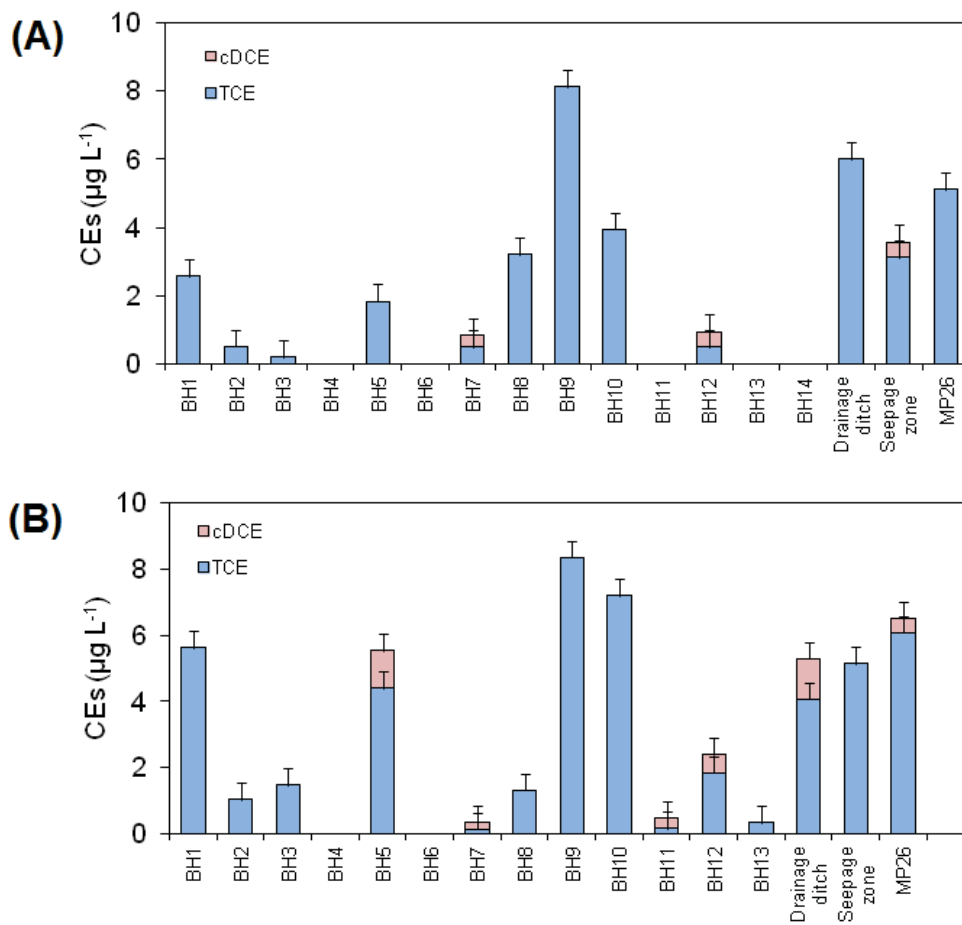


Fig. 6.2.2 Distribution of chlorinated ethenes (CEs) in the alluvial groundwater sampling locations for **(A)** Spring 2012 and **(B)** August 2012. Refer to Fig. 6.2.1B for the location of these monitoring points in the investigation area.

6.2.3 CE distributions in the riverbed

6.2.3.1 Spring 2012 snapshot

TCE concentrations in the riverbed (Fig. 6.2.3) were log-normally distributed (Shapiro-Wilk $p = 0.41$) and with a mean concentration of $16 \mu\text{g L}^{-1}$, a maximum of $44.3 \mu\text{g L}^{-1}$ at MP17 (100 cm) and a minimum of $4.51 \mu\text{g L}^{-1}$ at MP13 (20cm). The cross-channel concentration gradient apparent during the last sampling (December 2012, Chapter 4) was persistent at TB. At the 100 cm sampling depths, the highest TCE concentration ($37.2 \mu\text{g L}^{-1}$) was observed at MP12 on the Heathbrook Farm bank reducing to just $8.8 \mu\text{g L}^{-1}$ at MP16, on the opposite bank (Fig. 6.2.3A). Relatively high concentrations were observed in the downstream section of the longitudinal piezometer with levels in excess of $35 \mu\text{g L}^{-1}$ observed at 100 cm in MP17 ($44.3 \mu\text{g L}^{-1}$ at 80 cm), MP18 ($39.2 \mu\text{g L}^{-1}$ at 80cm) and MP20 ($42.3 \mu\text{g L}^{-1}$ at 80cm). The vertical variability of the plume within the top metre of the riverbed below Transect D is visualised in Fig. 6.2.3B. The position of the higher concentration ‘hotspot’ noted from the December campaign between MP17 and MP20 (Fig. 4.2.6, Chapter 4) was persistent. cDCE was observed in approximately 10% of pore water samples (Fig. 6.2.3C) mostly within the TA transect with a median concentration of $1.7 \mu\text{g L}^{-1}$ and a range of $0.9\text{--}4.6 \mu\text{g L}^{-1}$ (Fig. 6.2.3C). VC was detectable at trace levels ($\leq 1 \mu\text{g L}^{-1}$) in just 3 out of the 107 pore water samples (MP7 at 20 and 40 cm and MP13 at 20cm).

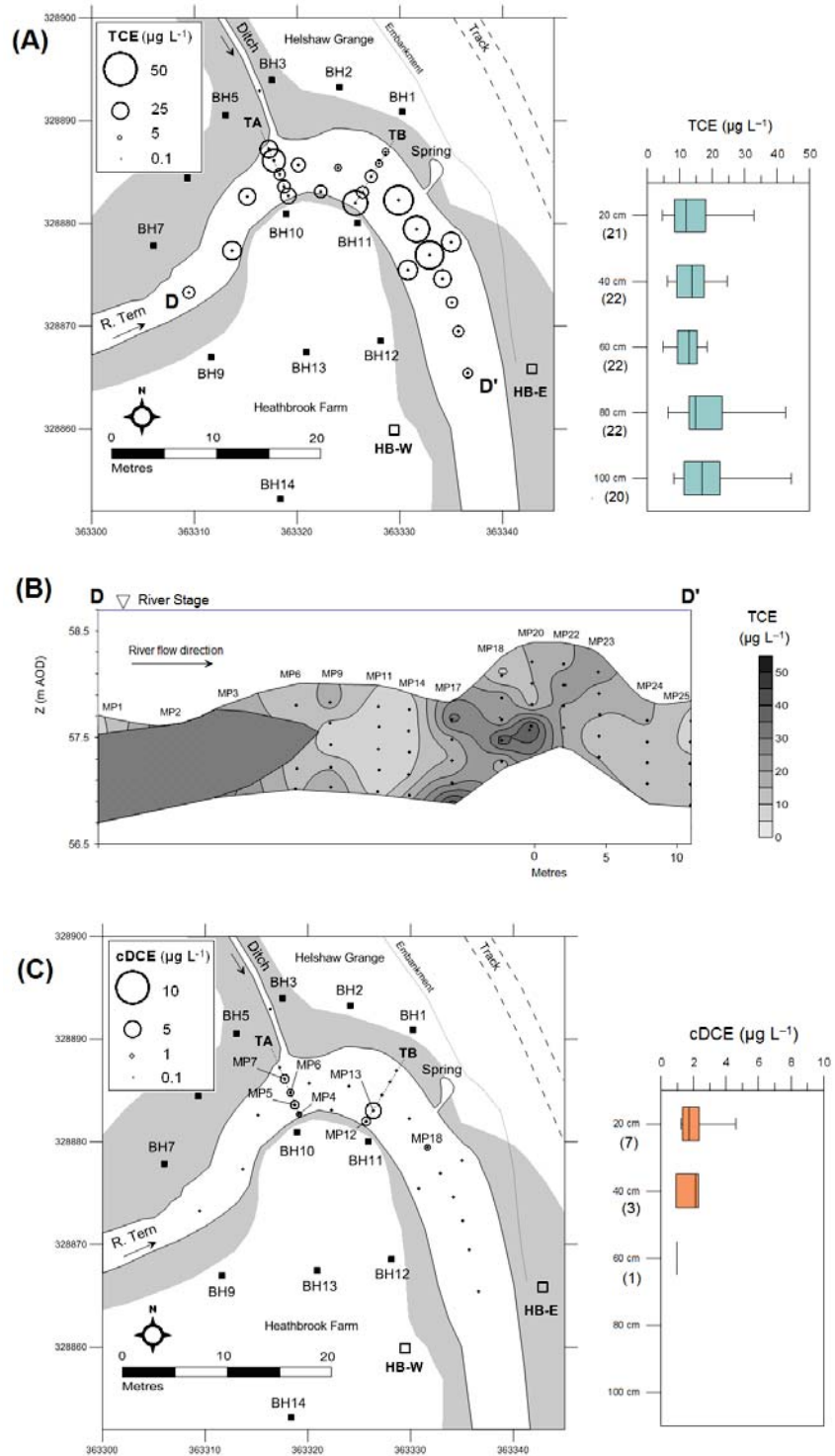


Fig. 6.2.3

(A) Spatial variability of maximum TCE concentrations for the Spring campaign, represented as scaled circles. Depth variability is included as box plots which present data as quartiles with the sample size indicated in parentheses. (B) Longitudinal interpolation of TCE concentrations along Transect D using Kriging. The solid grey area from MP1–MP3 denotes an area where samples could not be taken. (C) Spatial variability of maximum cDCE determined for the March campaign (as scaled circles). Depth variability is included as box plots as in (A).

6.2.3.2 *Summer 2012 snapshot*

The high flow events in July 2012 (Fig. 6.2.1A) significantly modified the topography of the riverbed along the channel margin at the head of the meander bend, removing up to 20 cm of the surficial sand layer in places. As a result, some of the 20 cm sampling tube openings (MP5, MP9, MP10, MP11, MP12 and MP13) were exposed to the surface water column and were not sampled. In the available samplers, TCE concentrations were again log-normally distributed ($p = 0.27$) with a mean of $13.6 \mu\text{g L}^{-1}$. As can be seen from Fig. 6.3.4, the spatial variation in TCE concentration was similar to the spring snapshot, as well as the December 2011 sampling (Chapter 4). This was confirmed by T-tests on paired sampling locations within the network which indicated no statistically significant differences ($p = >0.05$) between the means of each snapshot. MP18 (100 cm) had the maximum concentration of $39.4 \mu\text{g L}^{-1}$. In common with the previous snapshot campaigns, the concentration gradient at transect TB was apparent at the 100 cm sampling intervals ranging from $36.1 \mu\text{g L}^{-1}$ (at MP12) to $12.5 \mu\text{g L}^{-1}$, on the opposite bank at MP16. The upstream cross-channel piezometer transect (TA), showed a more significant gradient than that of the March campaign where the maximum concentration at 100 cm in MP8 of $34.5 \mu\text{g L}^{-1}$ reduced to $15.9 \mu\text{g L}^{-1}$ at the 80 cm level of MP4 on the opposite side of the channel, at Heathbrook Farm (Fig. 6.2.4A). cDCE was detected at 10 locations (10% of samples) in the riverbed with the highest at 40 cm in MP7 ($6.9 \mu\text{g L}^{-1}$) and the lowest at 40 cm in MP19 ($0.7 \mu\text{g L}^{-1}$). This was consistent with previous daughter product detections across the mini-piezometer transects. VC was only confirmed twice during the August campaign at 20 cm in MP18 ($0.5 \mu\text{g L}^{-1}$) and at MP23 ($0.7 \mu\text{g L}^{-1}$).

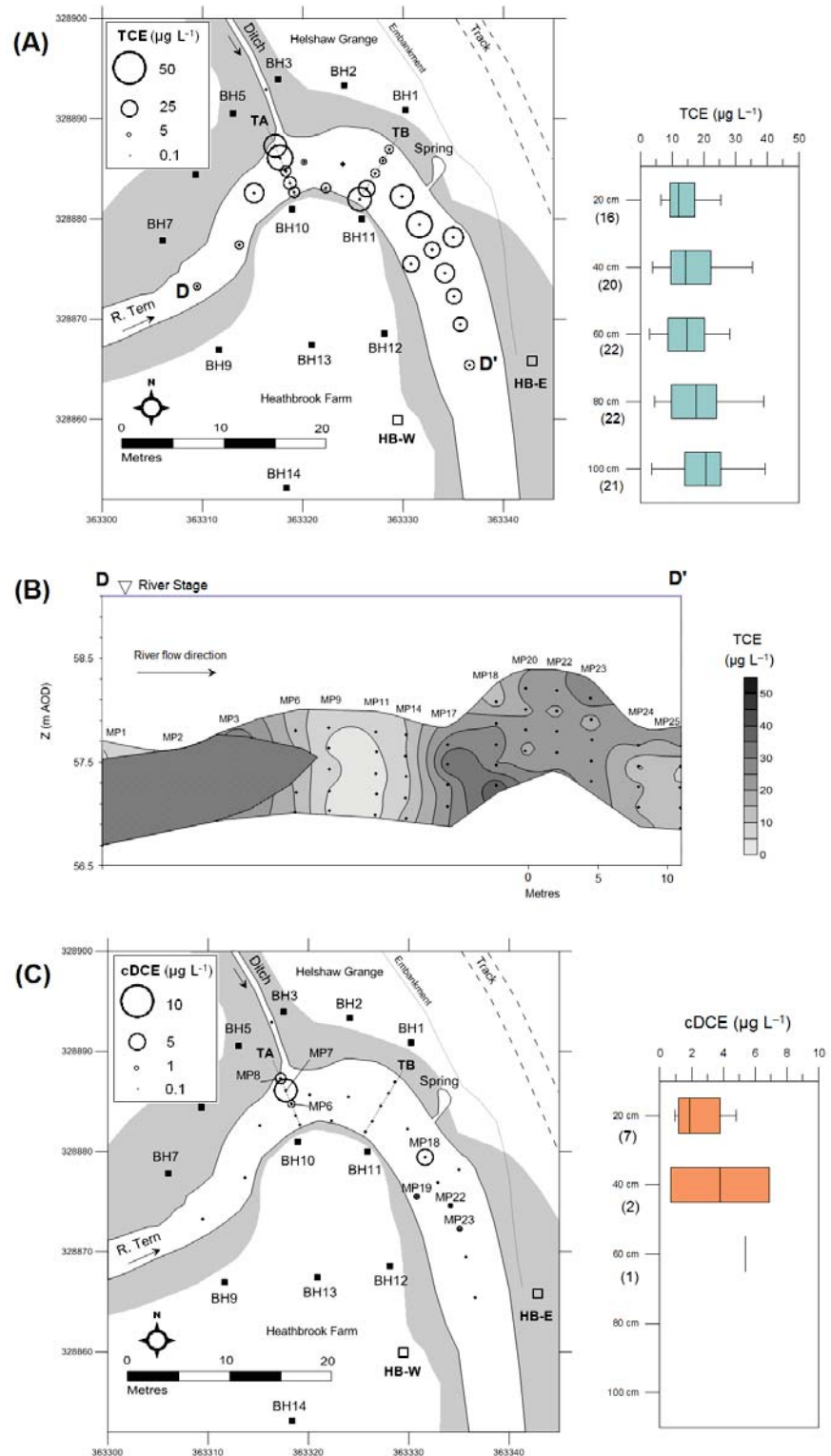


Fig. 6.2.4 (A) Spatial variability of maximum TCE concentrations for the Summer snapshot, represented as scaled circles. Depth variability is included as box plots which present data as quartiles with the sample size indicated in parentheses. (B) Longitudinal interpolation of TCE concentrations along Transect D using Kriging. The solid grey area from MP1–MP3 denotes an area where samples could not be taken. (C) Spatial variability of maximum cDCE determined for the March campaign (as scaled circles). Depth variability is included as box plots as in (A).

6.2.3.3 *Spatial variability of CEs at 'plot-scale'*

The persistent daughter product detections at MP7 (Fig. 6.2.4A), coupled with observations of organic-rich sediment accumulation beneath submerged *Ranunculus* stands, prompted a high-resolution sampling of the shallow pore water environment to investigate the possibility of locally-enhanced reductive dechlorination in this area. Due to clogging of the sampling tubes at some locations, it was only possible to sample 7 out of 13 locations at 30 cm and 11 out of 13 at 20 cm. TCE was again log-normally distributed ($p > 0.05$) and detectable in all but 4 samples from the array with a highly heterogeneous distribution over investigated depths (Fig. 6.2.5). However, comparison of means from 5, 10 and 20 cm did not reveal any statistically significant differences ($p > 0.05$) based on one-way analysis of variance (ANOVA). TCE concentrations declined along the array with a mean at the head of $10.7 \mu\text{g L}^{-1}$ in comparison to $1.4 \mu\text{g L}^{-1}$ at the tail. This difference was statistically significant ($p = < 0.05$) based on T-test results. In contrast to the preceding sampling campaigns, cDCE was widespread and observed in 75% of samples (Fig. 6.2.5). The highest concentrations were found at 10 cm in; PW4 ($15.87 \mu\text{g L}^{-1}$), PW11 ($13.1 \mu\text{g L}^{-1}$) and PW13 ($12.1 \mu\text{g L}^{-1}$). cDCE was not detectable in an adequate number of paired head-tail samplers to enable a comparison to be made between sections of the array, however, the overall mean was $1.6 \mu\text{g L}^{-1}$. VC was above detection limit in 27% of samples with an overall average concentration of $1 \mu\text{g L}^{-1}$. It was not possible to compare means of VC due to the majority of detections being concentrated in the tail section of the array, particularly at PW7 (maximum of $2.34 \mu\text{g L}^{-1}$ at 5 cm). PW4 was the only upstream pore water sampler to exhibit VC detections with a concentration range of $0.2\text{--}0.8 \mu\text{g L}^{-1}$.

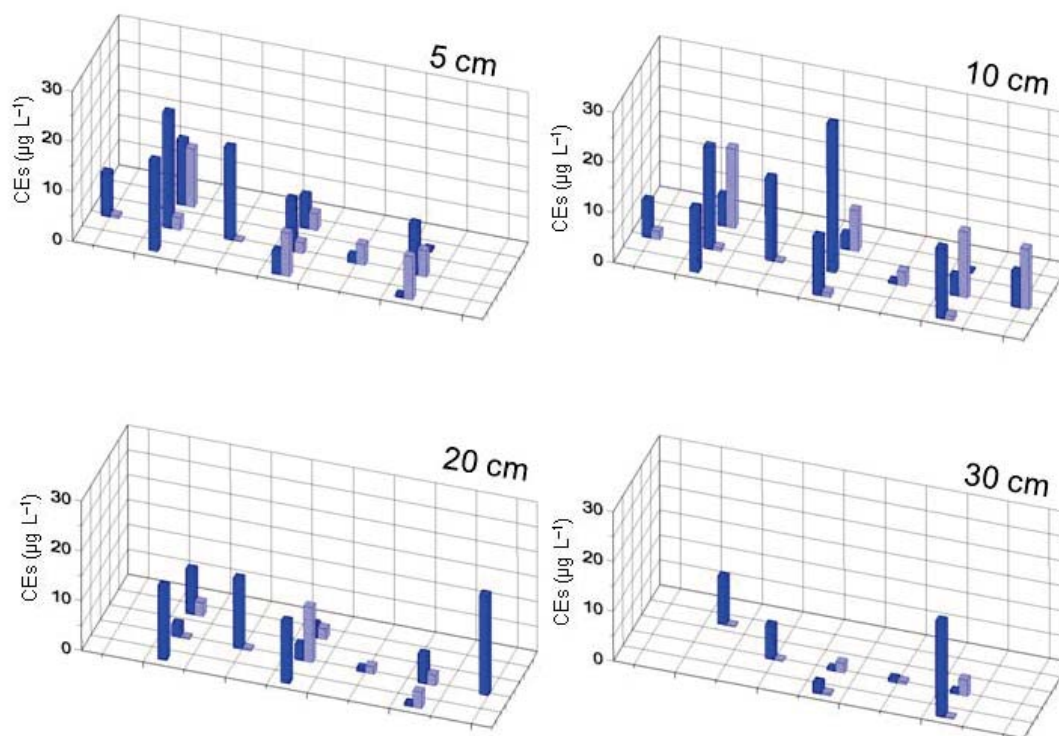


Fig. 6.2.5 Spatial variability of chlorinated ethenes in the plot-scale array. TCE is indicated by dark blue and cDCE by light blue (VC not shown). See Fig. 6.2.1B for the location of the array and Fig. 6.2.1C for the names of individual samplers.

6.2.4 Quantification of TCE reductive dechlorination

Because it was not possible to detect the non-chlorinated end product ethene and cDCE or VC were not generally detected in stoichiometric amounts, a mass balance evaluation for TCE degradation was unobtainable. In the absence of isotopic data, the extent of reductive dechlorination of TCE can be quantified using the metrics described in Chapter 2 (Section 2.6). The chlorine number (N_{Cl}) provides a useful metric that integrates daughter product observations into a single number (Weaver et al., 1997; Freitas et al., 2015) which was calculated using Equation 2.7 (in Chapter 2). Given that ethene data were not available, the lowest chlorine number possible was 1, (indicating complete dechlorination of TCE to VC) whereas an $N_{Cl} = 3$ indicated that no dechlorination had taken place with the plume consisting entirely of TCE.

6.2.4.1 *Reach-scale reductive dechlorination activity*

Fig. 6.2.6 presents the calculated N_{Cl} values for the four sampling campaigns of this study (both in the riverbed and in the alluvial groundwater system) plotted against the total CE concentration (in nmol). For clarity, only samples exhibiting cDCE and VC detections are included (e.g., $N_{Cl} < 3$). Fig. 6.2.6A presents observations from the initial monitoring campaign in September 2011 where it can be seen that all N_{Cl} values are > 2 , indicating only weak dechlorination had taken place (MP13, 20 cm and BH11 have the lowest N_{Cl} at 2.33 and 2.1, respectively). The December campaign (Fig. 6.2.6B) proved to have the highest number of daughter product detections in the riverbed together with the lowest chlorine numbers (indicating the highest level of in-situ degradation). No locations exhibited an N_{Cl} of < 2 , although significant conversion of TCE towards cDCE was indicated for MP13 (2.14) and MP18 (2.12). In the alluvial groundwater system, lower chlorine numbers were associated with low total CE concentrations (e.g., < 30 nmol) indicating near-complete conversion to cDCE, suggesting that dechlorination efficiency was sensitive to contaminant concentration. Note, however, this is clearly not the case with the higher concentrations at MP13 (344 nmol) and MP18 (458 nmol).

The March 2012 campaign (Fig. 6.2.6C) had the weakest level of in-situ dechlorination of all snapshots, indicated by the majority of calculated chlorine numbers > 2.7 . Although MP13 was consistent with previous campaigns at 2.22, MP18 did not show the same activity as observed in December (Fig. 6.2.6B). For the August campaign (Fig. 6.2.6D), a large number of the 20 cm sampling levels that previously showed dechlorination activity were unavailable to re-sample due to erosion of the surficial sediment and it was not possible to verify the persistence of reactive areas (e.g., MP13). Similar to the March 2012 campaign, the remaining mini-piezometer samples showed a relatively high N_{Cl} with the

majority being >2.7 , again indicating weak in-situ reduction of TCE. However, MP7 at 60 cm deep showed a greater activity than in previous campaigns ($N_{Cl} = 2.28$) with a large number of samples from the alluvial aquifer showing evidence of weak in-situ dechlorination. BH7 and BH11 proved to be relatively persistent degradation zones with N_{Cl} values of <2.5 , therefore indicating partial conversion of TCE to cDCE.

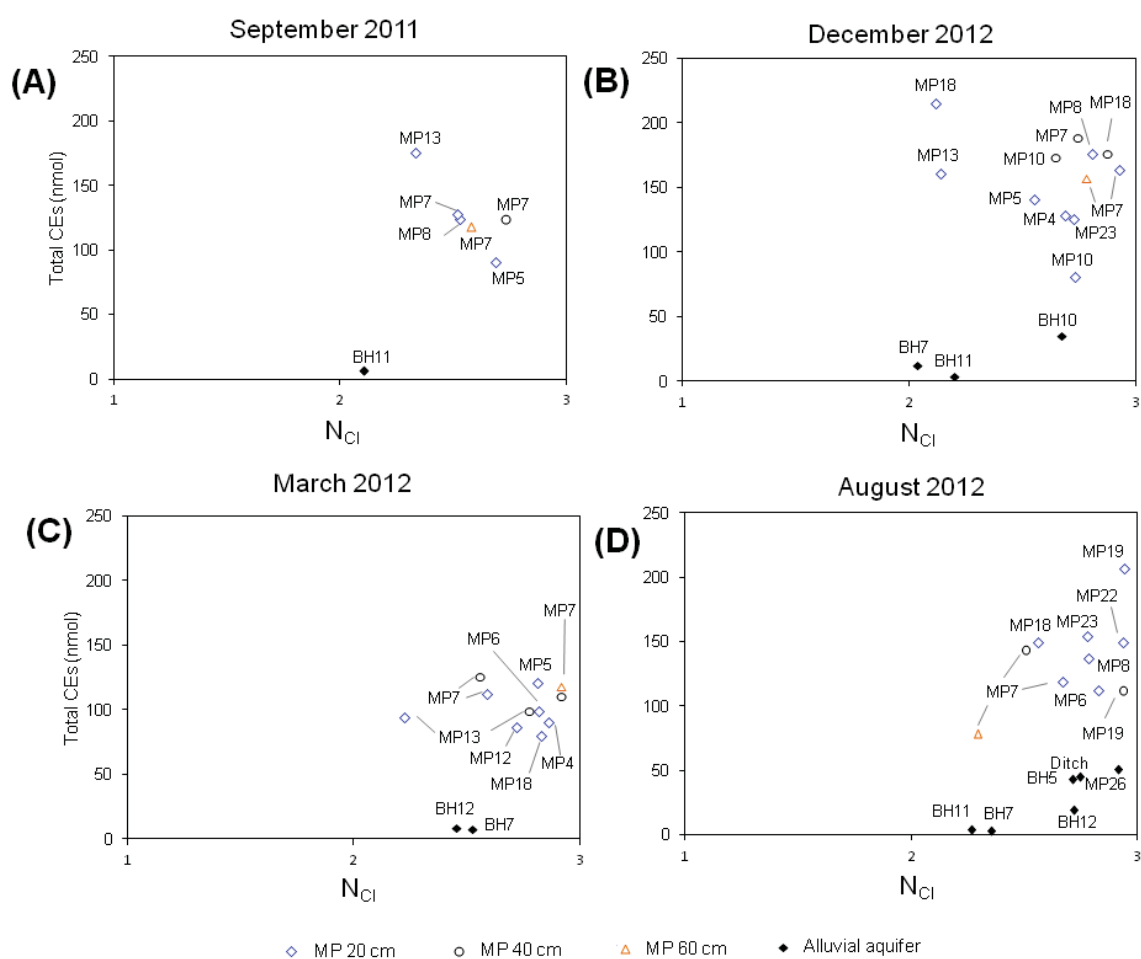


Fig. 6.2.6 Annotated TCE reductive dechlorination activity diagrams for both the riverbed and alluvial groundwater samples for all four CE monitoring campaigns in **(A)** September 2011 **(B)** December 2012 (which formed part of the plume delineation campaign in Chapter 4) **(C)** March 2012 and **(D)** August 2012. Depths and locations of samples are coded according to the key at the bottom of the figure.

6.2.5.2 *Plot-scale reductive dechlorination activity*

Fig. 6.2.7 illustrates the extent of reductive dechlorination of the plume observed in the shallow grid of pore water samplers (Fig. 6.2.1C) which have been separated by location along the array to aid in interpretation. Samples from the head of the array (Fig. 6.2.7A) exhibited chlorine numbers comparable in range to that of the reach-scale mini-piezometers, sampled at the same time in August (Fig. 6.2.6D). PW2 showed no dechlorination ($N_{Cl} = 3$) with PW4 showing the greatest activity at 10 cm (2.14) which was similar to the 20 cm levels of MP13 (2.14) and MP18 (2.12) in the December 2011 campaign (Fig. 6.2.6B). Fig. 6.2.7B presents the three central pore water samplers (PW6–8) situated between the head and tail sections (Fig. 6.2.1C). This area of the array had considerable variability in dechlorination activity with PW6 (10–30 cm) showing similar weak activity ($N_{Cl} = >2.7$) to that of the head section. However, PW7 (20 and 30 cm) exhibited an N_{Cl} value of <2 which was lower than all other samples from the plume. This chlorine number indicates that the majority of the organically-bound chlorine in the plume is in the form of cDCE. The tail section of the array (Fig. 6.2.7C) also exhibited lower values of N_{Cl} with all depth samples of PW9 being less than 2 (range 1.60–1.83). PW10 was similar, exhibiting values from 2.03–2.09 which were comparable to the lowest N_{Cl} estimated for the reach scale network at BH7 in the December campaign (Fig. 6.2.6B). These findings suggest a locally-enhanced dechlorination potential was present in the shallow sediment (PW7 to PW13) investigated by the array.

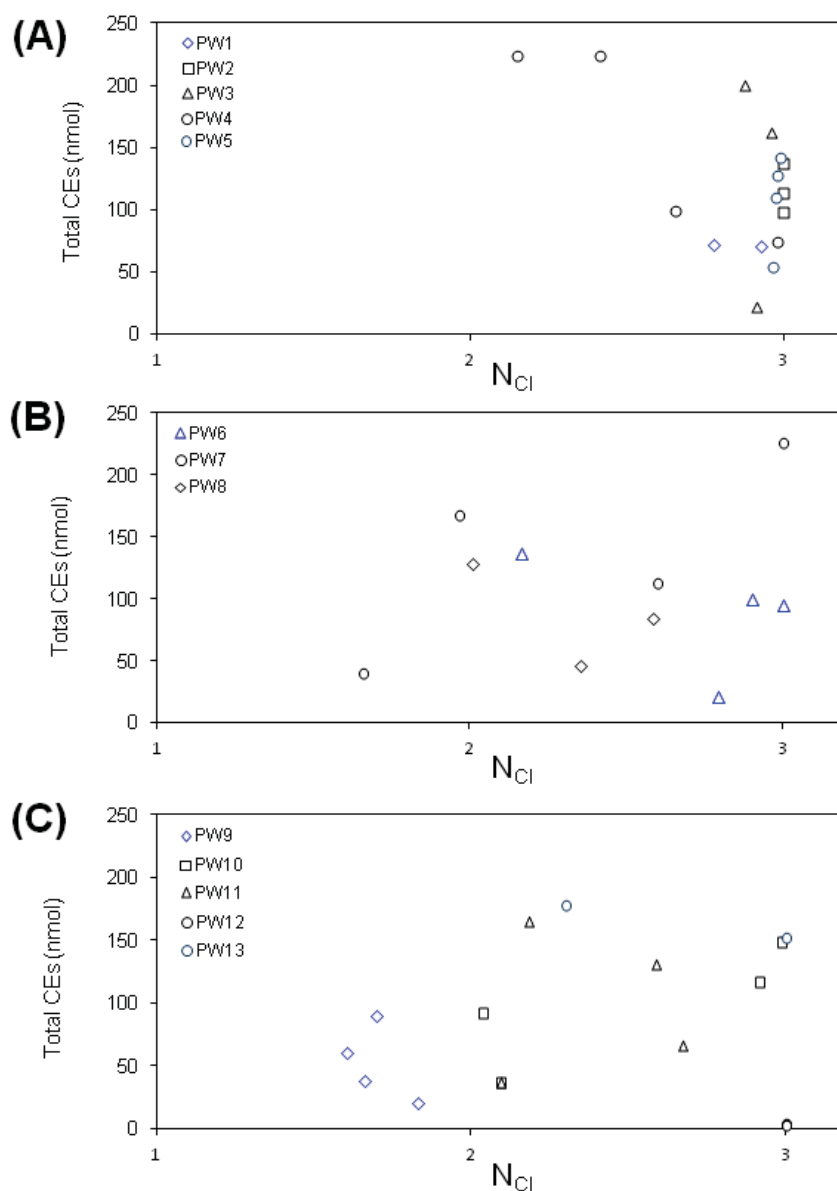


Fig. 6.2.7 Reductive dechlorination activity diagrams for the plot scale samplers. Samples are grouped into different plots where **(A)** are samples acquired at the head of the array, **(B)** mid-point and **(C)** the tail section. Refer to Fig. 6.2.1C for the locations of individual samplers and Fig. 6.2.1B for the location of the plot scale array within the wider reach.

6.3 Variation in redox conditions

6.3.1 Groundwater redox conditions

6.3.1.1 Permo-Triassic sandstone in Spring 2012

Groundwater samples from all the Permo-Triassic sandstone (PTS) boreholes were aerobic, even to a depth of 80 m, at the bottom of HGA (Table 6.2) and had a median DO concentration of 5.63 mg L⁻¹. NO₃⁻ was elevated throughout the PTS with a median concentration of 55.3 mg L⁻¹ (as NO₃⁻) with increased levels in the down-gradient boreholes (Fig. 6.3.1B) at 81.1 mg L⁻¹ (HBE) and 73.1 mg L⁻¹ HBW (Table 6.2). High NO₃⁻ concentrations would be expected in the area given the nitrate vulnerable zone designation of the study area (DEFRA, 2004) and aerobic conditions present in the PTS. SO₄²⁻ was present in the samples from the PTS with a median of 34.2 mg L⁻¹ which did not vary significantly between boreholes. As would be expected for aerobic conditions, dissolved Fe and Mn were below detection limits in all samples. Dissolved CH₄ was present at trace levels just above the limit of detection with a median of 0.16 µg L⁻¹ and showed little variation. These concentrations are approximately 12% of atmospheric equilibrium saturation suggesting that net consumption had taken place during groundwater recharge. These results are consistent with Darling and Goody (2006) who also found CH₄ to be present at trace levels in the unconfined Permo-Triassic sandstone of the East Midlands of England. DOC concentrations were low (median of 1.6 mg L⁻¹) and the highest concentrations were found at the shallowest depth sampled in HGA (2.19 mg L⁻¹ at 35 m) and HGO (2.01 mg L⁻¹ at 20 m). On the floodplain, HBE and HBW had similarly low DOC concentrations at 2.14 and 1.94 mg L⁻¹, respectively.

Table 6.2 Concentrations of redox-sensitive species and dissolved organic carbon (DOC) determined for HydraSleeve samples from the Bridgnorth sandstone in March 2012. Sample depths are indicated in parentheses for multi-level samples.

Borehole	DO	NO ₃	SO ₄	Fe	Mn	CH ₄	DOC
	(mg L ⁻¹)	(µg L ⁻¹)	(mg L ⁻¹)				
HGA (35 m)	5.13	66.2	24.8	<0.07	<0.05	0.16	2.19
HGA (60 m)	6.61	53.1	23.1	<0.07	<0.05	0.18	1.64
HGA (80 m)	6.2	66.7	20.0	<0.07	<0.05	0.16	1.35
HGO (20 m)	5.63	55.3	21.2	<0.07	<0.05	0.17	2.01
HGO (40 m)	5.01	52.8	20.5	<0.07	<0.05	0.15	1.58
HBE	6.35	81.1	28.4	<0.07	<0.05	0.14	2.14
HBW	6.79	73.0	22.0	<0.07	<0.05	0.17	1.94

6.3.1.2 Alluvial groundwater system in Spring 2012

The distribution of redox-sensitive solutes for the spring snapshot is presented in Fig. 6.3.1. All solute concentrations followed either normal or log-normal distributions ($p > 0.05$). DO concentrations (Fig. 6.3.1A) displayed considerably more variability than the PTS with a mean of 3.5 mg L⁻¹ in March 2012. The highest DO concentrations were measured in the drainage ditch (8.42 mg L⁻¹) and the seepage zone (6.69 mg L⁻¹). Three locations were anaerobic including BH7, BH11 and the 100 cm level of MP26 installed in the bed of drainage ditch. BH6, BH13 and the 20 cm of MP26 also had low DO levels of <3 mg L⁻¹ (Fig. 6.3.1A). NO₃⁻ concentrations were highly variable (Fig. 6.3.1B) with a mean of 27.1 mg L⁻¹ and ranged from 4 mg L⁻¹ at MP26 (100 cm) to 203 mg L⁻¹ at BH1 with the seepage zone also having elevated NO₃⁻ at 133 mg L⁻¹. All of the anaerobic locations had NO₃⁻ levels of <5 mg L⁻¹ (apart from BH11 at 9.3 mg L⁻¹). SO₄²⁻ had a mean of 24.6 mg L⁻¹ with the highest levels associated with BH4 (61 mg L⁻¹) and BH1 (57.8 mg L⁻¹) on the eastern edge of the site (Fig. 6.3.1C). Relatively low concentrations were associated with the anaerobic locations BH7 (6.2 mg L⁻¹) and MP26 100 cm (7 mg L⁻¹) but

not at BH11 (26.6 mg L⁻¹) indicating possible SO₄²⁻ reduction. However, low SO₄²⁻ was also found at BH9 (9 mg L⁻¹) and BH6 (5 mg L⁻¹), which were aerobic, suggesting an influence of background variability in groundwater SO₄²⁻ rather than in-situ SO₄²⁻ reduction. Mn was detectable at three locations (Fig. 6.3.1D) including BH6 (0.93 mg L⁻¹), BH7 (1.03 mg L⁻¹), BH11 (0.71 mg L⁻¹) suggesting some evidence of reductive dissolution of Mn, although only anaerobic conditions were present at BH7 and BH11. Dissolved CH₄ (Fig. 6.3.1E) displayed a high degree of variability spanning three orders of magnitude and ranged from 0.26 µg L⁻¹ (at BH1) to 469 µg L⁻¹ at MP26 (100 cm) with all values greater than those of the up-gradient aquifer. Mean CH₄ concentrations were 2.88 µg L⁻¹ and air-saturation equivalents ranged from <50% to greater than 300-fold (at MP26), suggesting significant methanogenic activity within the bed sediments of the drainage ditch. The ditch water at 2.8 µg L⁻¹ and seepage zone (2.4 µg L⁻¹) also had air over-saturations of 2 and 1.7 times, respectively indicating these flows to be net sources of CH₄ to the atmosphere.

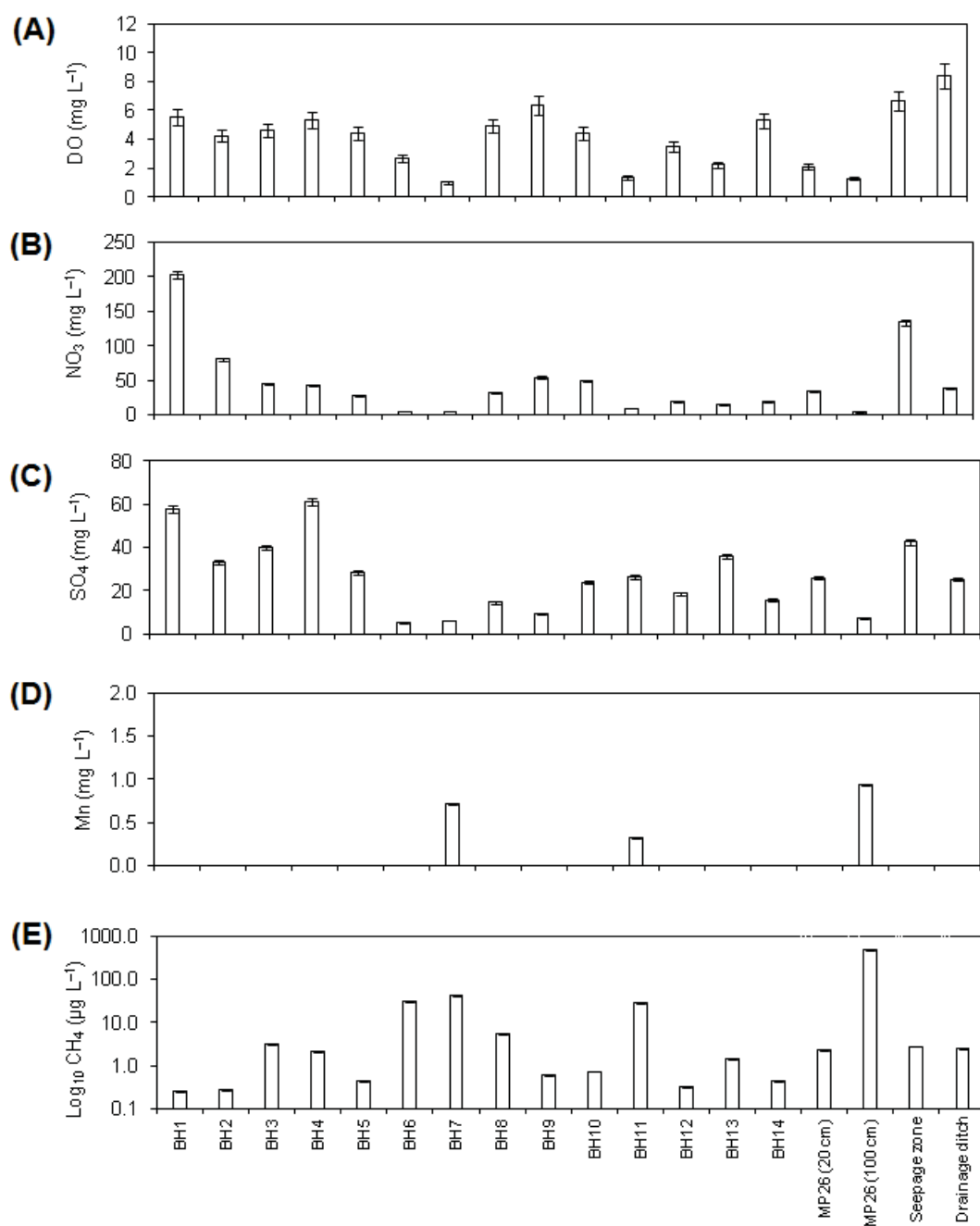


Fig. 6.3.1 Distribution of redox sensitive solutes in the alluvial groundwater monitoring network in Spring 2012. **(A)** Dissolved oxygen (DO) **(B)** nitrate (NO₃) **(C)** sulphate (SO₄) **(D)** soluble manganese (Mn) (assumed to be mostly Mn²⁺) and **(E)** dissolved methane (log₁₀-scaled CH₄). See Fig. 6.3.1A for the time of sampling and 6.3.1B for the location of these monitoring points.

6.3.1.3 *Alluvial groundwater system in Summer 2012*

Solute concentrations (DO, NO_3^- , SO_4^{2-} and CH_4) of the summer snapshot (Fig. 6.3.2) also followed normal or log-normal distributions ($p = >0.05$) which enabled the parametric comparison of means (using T-tests) from paired monitoring points in the spring campaign. Mean DO was lower in the summer campaign at 2.35 mg L^{-1} and was statistically significant ($p = <0.05$). DO ranged from 0.65 mg L^{-1} at BH5 to 6.21 mg L^{-1} at BH9 (Fig. 6.3.2A), whilst a greater number of locations exhibited anaerobic conditions, including BH3, BH5–BH7, BH11, BH12 and both levels of MP26 (Fig. 6.3.2A). Summer NO_3^- concentrations (Fig. 6.3.2B) had a mean of 20.3 mg L^{-1} which declined significantly ($p = <0.05$) from the spring mean. High NO_3^- at BH1 (193 mg L^{-1}) and the seepage zone (99.9 mg L^{-1}) were persistent. Minimum NO_3^- was observed in the anaerobic location BH6 (3.32 mg L^{-1}) with substantial decreases at the other anaerobic locations such as BH5, which declined by 85% to 3.94 mg L^{-1} . This suggests an increased level of NO_3^- attenuation in the alluvial groundwater system in summer. SO_4^{2-} variation in summer (Fig. 6.3.2C) was very similar to spring with a mean of 27.1 mg L^{-1} , which was not statistically different from the spring mean ($p = >0.05$). In contrast to the spring campaign, dissolved Mn was detectable at 13 out of 17 monitoring locations in the alluvial aquifer (Fig. 6.3.2D) including all anaerobic locations with a median concentration of 0.45 mg L^{-1} . In the denitrified locations, Mn ranged from 0.012 at BH12 to 1.69 at BH5 with Mn also prevalent in the anaerobic location BH3 (1.07 mg L^{-1}). NO_3^- was also present (32.5 mg L^{-1}) suggesting mixed redox conditions at BH3.

Mn was detectable in the drainage ditch (0.12 mg L^{-1}) and at the seepage zone (0.6 mg L^{-1}) despite aerobic conditions, suggesting a much higher prevalence of Mn-reduction in the alluvium during summer. Fe was also detected more frequently in summer (Fig. 6.3.2E). BH5–BH7 had significant Fe concentrations ($1.7\text{--}4.4 \text{ mg L}^{-1}$), coupled with low NO_3^- and

greater Mn, which suggests metal-reducing conditions were present in these wells with Fe-reducing conditions remaining similar to that of spring at MP26 (100 cm). The average CH₄ for the alluvial system displayed a significant rise ($p = <0.05$) to the summer mean of 29.6 $\mu\text{g L}^{-1}$ representing an average over-saturation of 21 times atmospheric equilibrium concentrations. All locations showed an increase in CH₄ (Fig. 6.3.2F) from 1.6 times the March concentration at BH1 (0.42 $\mu\text{g L}^{-1}$) and BH2 (0.43 $\mu\text{g L}^{-1}$) to as much as 634 times at BH5 at 506.1 $\mu\text{g L}^{-1}$, representing an air-equivalent over saturation of 367-fold. The drainage ditch dissolved CH₄ levels increased by 20 times to 48.7 $\mu\text{g L}^{-1}$ with an increase of 8 times for the seepage zone at 23.4 $\mu\text{g L}^{-1}$. These concentrations represent an over-saturation of 17 and 35 times, respectively, (in relation to atmospheric saturation) indicating that these groundwater discharge features are seasonally persistent sources of CH₄ to the atmosphere. DOC had a median concentration of 5.46 mg L^{-1} (Fig. 6.3.2G) which was approximately 3-fold greater than the PTS aquifer determined during the March campaign (Table 6.2). The highest DOC concentrations were observed in the drainage ditch at 9.9 mg L^{-1} with BH5 also being elevated (9.1 mg L^{-1}). The lowest DOC concentrations were observed at BH1 (2.4 mg L^{-1}), BH2 (3.2 mg L^{-1}) and BH9 (also 3.2 mg L^{-1}) which were only slightly higher than the underlying sandstone groundwater.

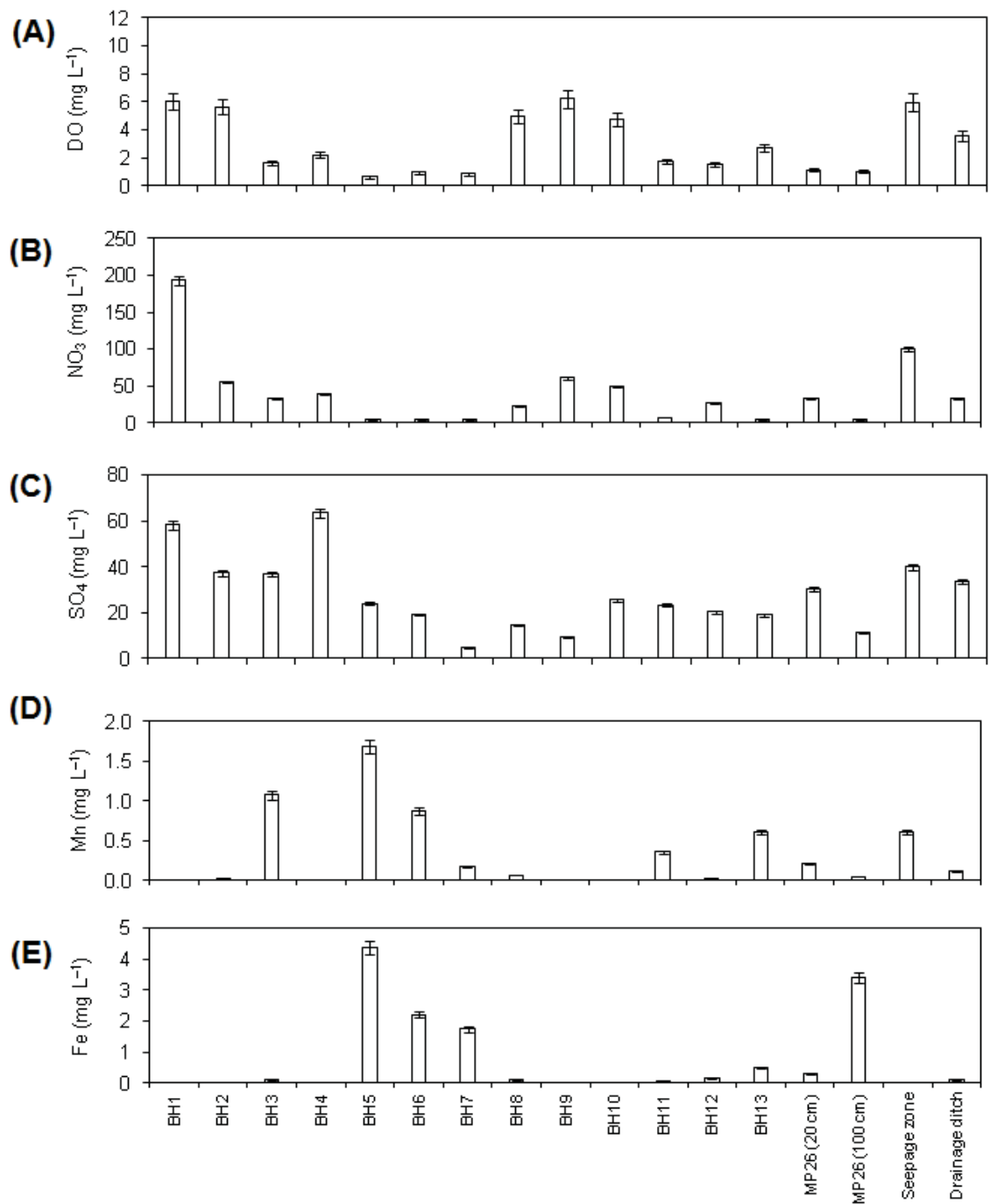


Fig. 6.3.2 Distribution of redox sensitive solutes in the alluvial groundwater monitoring network in Summer 2012. (A) Dissolved oxygen (DO) (B) nitrate (NO₃) (C) sulphate (SO₄) (D) soluble manganese (Mn) (assumed to be mostly Mn²⁺) and (E) dissolved iron (Fe) which is assumed to be predominantly the reduced (Fe²⁺) form.

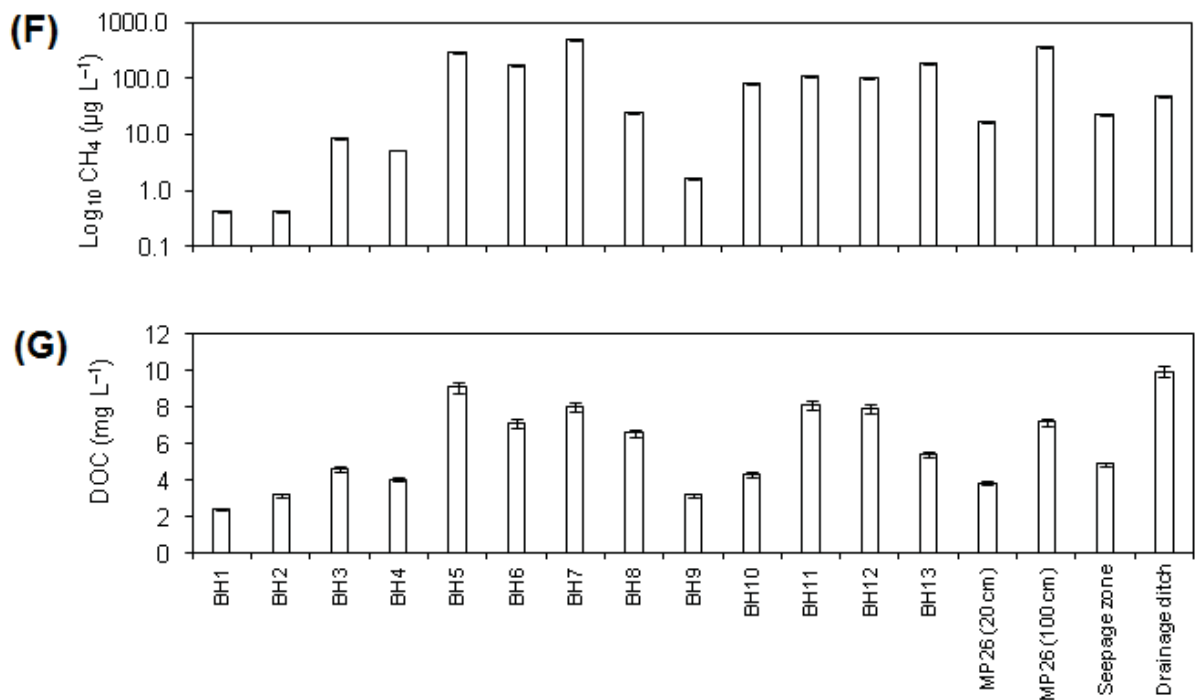


Fig. 6.3.2 Contd. Distribution of redox sensitive solutes in the alluvial groundwater monitoring network in Summer 2012. **(F)** Dissolved methane (log_{10} -scaled CH_4) **(G)** dissolved organic carbon (DOC). See Fig. 6.3.1A for the time of sampling and 6.3.1B for the location of these monitoring points.

6.3.2 Redox environment of the riverbed at reach-scale

All the pore water hydrochemical data from the riverbed mini-piezometers did not conform to either a normal or log-normal distribution (Shapiro-Wilk $p = <0.05$) over both snapshots. Therefore, non-parametric statistics were used for descriptors and comparisons. A subset of 16 mini-piezometers (where the 20 and 100 cm depth intervals could be sampled over the two campaigns) were used to compare medians (Mann-Whitney U-tests) at the two depths to determine whether any significant changes had occurred during transport through the riverbed. Differences in these medians between sampling snapshots were also examined. Chloride was also determined during snapshots for use as a geochemical tracer (data is included in Appendix D2) to investigate hyporheic mixing.

However, its concentration ranges in the groundwater and surface water end-members at the site were not sufficiently distinctive for it to be suitable for this purpose.

6.3.2.1 *Redox conditions in the riverbed in Spring 2012*

The riverbed was mostly aerobic during the spring campaign with much of the depth-dependent DO variability concentrated in the 20–60 cm sampling intervals (Fig. 6.3.3A). All sampling depths had DO concentration less than that of the overlying river of 11.52 mg L⁻¹ (99% saturation) with some locations showing anaerobic conditions at the 20 cm interval of the TA transect, MP10, MP12, MP13 and MP18 (Fig. 6.2.4A) with the lowest DO concentration at MP7 (1 mg L⁻¹). Comparison of medians at 20 cm and 100 cm (from the 16 mini-piezometers subset) revealed statistically significant differences in medians (3.14 mg L⁻¹ at 20 cm) and (6.7 mg L⁻¹ at 100 cm) using Mann-Whitney U test ($Z = -2.76$, $p = 0.006$). This represented an overall 47% apparent decrease in DO concentrations from 100 to 20 cm. NO₃⁻ showed significant spatial variability along the reach (Fig. 6.3.3B) as well as some vertical variability. High NO₃⁻ concentrations (>100 mg L⁻¹) were notable at MP11, MP15 and MP16 reaching a maximum of 157 mg L⁻¹ at 80 cm in MP16, close to BH1 on the bank (Fig. 6.3.3B) which also had elevated NO₃⁻. No locations showed near-complete denitrification like those associated with the anaerobic locations in the alluvial aquifer. However, lower NO₃⁻ concentrations (<35 mg L⁻¹) were observed at the shallowest sampling levels of the TA transect piezometers (as well as MP13, 20 cm). NO₃⁻ in the river water (38.8 mg L⁻¹) was less than those of the majority of the 20 cm sampling levels, suggesting the reach was a source of NO₃⁻ to the river at the time of sampling. Median concentrations were observed to decrease significantly ($Z = -2.55$, $p = 0.01$) from 100 cm (57 mg L⁻¹) to 20 cm (50 mg L⁻¹), producing an apparent NO₃⁻ attenuation of some 13%. SO₄²⁻ showed spatial variability along the reach but no significant ($p = >0.05$) vertical

variability (Fig. 6.3.3C) with all depths exhibiting concentrations less than that of the overlying river water (58 mg L^{-1}).

Dissolved Mn was only detectable at two 20 cm depth locations that were anaerobic, including MP5 (0.68 mg L^{-1}) and MP7 (0.32 mg L^{-1}), suggesting weak Mn-reduction at these locations. CH_4 (Fig. 6.3.3E) proved to be highly spatially variable, both laterally and vertically, with an exceptionally high value ($3053.7 \text{ } \mu\text{g L}^{-1}$) observed at MP13 (20 cm). From Fig. 6.3.3E, it can be seen that apparent methanogenic activity was localised within specific areas of the riverbed, particularly at the TA piezometer transect, MP11–MP14, MP18 and MP19. All mini-piezometer locations had air under-saturated concentrations (e.g., $<1.38 \text{ } \mu\text{g L}^{-1}$) below 80 cm. Apparent methanogenic activity was confined to levels between 60 and 20 cm below the sediment-water interface (Fig. 6.3.3E). Comparison of medians at 20 cm ($1.05 \text{ } \mu\text{g L}^{-1}$) and 100 cm ($0.47 \text{ } \mu\text{g L}^{-1}$) indicated a significant difference ($Z = -3.84$, $p = <0.001$), representing a 2-fold increase in concentrations over this depth range. River water CH_4 concentrations were $3.8 \text{ } \mu\text{g L}^{-1}$ or just under three times air-oversaturation.

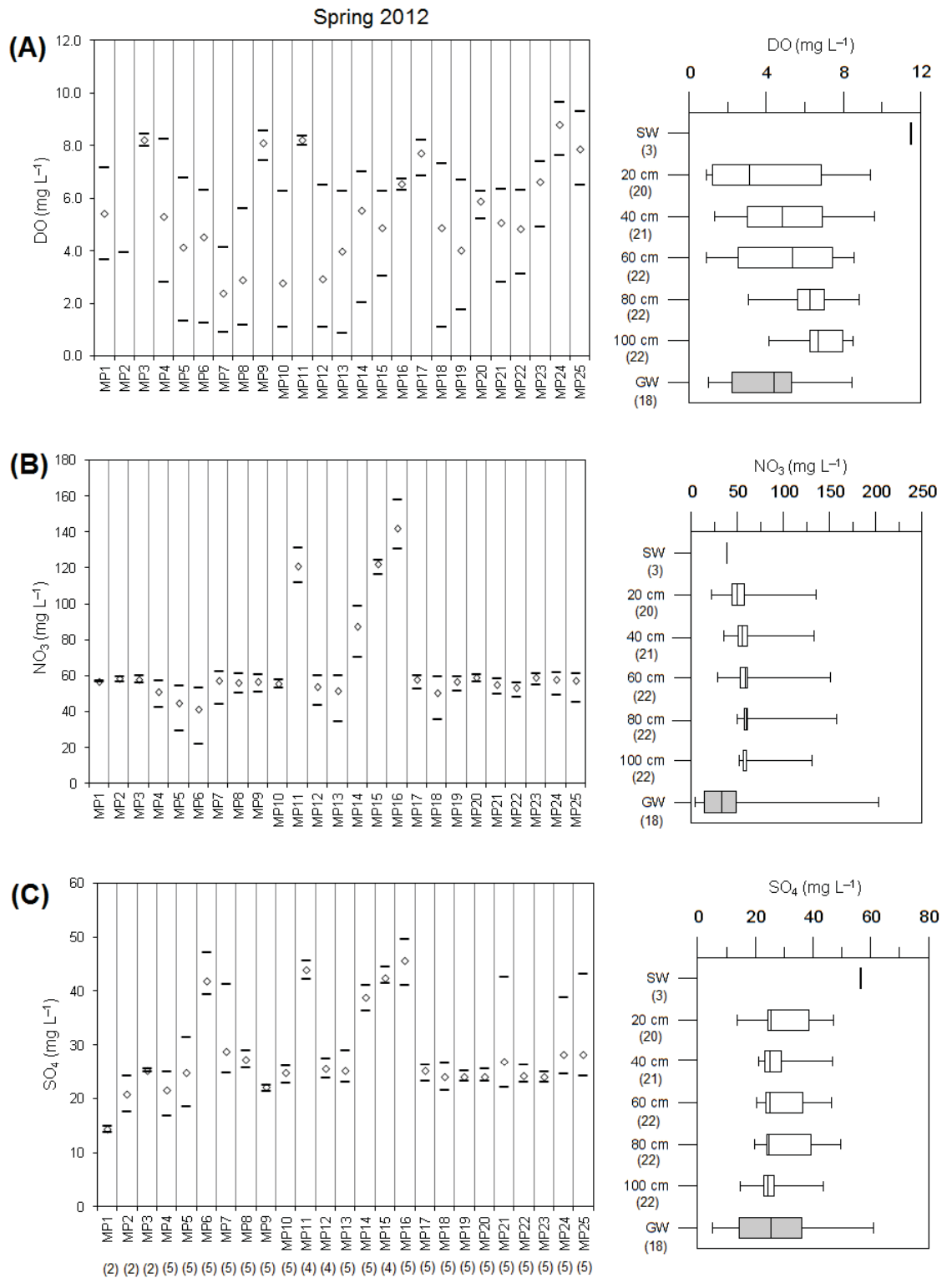


(Figure caption overleaf)

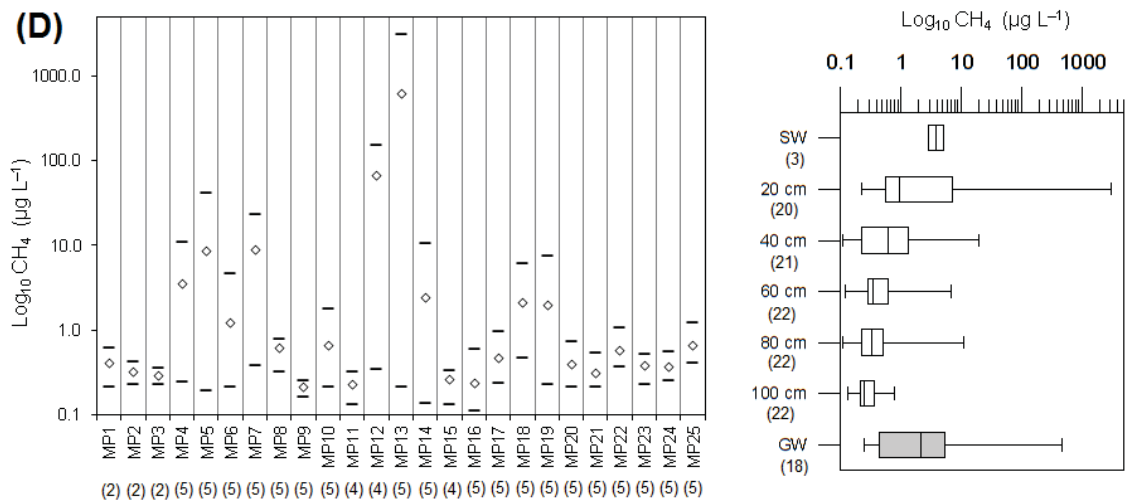


Fig. 6.3.3 Hydrochemical variables of the Spring 2012 snapshot, illustrating the reach-scale spatial variability of (A) dissolved oxygen (DO), (B) nitrate (NO₃), (C) sulphate (SO₄) and (D) log₁₀-scaled dissolved methane (CH₄), represented by median value (open diamond) with min and max values denoted by black lines for individual mini-piezometers. Sample size indicated in parentheses below location.

Depth variability (across all locations) is included on the right as box-plots which present data as quartiles with the central line representing the median. River water concentrations (SW) and alluvial groundwater concentrations (GW) are included for comparison. Sample size also included in parentheses below depth interval.

6.3.2.2 Redox conditions in the riverbed in Summer 2012

The majority of riverbed pore water samples were aerobic but with generally lower maxima (Fig. 6.3.4A). Similar to the spring snapshot, anaerobic conditions were concentrated in the top 20–40 cm of the sediment profile and all monitoring depths had DO concentrations less than that of the river water (9.6 mg L⁻¹ or 100% saturation). The most downstream piezometers (MP20–MP25) showed a substantial decrease in range relative to the spring campaign. The lowest DO concentrations (<1 mg L⁻¹) were observed at 20 cm in MP18 (0.91 mg L⁻¹) and MP7 (0.94 mg L⁻¹). Median DO concentrations at 20 cm (1.9 mg

L⁻¹) were significantly less (Mann-Whitney U test, $Z = -4.1$, $p = <0.001$) than those at the base (100 cm) of investigated profile (6.4 mg L⁻¹) amounting to an overall decline in DO of approximately 30%. However, seasonal differences in medians at both depths did not differ significantly ($p = >0.05$), suggesting that pore water aerobic respiration processes in the riverbed remained relatively similar between seasons (in contrast to the alluvial groundwater system). NO₃⁻ showed very similar spatial patterns (Fig. 6.3.4B) to that of the spring campaign with the persistence of the same high-concentration locations (>120 mg L⁻¹), but with generally lower minima (Fig. 6.3.3B). The lowest NO₃⁻ was observed at 20 cm in MP18 (12.1 mg L⁻¹) at the head of the riffle sequence where DO concentrations were lower than the spring campaign (Fig. 6.3.3A) and CH₄ concentrations elevated. The decrease in median NO₃⁻ concentrations from 100 cm (60 mg L⁻¹) to 20 cm (40 mg L⁻¹) was statistically significant ($Z = -2.55$, $p = 0.001$) producing an apparent attenuation of NO₃⁻ of approximately 30% over the 16 piezometer subset. This NO₃⁻ attenuation was greater in the summer campaign than the spring one (15%) which was verified by comparison of median concentrations at 20 cm for both spring and summer snapshots ($Z = -2.26$ $p = 0.023$). No differences were found at the 100 cm depth indicating that NO₃⁻ inputs at depth in the riverbed were relatively constant over the two seasons investigated. SO₄²⁻ (Fig. 6.3.4C) followed similar spatial patterns to the spring campaign and no statistically significant differences ($p = >0.05$) could be found between the medians at 20 cm (28 mg L⁻¹) and 100 cm (25.3 mg L⁻¹). This suggests that SO₄²⁻ was behaving conservatively in the riverbed throughout the two snapshots.

Dissolved Mn was detected at a greater frequency, indicating that increased Mn-reduction was taking place in summer. These observations were mainly in the TA piezometers where anaerobic conditions were present at the 20 cm level, including MP2 (0.65 mg L⁻¹) and

MP8 (0.32 mg L^{-1}). MP7 exhibited anaerobic conditions as far as 60 cm where Mn-reducing conditions were supported at 20 cm (2.7 mg L^{-1}), 40 cm (4.5 mg L^{-1}) and 60 cm (9.6 mg L^{-1}). Other locations where Mn was above detection limits at the 20 cm level included MP18 (2.52 mg L^{-1}), MP19 (1.51 mg L^{-1}) and MP23 (1.32 mg L^{-1}) which were all anaerobic. Fe was above detection limit at three locations (where Mn was also detected), suggesting local metal-reducing conditions at 60 cm in MP7 (0.61 mg L^{-1}), and 20 cm in both MP18 (0.74 mg L^{-1}) and MP23 (0.41 mg L^{-1}). CH_4 concentrations in the riverbed during summer (Fig. 6.3.4E) varied by three orders of magnitude from the detection limit of $0.1 \text{ } \mu\text{g L}^{-1}$ at MP16 100 cm (7% air saturation) to 420 times air saturation at MP18 20 cm ($582.2 \text{ } \mu\text{g L}^{-1}$). An increase in methanogenic activity (e.g., $\text{CH}_4 > 10 \text{ } \mu\text{g L}^{-1}$) was apparent at the most downstream piezometers of the reach (MP18–MP25, predominantly at the 20 cm levels) where values which were typically $< 1 \text{ } \mu\text{g L}^{-1}$ during the spring sampling campaign. River water CH_4 concentrations were higher in the summer at $15.8 \text{ } \mu\text{g L}^{-1}$ (11 times over-saturation). The median CH_4 concentration at 20 cm ($7 \text{ } \mu\text{g L}^{-1}$) was significantly greater ($Z = -4.62$, $p = < 0.001$) than at 100 cm ($0.3 \text{ } \mu\text{g L}^{-1}$), representing an apparent CH_4 increase of over 20 times from 100 cm to 20 cm, however no seasonal changes CH_4 at either depth were observed. DOC concentrations in the riverbed (Fig. 6.3.4F) were all higher than the median of the PTS boreholes in March 2012 (Table 6.2) but lower than the river water concentration of 7.9 mg L^{-1} . The maximum DOC concentration (6.82 mg L^{-1}) was observed at MP18 (20 cm) with MP7 at 20 cm similarly high (6.76 mg L^{-1}). The lowest DOC concentrations were associated with the deeper sampling levels (e.g., 60–100 cm) particularly at the TB transect and upstream of TA. Differences in median DOC concentrations from the 20 cm (4.7 mg L^{-1}) and 100 cm (2.6 mg L^{-1}) sampling levels were significant ($Z = -4.5$, $p = < 0.001$).

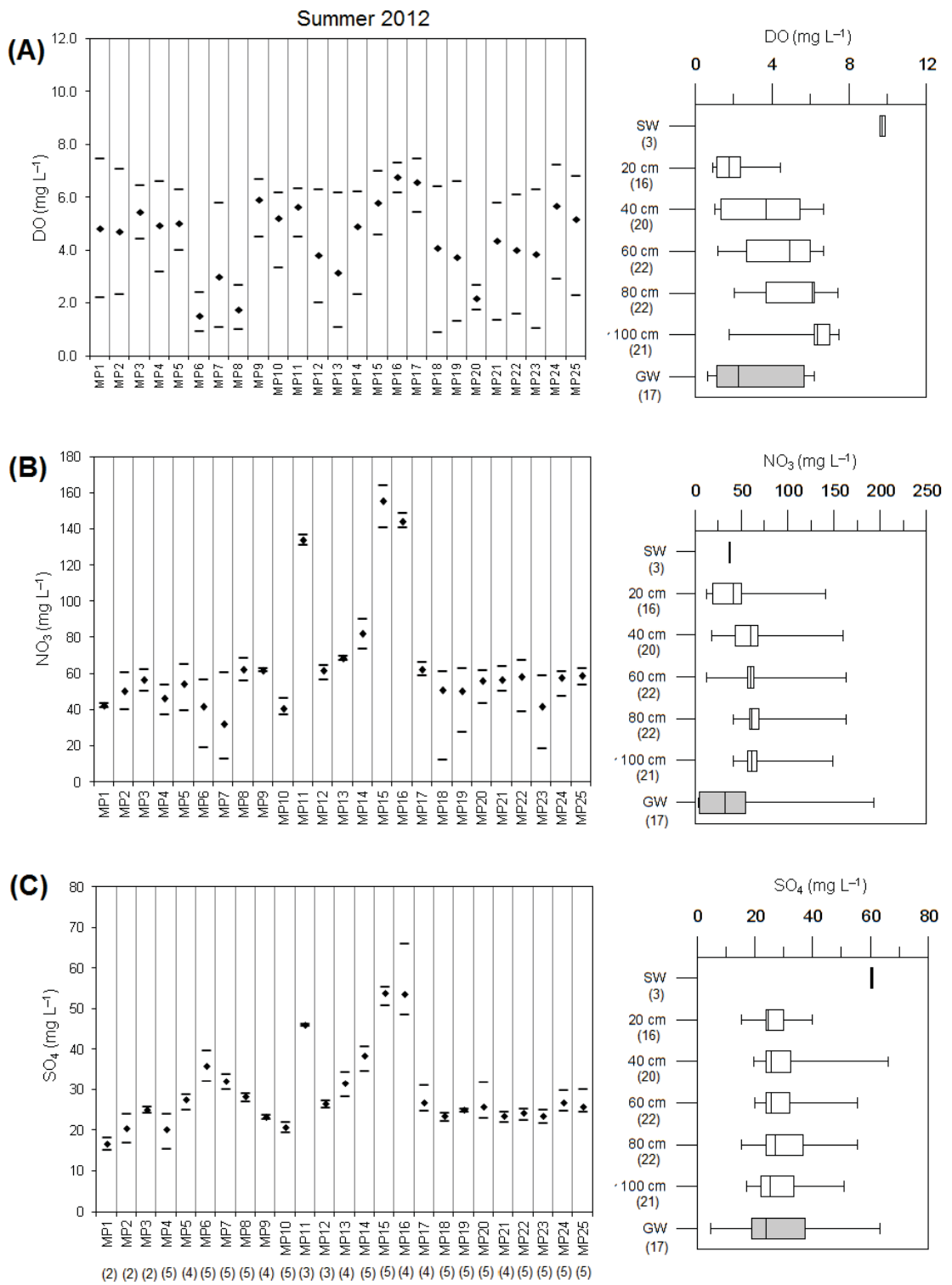


(Figure caption overleaf)

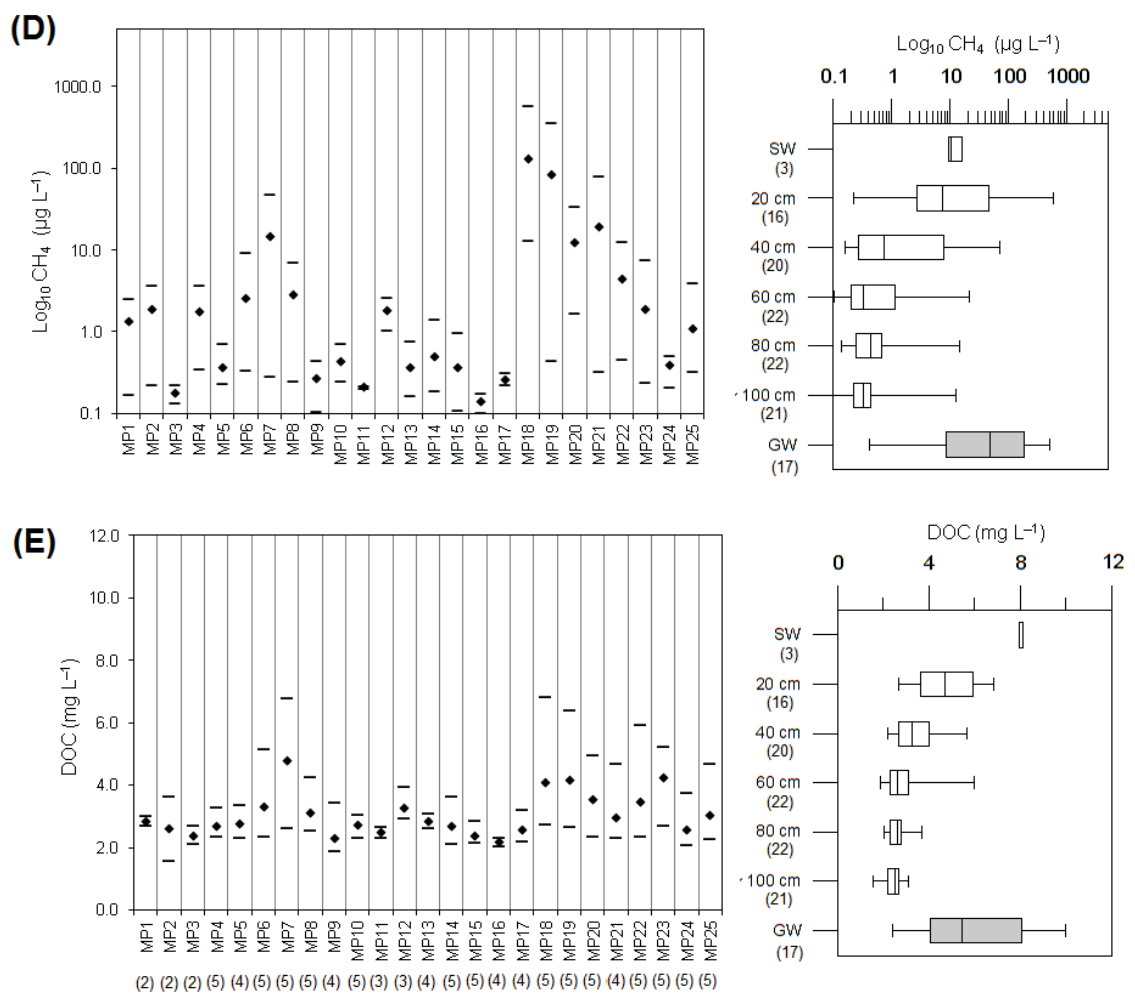


Fig. 6.3.4 Hydrochemical variables of the Summer 2012 snapshot, illustrating the reach-scale spatial variability of (A) dissolved oxygen (DO), (B) nitrate (NO_3), (C) sulphate (SO_4) (D) log_{10} -scaled dissolved methane (CH_4) and (E) dissolved organic carbon (DOC), represented by median value (open diamond) with min and max values denoted by black lines for individual mini-piezometers. Sample size indicated in parentheses below location.

Depth variability (across all locations) is included on the right as box-plots which present data as quartiles with the central line representing the median. River water concentrations (SW) and alluvial groundwater concentrations (GW) are included for comparison. Sample size also included in parentheses below depth interval.

6.3.2.3 *Representative redox profiles*

Individual profiles which capture the range of behaviours of the plume and redox gradients along upwelling flow paths during the summer 2012 snapshot is presented alongside representative riverbed stratigraphy in Fig. 6.3.5. At MP7, the influence of the peat horizon can be seen where large decreases in DO and NO_3^- are accompanied by increases in DOC, Mn and CH_4 , together with cDCE detections from 60 to 20 cm. This profile also exhibited consistent dechlorination through all four monitoring campaigns (Fig. 6.2.6). MP18 and MP23 showed significant redox reactivity, concentrated at the 20 cm level where cDCE detections were also found. These locations represent the majority of profiles which exhibited some level of in-situ transformation. Decreases in NO_3^- , as well as minor Mn detections under anaerobic conditions at the 20 cm level were also observed. In both profiles, substantial increases in CH_4 were evident in the top 20 cm. MP18 showed consistent dechlorination activity (Fig. 6.2.6) over the three campaigns where the location was monitored. The peat present in the stratigraphy at MP23 did not show the same influence on DO or DOC to that of MP7, suggesting a variable degree of reactivity of the organic matrix (discussed later in this chapter). No significant changes in pore water redox conditions can be seen in MP15, which was located within a predominately fine-grained sediment sequence with little previous depth-related variation in plume concentration. A very high concentration of NO_3^- (150 mg L^{-1}) can be seen at this location exhibiting little change over the one-metre depth range. This high NO_3^- concentration is associated with the western side of the TB transect (Figs. 6.3.4B and 6.3.3B) as well as BH1 and the seepage area (Figs. 6.3.1B and 6.3.2B) in the alluvial groundwater system. SO_4^{2-} did not show any appreciable changes with depth across any profile suggesting an absence of SO_4^{2-} reduction and, therefore, largely conservative transport of this TEA through the riverbed.

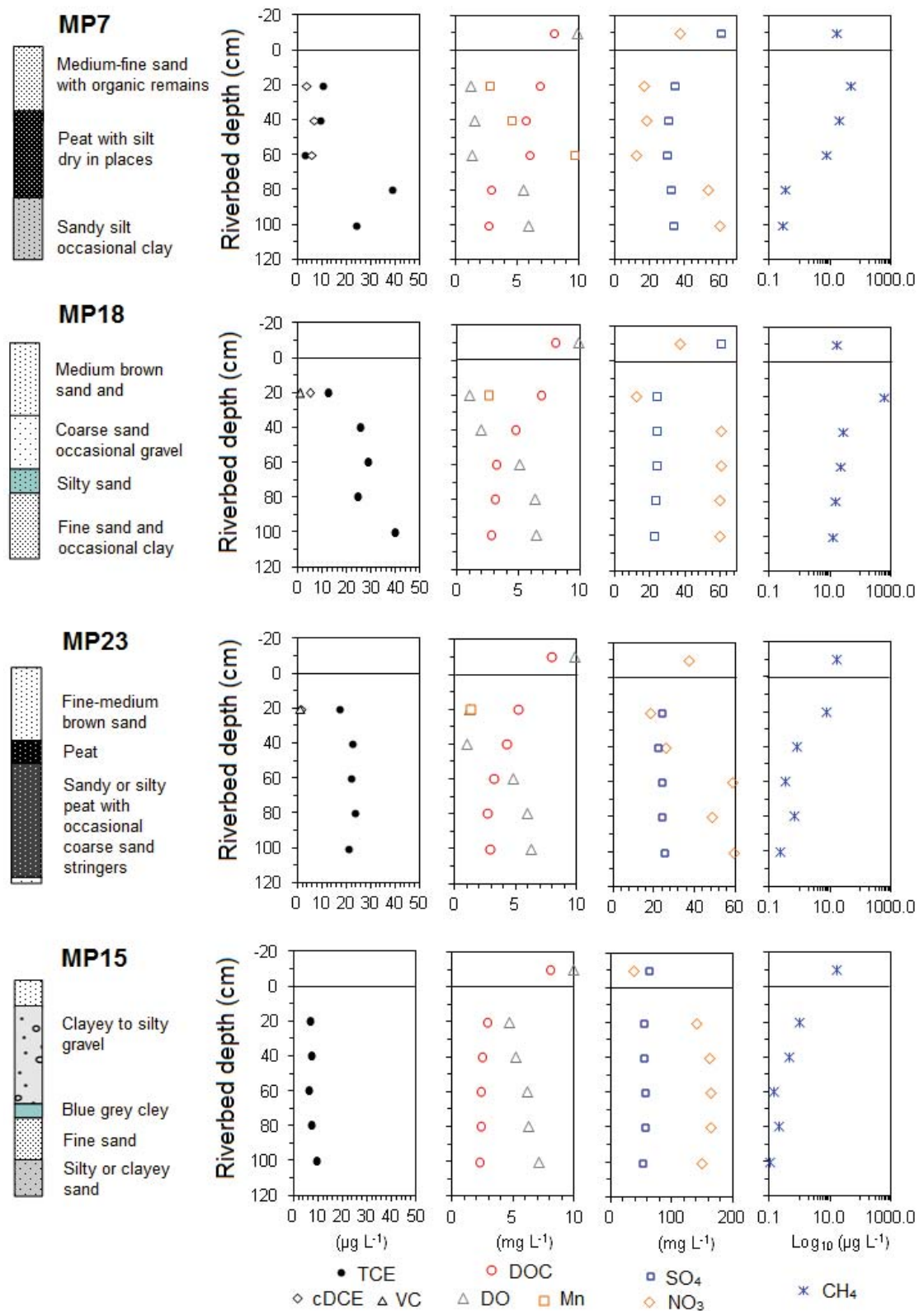


Fig. 6.3.5 Riverbed solute profiles exhibiting the range of redox behaviour observed in the multi-level profiles of the summer 2012 snapshot. See Fig. 6.2.1 for the location of these mini-piezometers. Representative riverbed stratigraphy is also included for comparison.

6.3.3 Redox conditions in the plot-scale sampler array

All hydrochemical variables from the plot-scale array were either normally or log-normally distributed based on the Shapiro-Wilk test of normality ($p = >0.05$). Therefore, it was possible to use parametric statistics. Comparison of means between 5, 10 and 20 cm depths using single factor ANOVA did not reveal any statistically significant differences ($p = >0.05$) between depths for all solutes. This suggested that the samplers were intercepting riverbed pore water above the prevailing redox gradient (e.g., 20–40 cm below bed level), which is indicated by the solute profile for MP7 (Fig. 6.3.5). Longitudinal zonation of TEAPs was also investigated with two sample T-tests (with two-tailed significance) on paired sampler locations, situated at the head and tail sections of the array (Fig. 6.2.1C) which are discussed in the following sections.

6.3.3.1 Terminal electron acceptors

All pore water sampler locations in the array were anaerobic ($<2 \text{ mg L}^{-1}$) with the low DO levels homogeneously distributed (Fig. 6.3.6A). Mean DO at the head of the sampler array (PW1–5) was 0.98 mg L^{-1} with a mean of 0.95 mg L^{-1} found for the tail section (PW9–13) which were not statistically different ($p = >0.05$). This suggests that biogeochemical drawdown of DO was relatively homogenous throughout the surficial sediment. NO_3^- was more spatially variable than DO (Fig. 6.3.6B) and was below detection limit in 13% of pore water samples with a further 34% showing NO_3^- concentrations of $<5 \text{ mg L}^{-1}$. Mean NO_3^- concentrations were significantly higher ($p = >0.05$) in the head of the array (14.7 mg L^{-1}) where the highest concentration of 33.4 mg L^{-1} was found (at 10 cm in PW5), when compared to the tail mean of 5.1 mg L^{-1} . SO_4^{2-} showed a greater overall range than NO_3^- and DO (Fig. 6.3.6C). The maximum SO_4^{2-} concentration of 66.4 mg L^{-1} was observed at 10 cm in PW1 with the lowest (7.8 mg L^{-1}) at 30 cm in PW7. Mean SO_4^{2-} concentrations in

the head area were 38 mg L^{-1} , which was higher than the tail at 26.5 mg L^{-1} , the difference being statistically significant ($p = <0.05$). This suggested possible SO_4^{2-} reduction may have taken place in the downstream section of the surficial sediment, given the high concentrations observed in the deeper piezometer profile MP7 ($30\text{--}34 \text{ mg L}^{-1}$). However, as the metabolites of SO_4^{2-} reduction (such as hydrogen sulphide, H_2S) were not determined, this difference in means may reflect spatial variability of SO_4^{2-} concentrations in the discharging groundwater. Nonetheless, given the high resolution and limited spatial extent of the sampler array, coupled with the discrete nature of the low SO_4^{2-} concentrations (Fig. 6.3.6C), it appears more likely that in-situ microbial SO_4^{2-} reduction was taking place.

6.3.3.2 *Reduced metabolites and DOC*

Dissolved Mn (Fig. 6.3.6D) was widespread and detectable in all but one location (PW4, 30 cm) with the highest Mn concentration of 26.6 mg L^{-1} recorded at 10 cm in PW11 with other locations situated in the tail section of the array showing values in excess of 20 mg L^{-1} . As might be suspected from Fig. 6.3.6F, the mean Mn concentration in the head of the array (1.7 mg L^{-1}) was lower than that of the tail mean (6.1 mg L^{-1}) which proved to be statistically significant ($p = <0.05$). Soluble Fe was also highly prevalent in the surficial sediment with 63% of the samples exhibiting dissolved Fe above detection limits (Fig. 6.3.6E). The highest Fe concentration was 12.7 mg L^{-1} at 10 cm in PW11 and the minimum 0.18 mg L^{-1} at 10 cm PW3 with a somewhat sporadic spatial distribution suggesting highly localised areas of enhanced Fe^{3+} reductive dissolution. Although Fe was not detectable in an adequate number of paired head-tail samplers to permit comparisons, from Fig. 6.3.6E it is clear that highest concentrations of Fe are clustered within the tail section of the array. All dissolved CH_4 concentrations were over-saturated with respect to

atmospheric equilibrium showing highly dynamic spatial variability (Fig. 6.3.6F) with a concentration range spanning three orders of magnitude. The minimum CH₄ concentration (2.7 µg L⁻¹, or twice air saturation) was recorded at 20 cm in PW2 which is situated at the head of the sampler array. The CH₄ concentrations in excess of 2 mg L⁻¹ were all associated with the tail end of the array (Fig. 6.3.6F) including the maximum value at PW9 (10 cm) of 3.39 mg L⁻¹ (equivalent to 2455 times air-saturation equivalent). Average CH₄ concentrations for the head and tail sections were 25.3 µg L⁻¹ and 512 µg L⁻¹, respectively which, as expected, was statistically significant ($p = <0.05$). DOC was prevalent at all these locations (Fig. 6.3.6G). Mean DOC within the head of the array (4.6 mg L⁻¹) was significantly lower than the mean of the tail section (6.7 mg L⁻¹). DOC was locally elevated at the tail section with a maximum of 17.8 mg L⁻¹ at PW12 which was nearly twice that of the highest alluvial aquifer concentration (9.9 mg L⁻¹) and three times the mini-piezometer network maximum (6.8 mg L⁻¹). DOC concentrations in excess of 10 mg L⁻¹ were notable at 20–30 cm in PW9 (10.4–12.1 mg L⁻¹) and 5–20 cm in PW12 (10.7–17.8 mg L⁻¹).

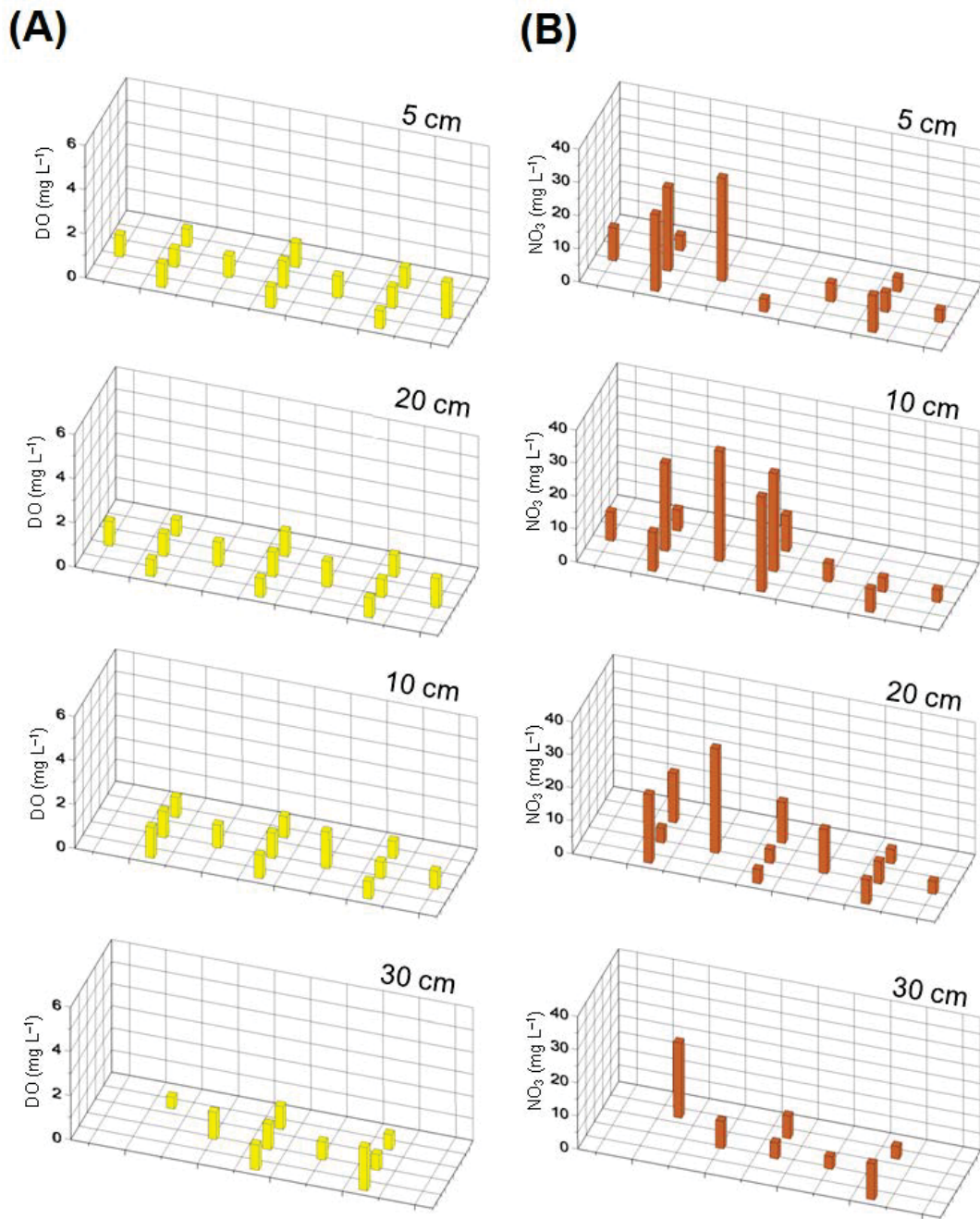


Fig. 6.3.6 Pore water concentrations in the plot scale array for (A) dissolved oxygen (DO) and (B) nitrate (NO₃). Note that it was only possible to sample 7 out of 13 locations at 30 cm and 11 out of 13 at 20 cm. See Fig. 6.2.1B for the location of the array and Fig. 6.2.1C for the names of individual samplers.

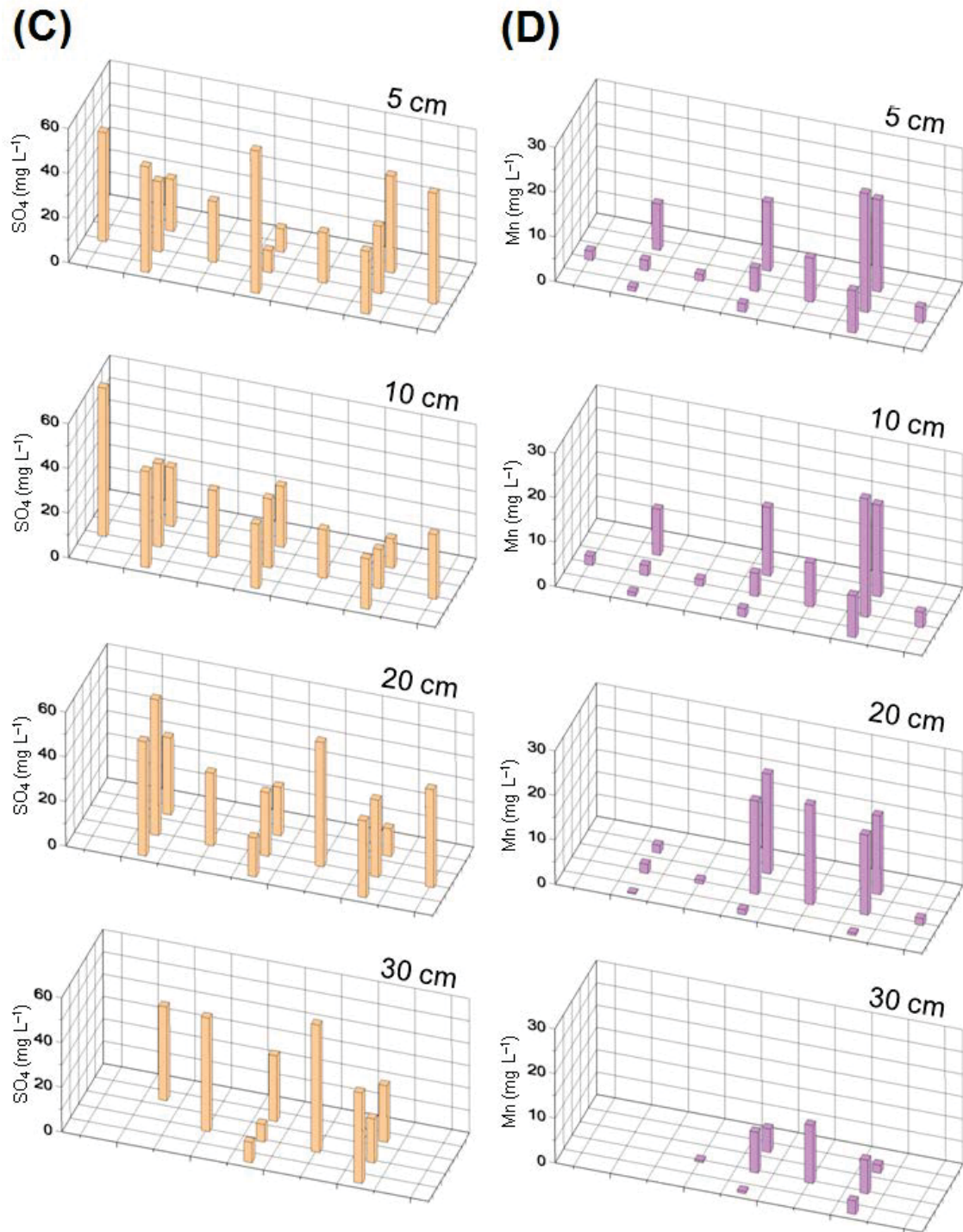


Fig. 6.3.6

Contd. Pore water concentrations in the plot scale array for (C) sulphate (SO₄) and (D) dissolved manganese (Mn), which is assumed to be predominantly Mn²⁺. Note that it was only possible to sample 7 out of 13 locations at 30 cm and 11 out of 13 at 20 cm. See Fig. 6.2.1B for the location of the array and Fig. 6.2.1C for the names of individual samplers.

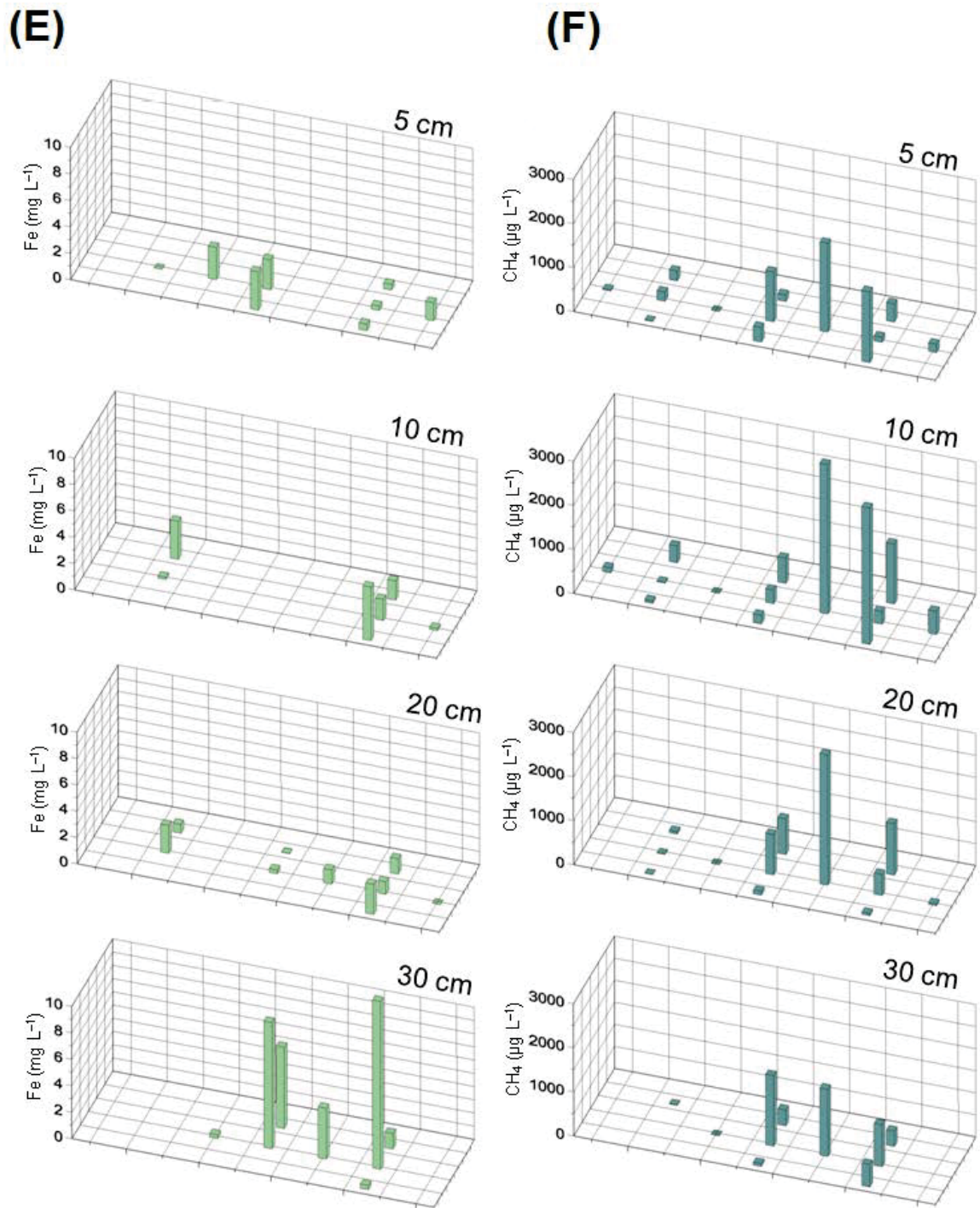


Fig. 6.3.6 Contd. Pore water concentrations in the plot scale array for (E) dissolved iron (Fe), which is assumed to be largely the reduced form of Fe²⁺ and (F) dissolved methane (CH₄). Note that it was only possible to sample 7 out of 13 locations at 30 cm and 11 out of 13 at 20 cm. See Fig. 6.2.1B for the location of the array and Fig. 6.2.1C for the names of individual samplers.

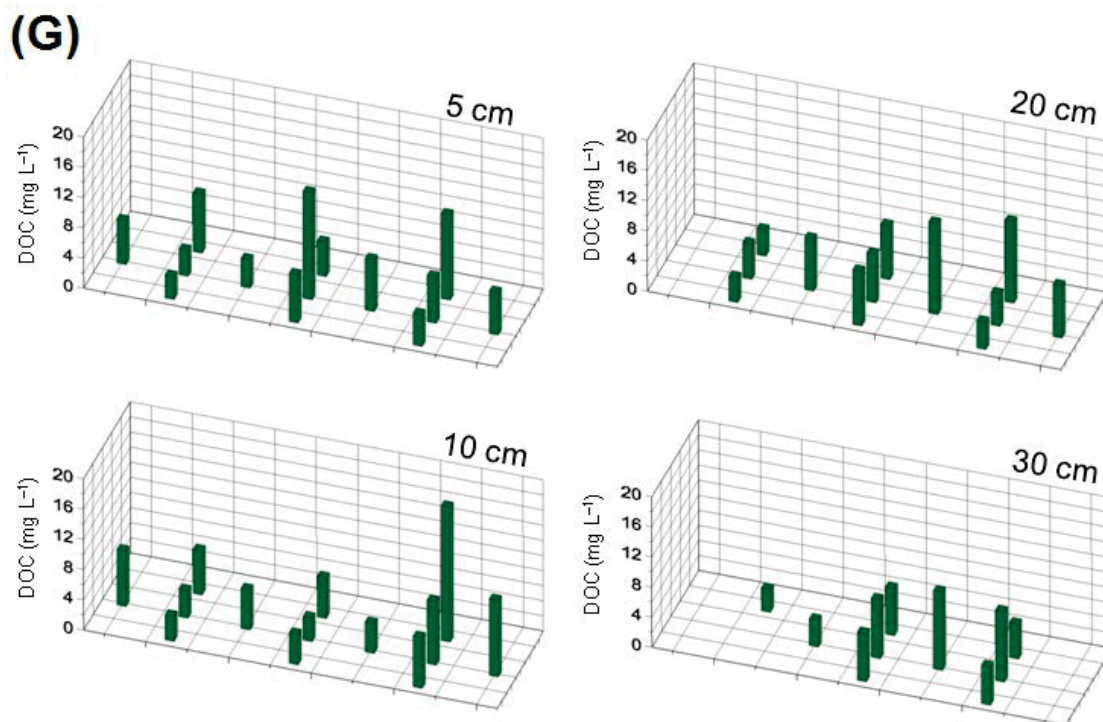


Fig. 6.3.6 (G) Pore water concentrations of dissolved organic carbon (DOC) in the plot scale array. Note that it was only possible to sample 7 out of 13 locations at 30 cm and 11 out of 13 at 20 cm. See Fig. 6.2.1B for the location of the array and Fig. 6.2.1C for the names of individual samplers.

6.3.4 Redox interactions with TCE dechlorination

With the chlorine number (N_{Cl}) approach used to quantify the extent of reductive dechlorination in Section 6.2.4, it was possible to compare the concentrations of the TEAs, reduced metabolites and DOC acquired during the sampling snapshots with calculated chlorine numbers. Full correlations matrices to support the discussion in this section are included in Appendix E.

6.3.4.1 *Redox interactions at reach-scale*

Bivariate scatter comparisons are presented in Fig. 6.3.7 for samples from the mini-piezometer and alluvial monitoring wells where some level of reductive dechlorination was observed (e.g., $N_{Cl} = <3$). From Fig. 6.3.7A, it can be seen that no specific relationship exists between N_{Cl} and DO which would be expected given that TCE transformation requires anaerobic conditions in order to be energy-yielding for microbial growth (Vogel et al., 1987). On the other hand, N_{Cl} was found to moderately correlate with NO_3^- (Fig. 6.3.7B) using the non-parametric Spearman's rank correlation ($\rho = 0.48$, $p = 0.001$) indicating that the extent of dechlorination of the plume is inversely related to ambient NO_3^- concentrations. SO_4^{2-} and N_{Cl} did not present any significant relationship (Fig. 6.3.7C), supporting the previous interpretation of the largely conservative behaviour of SO_4^{2-} in the riverbed, at reach scale. Much of the observed spatial variability in SO_4^{2-} is likely to be attributable to background variation in groundwater SO_4^{2-} concentrations. Although the detection of dissolved Mn generally coincided with the detection of cDCE a significant relationship between Mn and N_{Cl} was not observed using Spearman's rank. However, this is not surprising given the weak level of dechlorination and Mn-reduction were observed concomitantly within much of the anaerobic zones identified. Similarly no significant relationship is obtained with CH_4 , (Fig. 6.4.3D), however, it can be seen that the majority of dechlorination occurred at CH_4 levels of between 10 and 100 $\mu g L^{-1}$. Although some sporadic methanogenic activity was observed (e.g., MP13 20 cm in spring) overall, highly reducing methanogenic zones (e.g., $>1 mg L^{-1} CH_4$) were not observed at reach-scale in either the riverbed or the alluvial drift. DOC was moderately negatively correlated with N_{Cl} (Fig. 6.4.3E) based on Spearman's rho ($\rho = -0.54$, $p = 0.01$) and it is apparent that no dechlorination occurred with DOC concentrations of $<4 mg L^{-1}$. A negative association might be expected if DOC were being consumed as a source of electrons during reductive

dechlorination. The comparison between DOC and NO_3^- (Appendix E1) also revealed a similar negative relationship ($\rho = -0.57$, $p = 0.02$) and a positive correlation was obtained for CH_4 ($\rho = 0.66$, $p = 0.005$) suggesting DOC to be an important regulator of anaerobic microbial metabolism which is in accordance with previous work (Battin, 1999; Baker et al., 2000; Fisher et al., 2002; Vidon and Hill, 2004).

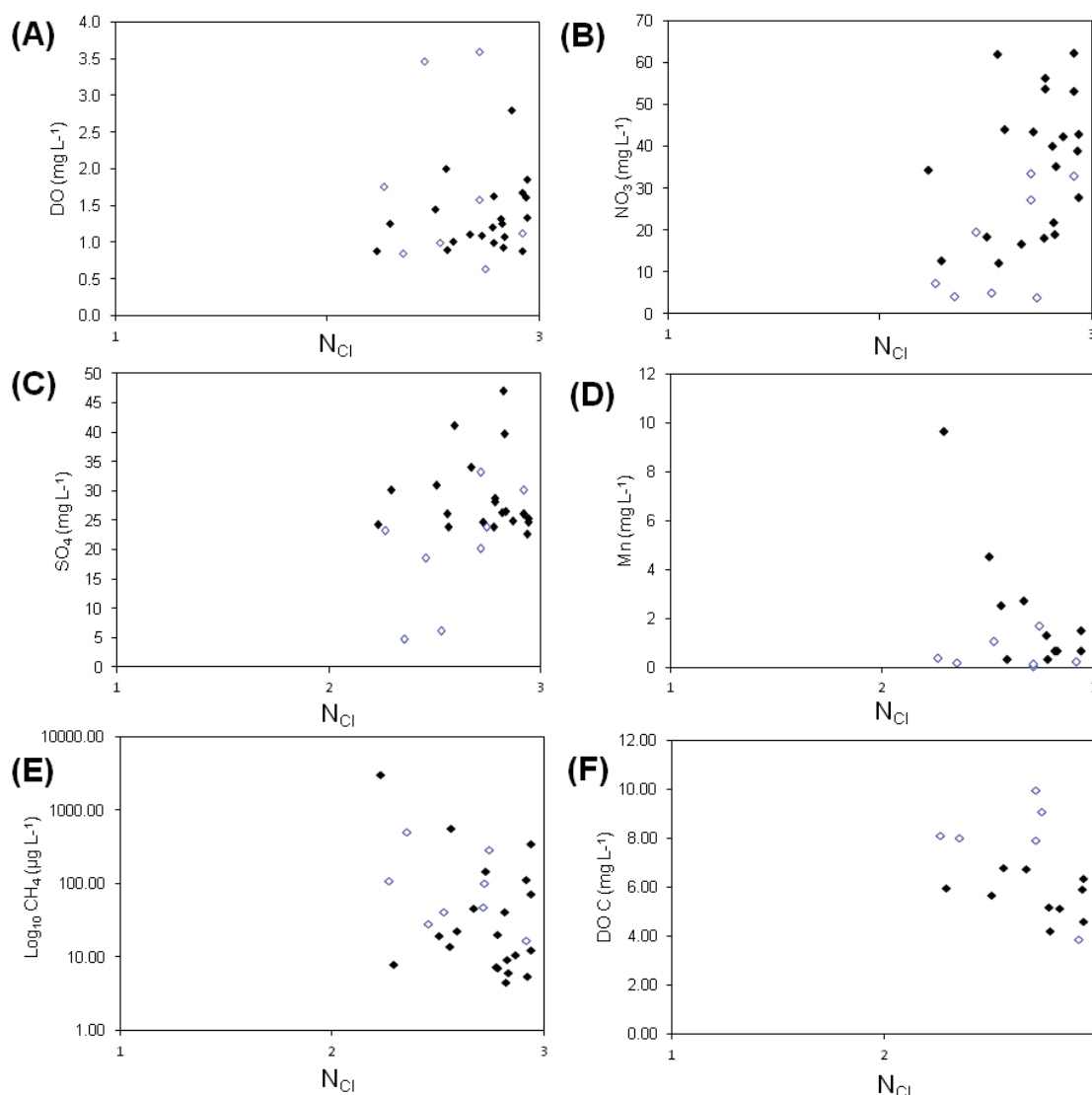


Fig. 6.3.7 Compositing bivariate scatter plots for the mini-piezometer samples (filled black diamonds) and alluvial groundwater samples (open blue diamonds) where chlorine numbers (N_{Cl}) were <3 throughout both the spring and summer sampling campaigns. (A) DO (B) NO_3^- (C) SO_4 (D) dissolved Mn (E) CH_4 and (F) DOC. Significant Spearman correlations are reported in the text with a full correlation matrix included in Appendix E1. Error bars have been omitted for clarity.

6.3.4.2 *Redox interactions in the plot-scale array*

Bivariate plots visualising the comparison of N_{Cl} (including locations where $N_{Cl} = 3$) with \log_{10} -transformed TEAs and reduced species (other than SO_4^{2-} which was normally distributed) are presented in Fig. 6.3.8. No significant relationship was seen with DO and N_{Cl} (Fig. 6.3.8A) given that little spatial variation was seen in DO in the predominantly anaerobic area of riverbed investigated (Fig. 6.3.7A). Also similar to the reach-scale samples, NO_3^- (Fig. 6.3.8B) was significantly positively associated ($\rho = 0.58$, $p = 0.001$) with calculated chlorine numbers, based on the non-parametric, Spearman's rank correlation. As can be seen from Fig. 6.3.8C, SO_4^{2-} and N_{Cl} showed no significant association in the plot scale array. Although some locally lower ($<10 \text{ mg L}^{-1}$) SO_4^{2-} concentrations were observed (e.g., PW7), overall, probable SO_4^{2-} reduction appeared to be localised despite the evidently highly reducing conditions in certain locations in the array. Dissolved Mn (Fig. 6.3.8D) was moderately negatively correlated with N_{Cl} ($\rho = -0.56$, $p = 0.001$). Given that Mn-reduction was evidently more widespread than in the reach-scale samples (Fig. 6.3.7D), a negative relationship with this metabolite would be expected given that Mn-reducing conditions are typically the minimum required for TCE dechlorination to cDCE (Mohn and Tiedje, 1992). It can be seen from Fig. 6.3.8D that a large majority of samples exhibiting dechlorination were observed with Mn concentrations $>1 \text{ mg L}^{-1}$. CH_4 and N_{Cl} (Fig. 6.3.8E) were highly negatively correlated ($\rho = -0.74$, $p = <0.001$) suggesting a strong coupling of methanogenesis with progressive dechlorination of TCE. This is in accordance with most laboratory studies of efficient CE reduction, possibly as far as ethene under methanogenic conditions (e.g., Freedman and Gosset, 1989). DOC and N_{Cl} (Fig. 6.3.8F) were more weakly negatively associated ($\rho = -0.43$, $p = 0.01$) than in the reach-scale samples. DOC was also more weakly negatively correlated with NO_3^- based on Pearson's parametric correlation ($\rho = -0.45$, $p = 0.01$) as well as being positively

correlated with Mn ($\rho = -0.45$, $p = 0.01$) and CH_4 ($\rho = 0.5$, $p = 0.002$) (Appendix E2). This suggests, with the higher DOC concentrations detected in the samples from this area than in the reach-scale samples (Figs. 6.3.7G and Fig. 6.3.5E), DOC variation was more closely linked to the lower energy yielding TEAPs (e.g., metal reduction and methanogenesis) where more energetic TEAs (e.g., DO, NO_3^- and TCE) were largely depleted.

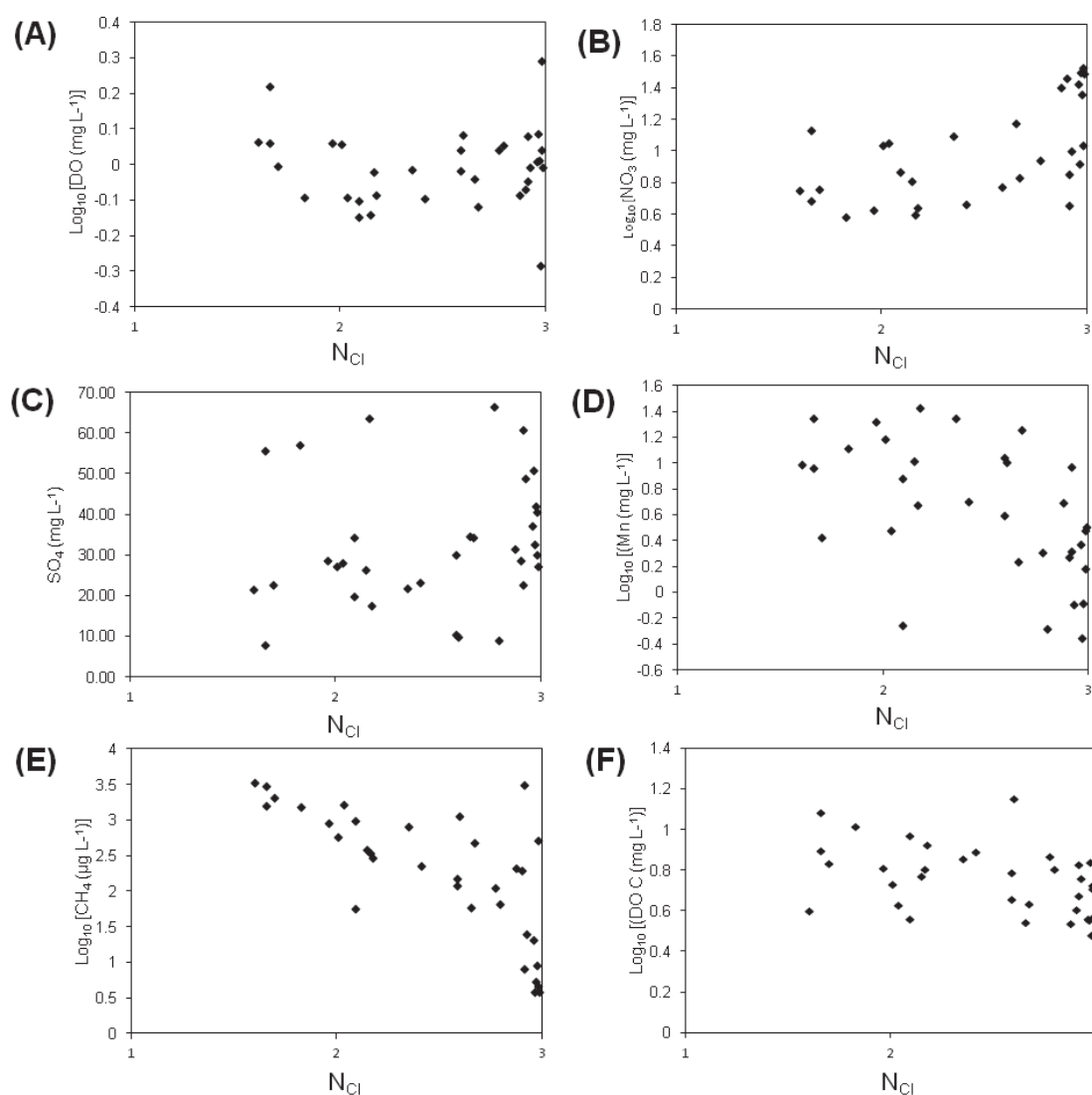


Fig. 6.3.8 Bivariate scatter plots for all pore water samples of the plot-scale array comparing chlorine number (N_{Cl}) with (A) \log_{10} transformed DO (B) \log_{10} transformed NO_3 (C) SO_4 (D) \log_{10} transformed dissolved Mn (E) \log_{10} transformed CH_4 and (F) \log_{10} transformed DOC. Significant Spearman correlations are reported in the text. Full Pearson correlation between all redox variables in the plot-scale array is included as a matrix in Appendix E2. Error bars omitted for clarity.

6.4 Discussion

6.4.1 Spatial variability of redox zones and transformation patterns

The redox regime of the regional groundwater system of the PTS (Table 6.2) through which the plume has been migrating is dominated by high DO (e.g., $>5 \text{ mg L}^{-1}$) and NO_3^- levels ($>50 \text{ mg L}^{-1}$) as well as low DOC (e.g., $\leq 2 \text{ mg L}^{-1}$), in which there is little possibility of transformation of TCE. Much of the alluvial groundwater system in the eastern of the part of the floodplain, e.g., BH1–BH4 (Fig. 6.2.1B) exhibited a similar aerobic redox regime to the sandstone (Figs. 6.3.1) with even greater NO_3^- concentrations in places (e.g., $>80 \text{ mg L}^{-1}$). However, further west, this regime was modified with Mn-reducing conditions identified in the bank-side monitoring wells, supporting a weak level of reductive dechlorination with chlorine numbers of 2.52 (BH7) and 2.45 (BH11) during the spring snapshot. For the summer campaign (Fig. 6.3.2), a significant shift in redox conditions to a more reducing environment across the floodplain groundwater system was suggested, with TEAPs ranging from denitrifying (BH4) to probably Fe-reducing (BH5–BH7). This was accompanied by a greater number of cDCE detections and thus an N_{Cl} of <3 for previously un-reactive parts of the alluvium. For example, at BH5 the spring N_{Cl} was 3 (no dechlorination) which reduced to 2.74, accompanied by a large TEAP transition in terms of potential microbial thermodynamic energy yields from aerobic respiration in spring to Fe-reducing in summer (see Fig. 2.5.2, Chapter 2). Weakly metal-reducing conditions were interpreted for BH11 and BH12 which represented a change from aerobic conditions (in spring) with greater dechlorination observed in summer for both these boreholes with a decrease in N_{Cl} to 2.26 from 2.45 (BH11) and 3 to 2.74 for (BH12). Despite being aerobic, the drainage ditch had an N_{Cl} of 2.71 together with low levels of Fe and Mn ($\sim 0.1 \text{ mg L}^{-1}$) as did the seepage zone (Mn 0.6 mg L^{-1}) suggesting reducing

conditions in the groundwater discharging through these pathways in summer. The reason for this seasonal shift in TEAPs in the alluvial groundwater system is not entirely clear and definitive conclusions are not possible from just two monitoring snapshots. However, from a comparison of Figs. 6.3.2 and 6.2.1B, it can be seen that most reactive monitoring wells are situated on the riverbanks. It is reasonable to expect a closer interaction of the floodplain water table during high river stage at these locations, with the possibility of increased organic matter supply to these bank-side wells from both the surface water catchment and floodplain soils (Vidon and Hill, 2004). The DOC range at metal-reducing locations in the alluvium was 7.1–9.1 mg L⁻¹ for the summer snapshot, which was several times greater than the PTS groundwater (Table 6.2), suggesting increased soluble organic matter availability in these areas of the floodplain.

The aerobic redox regime of the PTS and eastern part of the floodplain was largely unchanged at the base of the mini-piezometer transects in the riverbed (e.g., 80–100 cm) over the 40 m reach investigated (Figs. 6.3.3 and 6.3.4). However, from the differences in medians observed for DO, NO₃⁻, CH₄ and DOC between the base and top of the mini-piezometer levels, it is clear that a redox gradient was present along one metre upwelling flow paths, which was persistent over both sampling snapshots. In Chapter 5, the bulk residence time for advective solutes such as DO and NO₃⁻ over this vertical flow path was estimated to range from <1 day in the area of MP18 (piezometer SL5, Chapter 5) to up to 10 days in the silt/clay deposits in the area of MP1 (SL3, Chapter 5). However, due to the impact of hydrophobic sorption, residence times for TCE in these locations increases to 7.5 days (MP18) and over 3 years in the semi-confining deposits near MP1. From the multi-level observations presented in this chapter, it is clear that solute residence times were sufficiently long to enable development of significant anaerobic zones. These were

characterised by widespread but low level NO_3^- attenuation (e.g., <30%) concentrated in the top 20–40 cm of the sediment profile. In a subset of these anaerobic zones, weak Mn-reduction was observed with chlorine number reductions (3 to ≥ 2.5), accompanied by increases in CH_4 . In some cases (e.g., MP13 20 cm), even lower chlorine numbers (e.g., <2.5) were observed with high (e.g., $>1 \text{ mg L}^{-1}$) CH_4 concentrations. This redox gradient was observed to be mostly associated with the surficial sand sequence (Fig. 6.3.5) which drapes the underlying stratigraphy along the reach (Fig. 5.2.2, Chapter 5). In the summer snapshot, DOC concentrations were observed to approximately double from 100 cm to 20 cm over the reach (Fig. 6.3.4E), indicating a greater availability of soluble organic carbon in the shallowest sediment layers. The findings of the greatest biogeochemical turnover rates occurring in the shallowest (e.g., <60 cm) sediment layers of riverbeds is in accordance with previous studies of biogeochemical cycling in hyporheic zones (Morrice et al., 2000; Franken et al., 2001; Mermillod-Blondin et al., 2005) and CE plumes discharging to rivers (e.g., Roche et al., 2009; Ellis and Rivett, 2007). A greater degree of exchange with the river water would be expected above the level of the semi-confining deposits where groundwater upwelling pressures are inhibited and in the area of the geological window in the riverbed (around MP17 and MP18). However, without Cl^- (or other tracers), it is not possible to explore the potential relationship between hyporheic exchange and transformation patterns. The redox gradient was observed to extend into the semi-confining deposits around the TA transect over both campaigns (Figs. 6.3.3, 6.3.4 and 6.3.5) where peat horizons were present in the stratigraphy. The organic carbon content of these peat lenses typically exceeded 20% g g^{-1} (Fig. 5.2.3, Chapter 5) and greatly enhanced the adsorption capacity of the riverbed and associated plume residence times (Chapter 5). For example, at MP7 (Fig. 6.3.5), where significant transformation of the plume was repeatedly observed, the sorption-modified residence time was estimated to be around 100

days (piezometer SL4, Chapter 5). However, not all peat in the stratigraphy produced a significant modification of the prevailing redox gradient or increase in DOC provision. For example, at MP23 (Fig. 6.2.5) a sorption-modified residence time of 217 days was calculated (SL6, Chapter 5), however much less dechlorination activity was observed in this area throughout the study. This suggests significant differences exist in the composition and structure of the sedimentary organic matter forming the semi-confining deposits along the reach which affect its solubility and bioavailability. This may be explained by a greater component of ‘hard’ carbon in certain parts of the peat horizons which is poorly soluble and more kerogen-dominated. It is clear from the DOC profiles that the recent organic material present in the surficial sand layer contains more labile/soluble components, despite carbon forming $<3\% \text{ g g}^{-1}$ (Fig. 5.2.3, Chapter 5) of the sediment mass fraction over the reach.

Further evidence for the biogeochemical importance of the surficial sand sequence of the riverbed comes from the high-resolution grid of pore water samplers where extensive anaerobic conditions were documented (Figs. 6.2.1C and 6.3.6A). Clear evidence of a longitudinal TEAP gradient, parallel to the river flow direction can be seen from the concentration patterns presented in Fig. 6.3.6 B–G. Denitrifying conditions were indicated at the head of the array (PW1–PW5), transitioning to metal-reducing and highly methanogenic conditions, in the downstream samplers (Figs 6.3.6B and D–F). This redox ‘hotspot’ area was characterised by high CH_4 levels ($>1 \text{ mg L}^{-1}$) where the most efficient level of dechlorination was found throughout the site. Chlorine numbers of <2 indicated all organically-bound chlorine atoms in the plume to be in the form of either cDCE or VC, although, without ethene data, the true extent of dechlorination may be underestimated. Although no specific sediment samples were collected from macrophyte-impacted

sediment zones, sorption-modified residence times could be expected to be around 20 days (based on the bulk estimate for SL4/MP7, Chapter 5). However, this is likely to significantly underestimate true TCE residence times in these highly reactive sediment zones due to (1) locally increased organic matter content leading to increased sorption, (2) possible decreases in hydraulic conductivity due to the presence of gas bubbles in sediment pore spaces (Cuthbert et al., 2010) and (3) reduced vertical gradients due to the presence of the semi-confining layers below. Fig. 6.4.1 presents a longitudinal interpolation of pore water concentrations of NO_3^- , CH_4 and calculated N_{Cl} values for the plume over the centre line of the 1.8 m long sampler array. The highest DOC concentrations ($>10 \text{ mg L}^{-1}$) observed throughout the discharge zone were found within the array (Fig. 6.3.6G) with increasing concentrations observed toward the down-stream tail section. This elevated DOC most likely supported the accelerated biogeochemical turnover in this section of the riverbed.

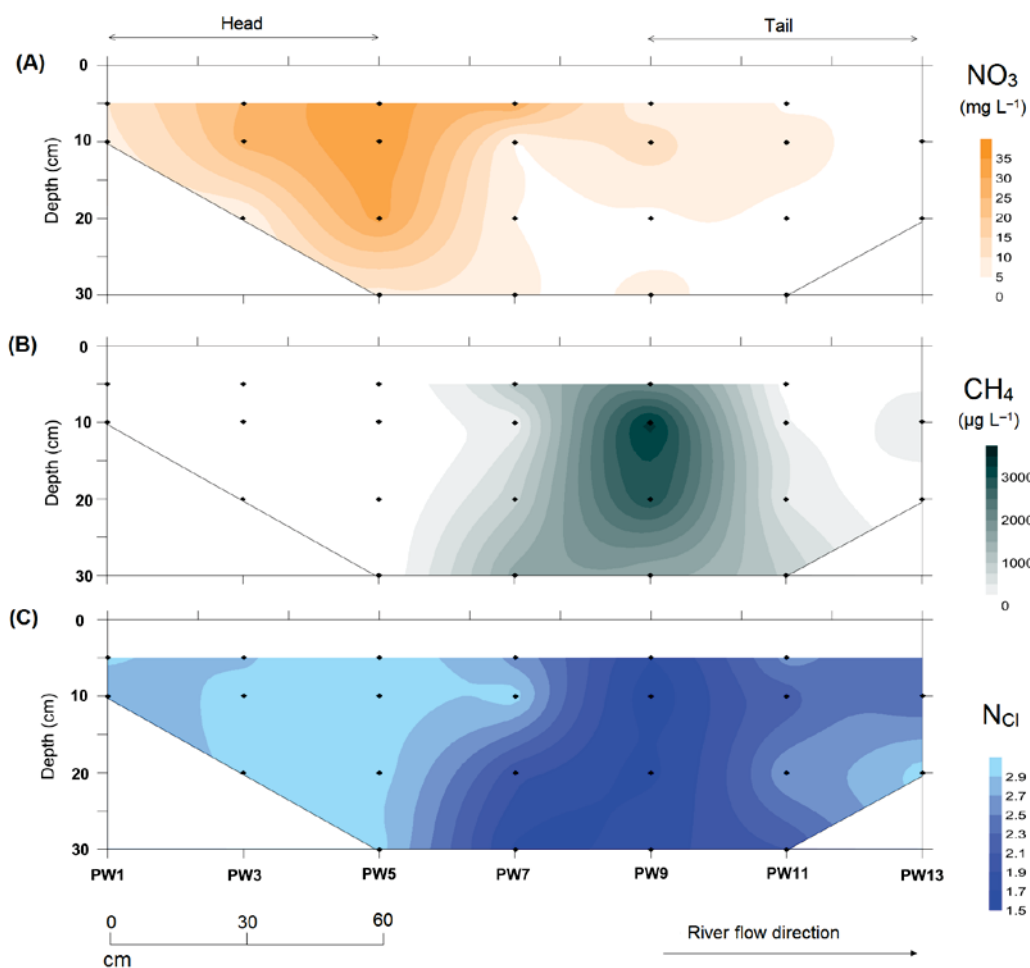


Fig. 6.4.1 Spatial variation of (A) NO_3 , (B) CH_4 and (C) N_{Cl} for TCE, interpolated using Kriging, showing a clear longitudinal zonation of TEAPs. ‘Head’ and ‘tail’ sections used to group samplers in order to compare means are labelled above. Individual sampling locations are indicated by the black dots. See Fig 6.2.1B and 6.2.1C for the location of this

Throughout much of the site, microbially-mediated TEAPs were not strictly segregated from one another spatially in a manner often described for other groundwater environments including both pristine settings (Jakobsen and Postma, 1999) as well as mixed contaminant plumes (Witt et al., 2002). Evidence of anaerobic TEAPs including denitrification, metal reduction and methanogenesis operating with DO concentrations in the range of 0.8–2.5 mg L^{-1} were observed in the alluvial groundwater system (Figs. 6.3.1 and 6.3.2), the mini-

piezometers (Figs. 6.3.4 and 6.3.5) as well as the plot-scale samplers (Fig. 6.3.6). Furthermore, evidence of reductive dechlorination was observed within this DO concentration range (Figs. 6.3.7A and 6.3.8A) and within a NO_3^- range of 3–60 mg L^{-1} (Fig. 6.3.7B) and 3–33 mg L^{-1} in the plot scale samplers (Fig. 6.3.8B). These observations run contrary to the classic thermodynamic sequence of microbial metabolic pathways where more energetically favourable TEAs are consumed in preference to less favourable species (see Fig. 2.5.2, Chapter 2). This suggests a significant degree of pore-scale heterogeneity where rate-limiting processes restrict the mixing of electron donors with electron acceptors at equal rates, resulting in the development of anaerobic pockets within the sediment matrix which are often described in hyporheic sediments (Triska et al., 1993; Storey et al., 1999) as well as in sedimentary aquifers (Murphy et al., 1992). In microcosm studies, Mermillod-Blondin et al. (2004) were able to demonstrate that this variability arose from rapid macropore flow occurring simultaneously with much slower diffuse flow between the sand grains. In a study using slow filtration columns to simulate hyporheic biogeochemical processes, Mermillod-Blondin et al. (2005) also found evidence of anaerobic processes (denitrification and fermentation) occurring at an average DO concentration of $>1.5 \text{ mg L}^{-1}$.

6.4.2 Implications of river macrophyte growth on dechlorination potential

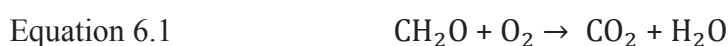
The grid of samplers of the plot-scale array were deployed to target an area of fine sediment accumulation beneath a stand of *Ranunculus* which was visibly rich in organic matter with significant ebullition (gas bubble formation) observed. The trapping of fine suspended sediment by seasonal macrophyte growth in rivers is recognised as an important sediment storage process in lowland river systems (Heppell et al., 2009). The reduction in current velocities promotes allochthonous sediment deposition and the enrichment of

surficial sediment in organic matter, as well as reducing riverbed permeability (Sand-Jensen, 1998). Enhanced biogeochemical turnover rates, promoting methanogenesis in association with macrophyte stand sedimentation patterns have been previously documented (Sanders et al., 2007, Trimmer et al., 2009; 2012). The strong negative relationship between CH₄ and TCE dechlorination suggested a tight coupling with methanogenesis beneath the *Ranunculus* stand (Fig. 6.3.8E). As already discussed, these CH₄ hotspots produced low chlorine numbers, however, further dechlorination of cDCE as far as VC (which would produce an N_{Cl} of ~1) was not observed and VC concentrations never exceeded ~3 µg L⁻¹. This stalling of the dechlorination chain at cDCE is regularly described (Lorah and Voytek, 2004, Abe et al., 2008). A possible reason for this is the diversion of available H₂ into methanogenesis which is known to be a competitive TEAP with reductive dechlorination (Ballapragada et al., 1997). However, without knowledge of the dissolved H₂ concentrations, this is not possible to verify. SO₄²⁻ reducers are also known to compete with dechlorinators for reducing equivalents, owing to their close affinities for particular ranges of H₂ partial pressures, although evidence of inhibitory effects from laboratory cultures is inconclusive (e.g., Nelson et al., 2002; Aulenta et al., 2008). However, SO₄²⁻ reduction was shown to be relatively limited across the reach.

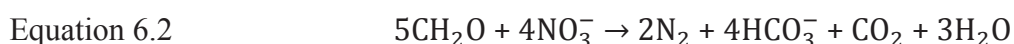
6.4.3 Impact of diffuse nitrate contamination on TCE transformation

Because the plume investigated in this study is composed entirely of TCE with no reduced carbon species present as co-contaminants (such as aliphatic hydrocarbons), microbial respiration will rely exclusively on the presence of natural organic carbon. From Fig. 2.5.2 (Chapter 2), it can be seen that the presence of NO₃⁻ will impose thermodynamic constraints on the development of redox conditions favourable to significant dechlorination of TCE (e.g., Mn reduction), in an electron donor-limited system. Although, actual

sequences of TEAPs have been shown to not always follow thermodynamic predictions (e.g., McGuire et al., 2002). Nonetheless, denitrifiers are sustained by a lower ambient H₂ concentration threshold (<0.05 nmol) than dechlorinating microbes (Lovely and Goodwin, 1988; Lovely et al., 1994; Chapelle et al., 1996) and will out-compete with them for H₂ as a result (Nelson et al., 2002). Regulation of the dechlorination extent by NO₃⁻ is suggested by the significant positive correlations observed between NO₃⁻ and N_{Cl} for both the reach-scale samples (Fig. 6.3.7B) as well as the plot-scale samples (Fig. 6.3.8B), despite the ‘overlapping’ of TEAPs discussed in Section 6.4.1. In order for denitrifying conditions to be established, DO must first be removed. Aerobic oxidation of DOC can be quantified using the ‘CH₂O’ model organic carbon molecule using the stoichiometry provided in Equation 6.2 (Tesoriero and Puckett, 2011):



With this stoichiometry, it can be seen that approximately 1.9–2.9 mg L⁻¹ of DOC would be required to deoxygenate groundwater discharging from the PTS, assuming all DOC is mineralised in the reaction (which is unlikely with complex organic matter). This DOC concentration is higher than what was observed in the PTS samples (Table 6.2) and hence, NO₃⁻ behaves conservatively in the regional aquifer, despite the decadal-scale residence times involved during transit to the river. Equation 6.2 (Jorgensen et al., 2004) provides a reaction stoichiometry for the complete reduction of NO₃⁻ to N₂ with organic carbon.



Using this stoichiometry and the DO and NO_3^- concentration ranges provided in Table 6.2, it can be seen that in order to fully de-oxygenate and denitrify groundwater in the up-gradient plume, 13–19 mg L^{-1} of DOC would be required to induce a redox environment conducive to Mn-reduction. For the mean DO and NO_3^- concentrations over both snapshots at the base of the riverbed mini-piezometers (6.5 and 67 mg L^{-1} , respectively), a minimum threshold of 16 mg L^{-1} of DOC would be required. The most extreme NO_3^- concentration of 202.7 mg L^{-1} at BH1 (DO 5.5 mg L^{-1}) would require in the region of 47 mg L^{-1} of DOC with a maximum residence time of about 10 days for complete denitrification to take place. Therefore, these excessive NO_3^- levels are likely to provide a substantial ‘redox buffer’ where a large stoichiometric demand on available labile organic carbon is created that will restrict any in-situ dechlorination to zones where there is an excess of bioavailable DOC or other forms of reactive carbon. Moreover, these DOC thresholds are only the minimum required for the likely onset of metal-reducing conditions and do not guarantee that significant dechlorination will take place, due to the direct competition for reducing equivalents by the lower-energy TEAPs discussed previously. This type of redox buffering was described by Diem et al. (2013) who demonstrated that NO_3^- could prevent release of Mn and Fe in drinking water after consumption of DO during organic matter respiration in a riverbank infiltrations scheme. It is clear from Fig. 6.4.1 and the previous discussions that this redox buffer was overcome at discrete locations. In particular, the downstream section of the plot-scale array, where DOC concentrations (up to 17 mg L^{-1}) approached the indicated threshold with a residence time apparently sufficient for complete nitrate attenuation allowing significant dechlorination of TCE to proceed.

6.5 Chapter summary

The two further ‘snapshot’ campaigns of this chapter revealed very persistent spatial patterns of TCE concentrations within the riverbed mini-piezometers and alluvial monitoring wells, installed in Chapter 4. The Permo-Triassic sandstone of the up-gradient plume was aerobic to a depth of 80 m with NO_3^- concentrations of up to 80 mg L^{-1} . In the electron donor-limited environment of the plume, this background NO_3^- presents a large demand for labile organic carbon by denitrifiers which regulates the onset of more reducing conditions where dechlorination of TCE becomes energetically favourable. However, metal-reducing conditions were observed in some alluvial monitoring wells screened within the alluvial aquitard along the riverbanks where weak dechlorination was frequently observed. A persistent redox gradient was present in piezometer profiles in the riverbed with denitrifying to weakly Mn-reducing conditions at 20–40 cm, favouring dechlorination. Higher DOC concentrations at these levels corresponded to the surficial sand layer of the sediment sequence. The semi-confining peat deposits also influenced the redox gradient with Mn-reducing conditions present up to 60 cm depth. A high-resolution grid of samplers revealed localised, highly methanogenic zones in the surficial sands, which supported a large number of cDCE detections. Elevated DOC concentrations ($10\text{--}17 \text{ mg L}^{-1}$) and a longitudinal zonation of redox processes was observed to be spatially associated with the position of a *Ranunculus* stand in the river. Using a ‘chlorine number’ metric, it was possible to quantify the extent of reductive dechlorination of the plume. The majority of samples indicated only partial conversion of TCE to cDCE ($N_{\text{Cl}} = >2$). However, the discrete methanogenic ‘hotspots’ in the surficial sand layer beneath the tail end of the macrophyte stand produced more significant dechlorination with chlorine numbers of ~ 1.5 , indicating all chlorine present in the plume to be in the form of cDCE and VC.

7. Conclusions and future research directions

7.1 Introduction

This chapter presents a synthesis of the main research findings of this thesis in the context of the four objectives outlined in Chapter 1. The wider implications of the research findings are discussed as are suggestions for future research directions arising from the insights and the limitations of this study.

7.2 Summary of key findings

The initial phase of this study was designed to delineate the principal mass transfer pathways that link a deep-seated TCE plume in a major aquifer with its natural discharge zone at a groundwater-fed lowland river (Objective 1). The results of the multi-scale investigation suggest a diffuse plume has the potential to affect a reach of over 100 m. The majority of dissolved TCE upwelling from near the interpreted base of the sandstone aquifer is expected to discharge over a smaller sub-reach where a higher concentration ‘core’ is centred on a meander bend in the floodplain (Fig. 7.2.1A-B). By combining single-screen monitoring well observations with targeted multi-level sampling from drive-point riverbed piezometers, it was possible to determine that localised zones of the riverbed act as the primary pathways or ‘geological windows’ for discharge of the groundwater plume (Fig. 7.2.1B). Evidence for this comes from the high vertical resolution provided by the mini-piezometer profiles where the spatial variability of pore water TCE concentrations showed metre-scale ‘hotspots’ of contamination. This conceptualisation is supported by low level detections of chlorinated ethenes in the drift deposits along the river corridor. It was demonstrated that inexpensive diffusion samplers, constructed from readily available

materials can provide useful tools for delineating contaminant plumes in shallow benthic sediments, in the absence of any other monitoring infrastructure.

Spatial patterns of contaminant concentrations in the discharge zone were found to be temporally persistent over successive ‘snapshot’ sampling programs, under steady-state baseflow conditions. This suggests the lowland geological framework exerts significant controls on the location and magnitude of contaminant discharge over a range of scales (Objective 2). At floodplain-scale, a low-permeability aquitard cap composed of soft alluvial clays and silt overlies the high-permeability Permo-Triassic sandstone below. The dominance of this feature in the alluvial stratigraphy along the river corridor was demonstrated through a combination of 2-D electrical resistivity imaging (ERI) and targeted intrusive sampling. Piezometric observations suggest this unit is likely to confine groundwater upwelling and constrict regional discharge towards permeable zones in the riverbed and along the banks. It is expected to influence the regional groundwater plume by focussing the more diffuse, peripheral flow lines towards the core zone in the riverbed (Fig. 7.2.1A). This study demonstrates the benefits of ERI as a non-invasive tool for delineating scale-dependent geological controls groundwater flow, in common with other published hydrogeophysical applications (e.g., Cuthbert et al., 2009; Nyquist et al., 2009). Although not all ERI locations exhibited distinctive resistivity contrasts, the aquitard was found to be discontinuous in the western parts of the site along the riverbanks. This area may provide a much larger geological window to capture regional groundwater discharge than those within the plume core zone with potential for unobserved ‘offset’ flow paths of higher TCE concentrations to be present (Fig. 7.2.1A).

At reach scale, stratified deposits of silt, clay and peat control the hydrology of the riverbed and are probably a riverward extension of the alluvial aquitard in the floodplain. The large organic matter fraction of the peat presents a retardation capacity for TCE that greatly exceeds the bedrock flow system. Low-permeability media present semi-confine regional groundwater upwelling and create significant vertical hydraulic gradients which closely follow river stage fluctuations. These are likely to restrict deep hyporheic exchange and influence lateral migration of plume beneath, through deeper more permeable strata (Fig. 7.2.1B). However, these geological controls are discontinuous and ‘leaky’ where geological windows are present and deeper hyporheic exchange is expected (Fig. 7.2.1B). Further evidence of this leakiness is provided by high-resolution temperature mapping where metre-scale heterogeneity in aquitard continuity was revealed. Centimetre-scale heterogeneities observed in riverbed cores (Fig. 7.2.1B) may also contribute to this leakiness and are known to present significant preferential pathways for contaminant transport in aquitard media (e.g., White et al., 2008). Along these multi-scale ‘bypass’ pathways, the retardation potential and permeability will not differ appreciably to the underlying Permo-Triassic sandstone. The overall significance of point-source pollutant retention by riverbed media will be controlled by the presence and size of these features as well as their position relative to contaminant flow lines.

The spatial distribution of groundwater fluxes through the riverbed will influence the location and magnitude of contaminant discharge and control the total dissolved contaminant flux from groundwater to surface water (Objective 3). Up-scaling from point measurements of the Darcy flux to the whole reach indicated typical baseflow rates to lie between 23.2 and 86.4 m³ d⁻¹. Heat flux modelling of temperature profiles suggests most of this baseflow accretion occurs via the geological windows where the Permo-Triassic

sandstone is close to the riverbed surface (Fig. 7.2.1B). Cross-channel variation in fluxes reflects the lateral concentration gradients observed previously in the plume. This supports the previous conceptualisation that contaminant input is dominated by these bypass zones (Fig. 7.2.1B). A good agreement between the two independent measures of flow was obtained although significant uncertainty arises in mass flux estimation where concentration and flow terms are observed at different spatial resolutions. Whole-reach TCE loading to surface water is estimated to be 0.43–1.5 g d⁻¹, which, on an annual basis, amounts to leaching of about 110–370 mL of pure TCE from the DNAPL source. However, the timeframe over which this mass is discharged will be influenced by adsorption to the peat lenses where vertical migration velocities may be reduced to <1 cm d⁻¹ (Fig. 7.2.1B). No impact from the plume on river water quality was found during any sampling campaign. Although ‘point impacts’ from preferential flow zones are a possibility, dilution will rapidly attenuate any point-source contaminant signal from groundwater. TCE concentrations many orders of magnitude greater would be needed to significantly degrade the quality of the surface water resource for this particular lowland river.

Assessing the plume transformation potential in an agricultural setting where groundwater and surface water quality are heavily impacted by NO₃⁻ from diffuse sources and macrophyte growth dominates the river channel during summer was important (Objective 4). Aerobic conditions and excess NO₃⁻ throughout the Permo-Triassic sandstone leads to quasi-conservative TCE transport behaviour over decadal residence times through the up-gradient regional aquifer. A large stoichiometric demand for labile DOC presents a ‘redox buffer’ to lower energy-yielding redox processes where dechlorination reactions are more energetically favourable. However, this buffer is overcome in places in the organic

horizons of the semi-confining deposits and surficial sands of the riverbed. Partial dechlorination of the plume (to cDCE) was associated with redox conditions characterised by (1) DO and NO_3^- depletion, (2) occasional Mn detection and (3) increases in CH_4 and DOC (Fig. 7.2.1C). Enhanced dechlorination (to cDCE and VC) was proved during 'plot-scale' investigation of shallow sedimentation around a submerged *Ranunculus* stand. Here, an excess of DOC lead to a redox regime dominated by metal reduction and accelerated methanogenesis (Fig. 7.2.1C). Dissolved CH_4 proved to be a useful indicator of the extent of dechlorination in this anaerobic environment.

In macrophyte-dominated summer conditions in lowland rivers, surficial sedimentation patterns on the riverbed surface are probably more important for destructive attenuation than deeper flow-constraining structures, even though these strata may contain a greater fraction of organic matter. Although the cumulative impact of these locally-reactive zones is difficult to quantify, from a remediation perspective, attenuation processes are unlikely to prevent migration of the majority of the contaminant mass to the river. In the timeframe of this study, degradation products were detected in <20% of samples collected from about-to-discharge groundwater. Although further exhaustive, plot-scale sampling might reveal more highly methanogenic zones, it is clear that extensive transformation is not occurring at a scale observed at other aquifer-river interfaces (e.g., Conant et al., 2004). At best, some conversion of the plume to cDCE can be expected which may then be amenable to aerobic mineralisation (Bradley and Chapelle, 1998a) although whether this process is actually significant at field-scale is debatable (Abe et al., 2009). However, because no degradation is occurring in the up-gradient plume, the natural attenuation capacity of the aquifer-river interface can be considered to exceed that of the underlying PTS aquifer in discrete zones (Fig. 7.2.1B, C).

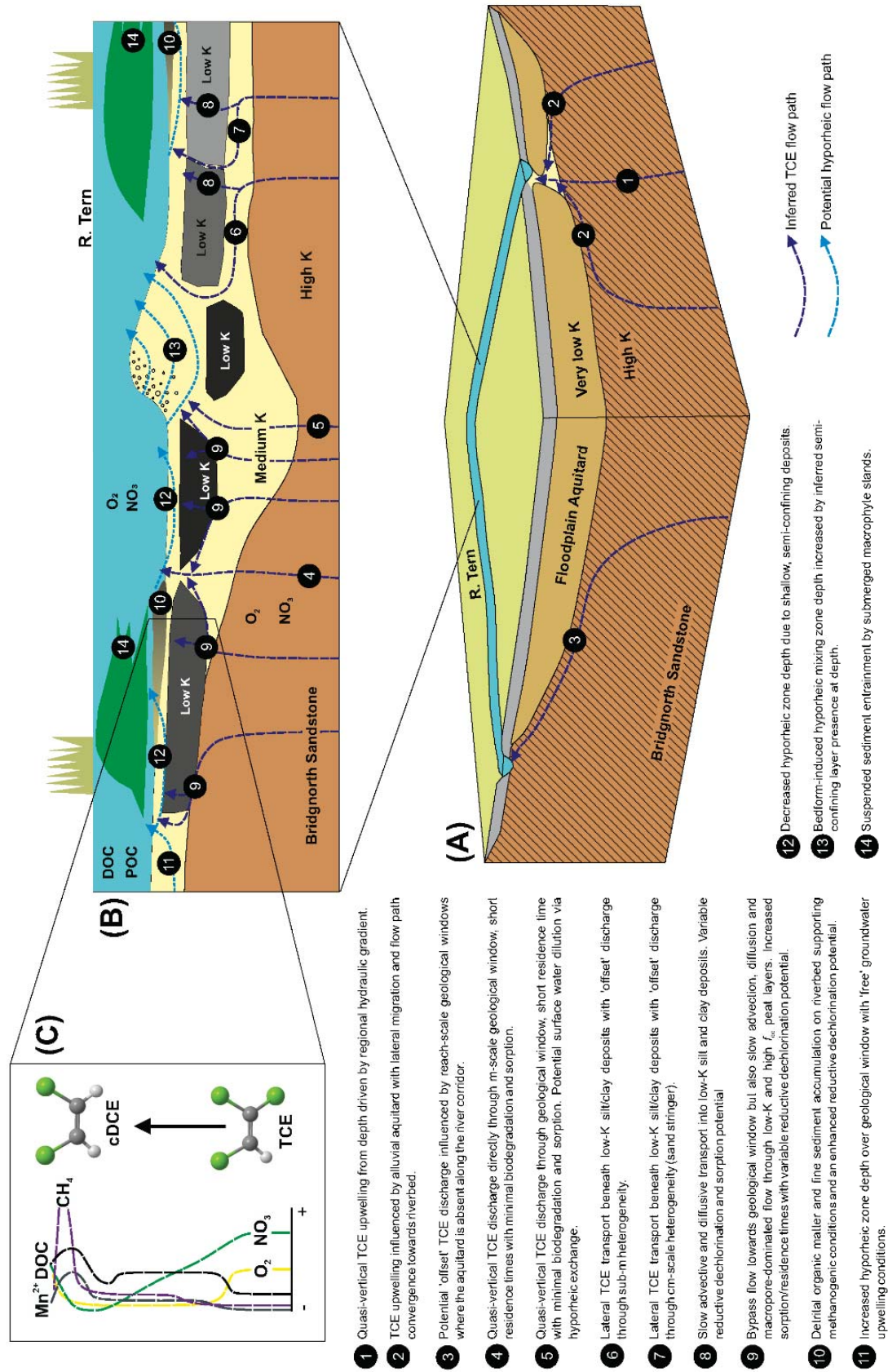


Figure caption overleaf

Fig. 7.2.1 Multi-scale and multi-process model presenting the integrated conceptual understanding of groundwater flow, contaminant transport and biodegradation potential derived from this case study. **(A)** Floodplain-scale flow controls **(B)** reach-scale flow controls, transport patterns and surface water interactions **(C)** biogeochemical gradients favouring reductive dechlorination of TCE to cDCE.

7.3 Wider implications of the research

In terms of the UK's implementation of EU Water Framework Directive (WFD) objectives for water quality, the risk posed by this particular groundwater plume is low at present from the perspective of a compliance point situated in the water column of the River Tern. The massive dilution potential afforded results in surface water TCE concentrations that are at least 3 orders of magnitude lower than the average annual environmental quality standard (EQS) of $10 \mu\text{g L}^{-1}$ for surface water under the DSD (CEC, 2008). This low risk assignment is due largely to the relatively low contamination levels ($<50 \mu\text{g L}^{-1}$) documented in the down-gradient plume over the timeframe of this study. However, historic monitoring by the EA (Chapter 3) and the two HydraSleeve campaigns presented in this study clearly indicate a rising trend in TCE concentrations from the SGS boreholes. This raises important questions regarding future risk management of the site. These were recently addressed using predictive contaminant transport modelling with forward extrapolation from observed rates of concentration rise in the SGS boreholes during the past decade of monitoring (Perkins, 2013). It was concluded that river water TCE concentrations would probably not ever exceed $4.7 \mu\text{g L}^{-1}$ by 2050 under the most extreme and unrealistic low flow scenarios. That study could demonstrate that advective-dispersive transport through the PTS aquifer over a distance of ~ 1.5 km (from the likely source area) provides a reduction in contaminant concentration necessary to achieve regulatory compliance after final dilution within the river for this particular plume. Therefore, although destructive attenuation processes at the aquifer-river interface are probably not capable of mitigating significant fractions of the contaminant load, sufficient natural

attenuation capacity is provided within the aquifer itself before the concentration front reaches the receptor.

This study highlights the importance of spatial scale of observation when attempting to decipher groundwater flow paths and interpret chemical gradients superimposed upon them in the complex hydrogeological environment of lowland aquifer-river interfaces. Future monitoring network design investigating the fate of point-source contaminant plumes should focus on nested observations, extending over multiple and overlapping scales for improved process understanding of solute transport and transformation. For example, in this study, regional groundwater discharge from the PTS to the River Tern is indicated by the position of piezometric contours at catchment scale with ‘gaining’ flow conditions indicated by observations of hydraulic head at the scale of the floodplain as well as positive VHGs at reach-scale in the riverbed. However, with the benefit of high-resolution temperature mapping, it is clear that the actual distribution of groundwater and (possible) contaminant fluxes to the river vary over metre scales with low or no flux areas immediately juxtaposed by high flux areas. Furthermore, with the application of 2-D ERI as a non-invasive imaging tool calibrated with actual geological information, ‘scale gaps’ which inherently arise from point-sampling over different scales can be rapidly bridged to provide laterally-continuous observations of boundary conditions which restrict or enhance groundwater flow over multiple depths. Similarly, at the scale of the plume, a lack of TCE daughter products obtained from the sandstone aquifer and initial sampling over the longer reach would suggest the whole plume is behaving conservatively. However, with sub-metre scale vertical resolutions provided by a nested configuration of mini-piezometers and pore water samplers, it can be shown that chemical modification of the plume is in fact occurring discretely, along the final 20–40 cm of a pathway extending several km from the

source.

The importance of accelerated biogeochemical turnover associated with fine organic matter deposition patterns on riverbeds around in-stream vegetation has recently been described for carbon cycling and nutrient retention (Sanders et al., 2007; Trimmer et al., 2009; 2012; Ullah et al., 2014). However, this study is the first to document a possible association with an increased reductive dechlorination potential for TCE. This has important implications for the destructive attenuation capacity of lowland rivers receiving CE-contamination baseflow in the UK and elsewhere which are subject extensive vegetation growth in the spring and summer months. Consideration should be paid by catchment managers of this possible additional buffering capacity for redox-sensitive groundwater pollutants where common management practices often involve removal of in-stream vegetation to reduce flood risk and improve oxygenation of bed sediments. River restoration scheme design along urban river reaches which may receive multiple chlorinated organic contaminant plumes could be adapted to incorporate structures which facilitate macrophyte stand development and fine sediment entrainment. This would have the added benefit of improving river water clarity by reducing suspended sediment loads.

7.4 Future research outlook

7.4.1 Numerical simulations

Although some MODFLOW-based simulations of contaminant transport have already been carried out at the site (e.g., Rahman and Shepley, 2005; Perkins, 2013), further modelling could aid in the conceptualisation of flow and transport processes observed in this study (e.g., Munz et al., 2011). New fully 3-D physically-based models (such as HydroGeoSphere) could be utilised to this end. Beginning with a simple flow model, further multi-scale complexity could be added to simulate the impacts of the floodplain aquitard, geological windows and semi-confining deposits. The flow model could be parameterised, calibrated and validated using primary field data collected during this study. Retardation and decay terms could be added to provide an integrated assessment of contaminant transport and fate. Finally, transient surface water interactions could be simulated to refine contaminant flux estimates and better understand the significance of hyporheic flows at the site.

7.4.2 Quantification of hyporheic exchange

A suitable geochemical tracer is needed to investigate hyporheic exchange patterns and ascertain whether dilution of the plume or biogeochemical turnover is being stimulated from infiltrating surface water to the riverbed. Chloride (Cl^-) concentrations were not suitably distinctive in the end-members to be used as a tracer in this investigation. Boron (B) could be explored as an alternative as it is a ubiquitous minor solute in effluent discharges to rivers across the UK and Europe (Wyness et al., 2003) and like Cl^- , exhibits generally chemically conservative behaviour (Neal et al., 1998). Alternatively, $\delta^{18}\text{O}$ could also be explored as an additional conservative species although end-members may only be

distinctive during certain times of the year (Clay et al., 2004). The end members of any tracer used must remain distinctive during high river flows when surface water invasion is most likely.

7.4.3 Investigation of TCE-sediment partitioning

The retardation capacity of the different geological strata present could be better constrained using laboratory experiments rather than literature estimates of K_{oc} . Batch experiments could be prepared with (1) Permo-Triassic sandstone (2) riverbed peat deposits (3) surficial sands and amended with serial dilutions of TCE. This would allow isotherms to be constructed and analysed and material-specific K_{oc} values could be derived. Total organic carbon should be determined with greater sensitivity using wet-chemical techniques or elemental analysis. The latter would also allow oxygen and hydrogen ratios to be examined to facilitate interpretation of sorption isotherms. Partitioned TCE could be quantified at field scale using similar methods to Conant et al (2004) in order to validate laboratory K_{oc} estimates.

7.4.4 Further investigation of in-situ biodegradation

Molecular biomarkers techniques could be applied to assess in-situ microbial communities in dechlorinating zones. A 16S rRNA approach using quantitative polymerase chain reaction (qPCR) assays could be applied to identify the presence and activity of populations of dechlorinators including *Dehalococcoides* spp. Functional genes which encode for dehalogenase enzymes associated with specific dehalorespiring steps of *Dehalococcoides* strains could be targeted using a PCR-based approach (e.g., Damgaard et al., 2013). Compound-specific isotope analysis (CSIA) could also be used in combination with the microbial assessment to verify a biological pathway for reductive dechlorination

(Hunkeler et al., 1999). Carbon isotope enrichment ($\delta^{13}\text{C}$) could be compared with chlorine number calculations (Weaver et al., 1997) with ethene determination included in the analytical method to produce a complete picture of reductive dechlorination activity.

7.4.5 Passive sampling of CEs and redox gradients beneath vegetation

The small scale (e.g., 5–10 cm) vertical variability of CEs and redox-sensitive solutes observed in the shallow riverbed in this study warrant further study to investigate the reactive transport of TCE. High-resolution vertical profiles could be obtained from passive sampling using Diffusive Equilibrium in Thin Films (DET) gel samplers (Ullah et al 2012). This would permit fine-scale (cm–mm), in-situ observations of redox stratification without the need for disruptive extractive sampling methods and provide important insights on biogeochemical gradients associated with sediment macropore structures. Future work should focus on adapting the DET approach for CE acquisition where samplers could be installed below macrophyte stands where seasonal changes in redox zonation and degradation patterns could be observed to better constrain the pollutant buffering potential.

8. References

Abe, Y., Aravena, R., Zopfi, J., Parker, B., Hunkeler, D., 2009. Evaluating the fate of chlorinated ethenes in streambed sediments by combining stable isotope, geochemical and microbial methods. *J. Contam. Hydrol.* 107, 10-21.

Abesser, C., Shand, P., Gooddy, D., Peach, D., 2008 The role of alluvial valley deposits in groundwater–surface water exchange in a Chalk river. In (Eds.) Abesser, C., Wagener, T., Nuetzmann, G., *Groundwater–Surface Water Interaction: Process Understanding, Conceptualization and Modelling*. International Association of Hydrological Sciences Press.

Acworth, R. I., Jorstad, L. B., 2006. Integration of multi-channel piezometry and electrical tomography to better define chemical heterogeneity in a landfill leachate plume within a sand aquifer. *Journal of Contaminant Hydrology* 83, 200-220.

Adams, B., Peach, D., Bloomfield, J., 2003. The LOCAR Hydrogeological Infrastructure in the Tern Catchment. *Groundwater Systems and Water Quality Programme, Internal Report IR/03/180*. British Geological Survey, Keyworth.

Agilent Technologies, 2008. *Analysis of Volatile Organic Compounds in Water Using Static Headspace-GC/MS*. Publication Number 5990-3285EN.

Agilent Technologies, 2010. *Simultaneous Analysis of Greenhouse Gases by Gas Chromatography*. Publication Number 5990-5129EN.

Allen, D. J., Brewerton, L. J., Coleby, L. M., Gibbs, B. R., Lewis, M. A., MacDonald, A. M., Wagstaff, S. J., Williams, A. T., 1997. The Physical Properties of Major Aquifers in England and Wales. *British Geological Survey Technical Report WD/97/34*. British Geological Survey, Keyworth.

Allen, D. J., Darling, W.G., Gooddy, C. D., Lapworth, D. J., Newell, A. J., Williams, A. T., Allen, D., Abesser, C., 2010. Interaction between groundwater, the hyporheic zone and a Chalk stream: a case study from the River Lambourn, UK. *Hydrogeology Journal* 18, 1125-1141.

Allen-King, R. M., Groenevelt, H., James Warren, C., Mackay, D. M., 1996. Non-linear chlorinated-solvent sorption in four aquitards. *Journal of Contaminant Hydrology* 22, 203-221.

Allen-King, R. M., Grathwohl, P., Ball, W. P., 2002. New modelling paradigms for the sorption of hydrophobic organic chemicals to heterogeneous carbonaceous matter in soils, sediments, and rocks. *Advances in Water Resources* 25, 985-1016.

Alvarez-Cohen, L., McCarty, P. L., 1991. Product toxicity and cometabolic competitive inhibition modelling of chloroform and trichloroethylene transformation by methanotrophic resting cells. *Applied and Environmental Microbiology* 57, 1031-1037.

Angermann, L., Krause, S., Lewandowski, J., 2012. Application of heat pulse injections for investigating shallow hyporheic flow in a lowland river. *Water Resour. Res.* 48, W00P02.

Anibas, C., Fleckenstein, J. H., Volze, N., Buis, K., Verhoeven, R., Meire, P., Batelaan, O., 2009. Transient or steady-state? Using vertical temperature profiles to quantify groundwater–surface water exchange. *Hydrological Processes* 15, 2165-2177.

Arciero, D., Vanelli, T., Logan, M., Hooper, D., 1989. Degradation of trichloroethylene by ammonia-oxidising bacterium *Nitrosomonas europaea*. *Biochem. Biophys. Res. Commun.* 159, 640-643.

Armbruster, D. A., Pry, T., 2008. Limit of blank, limit of detection and limit of quantitation. *Clin Biochem Rev* 29, S49-S52.

Arnold, W. A., Roberts, A. L., 2000. Pathways and kinetics of chlorinated ethylene and chlorinated acetylene reaction with Fe (0) particles. *Environmental Science & Technology* 34, 1794-1805.

Arp, D. J., Yeager, C. M., Hyman, M. R., 2001. Molecular and cellular fundamentals of aerobic cometabolism of trichloroethylene. *Biodegradation* 12, 81-103.

Aulenta, F., Beccari, M., Majone, M., Papini, M. P., Tandoi, V., 2008. Competition for H₂ between sulphate reduction and dechlorination in butyrate-fed anaerobic cultures. *Process Biochemistry* 43, 161-168.

Aulenta, F., Majone, M., Verbo, P., Tandoi, V., 2002. Complete dechlorination of tetrachloroethene to ethene in presence of methanogenesis and acetogenesis by an anaerobic sediment microcosm. *Biodegradation* 13, 411-424.

Aulenta, F., Pera, A., Rossetti, S., Petrangeli Papini, M., Majone, M., 2007. Relevance of side reactions in anaerobic reductive dechlorination microcosms amended with different electron donors. *Water Research* 41, 27-38.

Avery, C., 1994. *Interaction of ground water with the Rock River near Byron, Illinois*. U.S. Geological Survey Water-Resources Investigations Report 94-4034. U. S. Geological Survey, Virginia.

Azizian, M. F., Marshall, I. P., Behrens, S., Spormann, A. M., Semprini, L., 2010. Comparison of lactate, formate, and propionate as hydrogen donors for the reductive dehalogenation of trichloroethene in a continuous-flow column. *Journal of Contaminant Hydrology* 113, 77-92.

Bagley, D. M., Gossett, J. M., 1990. Tetrachloroethene transformation to trichloroethene and *cis*-1,2-dichloroethene by sulphate-reducing enrichment cultures. *Applied and Environmental Microbiology* 56, 2511-2516.

Baines, D., Smith, D. G., Froese, D. G., Bauman, P., Nimeck, G., 2002. Electrical resistivity ground imaging (ERGI): a new tool for mapping the lithology and geometry of channel-belts and valley-fills. *Sedimentology* 49, 441-449.

Baker, A., Cumberland, S., Hudson, N., 2008. Dissolved and total organic and inorganic carbon in some British rivers. *Area* 40, 117-127.

Baker, M. A., Dahm, C. N., Valett, H. M., 1999. Acetate retention and metabolism in the hyporheic zone of a mountain stream. *Limnology and Oceanography* 44, 1530-1539.

Baker, M. A., Dahm, C. N., Valett, H. M., 2000. Anoxia, anaerobic metabolism, and biogeochemistry of the stream water-groundwater interface. In (Eds.) Jones J. B., Mulholland P. J., *Streams and groundwater waters*. Academic Press, New York.

Baker, M. A., Vervier, P., 2004. Hydrological variability, organic matter supply and denitrification in the Garonne River ecosystem. *Freshwater Biology* 49, 181-190.

Ball, W. P., Roberts, P. V., 1991. Long-term sorption of halogenated organic chemicals by aquifer material. 1. Equilibrium. *Environmental Science & Technology* 25, 1223-1237.

Ballapragada, B. S., Stensel, H. D., Puhakka, J. A., Ferguson, J. F., 1997. Effect of hydrogen on reductive dechlorination of chlorinated ethenes. *Environmental Science & Technology* 31, 1728-1734.

Basu, N. B., Rao, P. S. C., Poyer, I. C., Annable, M. D., Hatfield, K., 2006. Flux-based assessment at a manufacturing site contaminated with trichloroethylene. *J. Contam. Hydrol.* 86, 105-127.

Battin, T. J., Kaplan, L. A., Findlay, S., Hopkinson, C. S., Marti, E., Packman, A. I., Newbold, J. D., Sabater, F., 2008. Biophysical controls on organic carbon fluxes in fluvial networks. *Nature Geoscience* 1, 95-100.

Bellar, T. A., Lichtenberg, J. J., Kroner, R. C., 1974. The occurrence of organohalides in chlorinated drinking waters. *Journal American Water Works Association* 66, 703-706.

Bencala, K. E., 1993. A perspective on stream-catchment connections. *Journal of the North American Benthological Society* 44-47.

Benker, E. B., Davis, G., Barry, D., 1997. Factors controlling the distribution and transport of trichloroethene in a sand aquifer: hydrogeology and results of an in situ transport experiment. *Journal of Hydrology* 202, 315-340.

Benker, E., Davis, G. B., Barry, D. A., 1998. Estimating the retardation coefficient of trichloroethene for a sand aquifer low in sediment organic carbon—a comparison of methods. *Journal of Contaminant Hydrology* 30, 157-178.

Binley, A., Cassiani, G., Deiana, R., 2010. Hydrogeophysics: opportunities and challenges. *Bollettino di Geofisica Teorica ed Applicata* 51, 267-284.

Binley, A., Kemna, A., 2005. DC resistivity and induced polarization methods. In (Eds.) Rublin, Y., Hubbard, S. S., *Hydrogeophysics* Springer Netherlands.

Binley, A., Ullah, S., Heathwaite, A. L., Heppell, C., Byrne, P., Lansdown, K., Trimmer, M., Zhang, H., 2013. Revealing the spatial variability of water fluxes at the groundwater-surface water interface. *Water Resour. Res.* DOI: 10.1002/wrcr.20214.

Bishop, P., Lerner, D., Jakobsen, R., Gosk, E., Burston, M., Chen, T., 1993. Investigation of a Solvent Polluted Industrial Site on a Deep Sandstone Mudstone Sequence in the UK. 2. Contaminant Sources, Distributions, Transport and Retardation. *J. Hydrol.* 149, 231-256.

Blackwell, J., 2002. *Recharge characterisation through drift in the Tern catchment, Shropshire*. MSc thesis, School of Geography, Earth and Environmental Sciences, University of Birmingham.

Blume, T., Krause, S., Meinikmann, K., Lewandowski, J., 2013. Upscaling lacustrine groundwater discharge rates by fiber-optic distributed temperature sensing. *Water Resources Research* 49, 7929-7944.

Bouch, J., Hough, E., Kemp, S. J., McKeeverny, J. A., Williams, G. M., Greswell, R. B., 2006. Sedimentary and diagenetics of the Wildmoor Sandstone Formation: implications for groundwater and contaminant, and sand production. In (Eds.) Barker, R. D., Tellam, J. H., *Fluid Flow and Solute Movement in Sandstones: The Onshore UK Permo-Triassic Red Bed Sequence*. Geological Society of London, London.

Boulton, A. J., Findlay, S., Marmonier, P., Stanley, E. H., Valett, H. M., 1998. The functional significance of the hyporheic zone in streams and rivers. *Annual Review of Ecology and Systematics* 38, 59-81.

Bourg, A. C., Mouvet, C., Lerner, D. N., 1992. A review of the attenuation of trichloroethylene in soils and aquifers. *Quarterly Journal of Engineering Geology and Hydrogeology* 25, 359-370.

Bouwer E. J., 1994. Bioremediation of chlorinated solvents using alternate electron acceptors. In (Eds.) Norris R. D., Hinchee, R. E., Brown, R., McCarty, P. L., Semprini, L., Wilson, D. H., Kampbell M, Reinhard, E. G, Bouwer, R, Borden, C., Vogel, T.M., Thomas, J. M., Ward, C.H., *Handbook of bioremediation*, Lewis Publishers, Boca Raton.

Bradley P. M., Chapelle F. H., Wilson J. T., 1998b. Field and laboratory evidence for intrinsic biodegradation of vinyl chloride contamination in a Fe(III)-reducing aquifer. *Journal of Contaminant Hydrology* 31, 111–127.

Bradley, P. M., 2000. Microbial degradation of chloroethenes in groundwater systems. *Hydrogeology Journal* 8, 104-111.

Bradley, P. M., 2003. History and ecology of chloroethene biodegradation: a review. *Bioremediation Journal* 7, 81-109.

Bradley, P. M., Chapelle, F. H., 1996. Anaerobic mineralization of vinyl chloride in Fe (III)-reducing, aquifer sediments. *Environmental Science & Technology* 30, 2084-2086.

Bradley, P. M., Chapelle, F. H., 1998a. Effect of contaminant concentration on aerobic microbial mineralization of DCE and VC in stream-bed sediments. *Environ. Sci. Technol.* 32, 553-557.

Bradley, P. M., Chapelle, F. H., 1998b. Microbial mineralization of VC and DCE under different terminal electron accepting conditions. *Anaerobe* 4, 81-87.

Bradley, P. M., Chapelle, F. H., 1999a. Methane as a product of chloroethene biodegradation under methanogenic conditions. *Environmental Science & Technology* 33, 653-656.

Bradley, P. M., Chapelle, F. H., 1999b. Role for acetotrophic methanogens in methanogenic biodegradation of vinyl chloride. *Environmental Science & Technology* 33, 3473-3476.

Bradley, P. M., Chapelle, F. H., 2000a. Aerobic microbial mineralization of dichloroethene as sole carbon substrate. *Environ. Sci. Technol.* 34, 221-223

Bradley, P. M., Chapelle, F. H., 2000b. Acetogenic microbial degradation of vinyl chloride. *Environ. Sci. Technol.* 34, 2761-2763.

Bradley, P. M., Landmeyer, J. E., Dinicola, R. S., 1998a. Anaerobic oxidation of [1,2-¹⁴C] dichloroethene under Mn (IV)-reducing conditions. *Applied and Environmental Microbiology* 64, 1560-1568.

Brennan, R. A., Sanford, R. A., Werth, C. J., 2006. Chitin and corncobs as electron donor sources for the reductive dechlorination of tetrachloroethene. *Water Research* 40, 2125-2134.

Brereton, N. R., 1976. *The Groundwater Hydraulic of the Bunter Sandstone near Helshaw Grange, Shropshire*. Water Research Centre, UK. (Unpublished).

Bridge, D. McC., Humpage, A. J., Sheppard, H. Lelliott, M. and Garcia-Bajo, M., 2002. *Geological framework study – east Shropshire Permo-Triassic Sandstone groundwater modelling project. British Geological Survey Commissioned Report CR/02/176*. British Geological Survey, Keyworth, UK.

Brunke, M., Gonser, T. O. M., 1997. The ecological significance of exchange processes between rivers and groundwater. *Freshwater Biology* 37, 1-33.

Burston, M., Nazari, M., Bishop, P., Lerner, D., 1993. Pollution of Groundwater in the Coventry Region (UK) by Chlorinated Hydrocarbon Solvents. *J. Hydrol.* 149, 137-161.

Burton, G. A., Greenberg, M. S., Rowland, C. D., Irvine, C. A., Lavoie, D. R., Brooker, J., Moore, L., Raymer, D. F. N., McWilliam, R. A., 2005. In situ exposures using caged organisms: a multi-compartment approach to detect aquatic toxicity and bioaccumulation. *Environmental Pollution* 134, 133-144.

Buss, S., Cai, Z., Cardenas, M. B., Fleckenstein, J. H., Hannah, D. M., Heppell, K., Hulme, P., Ibrahim, T., Kaiser, D., Krause, S., Lawler, D., Lerner, D., Mant, J., Malcolm, I., Old, G., Parkin, G., Pickup, R., Pinay, G., Porter, J., Rhodes, G., Richie, A., Riley, J., Robertson, A., Sear, D., Shields, B., Smith, J., Tellam, J. H., Wood, P., 2009. *The Hyporheic Handbook - A handbook on the groundwater-surface water interface and hyporheic zone for environmental managers, Science Report SC050070*. Environment Agency, Bristol.

Butler, E. C., Hayes, K. F., 1999. Kinetics of the transformation of trichloroethylene and tetrachloroethylene by iron sulfide. *Environmental Science & Technology* 33, 2021-2027.

Byrne, P., Binley, A., Heathwaite, A. L., Ullah, S., Heppell, C. M., Lansdown, K., Zhang, H., Trimmer, M., Keenan, P., 2013. Control of river stage on the reactive chemistry of the hyporheic zone. *Hydrological Processes* 28, 4766-4779.

Cardenas, M. B., Zlotnik, V. A., 2003. Three-dimensional model of modern channel bend deposits. *Water Resources Research* DOI: 10.1029/2002WR001383.

Carter, J. M., Lapham, W. W., Zogorski, J. S., 2008. Occurrence of volatile organic compounds in aquifers of the United States. *J. Am. Water Resour. Assoc.* 44, 399-416.

Chambon, J. C., Bjerg, P. L., Scheutz, C., Bælum, J., Jakobsen, R., Binning, P. J., 2013. Review of reactive kinetic models describing reductive dechlorination of chlorinated ethenes in soil and groundwater. *Biotechnology and Bioengineering* 110, 1-23.

Chapelle, F. H., McMahon, P. B., Dubrovsky, N. M., Fujii, R. F., Oaksford, E. T., Vroblesky, D. A., 1995. Deducing the distribution of terminal electron-accepting processes in hydrologically diverse groundwater systems. *Water Resources Research* 31, 359-371.

Chapman, S. W., Parker, B. L., Cherry, J. A., Aravena, R., Hunkeler, D., 2007. Groundwater-surface water interaction and its role on TCE groundwater plume attenuation. *J. Contam. Hydrol.* 91, 203-232.

Cheng, D., He, J., 2009. Isolation and characterization of "Dehalococcoides" sp. Strain MB, which dechlorinates tetrachloroethene to trans-1, 2-dichloroethene. *Applied and Environmental Microbiology* 75, 5910-5918.

Cherry, J. A., 1997. Conceptual models for Chlorinated Solvent Plumes and Their Relevance to Intrinsic Remediation. *Proceedings of the Symposium on Natural Attenuation of Chlorinated Organics in Ground Water*. U.S. Environmental Protection Agency, Washington, DC.

Chiou, C. T., Peters, L. J., Freed, V. H., 1979. A physical concept of soil-water equilibria for nonionic organic compounds. *Science* 206, 831-832.

Christiansen, N., Ahring, B. K., 1996. *Desulfitobacterium hafniense* sp. nov., an anaerobic, reductively dechlorinating bacterium. *International Journal of Systematic Bacteriology* 46, 442-448.

Church, P. E., Vroblesky, D. A., Lyford, F. P., Willey, R., 2002. *Guidance on the use of Passive-Vapor-Diffusion Samplers to Detect Volatile Organic Compounds in Ground-Water-Discharge Areas, and Example Applications in New England*. U.S. Geological Survey, Virginia.

Clark, L., 1976. *Shropshire Groundwater Investigation Determination of the Permeability of the bed of the River Tern*. Water Research Centre, London. (Unpublished).

Clay, A., Bradley, C., Gerrard, A. J., Leng, M. J., 2004. Using stable isotopes of water to infer wetland hydrological dynamics. *Hydrology and Earth System Sciences* 8, 1164-1173.

Clewell, H. J., Gentry, P. R., Gearhart, J. M., Allen, B. C., Andersen, M. E., 2001. Comparison of cancer risk estimates for vinyl chloride using animal and human data with a PBPK model. *Science of the Total Environment* 274, 37-66.

Clifford, J., Binley, A., 2010. Geophysical characterization of riverbed hydrostratigraphy using electrical resistance tomography. *Near Surface Geophysics* 8, 493-501.

Cole, J. R., Fathepure, B. Z., Tiedje, J. M., 1995. Tetrachloroethene and 3-chlorobenzoate dechlorination activities are co-induced in *Desulfomonile tiedjei* DCB-1. *Biodegradation* 6, 167-172.

Coleman, N. V., Mattes, T. E., Gossett, J. M., Spain, J. C., 2002. Phylogenetic and kinetic diversity of aerobic vinyl chloride-assimilating bacteria from contaminated sites. *Applied and Environmental Microbiology* 68, 6162-6171.

Conant Jr, B., 2000. Ground-water plume behaviour near the ground-water/surface water interface of a river. *Proceeding of the Ground-Water/Surface-Water Interactions Workshop* EPA/542/R-00/007. U.S. Environmental Protection Agency, Washington DC.

Conant Jr, B., 2004. Delineating and quantifying ground water discharge zones using streambed temperatures. *Ground Water* 42, 243-257.

Conant Jr, B., Cherry, J.A., Gillham, R. W., 2004. A PCE groundwater plume discharging to a river: influence of the streambed and near-river zone on contaminant distributions. *J. Contam. Hydrol.* 73, 249-279.

Conrad, M. E., Brodie, E. L., Radtke, C. W., Bill, M., Delwiche, M. E., Lee, M. H., Swift, D. L., Colwell, F. S., 2010. Field evidence for co-metabolism of trichloroethene stimulated by addition of electron donor to groundwater. *Environmental Science & Technology* 44, 4697-4704.

Constantz, J., 2008. Heat as a tracer to determine streambed water exchanges. *Water Resources Research* DOI: 10.1029/2008WR006996

Cook, S. J., 2010. The glacial geology of Shropshire: insights from modern glaciology. *Proceedings of the Shropshire Geological Society* 15, 20-27.

Council of European Communities, (CEC)., 1976. Council Directive 76/464/EEC of 4 May 1976 on pollution caused by certain dangerous substances discharged into the aquatic environment of the Community. *Official Journal of the European Communities* L129.

Council of European Communities, (CEC)., 1998. Directive 98/83/EC of the European Parliament and of the Council of 3 November 1998 on the quality of water intended for human consumption. *Official Journal of the European Communities* L33032.

Council of European Communities, (CEC)., 2000. Directive 2000/60/EC of the European Parliament and of the Council of 23 October 2000 Establishing a Framework for Community Action in the Field of Water Policy. *Official Journal of the European Communities* L327.

Council of European Communities, (CEC)., 2008. Directive 2008/105/EC of the European Parliament and of the Council of 16 December 2008 on environmental quality standards in the field of water policy, amending and subsequently repealing Council Directives 82/176/EEC, 83/513/EEC, 84/156/EEC, 84/491/EEC, 86/280/EEC and amending Directive 2000/60/EC of the European Parliament and of the Council. *Official Journal of the European Communities* L348.

Crook, N., Binley, A., Knight, R., Robinson, D. A., Zarnetske, J., Haggerty, R., 2008. Electrical resistivity imaging of the architecture of substream sediments. *Water Resources Research* DOI: 10.1029/2008WR006968

Cuthbert, M. O., Mackay, R., Durand, V., Aller, M. F., Greswell, R. B., Rivett, M. O., 2010. Impacts of river bed gas on the hydraulic and thermal dynamics of the hyporheic zone. *Advances in Water Resources* 33, 1347-1358.

Cuthbert, M. O., Mackay, R., Tellam, J. H., Barker, R. D., 2009. The use of electrical resistivity tomography in deriving local-scale models of recharge through superficial deposits. *Quarterly Journal of Engineering Geology and Hydrogeology* 42, 199-209.

Dahm, C. N., Grimm, N. B., Marmonier, P., Valett, H. M., Vervier, P., 1998. Nutrient dynamics at the interface between surface waters and groundwaters. *Freshwater Biology* 40, 427-451.

Damgaard, I., Bjerg, P. L., Baelum, J., Scheutz, C., Hunkeler, D., Jacobsen, C. S., Tuxen, N., Broholm, M. M., 2013. Identification of chlorinated solvents degradation zones in clay till by high resolution chemical, microbial and compound specific isotope analysis. *Journal of Contaminant Hydrology* 146, 37-50.

Darcy, H., 1856. *Les Fontaines Publiques de la Ville de Dijon*. Dalmont, Paris.

Darling, W. G., Gooddy, D. C., 2006. The hydrogeochemistry of methane: evidence from English groundwaters. *Chemical Geology* 229, 293-312.

Darlington, R., Lehmicke, L. G., Andrachek, R. G., Freedman, D. L., 2013. Anaerobic abiotic transformations of *cis*-1,2-dichloroethene in fractured sandstone. *Chemosphere* 90, 2226-2232.

Davis, J. W., Carpenter, C. L., 1990. Aerobic biodegradation of vinyl chloride in groundwater samples. *Applied and Environmental Microbiology* 56, 3878-3880.

Dean Jr, W. E., 1974. Determination of carbonate and organic matter in calcareous sediments and sedimentary rocks by loss on ignition: comparison with other methods. *Journal of Sedimentary Research* 44, 242-248.

Dennie, D., Gladu, I., Lépine, F., Villemur, R., Bisailon, J. G., Beaudet, R., 1998. Spectrum of the reductive dehalogenation activity of *Desulfitobacterium frappieri* PCP-1. *Applied and environmental microbiology* 64, 4603-4606.

Department for Environment, Food and Rural Affairs, (DEFRA). 2005. *Risk reduction strategy and analysis of advantages and drawbacks for trichloroethylene*. (<http://archive.defra.gov.uk/environment/quality/chemicals/documents/report060203.pdf>).

Department of Environment Food and Rural Affairs, (DEFRA)., 2004. *Nitrate Vulnerable Zones – 2003 Re-Survey Report*. DEFRA, London.

Diem, S., Rudolf von Rohr, M., Hering, J. G., Kohler, H. P. E., Schirmer, M., Von Gunten, U., 2013. NOM degradation during river infiltration: Effects of the climate variables temperature and discharge. *Water Research* 47, 6585-6595.

Divine, C. E., McCray, J. E., 2004. Estimation of membrane diffusion coefficients and equilibration times for low-density polyethylene passive diffusion samplers. *Environ. Sci. Technol.* 38, 1849-1857.

Doherty, R. E., 2000. A History of the Production and Use of Carbon Tetrachloride, Tetrachloroethylene, Trichloroethylene and 1, 1, 1-Trichloroethane in the United States: Part 2--Trichloroethylene and 1, 1, 1-Trichloroethane. *Environmental Forensics* 1, 83-93.

Domenico, P. A., Schwartz, F. W., 1990. *Physical and chemical hydrogeology*. John Wiley & Sons, New York.

Ehlke, T. A., Imbrigiotta, T. E., Dale, J. M., 2004. Laboratory comparison of polyethylene and dialysis membrane diffusion samplers. *Ground Water Monitoring & Remediation* 24, 53-59.

Elango, V. K., Ligginstoffer, A. S., Fathepure, B. Z., 2006. Biodegradation of vinyl chloride and *cis*-dichloroethene by a *Ralstonia* sp. strain TRW-1. *Applied microbiology and biotechnology* 72, 1270-1275.

Ellis, P. A., Rivett, M. O., 2007. Assessing the impact of VOC-contaminated groundwater on surface water at the city scale. *Journal of Contaminant Hydrology* 91, 107-127.

Ellis, P.A., 2003. The impact of urban groundwater upon surface water quality: Birmingham—River Tame study, UK. PhD thesis, School of Geography, Earth and Environmental Sciences, University of Birmingham.

Engelhardt, I., Piepenbrink, M., Trauth, N., Stadler, S., Kludt, C., Schulz, M., Schuth, C., Ternes, T. A., 2011. Comparison of tracer methods to quantify hydrodynamic exchange within the hyporheic zone. *Journal of Hydrology* 400, 255-266.

Environment Agency, (EA)., 2008. *T348 Conceptual Modelling Assignment January 2008 – Tern Valley Permo-Triassic Sandstone Aquifer*. Environment Agency, Bristol.

Environment Agency, (EA)., 2009. *Unpublished data*. Environment Agency, Bristol.

Environment Agency, (EA)., 2010. *Unpublished data*. Environment Agency, Bristol.

Environment Agency, (EA)., 2012. *Unpublished data*. Environment Agency, Bristol.

Environment Agency, (EA)., 2013. *Unpublished data*. Environment Agency, Bristol.

Enviros Consulting Limited, (ECL)., 2009. *Part 2A Compliant B20C Inspection of a Potential Special Site, “Former RAF Facility, Tern Hill”*. Enviro Consulting Limited, Shrewsbury, UK. (Unpublished).

European Chlorinated Solvents Association, (ECSA)., 2011. *Heath Profile on Trichloroethylene*. ECSA, Belgium.

Fathepure, B. Z., Boyd, S. A., 1988. Reductive dechlorination of perchloroethylene and the role of methanogens. *FEMS Microbiology Letters*, 49, 149-156.

Fennell, D. E., Gossett, J. M., Zinder, S. H., 1997. Comparison of butyric acid, ethanol, lactic acid, and propionic acid as hydrogen donors for the reductive dechlorination of tetrachloroethene. *Environmental Science & Technology* 31, 918-926.

Ferrey, M. L., Wilkin, R. T., Ford, R. G., Wilson, J. T., 2004. Nonbiological removal of cis-dichloroethylene and 1, 1-dichloroethylene in aquifer sediment containing magnetite. *Environmental Science & Technology* 38, 1746-1752.

Fetter, C. W., 1997. *Applied Hydrogeology*. Macmillan College Publishing Company, New York.

Field, A., 2005. *Discovering Statistics Using SPSS*, 2nd ed., SAGE Publications, London.

Fischer, H., Kloep, F., Wilzcek, S. and Pusch, M. T., 2005. A river’s liver – microbial processes within the hyporheic zone of a large lowland river. *Biogeochem.* 76, 349-371.

Fleckenstein, J. H., Niswonger, R. G., Fogg, G.E., 2006. River-aquifer interactions, geologic heterogeneity and low-flow management. *Ground Water* 44, 837-852.

Fogel, M. M., Taddeo, A. R., Fogel, S., 1986. Biodegradation of chlorinated ethenes by a methane-utilizing mixed culture. *Applied and Environmental Microbiology* 51, 720-724.

-
- Folkard, G. G., 1986. The significance, occurrence and removal of volatile chlorinated hydrocarbon solvents in groundwaters. *Water Pollut. Contr.* 85, 63–70
- Franken, R. J., Storey, R. G., Williams, D. D. 2001. Biological, chemical and physical characteristics of downwelling and upwelling zones in the hyporheic zone of a north-temperate stream. *Hydrobiologia* 444, 183-195.
- Fraser, B. G., Williams, D. D., 1998. Seasonal boundary dynamics of a groundwater/surface-water ecotone. *Ecology* 79, 2019-2031.
- Freedman, D. L., Danko, A. S., Verce, M. F., 2001. Substrate interactions during aerobic biodegradation of methane, ethene, vinyl chloride and 1,2-dichloroethenes. *Water Science and Technology* 43, 333-340.
- Freedman, D. L., Gossett, J. M., 1989. Biological reductive dechlorination of tetrachloroethylene and trichloroethylene to ethylene under methanogenic conditions. *Applied and Environmental Microbiology* 55, 2144-2147.
- Freedman, D. L., Herz, S. D. 1996. Use of ethylene and ethane as primary substrates for aerobic cometabolism of vinyl chloride. *Water Environment Research* 68, 320-328.
- Freeze, R. A., Cherry, J. A., 1979. *Groundwater*, Prentice Hall, New Jersey.
- Freitas, J. G., Rivett, M. O., Roche, R. S., Tellam, J. H., Durrant, M., Walker, C., 2015. Heterogeneous hyporheic zone dechlorination of a TCE groundwater plume discharging to an urban river reach. *Science of the Total Environment* 505, 236-252.
- Fryar, A. E., Wallin, E. J., Brown, D. L., 2000. Spatial and temporal variability in seepage between a contaminated aquifer and tributaries to the Ohio River. *Ground Water Monitoring & Remediation* 20, 129-146.
- Fuller, R. M., Smith, G. M., Sanderson, J. M., Hill, R. A., Thomson, A. G., Cox, Brown, N. J., Clarke, R. T., Rothery, P., Gerard, F. F., 2002. *Countryside Survey 2000 Module 7. Land Cover Map 2000. Final Report*. Centre for Ecology and Hydrology, Wallingford.
- Fung, J. M., Morris, R. M., Adrian, L., Zinder, S. H., 2007. Expression of reductive dehalogenase genes in *Dehalococcoides ethenogenes* strain 195 growing on tetrachloroethene, trichloroethene, or 2,3-dichlorophenol. *Applied and Environmental Microbiology* 73, 4439-4445.
- Gandy, C. J., Smith, J. W. N., Jarvis, A. P., 2007. Attenuation of mining-derived pollutants in the hyporheic zone: a review. *Science of the Total Environment* 373, 435-446.
- Garbarini, D. R., Lion, L. W., 1986. Influence of the nature of soil organics on the sorption of toluene and trichloroethylene. *Environmental Science & Technology* 20, 1263-1269.
- Gerritse, J., Renard, V., Gomes, T. P., Lawson, P. A., Collins, M. D., Gottschal, J. C., 1996. *Desulfitobacterium* sp. strain PCE1, an anaerobic bacterium that can grow by

reductive dechlorination of tetrachloroethene or ortho-chlorinated phenols. *Archives of Microbiology* 165, 132-140.

Gosset, J. M., 2010. Sustained Aerobic Oxidation of Vinyl Chloride at Low Oxygen Concentrations. *Environ. Sci. Technol.* 44, 1405-1411.

Grapes, T. R., Bradley, C., Petts, G. E., 2006. Hydrodynamics of floodplain wetlands in a chalk catchment: The River Lambourn, UK. *Journal of Hydrology* 320, 324-341.

Grathwohl, P., 1990. Influence of organic matter from soils and sediments from various origins on the sorption of some chlorinated aliphatic hydrocarbons: implications on Koc correlations. *Environmental Science & Technology* 24, 1687-1693.

Guilbeault, M., Parker, B., Cherry, J., 2005. Mass and flux distributions from DNAPL zones in sandy aquifers. *Ground Water* 43, 70-86.

Haggerty, R., Wondzell, S. M., Johnson, M. A., 2002. Power-law residence time distribution in the hyporheic zone of a 2nd-order mountain stream. *Geophysical Research Letters* 29, 18-1.

Hamonts, K., Kuhn, T., Maesen, M., Bronders, J., Lookman, R., Kalka, H., Diels, L., Meckenstock, R. U., Springael, D., Dejonghe, W., 2009. Factors determining the attenuation of chlorinated aliphatic hydrocarbons in eutrophic river sediment impacted by discharging polluted groundwater. *Environ. Sci. Technol.* 43, 5270-5275.

Hamonts, K., Kuhn, T., Vos, J., Maesen, M., Kalka, H., Smidt, H., Springael, D., Meckenstock, R., Dejonghe, W., 2012. Temporal variations in natural attenuation of chlorinated aliphatic hydrocarbons in eutrophic river sediments impacted by a contaminated groundwater plume. *Water Research* 46, 1873-1888.

Hamonts, K., Ryngaert, A., Smidt, H., Springael, D., Dejonghe, W., 2014. Determinants of the microbial community structure of eutrophic, hyporheic river sediments polluted with chlorinated aliphatic hydrocarbons. *FEMS microbiology ecology* 87, 715-732.

Hancock, P. J., 2002. Human impacts on the stream-groundwater exchange zone. *Environmental Management* 29, 763-781.

Hannah, D. M., Malcolm, I. A., Bradley, C., 2009. Seasonal hyporheic temperature dynamics over riffle bedforms. *Hydrological processes* 23, 2178-2194.

Hartmans, S., De Bont, J. A. M., Tramper, J., Luyben, K. C. A., 1985. Bacterial degradation of vinyl chloride. *Biotechnology Letters* 7, 383-388.

Harvey, J. W., Bencala, K. E., 1993. The effect of streambed topography on surface-subsurface water exchange in mountain catchments. *Water Resources Research* 29, 89-98.

Hatch, C. E., Fisher, A. T., Revenaugh, J. S., Constantz, J., Ruehl, C., 2006. Quantifying

surface water–groundwater interactions using time series analysis of streambed thermal records: Method development. *Water Resources Research* DOI: 10.1029/2005WR004787

He, J., Sung, Y., Dollhopf, M. E., Fathepure, B. Z., Tiedje, J. M., Löffler, F. E., 2002. Acetate versus hydrogen as direct electron donors to stimulate the microbial reductive dechlorination process at chloroethene-contaminated sites. *Environmental Science & Technology* 36, 3945-3952.

Heimann, A., Jakobsen, R., Blodau, C., 2010. Energetic constraints on H₂ dependent terminal electron accepting processes in anoxic environments: a review of observations and model approaches. *Environ. Sci. Technol.* 44, 24–33.

Heiri, O., Lotter, A. F., Lemcke, G., 2001. Loss on ignition as a method for estimating organic and carbonate content in sediments: reproducibility and comparability of results. *Journal of paleolimnology* 25, 101-110.

Hendrickson, E. R., Payne, J. A., Young, R. M., Starr, M. G., Perry, M. P., Fahnestock, S., Ellis, D., Ebersole, R. C., 2002. Molecular analysis of Dehalococcoides 16S ribosomal DNA from chloroethene-contaminated sites throughout North America and Europe. *Applied and Environmental Microbiology* 68, 485-495.

Heppl, C. M., Wharton, G., Cotton, J. A. C., Bass, J. A. B., Roberts, S. E., 2009. Sediment storage in the shallow hyporheic of lowland vegetated river reaches. *Hydrological Processes* 23, 2239-2251.

Holliger, C., Wohlfarth, G., Diekert, G., 1999. Reductive dechlorination in the energy metabolism of anaerobic bacteria. *FEMS Microbiology Reviews* 22, 383–398.

Horvath, R. S., 1972. Microbial co-metabolism and the degradation of organic compounds in nature. *Bacteriological Reviews* 36, 146.

Huang, W., Peng, P. A., Yu, Z., Fu, J., 2003. Effects of organic matter heterogeneity on sorption and desorption of organic contaminants by soils and sediments. *Applied Geochemistry* 18, 955-972.

Huang, W., Weber, W. J., 1997. A distributed reactivity model for sorption by soils and sediments. 10. Relationships between desorption, hysteresis, and the chemical characteristics of organic domains. *Environmental Science & Technology* 31, 2562-2569.

Huggenberger, P., Hoehn, E., Beschta, R., Woessner, W., 1998. Abiotic aspects of channels and floodplains in riparian ecology. *Freshwat. Biol.* 40, 407-425.

Hunkeler, D., Abe, Y., Broholm, M. M., Jeannotat, S., Westergaard, C., Jacobsen, C. S., Aravena, R., Bjerg, P.L. 2011. Assessing chlorinated ethene degradation in a large scale contaminant plume by dual carbon-chlorine isotope analysis and quantitative PCR. *Journal of Contaminant Hydrology* 119, 69-79.

Hunkeler, D., Aravena, R., Butler, B. J., 1999. Monitoring microbial dechlorination of tetrachloroethene (PCE) in groundwater using compound-specific stable carbon isotope ratios: microcosm and field studies. *Environmental Science & Technology* 33, 2733-2738.

Hunkeler, D., Chollet, N., Pittet, X., Aravena, R., Cherry, J. A., Parker, B. L., 2004. Effect of source variability and transport processes on carbon isotope ratios of TCE and PCE in two sandy aquifers. *Journal of Contaminant Hydrology* 74, 265-282.

Hvorslev, M. J., 1951. *Time lag and soil permeability in ground-water observations*. U.S. Corps of Engineers, Waterways Experiment Station, Bulletin 36. Mississippi.

Interstate Technology & Regulatory Council, (ITRC), 2006. *Technology Overview of Passive Sampler Technologies*. DSP-4. Washington, DC. Interstate Technology & Regulatory Council, Authoring Team. (www.itrcweb.org).

Jackson, R.E., 1998. The migration, dissolution, and fate of chlorinated solvents in the urbanized alluvial valleys of the southwestern USA. *Hydrogeol. J.* 6, 144-155.

Jakobsen, R., Postma, D., 1999. Redox zoning, rates of sulphate reduction and interactions with Fe-reduction and methanogenesis in a shallow sandy aquifer, Rømø, Denmark. *Geochimica et Cosmochimica Acta* 63, 137-151.

Jeong, H. Y., Anantharaman, K., Han, Y. S., Hayes, K. F., 2011. Abiotic reductive dechlorination of cis-dichloroethylene by Fe species formed during iron-or sulphate-reduction. *Environmental Science & Technology* 45, 5186-5194.

Jeong, H. Y., Hayes, K. F., 2007. Reductive dechlorination of tetrachloroethylene and trichloroethylene by mackinawite (FeS) in the presence of metals: reaction rates. *Environmental Science & Technology* 41, 6390-6396.

Johnson, R. L., Pankow, J. F., 1992. Dissolution of dense chlorinated solvents into groundwater. 2. Source functions for pools of solvent. *Environmental Science & technology* 26, 896-901.

Jørgensen, P. R., Urup, J., Helstrup, T., Jensen, M. B., Eiland, F., Vinther, F. P., 2004. Transport and reduction of nitrate in clayey till underneath forest and arable land. *J. Contam. Hydrol.* 73, 207-226.

Joseph, J. B., Brereton, N. R., 1975. *Report on a pumping test at Helshaw Grange, Shropshire – January/February 1975*. Water Research Centre, UK. (Unpublished).

Kalbus, E., Reinstorf, F., Schirmer, M., 2006. Measuring methods for groundwater surface water interactions: a review. *Hydrology and Earth System Sciences* 10, 873-887.

Kalbus, E., Schmidt, C., Bayer-Raich, M., Leschik, S., Reinstorf, F., Balcke, G. U., Schirmer, M., 2007. New methodology to investigate potential contaminant mass fluxes at the stream-aquifer interface by combining integral pumping tests and streambed temperatures. *Environmental Pollution* 148, 808-816.

Kalbus, E., Schmidt, C., Molson, J., Reinstorf, F., Schirmer, M., 2009. Influence of aquifer and streambed heterogeneity on the distribution of groundwater discharge. *Hydrology and Earth System Sciences* 13, 69-77.

Kampbell, D. H., Vandegrift, S. A., 1998. Analysis of dissolved methane, ethane, and ethylene in ground water by a standard gas chromatographic technique. *Journal of chromatographic Science* 36, 253-256.

Karpeta, W. P., 1990. The morphology of Permian palaeodunes—a reinterpretation of the Bridgnorth Sandstone around Bridgnorth, England, in the light of modern dune studies. *Sedimentary Geology* 69, 59-75.

Käser, D. H., Binley, A., Heathwaite, A. L., Krause, S., 2009. Spatio-temporal variations of hyporheic flow in a riffle-step-pool sequence. *Hydrological Processes* 23, 2138-2149.

Keery, J., 2005. *Quantifying vertical water fluxes between groundwater and a lowland river, using temperature time series*. MSc thesis, Lancaster Environment Centre, Lancaster University.

Keery, J., Binley, A., Crook, N., Smith, J.W., 2007. Temporal and spatial variability of groundwater–surface water fluxes: development and application of an analytical method using temperature time series. *Journal of Hydrology* 336, 1-16.

Kennedy, L. G., Everett, J. W., 2001. Microbial degradation of simulated landfill leachate: solid iron/sulfur interactions. *Advances in Environmental Research* 5, 103-116.

Kennedy, L. G., Everett, J. W., Gonzales, J., 2006. Assessment of biogeochemical natural attenuation and treatment of chlorinated solvents, Altus Air Force Base, Altus, Oklahoma. *Journal of contaminant hydrology* 83, 221-236.

Keuper, B. H., Redman, D., Starr, R. C., Reitsma, S., Mah, M., 1993. A field experiment to study the behavior of tetrachloroethylene below the water table: Spatial distribution of residual and pooled DNAPL. *Ground Water* 31, 756-766.

Kim, H., Hemond, H. F., 1998. Natural discharge of volatile organic compounds from contaminated aquifer to surface waters. *J. Environ. Eng.* 124, 744-751.

Klier, N. J., West, R. J., Donberg, P. A., 1999. Aerobic biodegradation of dichloroethylenes in surface and subsurface soils. *Chemosphere* 38, 1175-1188.

Kocamemi, B. A., Cecen, F., 2010. Biological removal of the xenobiotic trichloroethylene (TCE) through cometabolism in nitrifying systems. *Bioresource Technology* 101, 430-433.

Krajmalnik-Brown, R., Sung, Y., Ritalahti, K. M., Michael Saunders, F., Löffler, F. E., 2007. Environmental distribution of the trichloroethene reductive dehalogenase gene (*tceA*) suggests lateral gene transfer among Dehalococcoides. *FEMS Microbiology Ecology* 59, 206-214.

Krause, S., Blume, T., Cassidy, N., 2012. Investigating patterns and controls of groundwater up-welling in a lowland river by combining Fibre-optic Distributed Temperature Sensing with observations of vertical hydraulic gradients. *Hydrology and Earth System Sciences* 16, 1775-1792.

Krause, S., Hannah, D. M., Blume, T., 2011b. Interstitial pore-water temperature dynamics across a pool-riffle-pool sequence. *Ecohydrology* 4, 549-563.

Krause, S., Hannah, D. M., Fleckenstein, J. H., Heppell, C. M., Kaiser, D., Pickup, R., Pinay, G., Robertson, A. L., Wood, P. J., 2011a. Inter-disciplinary perspectives on processes in the hyporheic zone. *Ecohydrology* 4, 481-499.

Krause, S., Heathwaite, L., Binley, A., Keenan, P., 2009. Nitrate concentration changes at the groundwater-surface water interface of a small Cumbrian river. *Hydrol. Process.* 23, 2195-2211.

Krause, S., Tecklenburg, C., Munz, M., Naden, E., 2013. Streambed nitrogen cycling beyond the hyporheic zone: Flow controls on horizontal patterns and depth distribution of nitrate and dissolved oxygen in the upwelling groundwater of a lowland river. *Journal of Geophysical Research: Biogeosciences*, 118, 54-67.

Krumholz, L. R., 1997. *Desulfuromonas chloroethenica* sp. nov. uses Tetrachloroethylene and trichloroethylene as electron acceptors. *International Journal of Systematic Bacteriology* 47, 1262-1263.

Landmeyer, J. E., Bradley, P. M., Trego, D. A., Hale, K. G., Haas, J. E., 2010. MTBE, TBA, and TAME attenuation in diverse hyporheic zones. *Ground water* 48, 30-41.

LaSage, D. M., Fryar, A. E., Mukherjee, A., Sturchio, N. C., Heraty, L. J., 2008. Groundwater-derived contaminant fluxes along a channelized Coastal Plain stream. *Journal of Hydrology* 360, 265-280.

Lautz, L. K., Fanelli, R. M., 2008. Seasonal biogeochemical hotspots in the streambed around restoration structures. *Biogeochemistry* 91, 85-104.

Le, N. B., Coleman, N. V., 2011. Biodegradation of vinyl chloride, cis-dichloroethene and 1, 2-dichloroethane in the alkene/alkane-oxidising Mycobacterium strain NBB4. *Biodegradation* 22, 1095-1108.

Lee, I. S., Bae, J. H., Yang, Y., McCarty, P. L., 2004. Simulated and experimental evaluation of factors affecting the rate and extent of reductive dehalogenation of chloroethenes with glucose. *Journal of Contaminant Hydrology* 74, 313-331.

Lee, W., Batchelor, B., 2002a. Abiotic reductive dechlorination of chlorinated ethylenes by iron-bearing soil minerals. 1. Pyrite and magnetite. *Environmental Science & Technology*, 36, 5147-5154.

Lee, W., Batchelor, B., 2002b. Abiotic reductive dechlorination of chlorinated ethylenes by iron-bearing soil minerals. 2. Green rust. *Environmental Science & Technology*, 36, 5348-5354.

Lee, W., Batchelor, B., 2004. Abiotic reductive dechlorination of chlorinated ethylenes by iron-bearing phyllosilicates. *Chemosphere* 56, 999-1009.

Lerner, D. N., Barrett, M. H., 1996. Urban groundwater issues in the United Kingdom. *Hydrogeology Journal* 4, 80-89.

Li, J., Werth, C. J., 2004. Slow desorption mechanisms of volatile organic chemical mixtures in soil and sediment micropores. *Environmental Science & Technology* 38, 440-448.

Little, C. D., Palumbo, A. V., Herbes, S. E., Lidstrom, M. E., Tyndall, R. L., Gilmer, P. J. 1988. Trichloroethylene biodegradation by a methane-oxidizing bacterium. *Applied and Environmental Microbiology* 54, 951-956.

Löffler, F. E., Tiedje, J. M., Sanford, R. A. 1999. Fraction of electrons consumed in electron acceptor reduction and hydrogen thresholds as indicators of halorespiratory physiology. *Applied and Environmental Microbiology* 65, 4049-4056.

Löffler, F. E., Yan, J., Ritalahti, K. M., Edwards, E. A., Konstantinidis, K. T., Muller, J. A., Fullerton, H., Zinder, S. H., Sporman, A. M., 2013. *Dehalococcoides mccartyi* gen. nov., sp. nov., obligately organohalide-respiring anaerobic bacteria relevant to halogen cycling and bioremediation, belong to a novel bacterial class, *Dehalococcoidia* classis nov., order *Dehalococcoidales* ord. nov. and family *Dehalococcoidaceae* fam. nov., within the phylum *Chloroflexi*. *International journal of systematic and evolutionary microbiology* 63, 625-635.

Loke, M. H., Barker, R. D., 1995. Least-squares deconvolution of apparent resistivity pseudosections. *Geophysics* 60, 1682-1690.

Lorah, M. M., Olsen, L. D., 1999. Natural attenuation of chlorinated volatile organic compounds in a freshwater tidal wetland: Field evidence of anaerobic biodegradation. *Water Resources Research* 35, 3811-3827.

Lorah, M. M., Voytek, M. A., 2004. Degradation of 1, 1, 2, 2-tetrachloroethane and accumulation of vinyl chloride in wetland sediment microcosms and in situ pore water: biogeochemical controls and associations with microbial communities. *Journal of Contaminant Hydrology* 70, 117-145.

Lovely, D. R., Goodwin, S., 1988. Hydrogen concentrations as an indicator of the predominant terminal electron accepting process in aquatic sediments. *Geochimica Cosmochimica Acta* 52, 11-18.

Lovley, D. R., Chapelle, F. H., Woodward, J. C., 1994. Use of dissolved H₂ concentrations to determine distribution of microbially catalyzed redox reactions in anoxic groundwater. *Environmental Science & Technology* 28, 1205-1210.

Lowry, C. S., Walker, J. F., Hunt, R. J., Anderson, M. P., 2007. Identifying spatial variability of groundwater discharge in a wetland stream using a distributed temperature sensor. *Water Resources Research* DOI: 10.1029/2007WR006145

Lu, C., Bjerg, P. L., Zhang, F., Broholm, M. M., 2011. Sorption of chlorinated solvents and degradation products on natural clayey tills. *Chemosphere* 83, 1467-1474.

Luijten, M. L., de Weert, J., Smidt, H., Boschker, H. T., de Vos, W. M., Schraa, G., Stams, A. J., 2003. Description of *Sulfurospirillum halorespirans* sp. nov., an anaerobic, tetrachloroethene-respiring bacterium, and transfer of *Dehalospirillum multivorans* to the genus *Sulfurospirillum* as *Sulfurospirillum multivorans* comb. nov. *International Journal of Systematic and Evolutionary Microbiology* 53, 787-793.

Luijten, M. L., Roelofsen, W., Langenhoff, A. A., Schraa, G., Stams, A. J., 2004. Hydrogen threshold concentrations in pure cultures of halorespiring bacteria and at a site polluted with chlorinated ethenes. *Environmental Microbiology* 6, 646-650.

Luthy, R. G., Aiken, G. R., Brusseau, M. L., Cunningham, S. D., Gschwend, P. M., Pignatello, J. J., Reinhard, M., Traina, S. J., Weber, W. J., Westall, J. C., 1997. Sequestration of hydrophobic organic contaminants by geosorbents. *Environmental Science & Technology* 31, 3341-3347.

Lyford, F. P., Flight, L., Stone, J. R., Clifford, S., 1999. *Distribution of Trichloroethylene and Geologic Controls on Contaminant Pathways Near the Royal River, McKin Superfund Site Area, Gray, Maine*. U.S. Geological Survey, Virginia.

Lyman, W. J., 1982. Adsorption coefficients for soils and sediment. In (Eds.) Lyman, W. J., Reehl, W. H., Rosenblatt, D. H., *Handbook of Chemical Property Estimation Methods*. McGraw-Hill, New York.

Lyne, F. A., McLachlan, T., 1949. Contamination of water by trichloroethylene. *The Analyst* 74, 882-893.

Maphosa, F., de Vos, W. M., Smidt, H., 2010. Exploiting the ecogenomics toolbox for environmental diagnostics of organohalide-respiring bacteria. *Trends in biotechnology* 28, 308-316.

Marsh, T. J., Hannaford, J. 2008. (Eds.) *UK Hydrometric Register – Hydrological data UK series*. Centre for Ecology and Hydrology, Wallingford, UK.

Mattes, T. E., Alexander, A. K., Coleman, N. V., 2010. Aerobic biodegradation of the chloroethenes: pathways, enzymes, ecology, and evolution. *FEMS microbiology reviews* 34, 445-475.

Maymo-Gatell, X., Chien, Y. T., Gossett, J. M., Zinder, S. H., 1997. Isolation of a bacterium that reductively dechlorinates tetrachloroethene to ethene. *Science* 276, 1568-1571.

Maymó-Gatell, X., Nijenhuis, I., Zinder, S.H., 2001. Reductive dechlorination of *cis* 1,2-dichloroethene and vinyl chloride by “*Dehalococcoides ethenogenes*”. *Environ. Sci. Technol.* 35, 516-521

McCarty, P. L., 1997. Breathing with chlorinated solvents. *Science* 276, 1521-1522.

McGuire, J. T., Long, D. T., Klug, M. J., Haack, S. K., Hyndman, D. W., 2002. Evaluating behavior of oxygen, nitrate, and sulfate during recharge and quantifying reduction rates in a contaminated aquifer. *Environmental Science & Technology* 36, 2693-2700.

McGuire, T. M., Newell, C. J., Looney, B. B., Vangelas, K. M., Sink, C. H., 2004. Historical analysis of monitored natural attenuation: A survey of 191 chlorinated solvent sites and 45 solvent plumes. *Remediation Journal* 15, 99-112.

McKnight, U. S., Funder, S. G., Rasmussen, J. J., Finkel, M., Binning, P. J., Bjerg P. L., 2010. An integrated model for assessing the risk of TCE groundwater contamination to human receptors and surface water ecosystems. *Ecol. Eng.* 36, 1126–37.

McKnight, U. S., Rasmussen, J. J., Kronvang, B., Bjerg, P. L., Binning, P. J., 2012. Integrated assessment of the impact of chemical stressors on surface water ecosystems. *Sci Total Environ* 427-8, 319-331.

Meckenstock, R. U., Morasch, B., Griebler, C., Richnow, H. H., 2004. Stable isotope fractionation analysis as a tool to monitor biodegradation in contaminated aquifers. *Journal of Contaminant Hydrology* 75, 215-255.

Mercer, J. W., Cohen, R. M., 1990. A review of immiscible fluids in the subsurface: Properties, models, characterization and remediation. *Journal of Contaminant Hydrology* 6, 107-163.

Mermillod-Blondin, F., Gaudet, J. P., Gerino, M., Desrosiers, G., Jose, J., Châtelliers, M. C. D., 2004. Relative influence of bioturbation and predation on organic matter processing in river sediments: a microcosm experiment. *Freshwater Biology* 49, 895-912.

Mermillod-Blondin, F., Mauclaire, L., Montuelle, B. 2005. Use of slow filtration columns to assess oxygen respiration, consumption of dissolved organic carbon, nitrogen transformations, and microbial parameters in hyporheic sediments. *Water Research* 39, 1687-1698.

Middeldorp, P. J. M., Luijten, M. L., Van de Pas, B.A., Van Eekert, M. H. A., Kengen, S. W. M., Schraa, G. W. M., Stams, A. J. M., 1999. Anaerobic microbial reductive dehalogenation of chlorinated ethenes. *Bioem. J.* 3, 151-169.

Milosevic, N., Thomsen, N. I., Juhler, R. K., Albrechtsen, H.-J., Bjerg, P. L., 2012. Identification of discharge zones and quantification of contaminant mass discharges into a local stream from a landfill in a heterogeneous geologic setting. *Journal of Hydrology* 446-447, 13-23.

Milsom, J., 2004. *Field geophysics*, 3rd rev. edn. Chichester, UK: The Geological Field Guide Series, John Wiley & Sons.

Missteat, B. D. R., Ashley, R. P., Lawrence, A. R., 1998. Groundwater pollution by chlorinated solvents: the landmark Cambridge Water Company case. *Geological Society, London, Special Publications* 128, 201-215.

Mohn, W. W., Tiedje, J. M., 1992. Microbial reductive dehalogenation. *Microbiological Reviews* 56, 482-507.

Morasch, B., Höhener, P., Hunkeler, D. 2007. Evidence for in situ degradation of mono- and polyaromatic hydrocarbons in alluvial sediments based on microcosm experiments with ¹³C-labeled contaminants. *Environmental Pollution* 148, 739-748.

Morrice, J. A., Dahm, C. N., Valett, H. M., Unnikrishna, P. V., Campana, M. E., 2000. Terminal electron accepting processes in the alluvial sediments of a headwater stream. *Journal of the North American Benthological Society* 19, 593-608.

Morse, J. W., Cornwell, J. C., 1987. Analysis and distribution of iron sulfide minerals in recent anoxic marine sediments. *Marine Chemistry* 22, 55-69.

Mouvet, C., Barberis, D., Bourg, A., 1993. Adsorption isotherms of tri- and tetrachloroethylene by various natural solids. *Journal of Hydrology* 149, 163-182.

Mukherjee, A., Fryar, A. E., LaSage, D. M., 2005. Using tracer tests to assess natural attenuation of contaminants along a channelized Coastal Plain stream. *Environmental & Engineering Geoscience* 11, 371-382.

Muller, J. A., Rosner, B. M., von Abendroth, G., Meshulam-Simon, G., McCarty, P. L., Spormann, A. M., 2004. Molecular identification of the catabolic vinyl chloride reductase from *Dehalococcoides* sp strain VS and its environmental distribution. *Applied and Environmental Microbiology* 70, 4880-4888.

Munz, M., Krause, S., Tecklenburg, C., Binley, A., 2011. Reducing monitoring gaps at the aquifer–river interface by modelling groundwater–surface water exchange flow patterns. *Hydrological Processes* 25, 3547-3562.

Murphy, E. M., Schramke, J. A., Fredrickson, J. K., Bledsoe, H. W., Francis, A. J., Sklarew, D. S., Linehan, J. C., 1992. The influence of microbial activity and sedimentary organic carbon on the isotope geochemistry of the Middendorf aquifer. *Water Resources Research* 28, 723-740.

National Research Council, (NRC)., 1994. *Alternatives for Groundwater Cleanup*. National Academy Press, Washington DC.

Neal, C., Fox, K. K., Harrow, M., Neal, M., 1998. Boron in the major UK rivers entering the North Sea. *Science of The Total Environment* 210, 41-51.

Nelson, D. K., Hozalski, R. M., Clapp, L. W., Semmens, M. J., Novak, P. J., 2002. Effect of nitrate and sulfate on dechlorination by a mixed hydrogen-fed culture. *Bioremediation Journal* 6, 225-236.

Newell, C. J., Cowie, I., McGuire, T. M., McNab Jr, W. W., 2006. Multiyear temporal changes in chlorinated solvent concentrations at 23 monitored natural attenuation sites. *Journal of Environmental Engineering* 132, 653-663.

Newman, W. A., Pelle, R. C. 2006. Enhanced anaerobic bioremediation of chlorinated solvents utilizing vegetable oil emulsions. *Remediation Journal* 16, 109-122.

Nierop, K. G., Jansen, B., Verstraten, J. M., 2002. Dissolved organic matter, aluminium and iron interactions: precipitation induced by metal/carbon ratio, pH and competition. *Science of the Total Environment* 300, 201-211.

Norman, W. R., Ostrye, D. P., Hobin, J. S., 1986. Use of seepage meters to quantify groundwater discharge and contaminant flux into surface water at the Baird and McGuire site (NPL No. 14). *Proceedings of the Third Annual Eastern Regional Ground Water Conference, Springfield, Massachusetts, July 28–30, 1986*. National Water Well Association, Dublin, Ohio.

Nyquist, J. E., Freyer, P. A., Toran, L., 2008. Stream bottom resistivity tomography to map ground water discharge. *Ground Water* 46, 561-569.

Pallant, J., 2005. *SPSS Survival Manual, 2nd ed.* McGraw-Hill, New York.

Pallasser, R., Minasny, B., McBratney, A. B., 2013. Soil carbon determination by thermogravimetrics. *PeerJ* 1, e6.

Pankow, J. F., Cherry, J. A. 1996. *Dense chlorinated solvents and other DNAPLs in groundwater: History, behavior and remediation*. Wiley Publishing, New York.

Papatolios, K.T., Lerner, D.N., 1993. Defining a borehole capture zone in a complex sandstone aquifer: a modelling case study from Shropshire, UK. *Quarterly Journal of Engineering Geology and Hydrogeology* 26, 193-204.

Papiernik, S. K., 2001. A review of in situ measurement of organic compound transformation in groundwater. *Pest Manag. Sci.* 57, 325-332.

Parker, B. L., Chapman, S.W., Guilbeault, M. A., 2008. Plume persistence caused by back diffusion from thin clay layers in a sand aquifer following TCE source-zone hydraulic isolation. *Journal of contaminant hydrology* 102, 86-104.

Pearson, A., Environment Agency, *Personal Communication*.

Perkins, S., 2013. *Risk assessment of a TCE plume impact on a Shropshire lowland stream by multi-scale flow and contaminant transport modelling*. MSc thesis, School of Geography, Earth and Environmental Science, University of Birmingham.

Peterson, E. W., Sickbert, T. B., 2006. Stream water bypass through a meander neck, laterally extending the hyporheic zone. *Hydrogeology Journal* 14, 1443-1451.

Pitkin, S. E., Cherry, J. A., Ingleton, R. A., Broholm, M., 1999. Field demonstrations using the Waterloo ground water profiler. *Ground Water Monitoring & Remediation* 19, 122-131.

Pusch, M., Schwoerbel, J., 1994. Community respiration in hyporheic sediments of a mountain stream (Steina, Black Forest). *Archiv für Hydrobiologie* 130, 35-52.

Rahman, A., Shepley, M. 2005. *Technical Note, East Shropshire Groundwater Scheme – Solute Transport Modelling, Helshaw Grange, Version 2*. Environment Agency, Bristol, UK (Unpublished).

Rathbun, R. E., 2000. Transport, behaviour, and fate of volatile organic compounds in streams. *Critical Reviews in Environmental Science and Technology* 30, 129-295.

Razali, N. M., Wah, Y. B., 2011. Power comparisons of shapiro-wilk, kolmogorov-smirnov, lilliefors and anderson-darling tests. *Journal of Statistical Modelling and Analytics* 2, 21-33.

Reynolds, J. M., 2011. *An introduction to applied and environmental geophysics*. John Wiley & Sons, New York.

Ritz M, Robain H, Albouy Y, Camerlynck C, Descloitres M, Mariko A., 1999. Improvement to resistivity pseudosection modelling by removal of near-surface inhomogeneity effects: application to a soil system in south Cameroon. *Geophys Prosp* 47, 85–101.

Rivett, M. O., Feenstra, S, Clark, L., 2006. Lyne and McLachlan (1949): Influence of the first publication on groundwater contamination by trichloroethene. *Environmental Forensics* 7, 313-323.

Rivett, M. O., Lerner, D. N., Lloyd, J. W., 1990b. Chlorinated solvents in U.K. aquifers. *Journal of the Institution of Water and Environmental Management* 4, 242-250.

Rivett, M. O., Lerner, D. N., Lloyd, J. W., Clark, L., 1990a. Organic contamination of the Birmingham aquifer, UK. *Journal of Hydrology* 113, 307-323.

Rivett, M. O., Petts, J., Butler, B., Martin, I., 2002. Remediation of contaminated land and groundwater: Experience in England and Wales. *Journal of Environmental Management* 65, 251-268.

Rivett, M. O., Thornton, S. F., 2008. Monitored natural attenuation of organic contaminants in groundwater: principles and application. *Water Management* 161, 381-392.

Rivett, M. O., Turner, R. J., Glibbery (nee Murcott), P., Cuthbert, M. O., 2012. The legacy of chlorinated solvents in the Birmingham aquifer, UK: Observations spanning three decades and the challenge of future urban groundwater development. *J. Contam. Hydrol.* 140, 107-123.

Rivett, M., Ellis, P., Greswell, R., Ward, R., Roche, R., Cleverly, M., Walker, C., Conran, D., Fitzgerald, P., Willcox, T., 2008. Cost-effective mini drive-point piezometers and multilevel samplers for monitoring the hyporheic zone. *Quarterly Journal of Engineering Geology and Hydrogeology* 41, 49-60.

Rivett, M., Feenstra, S., Cherry, J., 2001. A controlled field experiment on groundwater contamination by a multicomponent DNAPL: creation of the emplaced-source and overview of dissolved plume development. *J. Contam. Hydrol.* 49, 111-149.

Rivett, M., Shepherd, K., Keeys, L., Brennan, A., 2005. Chlorinated solvents in the Birmingham aquifer, UK: 1986-2001. *Q. J. Eng. Geol. Hydrogeol.* 38, 337-350.

Roche, R. S., Rivett, M. O., Tellam, J. H., Cleverly, M. G., Walker, M., 2008. Natural attenuation of a TCE plume at the groundwater – surface-water interface: spatial and temporal variability within a 50 m reach. *GQ07: Securing Groundwater Quality in Urban and Industrial Environments* 324, IAHS-AISH publication, 475-482.

Romaní, A. M., Vázquez, E., Butturini, A., 2006. Microbial availability and size fractionation of dissolved organic carbon after drought in an intermittent stream: biogeochemical link across the stream–riparian interface. *Microbial ecology* 52, 501-512.

Rose, L., Krause, S., Cassidy, N. J., 2013. Capabilities and limitations of tracing spatial temperature patterns by fiber-optic distributed temperature sensing. *Water Resources Research* 49, 1741-1745.

Rosenberry, D. O., 2008. A seepage meter designed for use in flowing water. *Journal of Hydrology* 359, 118-130.

Rosenberry, D. O., Pitlick, J., 2009. Local-scale variability of seepage and hydraulic conductivity in a shallow gravel-bed river. *Hydrological Processes* 23, 3306-3318.

Roy, J. W., Bickerton, G., 2010. Proactive screening approach for detecting groundwater contaminants along urban streams at the reach-scale. *Environmental Science & Technology* 44, 6088-6094.

Rulík, M., Čáp, L., & Hlaváčová, E., 2000. Methane in the hyporheic zone of a small lowland stream (Sitka, Czech Republic). *Limnologia-Ecology and Management of Inland Waters* 30, 359-366.

Rulík, M., Hereka, P., 1998. Occurrence of both acetic and lactic acids in subsurface water of the bed sediments: comparison of two different localities. In (Eds.) Bretschko, G., Hele, I. C., *Advances in River Bottom Ecology*, Backhuys Publishers, Leiden.

Ryan, R. J., Boufadel, M. C., 2007. Evaluation of streambed hydraulic conductivity heterogeneity in an urban watershed. *Stochastic Environmental Research and Risk Assessment* 21, 309-316.

Ryoo, D., Shim, H., Arengi, F., Barbieri, P., Wood, T. 2001. Tetrachloroethylene, trichloroethylene, and chlorinated phenols induce toluene-o-xylene monooxygenase activity in *Pseudomonas stutzeri* OX1. *Applied Microbiology and Biotechnology* 56, 545-549.

Sachse, A., Henrion, R., Gelbrecht, J., Steinberg, C. E. W., 2005. Classification of dissolved organic carbon (DOC) in river systems: influence of catchment characteristics and autochthonous processes. *Organic Geochemistry* 36, 923-935.

Sanders, I. A., Heppell, C. M., Cotton, J. A., Wharton, G., Hildrew, A. G., Flowers, E. J., Trimmer, M., 2007. Emission of methane from chalk streams has potential implications for agricultural practices. *Freshwater Biology* 52, 1176-1186.

Sand-Jensen, K., 1998. Influence of submerged macrophytes on sediment composition and near-bed flow in lowland streams. *Freshwater Biology*, 39, 663-679.

Schirmer, M., Dahmke, A., Dietrich, P., Dietze, M., Goedeke, S., Richnow, H.H., Schirmer, K., Weiss, H., Teutsch, G., 2006. Natural attenuation research at the contaminated megasite Zeitz. *J. Hydrol.* 328, 393-407.

Schmidt, C., Bayer-Raich, M., Schirmer, M., 2006. Characterization of spatial heterogeneity of groundwater-stream water interactions using multiple depth streambed temperature measurements at the reach scale. *Hydrology and Earth System Sciences Discussions* 3, 1419-1446.

Schmidt, C., Conant, B., Bayer-Raich, M., Schirmer, M., 2007. Evaluation and field-scale application of an analytical method to quantify groundwater discharge using mapped streambed temperatures. *Journal of Hydrology* 347, 292-302.

Schmidt, C., Kalbus, E., Martiensen, M., Schirmer, M., 2008. The influence of heterogeneous groundwater discharge on the timescales of contaminant mass flux from streambed sediments—field evidence and long-term predictions. *Hydrology and Earth System Sciences Discussions* 5, 971-1001.

Schmidt, C., Martiensen M., Kalbus, E. 2011. Influence of water flux and redox conditions on chlorobenzene concentrations in a contaminated streambed. *Hydrological Processes* 25, 234–245.

Schmidt, K. R., Augenstein, T., Heidinger, M., Ertl, S., Tiehm, A., 2010. Aerobic biodegradation of *cis*-1,2-dichloroethene as sole carbon source: Stable carbon isotope fractionation and growth characteristics. *Chemosphere* 78, 527-532.

Schmidt, K., Tiehm, A., 2008. Natural attenuation of chloroethenes: identification of sequential reductive/oxidative biodegradation by microcosm studies. *Water Science & Technology*, 55, 1137-1145.

Schneidewind, U., Haest, P. J., Atashgahi, S., Maphosa, F., Hamonts, K., Maesen, M., Calderer, M., Seutjens, P., Smidt, H., Springael, D., Dejonghe, W., 2014. Kinetics of dechlorination by *Dehalococcoides mccartyi* using different carbon sources. *Journal of Contaminant Hydrology* 157, 25-36.

Schuenemeyer, J., Drew, L., 2011. *Statistics for Earth and Environmental Scientists*. John Wiley & Sons.

Schwarzenbach, R. P., Westall, J., 1981. Transport of non-polar organic compounds from surface water to groundwater. Laboratory sorption studies. *Environmental Science & Technology* 15, 1360-1367.

Schwille, F., 1988. *Dense Chlorinated Solvents in Porous and Fractured Media*. Lewis Publishers, Chelsea, MI.

Selker, J., van de Giesen, N., Westhoff, M., Luxemburg, W., Parlange, M. B., 2006. Fiber optics opens window on stream dynamics. *Geophysical Research Letters* DOI: 10.1029/2006GL027979

Seshadri, R., Adrian, L., Fouts, D. E., Eisen, J. A., Phillippy, A. M., Methe, B. A., Ward, N. L., Nelson, W. C., Deboy, R. T., Khouri, H. M., Kolonay, J. F., Dodson, R. J., Daugherty, S. C., Brinkac, L. M., Sullivan, S. A., Madupu, R., Nelson, K. T., Kang, K. H., Impraim, M., Tran, K., Robinson, J. M., Forberger, H. A., Fraser, C. M., Zinder, S. H., Heidelberg, J. F., 2005. Genome sequence of the PCE dechlorinating bacterium *Dehalococcoides ethenogenes*. *Science* 307, 105-108.

Seth, R., Mackay, D., Muncke, J., 1999. Estimating the organic carbon partition coefficient and its variability for hydrophobic chemicals. *Environmental Science & Technology* 33, 2390-2394.

Severn River Authority, 1974. *Shropshire Groundwater Investigation. Second Report*. Severn Trent, Coventry. (Unpublished).

Sharma, P. K., McCarty, P. L., 1996. Isolation and characterization of a facultatively aerobic bacterium that reductively dehalogenates tetrachloroethene to cis-1, 2-dichloroethene. *Applied and Environmental Microbiology* 62, 761-765.

Shepley, M., Streetly, M., 2007. The estimation of 'natural' summer outflows from the Permo-Triassic Sandstone aquifer, UK. *Quarterly Journal of Engineering Geology and Hydrogeology* 40, 213-227.

Smedley, P., Neumann, I., Brown, S., 2005. Baseline report series. 20, the Permo-Triassic sandstone aquifer of Shropshire. *Environment Agency Science Group Technical Report NC/99/74/20*. Environment Agency, Bristol.

Smidt, H., de Vos, W. M., 2004. Anaerobic microbial dehalogenation. *Annu. Rev. Microbiol.* 58, 43-73.

Smith, J., 2005. Groundwater-surface water interactions in the hyporheic zone. *Environment Agency Science report SC030155/SR1*. Environment Agency, Bristol, UK.

Smith, J., Bonell, M., Gibert, J., McDowell, W., Sudicky, E., Turner, J., Harris, R., 2008. Groundwater-surface water interactions, nutrient fluxes and ecological response in river corridors: Translating science into effective environmental management. *Hydrol. Process.* 22, 151-157.

Smith, J., Lerner, D., 2008. Geomorphologic control on pollutant retardation at the groundwater–surface water interface. *Hydrol. Process.* 22, 4679-4694.

Sobczak, W. V., Findlay, S., 2002. Variation in bioavailability of dissolved organic carbon among stream hyporheic flowpaths. *Ecology* 83, 3194-3209.

Song, D. L., Conrad, M. E., Sorenson, K. S., Alvarez-Cohen, L., 2002. Stable carbon isotope fractionation during enhanced in situ bioremediation of trichloroethene. *Environmental Science & Technology* 36, 2262-2268.

Sophocleous, M., 2002. Interactions between groundwater and surface water: the state of the science. *Hydrogeol. J.* 10, 52-67.

Soulsby, C., Malcolm, I. A., Youngson, A. F., 2001. Hydrochemistry of the hyporheic zone in salmon spawning gravels: a preliminary assessment in a degraded agricultural stream. *Regulated Rivers: Research & Management* 17, 651-665.

Squillace, P., Moran, M., Price, C., 2004. VOCs in shallow groundwater in new residential/commercial areas of the United States. *Environ. Sci. Technol.* 38, 5327-5338.

Stallman, S., 1965. Steady one-dimensional fluid flow in a semi-infinite porous medium with sinusoidal surface temperature, *J. Geophys. Res.* 70, 2821–2827.

Stonestrom, D. A., Constantz, J., 2003. *Heat as a tool for studying the movement of ground water near streams* No. 1260. U.S. Dept. of the Interior, U.S. Geological Survey, Virginia.

Storey, R. G., Fulthorpe, R. R., Williams, D. D., 1999. Perspectives and predictions on the microbial ecology of the hyporheic zone. *Freshwater Biology* 41, 119-130.

Streetly, M., Shepley, M.G., (Eds.), 2005. *Final Report, East Shropshire Permo-Triassic Sandstone Groundwater Modelling Project – Task 8*. Environment Agency, Bristol.

Sung, Y., Fletcher, K. E., Ritalahti, K. M., Apkarian, R. P., Ramos-Hernandez, N., Sanford, R. A., Mesbah, N. M. and Löffler, F. E., 2006. *Geobacter lovleyi* strain SZ sp. nov., a novel-metal reducing and tetrachloroethene (PCE)-dechlorinating bacterium. *Appl. Environ. Microbiol.* 72, 2775-2782.

Sung, Y., Ritalahti, K. M., Sanford, R. A., Urbance, J. W., Flynn, S. J., Tiedje, J. M., Löffler, F. E., 2003. Characterization of two tetrachloroethene-reducing, acetate-oxidizing anaerobic bacteria and their description as *Desulfuromonas michiganensis* sp. nov. *Applied and Environmental Microbiology* 69, 2964-2974.

Suttinun, O., Luepromchai, E., Müller, R., 2013. Cometabolism of trichloroethylene: concepts, limitations and available strategies for sustained biodegradation. *Reviews in Environmental Science and Biotechnology* 12, 99-114.

Suzuki, S., 1960. Percolation measurements based on heat flow through soil with special reference to paddy fields, *J. Geophys. Res.* 65, 2883–2885.

Tait, N. G., Lerner, D. N., Smith, J. W. N., Leharne, S. A., 2004. Prioritisation of abstraction boreholes at risk from chlorinated solvent contamination on the UK Permo-Triassic Sandstone aquifer using a GIS. *Science of The Total Environment* 319, 77-98.

Taş, N., Eekert, V., Miriam, H. A., De Vos, W. M., Smidt, H., 2010. The little bacteria that can—diversity, genomics and ecophysiology of ‘Dehalococcoides’ spp. in contaminated environments. *Microbial Biotechnology* 3, 389-402.

Taş, N., van Eekert, M. H., Wagner, A., Schraa, G., de Vos, W. M., Smidt, H., 2011. Role of “Dehalococcoides” spp. in the anaerobic transformation of hexachlorobenzene in European rivers. *Applied and Environmental Microbiology* 77, 4437-4445.

Tesoriero, A. J., Puckett, L. J. 2011. O₂ reduction and denitrification rates in shallow aquifers. *Water Resources Research* 47, DOI: 10.1029/2011WR010471.

Thomas, H. E., 1951. *The Conservation of Groundwater*. McGraw-Hill, New York.

Tiehm, A., Schmidt, K. R., Pfeifer, B., Heidinger, M., Ertl, S., 2008. Growth kinetics and stable carbon isotope fractionation during aerobic degradation of *cis*-1,2-dichloroethene and vinyl chloride. *Water Research* 42, 2431-2438.

Toth, J., 1963. A theoretical analysis of groundwater flow in small drainage basins. *Journal of Geophysical Research* 68, 4785-4812.

Townsend, G. T., Suflita, J. M., 1997. Influence of sulfur oxyanions on reductive dehalogenation activities in *Desulfomonile tiedjei*. *Applied and Environmental microbiology* 63, 3594-3599.

Trimmer, M., Grey, J., Heppell, C. M., Hildrew, A. G., Lansdown, K., Stahl, H., Yvon-Durocher, G., 2012., River bed carbon and nitrogen cycling: state of play and some new directions. *Science of the Total Environment* 434, 143-158.

Trimmer, M., Maanoja, S., Hildrew, A. G., Pretty, J. L., Grey, J., 2010. Potential carbon fixation via methane oxidation in well-oxygenated riverbed gravels. *Limnology and Oceanography* 55, 560.

Trimmer, M., Sanders, I. A., Heppell, C. M., 2009. Carbon and nitrogen cycling in a vegetated lowland chalk river impacted by sediment. *Hydrological Processes* 23, 2225-2238.

Triska, F. J., Duff, J. H., Avanzino, R. J., 1993. The role of water exchange between a stream channel and its hyporheic zone in nitrogen cycling at the terrestrial—aquatic interface. In *Nutrient Dynamics and Retention in Land/Water Ecotones of Lowland, Temperate Lakes and Rivers* Springer, Netherlands.

Triska, F. J., Kennedy, V. C., Avanzino, R. J., Zellweger, G. W., Bencala, K. E., 1989. Retention and transport of nutrients in a third-order stream in northwestern California: hyporheic processes. *Ecology* 70, 1893-1905.

Turncotte, D. L., Schubert, G., 1982. *Geodynamics: Applications of Continuum Physics to Geological Problems*. John Wiley & Sons.

U.S. Environmental Protection Agency, (USEPA)., 1991. Superfund NPL Characterization Project: National Results. U.S. Environmental Protection Agency, Office of Emergency and Remedial Response. EPA/540/8-91/069. U.S. Environmental Protection Agency, Washington, DC.

U.S. Environmental Protection Agency, (USEPA)., 1992. *Measurement of purgeable organic compounds in water by capillary gas chromatography/mass spectrometry, Method 524.2*. Environmental Monitoring Systems Laboratory Office of Research and Development. U.S. Environmental Protection Agency, Ohio.

U.S. Environmental Protection Agency, (USEPA)., 1995. *Contaminant specific fact sheets, Volatile organic chemicals-Technical version: EPA 811-F-95-004-T*. U.S. Environmental Protection Agency, Washington, DC.

U.S. Environmental Protection Agency, (USEPA)., 1996. *Soil screening guidance. U.S. Environmental Protection Agency, Office of Emergency and Remedial Response, EPA/540/R95/128*. U.S. Environmental Protection Agency, Washington, DC.

U.S. Environmental Protection Agency, (USEPA)., 2004. *Standard Operating Procedure – Sample Preparation and Calculations for Dissolved Gas Analysis Using a GC Headspace Equilibration Technique. RSKSOP-175*. USEPA, U.S. Environmental Protection Agency, Washington, DC. (Unpublished).

U.S. Geological Survey, (USGS)., 1998. *Occurrence and seasonal variability of volatile organic compounds in seven New Jersey streams. USGS Water-Resources Investigations Report, vol. 98-4074*. U.S. Geological Survey, Virginia.

Ullah, S., Zhang, H., Heathwaite, A. L., Binley, A., Lansdown, K., Heppell, K., Trimmer, M., 2012. In situ measurement of redox sensitive solutes at high spatial resolution in a riverbed using Diffusive Equilibrium in Thin Films (DET). *Ecological Engineering* 49, 18-26.

Ullah, S., Zhang, H., Heathwaite, A. L., Heppell, C., Lansdown, K., Binley, A., Trimmer, M., 2014. Influence of emergent vegetation on nitrate cycling in sediments of a groundwater-fed river. *Biogeochemistry* 118, 121-134.

Utkin, I., Woese, C., Wiegel, J., 1994. Isolation and characterization of *Desulfitobacterium dehalogenans* gen. nov., sp. nov., an anaerobic bacterium which reductively dechlorinates chlorophenolic compounds. *International Journal of Systematic Bacteriology* 44, 612-619.

Verce, M. F., Gunsch, C. K., Danko, A. S., Freedman, D. L., 2002. Cometabolism of *cis*-1,2 dichloroethene by aerobic cultures grown on vinyl chloride as the primary substrate. *Environmental Science and Technology* 36, 2171-2177

Vereecken, H., Binley, A., Cassiani, G., Revil, A., Titov, K., 2006. *Applied Hydrogeophysics*. Springer, The Netherlands.

Vidon, P., Hill, A. R., 2005. Denitrification and patterns of electron donors and acceptors in eight riparian zones with contrasting hydrogeology. *Biogeochemistry* 71, 259-283.

Vogel, T. M., Criddle, C. S., McCarty, P. L., 1987. Transformation of halogenated aliphatic compounds. *Environmental Science & Technology* 21, 722-736.

Voyce, K., 2008. Groundwater Management: the Shropshire Groundwater Scheme. *Proceedings of the Shropshire Geological Society* 14, 20-29.

Voyce, K., Environment Agency, *Personal Communication*.

Vrana, B., Allan, I. J., Greenwood, R., Mills, G. A., Dominiak, E., Svensson, K., Knutsson, J., Morrison, G., 2005. Passive sampling techniques for monitoring pollutants in water. *Trends in Analytical Chemistry* 24, 845-868.

Vroblesky, D. A., Campbell, T. R., 2001. Equilibration times, compound selectivity, and stability of diffusion samplers for collection of ground-water VOC concentrations. *Adv. Environ. Res.* 5, 1-12.

Vroblesky, D. A., Hyde, W. T., 1997. Diffusion samplers as an inexpensive approach to monitoring VOCs in ground water. *Ground Water Monitoring & Remediation* 17, 177-184.

Vroblesky, D. A., Lorah, M. M., Trimble, S. P., 1991. Mapping Zones of Contaminated Ground-Water Discharge Using Creek-Bottom-Sediment Vapour Samplers, Aberdeen Proving Ground, Maryland. *Ground Water* 29, 7-12.

Vroblesky, D., Rhodes, L., Robertson, J., Harrigan, J., 1996. Locating VOC Contamination in a Fractured-Rock Aquifer at the Ground-Water/Surface-Water Interface Using Passive Vapor Collectors. *Ground Water* 34, 223-230.

Vroblesky, D., Robertson, J., 1996. Temporal changes in VOC discharge to surface water from a fractured rock aquifer during well installation and operation, Greenville, South Carolina. *Ground Water Monitoring & Remediation* 16, 196-201.

Warrington, G., 1970. The stratigraphy and palaeontology of the 'Keuper' Series of the central Midlands of England. *Quarterly Journal of the Geological Society of London* 126, 183-223.

Weatherill, J., Krause, S., Voyce, K., Drijfhout, F., Levy, A., Cassidy, N., 2014. Nested monitoring approaches to delineate groundwater trichloroethene discharge to a UK lowland stream at multiple spatial scales. *Journal of Contaminant Hydrology* 158, 38-54.

Weaver, J. W., Wilson, J. T., Kampbell, D. H., 1997. Case study of natural attenuation of trichloroethene at St. Joseph, Michigan. *Proceedings of the Symposium on Natural Attenuation of Chlorinated Organics in Ground Water*. U. S. Environmental Protection Agency, Washington, DC.

Weber, W. J., McGinley, P. M., Katz, L. E., 1992. A distributed reactivity model for sorption by soils and sediments. 1. Conceptual basis and equilibrium assessments. *Environmental Science & Technology* 26, 1955-1962.

Weiss, J. V., Cozzarelli, I. M., 2008. Biodegradation in contaminated aquifers: incorporating microbial/molecular methods. *Ground Water* 46, 305-322.

Wentworth, C. K., 1922. A scale of grade and class terms for clastic sediments. *The Journal of Geology* 377-392.

Westbrook, S. J., Rayner, J. L., Davis, G. B., Clement, T. P., Bjerg, P. L., Fisher, S. J., 2005. Interaction between shallow groundwater, saline surface water and contaminant discharge at a seasonally and tidally forced estuarine boundary. *Journal of Hydrology* 302, 255-269.

Westrick, J. J., Mello, W., Thomas, R. F., 1984. The groundwater supply survey. *Journal of American Water Works Association*, 52-59.

Wheater, H. S., Peach, D., 2004. Developing interdisciplinary science for integrated catchment management: the UK lowland catchment research (LOCAR) programme. *Int. J. Water Resour. Dev.* 20, 369-385.

White, D.S., 1993. Perspectives of Defining and Delineating Hyporheic Zones. *Journal of North American Benthological Society*, 12, 61-69.

Wiedemeier, T. D. H., Swanson, M. A., Moutoux, D. E. Gordon, K., Wilson, J. T., Wilson, B. H., Kampbell, D. H., Haas, P. E., Miller, R. N., Hansen, J. E., Chapelle, F. H. 1998. *Technical Protocol for Evaluating Natural Attenuation of Chlorinated Solvents in Ground Water*, IAG: RW57936164. US Environmental Protection Agency, USA.

Wilson, J. T., Wilson, B. H., 1985. Biotransformation of trichloroethylene in soil. *Applied and Environmental Microbiology* 49, 242.

Winter, T. C., Harvey, J. W., Franke, O. L., Alley, W. M., 1998. Groundwater and surface water: A single resource. *USGS Circular 1139*. USGS, Washington DC.

Witt, M., Klecka, G., Lutz, E., Ei, T., Grosso, N., Chapelle, F., 2002. Natural attenuation of chlorinated solvents at Area 6, Dover Air Force Base: groundwater biogeochemistry. *J. Contam. Hydrol.* 57, 61-80.

Woessner, W. W., 2000. Stream and fluvial plain ground water interactions: rescaling hydrogeologic thought. *Ground Water* 38, 423-429.

World Health Organisation, (WHO), 2004. *Guidelines for drinking-water quality 3rd ed. Vol. 1. Recommendations*. World Health Organisation, Geneva.

Wright, J. F., Sutcliffe, D. W., Furse, M. T., 2000. Assessing the biological quality of freshwaters. *RIVPACS and other techniques*. *Freshwater Biological Association, Ambleside, England*. Centre for Ecology and Hydrology, Wallingford.

Wu, W. M., Nye, J., Jain, M. K., Hickey, R. F., 1998. Anaerobic dechlorination of trichloroethylene (TCE) to ethylene using complex organic materials. *Water Research* 32, 1445-1454.

Wymore, R. A., Lee, M. H., Keener, W. K., Miller, A. R., Colwell, F. S., Watwood, M. E., Sorenson Jr, K. S., 2007. Field evidence for intrinsic aerobic chlorinated ethene cometabolism by methanotrophs expressing soluble methane monooxygenase. *Bioremediation Journal*, 11, 125-139.

Wyness, A. J., Parkman, R. H., Neal, C., 2003. A summary of boron surface water quality data throughout the European Union. *Science of The Total Environment* 314, 255-269.

Yamamoto, K., Fukushima, M., Kakutani, N., Tsuruho, K., 2001. Contamination of vinyl chloride in shallow urban rivers in Osaka, Japan. *Water Res.* 35, 561-566.

Yang, J.-H., Lee, K.-K., Clement, T. P., 2012. Impact of seasonal variations in hydrological stresses and spatial variations in geologic conditions on a TCE plume at an industrial complex in Wonju, Korea. *Hydrological Processes* 26, 317-325.

Yang, Y., McCarty, P. L. 2000. Biomass, oleate, and other possible substrates for chloroethene reductive dehalogenation. *Bioremediation journal*, 4, 125-133.

Yu S. H., Dolan, M. E, Semprini, L., 2005. Kinetics and inhibition of reductive dechlorination of chlorinated ethylenes by two different mixed cultures. *Environ. Sci. Technol.* 39, 195–205.

Zarnetske, J. P., Haggerty, R., Wondzell, S. M., Baker, M. A., 2011. Dynamics of nitrate production and removal as a function of residence time in the hyporheic zone. *Journal of Geophysical Research: Biogeosciences* (2005–2012), 116(G1).

Zeigler, P. A., 1990. *Geological Atlas of Western and Central Europe*. Shell Nederland, The Hague.

9. Appendices

Appendix A Mini-piezometer location details

(A1) Locations details of all drive-point mini-piezometers used in this study (see Chapters 3, 4 and 6).

Name	Transect	Easting	Northing	Z*
		(m)	(m)	(m AOD)
MP1	D	363309.5	328873.3	57.929
MP2	D	363313.7	328877.4	57.799
MP3	D	363315.2	328882.6	57.902
MP4	TA	363319.2	328882.7	58.357
MP5	TA	363318.7	328883.6	58.236
MP6	TA/D	363318.3	328884.8	58.143
MP7	TA	363317.8	328886.1	58.074
MP8	TA	363317.2	328887.3	58.113
MP9	D	363324.0	328885.4	58.065
MP10		363322.3	328883.1	58.523
MP11	D	363320.1	328885.7	58.042
MP12	TB	363325.7	328882.0	58.607
MP13	TB	363326.4	328883.0	58.272
MP14	TB/D	363327.2	328884.5	57.964
MP15	TB	363328.0	328885.8	57.798
MP16	TB	363328.6	328887.0	57.98
MP17	D	363329.9	328882.2	57.884
MP18	D	363331.6	328879.4	58.339
MP19	D	363330.8	328875.5	58.422
MP20	D	363332.9	328876.9	58.453
MP21	D	363335.0	328878.2	58.298
MP22	D	363336.6	328865.4	58.393
MP23	D	363335.1	328872.1	58.338
MP24	D	363335.7	328869.5	57.808
MP25	D	363334.2	328874.6	57.93
MP26		363315.2	328892.8	59.43

*Elevation measured at riverbed level beside the piezometer.

Appendix B VHG-derived flux calculations

(B1) Calculated VHG-derived groundwater fluxes from the perspective of K_s and VHGs measured at 25 cm below riverbed level (shallow seepage area) for the Transect S piezometers. Shaded cells denote measured values. Un-shaded cells represent linear interpolations of K_s , VHG and TCE between neighbouring values, used to up-scale for the whole reach estimates. Refer to Sections 5.2 and 5.3 in Chapter 5 for the explanation of the terms.

Location	K_s ($m\ d^{-1}$)	x.y (m^2)	VHG ($m\ m^{-1}$)	q_z ($L\ d^{-1}\ m^{-2}$)	Q_z ($L\ d^{-1}$)	TCE ($\mu g\ L^{-1}$)	q_c ($\mu\ d^{-1}\ m^{-2}$)	Q_c ($\mu\ d^{-1}$)
SL1	0.903	10	0.107	96	964	4.3	410	4098
	0.808	10	0.116	93	935	5.9	549	5493
	0.712	7.5	0.125	89	666	7.5	666	4999
	0.616	7.5	0.134	82	619	9.1	753	5646
SL2	0.521	7.5	0.143	74	558	10.8	800	5999
	0.398	7.5	0.174	69	518	20.1	1388	10410
	0.275	10	0.205	56	563	29.4	1655	16545
	0.152	10	0.236	36	358	38.7	1387	13867
SL3	0.029	10	0.267	8	77	48.0	372	3716
	0.259	10	0.213	55	553	45.6	2521	25211
	0.490	10	0.160	78	784	43.1	3376	33757
	0.720	12.5	0.107	77	960	40.6	3118	38979
SL4	0.950	12.5	0.053	51	634	38.1	1932	24151
	1.086	12.5	0.049	54	670	38.0	2037	25463
	1.221	12.5	0.045	55	692	37.9	2100	26255
	1.356	12.5	0.041	56	701	37.9	2123	26531
	1.492	12.5	0.037	56	696	37.8	2104	26295
SL5	1.627	10	0.033	54	542	37.7	2044	20439
	1.782	12.5	0.028	50	631	30.4	1534	19178
	1.936	12.5	0.023	45	565	23.1	1044	13046
	2.091	10	0.018	38	383	15.8	606	6060
SL6	2.245	12.5	0.013	30	374	8.5	255	3187
	1.712	12.5	0.046	78	978	8.2	645	8062
	1.178	12.5	0.078	92	1150	8.0	733	9163
	0.644	12.5	0.110	71	889	7.7	548	6844
SL7	0.110	12.5	0.143	16	197	7.4	117	1460
	0.351	12.5	0.157	55	690	7.4	407	5090
	0.592	12.5	0.171	101	1269	7.3	745	9309
	0.833	12.5	0.186	155	1934	7.3	1129	14108
SL8	1.074	12.5	0.200	215	2685	7.3	1558	19475

(B2) Calculated VHG-derived groundwater fluxes from the perspective of K_s and VHGs measured at 44–85 cm below riverbed level (deep seepage area). Shaded cells denote measured values. Un-shaded cells represent linear interpolations of K_s , VHG and TCE between neighbouring values, used to up-scale for the whole reach estimates. Refer to Sections 5.2 and 5.3 in Chapter 5 for the explanation of the terms.

Location	K_s	A	VHG	q_z	Q_z	TCE	q_c	Q_c
	(m d ⁻¹)	(m ²)	(m m ⁻¹)	(L d ⁻¹ m ⁻²)	(L d ⁻¹)	(μg L ⁻¹)	(μ d ⁻¹ m ⁻²)	(μ d ⁻¹)
SL1	0.172	10	0.447519	77	770	4.3	327	3275
	0.400	10	0.444954	178	1781	5.9	1047	10467
	0.628	7.5	0.44239	278	2085	7.5	2086	15642
	0.856	7.5	0.439825	377	2825	9.1	3438	25788
SL2	1.085	7.5	0.437261	474	3557	10.8	5100	38247
	0.835	7.5	0.414668	346	2596	20.1	6951	52129
	0.585	10	0.392075	229	2294	29.4	6745	67454
	0.335	10	0.369482	124	1239	38.7	4800	47998
SL3	0.086	10	0.346889	30	297	48.0	1429	14294
	0.158	10	0.375047	59	592	45.6	2698	26981
	0.230	10	0.403204	93	927	43.1	3996	39956
	0.302	12.5	0.431362	130	1629	40.6	5291	66143
SL4	0.374	12.5	0.45952	172	2150	38.1	6555	81943
	0.489	12.5	0.420326	205	2567	38.0	7810	97623
	0.603	12.5	0.381132	230	2872	37.9	8719	108982
	0.717	12.5	0.341938	245	3065	37.9	9284	116048
	0.831	12.5	0.302745	252	3147	37.8	9508	118851
SL5	0.946	10	0.263551	249	2493	37.7	9394	93935
	1.055	12.5	0.216046	228	2848	30.4	6926	86574
	1.164	12.5	0.168541	196	2452	23.1	4531	56637
	1.273	10	0.121037	154	1540	15.8	2435	24353
SL6	1.382	12.5	0.073532	102	1270	8.5	865	10816
	1.049	12.5	0.211573	222	2773	8.2	1829	22860
	0.716	12.5	0.349613	250	3127	8.0	1994	24921
	0.382	12.5	0.487653	186	2331	7.7	1435	17942
SL7	0.049	12.5	0.625694	31	386	7.4	229	2866
	0.485	12.5	0.609094	296	3695	7.4	2182	27274
	0.921	12.5	0.592493	546	6824	7.3	4006	50075
	1.357	12.5	0.575893	782	9771	7.3	5703	71293
SL8	1.793	12.5	0.559293	1003	12537	7.3	7276	90950

Appendix C Temperature-derived flux calculations

(C1) Calculated vertical groundwater fluxes from temperature measurements. T1–T23 refers to the temperature transect number and the measurement position along transect (0–5 m) is indicated in the top left corner. The number of measurements per transect varies with channel width. See Chapter 5 for the meaning of the terms and locations of temperature transects. Refer to Section 5.3 in Chapter 5 for the explanation of the terms.

0 m	T₀	T_Z	T_L	T_Z-T_L	T₀-T_L	ln(T_Z-T_L/T₀-T_L)	K_{fs}	ρ_rC_fZ	q_z
	(°C)	(°C)	(°C)	(°C)	(°C)	Ln(°C)	(J s ⁻¹ m ⁻¹ K ⁻¹)	(J m ⁻³ K ⁻¹)	(L d ⁻¹ m ⁻²)
T1	15.09	13.62	9.91	3.71	5.18	-0.34	1.45	838000	50.09
T2	15.09	12.05	9.91	2.14	5.18	-0.88	1.45	838000	132.26
T3	15.09	13.28	9.91	3.37	5.18	-0.43	1.45	838000	64.33
T4	15.09	11.76	9.91	1.85	5.18	-1.03	1.45	838000	154.11
T5	15.09	12.03	9.91	2.12	5.18	-0.90	1.45	838000	134.02
T6	15.09	11.71	9.91	1.80	5.18	-1.06	1.45	838000	158.13
T7	15.09	12.12	9.91	2.21	5.18	-0.85	1.45	838000	127.32
T8	15.09	11.20	9.91	1.29	5.18	-1.39	1.45	838000	207.93
T9	15.09	13.09	9.91	3.18	5.18	-0.49	1.45	838000	73.14
T10	15.09	13.38	9.91	3.47	5.18	-0.40	1.45	838000	60.13
T11	15.09	13.23	9.91	3.32	5.18	-0.44	1.45	838000	66.47
T12	15.09	13.21	9.91	3.30	5.18	-0.45	1.45	838000	67.56
T13	15.09	14.03	9.91	4.12	5.18	-0.23	1.45	838000	34.48
T14	15.09	13.64	9.91	3.73	5.18	-0.33	1.45	838000	49.12
T15	15.09	13.79	9.91	3.88	5.18	-0.29	1.45	838000	43.46
T16	15.09	14.34	9.91	4.43	5.18	-0.16	1.45	838000	23.59
T17	15.09	14.39	9.91	4.48	5.18	-0.15	1.45	838000	21.98
T18	15.09	14.33	9.91	4.42	5.18	-0.16	1.45	838000	23.76
T19	15.09	13.52	9.91	3.61	5.18	-0.36	1.45	838000	54.01
T20	15.09	12.10	9.91	2.19	5.18	-0.86	1.45	838000	128.95
T21	15.09	12.97	9.91	3.06	5.18	-0.53	1.45	838000	78.90
T22	15.09	13.19	9.91	3.28	5.18	-0.46	1.45	838000	68.65
T23	15.09	14.10	9.91	4.19	5.18	-0.21	1.45	838000	31.74

1 m	T₀	T_Z	T_L	T_Z-T_L	T₀-T_L	ln(T_Z-T_L/T₀-T_L)	K_{fs}	p_rc_fz	q_z
	(°C)	(°C)	(°C)	(°C)	(°C)	Ln(°C)	(J s ⁻¹ m ⁻¹ K ⁻¹)	(J m ⁻³ K ⁻¹)	(L d ⁻¹ m ⁻²)
T1	15.09	11.01	9.91	1.10	5.18	-1.55	1.45	838000	232.44
T2	15.09	11.54	9.91	1.63	5.18	-1.16	1.45	838000	172.96
T3	15.09	12.44	9.91	2.53	5.18	-0.72	1.45	838000	107.41
T4	15.09	12.78	9.91	2.87	5.18	-0.59	1.45	838000	88.65
T5	15.09	13.09	9.91	3.18	5.18	-0.49	1.45	838000	73.14
T6	15.09	11.49	9.91	1.58	5.18	-1.19	1.45	838000	177.43
T7	15.09	10.83	9.91	0.92	5.18	-1.72	1.45	838000	257.82
T8	15.09	12.39	9.91	2.48	5.18	-0.74	1.45	838000	110.28
T9	15.09	12.73	9.91	2.82	5.18	-0.61	1.45	838000	91.17
T10	15.09	12.94	9.91	3.03	5.18	-0.54	1.45	838000	80.23
T11	15.09	13.62	9.91	3.71	5.18	-0.34	1.45	838000	50.09
T12	15.09	13.76	9.91	3.85	5.18	-0.30	1.45	838000	44.39
T13	15.09	13.02	9.91	3.11	5.18	-0.51	1.45	838000	76.57
T14	15.09	12.82	9.91	2.91	5.18	-0.58	1.45	838000	86.16
T15	15.09	13.95	9.91	4.04	5.18	-0.25	1.45	838000	37.12
T16	15.09	14.43	9.91	4.52	5.18	-0.14	1.45	838000	20.38
T17	15.09	14.27	9.91	4.36	5.18	-0.17	1.45	838000	26.01
T18	15.09	14.27	9.91	4.36	5.18	-0.17	1.45	838000	26.01
T19	15.09	12.75	9.91	2.84	5.18	-0.60	1.45	838000	89.90
T20	15.09	12.87	9.91	2.96	5.18	-0.56	1.45	838000	83.72
T21	15.09	11.95	9.91	2.04	5.18	-0.93	1.45	838000	139.20
T22	15.09	13.45	9.91	3.54	5.18	-0.38	1.45	838000	57.06
T23	15.09	13.52	9.91	3.61	5.18	-0.36	1.45	838000	54.01

z m	T₀	T_Z	T_L	T_Z-T_L	T₀-T_L	ln(T_Z-T_L/T₀-T_L)	K_{fs}	p_rc_fz	q_z
	(°C)	(°C)	(°C)	(°C)	(°C)	Ln(°C)	(J s ⁻¹ m ⁻¹ K ⁻¹)	(J m ⁻³ K ⁻¹)	(L d ⁻¹ m ⁻²)
T1	15.09	12.85	9.91	2.94	5.18	-0.57	1.45	838000	84.93
T2	15.09	11.93	9.91	2.02	5.18	-0.94	1.45	838000	140.97
T3	15.09	12.82	9.91	2.91	5.18	-0.58	1.45	838000	86.16
T4	15.09	13.14	9.91	3.23	5.18	-0.47	1.45	838000	70.86
T5	15.09	12.75	9.91	2.84	5.18	-0.60	1.45	838000	89.90
T6	15.09	13.09	9.91	3.18	5.18	-0.49	1.45	838000	73.24
T7	15.09	12.87	9.91	2.96	5.18	-0.56	1.45	838000	83.72
T8	15.09	12.51	9.91	2.60	5.18	-0.69	1.45	838000	103.21
T9	15.09	13.47	9.91	3.56	5.18	-0.37	1.45	838000	56.05
T10	15.09	13.83	9.91	3.92	5.18	-0.28	1.45	838000	41.62
T11	15.09	13.91	9.91	4.00	5.18	-0.26	1.45	838000	38.90
T12	15.09	13.81	9.91	3.90	5.18	-0.28	1.45	838000	42.54
T13	15.09	13.43	9.91	3.52	5.18	-0.39	1.45	838000	58.08
T14	15.09	12.85	9.91	2.94	5.18	-0.57	1.45	838000	84.93
T15	15.09	12.80	9.91	2.89	5.18	-0.58	1.45	838000	87.40
T16	15.09	14.31	9.91	4.40	5.18	-0.16	1.45	838000	24.37
T17	15.09	14.07	9.91	4.16	5.18	-0.22	1.45	838000	32.75
T18	15.09	13.69	9.91	3.78	5.18	-0.32	1.45	838000	47.21
T19	15.09	12.85	9.91	2.94	5.18	-0.57	1.45	838000	84.93
T20	15.09	13.55	9.91	3.64	5.18	-0.35	1.45	838000	53.02
T21	15.09	13.04	9.91	3.13	5.18	-0.50	1.45	838000	75.42
T22	15.09	13.57	9.91	3.66	5.18	-0.35	1.45	838000	52.03
T23	15.09	13.52	9.91	3.61	5.18	-0.36	1.45	838000	54.01

3 m	T₀	T_Z	T_L	T_Z-T_L	T₀-T_L	ln(T_Z-T_L/T₀-T_L)	K_{fs}	p_rc_fz	q_z
	(°C)	(°C)	(°C)	(°C)	(°C)	Ln(°C)	(J s ⁻¹ m ⁻¹ K ⁻¹)	(J m ⁻³ K ⁻¹)	(L d ⁻¹ m ⁻²)
T1	15.09	13.40	9.91	3.49	5.18	-0.40	1.45	838000	59.10
T2	15.09	11.49	9.91	1.58	5.18	-1.19	1.45	838000	177.43
T3	15.09	11.30	9.91	1.39	5.18	-1.32	1.45	838000	197.10
T4	15.09	11.88	9.91	1.97	5.18	-0.97	1.45	838000	144.64
T5	15.09	11.96	9.91	2.05	5.18	-0.93	1.45	838000	139.05
T6	15.09	12.03	9.91	2.12	5.18	-0.90	1.45	838000	134.02
T7	15.09	12.30	9.91	2.39	5.18	-0.78	1.45	838000	115.93
T8	15.09	13.55	9.91	3.64	5.18	-0.35	1.45	838000	53.02
T9	15.09	12.39	9.91	2.48	5.18	-0.74	1.45	838000	110.52
T10	15.09	13.64	9.91	3.73	5.18	-0.33	1.45	838000	49.12
T11	15.09	13.52	9.91	3.61	5.18	-0.36	1.45	838000	54.01
T12	15.09	13.79	9.91	3.88	5.18	-0.29	1.45	838000	43.46
T13	15.09	14.03	9.91	4.12	5.18	-0.23	1.45	838000	34.48
T14	15.09	12.27	9.91	2.36	5.18	-0.79	1.45	838000	117.76
T15	15.09	13.14	9.91	3.23	5.18	-0.47	1.45	838000	70.86
T16	15.09	13.40	9.91	3.49	5.18	-0.40	1.45	838000	59.10
T17	15.09	12.34	9.91	2.43	5.18	-0.76	1.45	838000	113.26
T18	15.09	14.07	9.91	4.16	5.18	-0.22	1.45	838000	32.75
T19	15.09	13.76	9.91	3.85	5.18	-0.30	1.45	838000	44.39
T20	15.09	13.76	9.91	3.85	5.18	-0.30	1.45	838000	44.39
T21	15.09	13.04	9.91	3.13	5.18	-0.50	1.45	838000	75.42
T22	15.09	13.64	9.91	3.73	5.18	-0.33	1.45	838000	49.12
T23	15.09	13.83	9.91	3.92	5.18	-0.28	1.45	838000	41.62

4 m	T ₀	T _Z	T _L	T _Z -T _L	T ₀ -T _L	ln(T _Z -T _L /T ₀ -T _L)	K _{fs}	p _r c _f z	q _z
	(°C)	(°C)	(°C)	(°C)	(°C)	Ln(°C)	(J s ⁻¹ m ⁻¹ K ⁻¹)	(J m ⁻³ K ⁻¹)	(L d ⁻¹ m ⁻²)
T1	15.09	13.06	9.91	3.15	5.18	-0.50	1.45	838000	74.28
T2	15.09	11.27	9.91	1.36	5.18	-1.34	1.45	838000	199.71
T7	15.09	13.69	9.91	3.78	5.18	-0.32	1.45	838000	47.21
T8	15.09	14.31	9.91	4.40	5.18	-0.16	1.45	838000	24.37
T9	15.09	14.44	9.91	4.53	5.18	-0.14	1.45	838000	20.28
T10	15.09	14.36	9.91	4.45	5.18	-0.15	1.45	838000	22.78
T11	15.09	13.52	9.91	3.61	5.18	-0.36	1.45	838000	54.01
T12	15.09	12.65	9.91	2.74	5.18	-0.64	1.45	838000	95.10
T13	15.09	13.57	9.91	3.66	5.18	-0.35	1.45	838000	52.03
T14	15.09	12.27	9.91	2.36	5.18	-0.79	1.45	838000	117.76
T15	15.09	13.47	9.91	3.56	5.18	-0.37	1.45	838000	56.05
T16	15.09	13.47	9.91	3.56	5.18	-0.37	1.45	838000	56.05
T17	15.09	13.28	9.91	3.37	5.18	-0.43	1.45	838000	64.33
T18	15.09	14.48	9.91	4.57	5.18	-0.13	1.45	838000	18.81
T19	15.09	14.10	9.91	4.19	5.18	-0.21	1.45	838000	31.89
T20	15.09	13.33	9.91	3.42	5.18	-0.42	1.45	838000	62.30
T21	15.09	13.79	9.91	3.88	5.18	-0.29	1.45	838000	43.50
T22	15.09	12.15	9.91	2.24	5.18	-0.84	1.45	838000	125.64
T23	15.09	14.17	9.91	4.26	5.18	-0.20	1.45	838000	29.34

5 m	T ₀	T _Z	T _L	T _Z -T _L	T ₀ -T _L	ln(T _Z -T _L /T ₀ -T _L)	K _{fs}	p _r c _f z	q _z
	(°C)	(°C)	(°C)	(°C)	(°C)	Ln(°C)	(J s ⁻¹ m ⁻¹ K ⁻¹)	(J m ⁻³ K ⁻¹)	(L d ⁻¹ m ⁻²)
T12	15.09	14.36	9.91	4.45	5.18	-0.15	1.45	838000	22.78
T13	15.09	14.24	9.91	4.33	5.18	-0.18	1.45	838000	26.83
T14	15.09	14.22	9.91	4.31	5.18	-0.19	1.45	838000	27.66
T15	15.09	13.93	9.91	4.02	5.18	-0.25	1.45	838000	38.01
T16	15.09	13.40	9.91	3.49	5.18	-0.40	1.45	838000	59.10
T17	15.09	13.50	9.91	3.59	5.18	-0.37	1.45	838000	55.05
T19	15.09	14.70	9.91	4.79	5.18	-0.08	1.45	838000	11.90
T20	15.09	13.28	9.91	3.37	5.18	-0.43	1.45	838000	64.33
T21	15.09	14.07	9.91	4.16	5.18	-0.22	1.45	838000	32.75
T22	15.09	14.04	9.91	4.13	5.18	-0.23	1.45	838000	34.12
T23	15.09	14.40	9.91	4.49	5.18	-0.14	1.45	838000	21.44

(C2) Calculated volumetric groundwater fluxes from each temperature measurement used for baseflow flux estimate. T1–T23 refers to the temperature transect number and 0–5 m indicates the measurement position along the transect. See Section 5.3 in Chapter 5 for further details.

	0 m	1 m	2 m	3 m	4 m	5 m
	(L d ⁻¹)					
T1	125.2	581.1	212.3	147.8	185.7	nd
T2	330.7	432.4	352.4	443.6	499.3	nd
T3	160.8	268.5	215.4	492.7	nd	nd
T4	385.3	221.6	177.1	361.6	nd	nd
T5	335.1	182.9	224.8	347.6	nd	nd
T6	395.3	443.6	183.1	335.1	nd	nd
T7	318.3	644.6	209.3	289.8	118.0	nd
T8	519.8	275.7	258.0	132.5	60.9	nd
T9	182.9	227.9	140.1	276.3	50.7	nd
T10	150.3	200.6	104.1	122.8	57.0	nd
T11	166.2	125.2	97.3	135.0	135.0	nd
T12	168.9	111.0	106.3	108.7	237.7	57.0
T13	86.2	191.4	145.2	86.2	130.1	67.1
T14	122.8	215.4	212.3	294.4	294.4	69.2
T15	108.7	92.8	218.5	177.1	140.1	95.0
T16	59.0	51.0	60.9	147.8	140.1	147.8
T17	54.9	65.0	81.9	283.2	160.8	137.6
T18	59.4	65.0	118.0	81.9	47.0	nd
T19	135.0	224.8	212.3	111.0	79.7	29.8
T20	322.4	209.3	132.5	111.0	155.8	160.8
T21	197.2	348.0	188.6	188.6	108.8	81.9
T22	171.6	142.7	130.1	122.8	314.1	85.3
T23	79.4	135.0	135.0	104.1	73.3	53.6

(C3) Calculated TCE mass fluxes from each temperature measurement used for baseflow flux estimate. T1–T23 refers to the temperature transect number and 0–5 m indicates the measurement position along the transect. See Section 5.3 in Chapter 5 for further details.

	TCE	0 m	1 m	2 m	3 m	4 m	5 m
	($\mu\text{g L}^{-1}$)	($\mu\text{g d}^{-1}$)					
T1	4.25	532.6	2471.5	903.1	628.4	789.8	nd
T2	5.88	1943.7	2541.8	2071.6	2607.4	2934.8	nd
T3	7.50	1206.7	2014.9	1616.2	3697.1	nd	nd
T4	9.13	3517.0	2022.9	1617.0	3300.7	nd	nd
T5	10.75	3602.9	1966.4	2416.9	3738.1	nd	nd
T6	20.08	7937.0	8905.7	3676.1	6726.9	nd	nd
T7	29.40	9358.2	18950.6	6153.6	8521.5	3470.2	nd
T8	38.73	20130.8	10676.6	9992.4	5132.8	2359.3	nd
T9	48.05	8786.4	10951.8	6732.9	13276.2	2436.6	nd
T10	45.57	6850.1	9138.9	4741.4	5595.7	2595.3	nd
T11	43.08	7159.9	5394.7	4190.2	5817.0	5817.0	nd
T12	40.60	6857.2	4505.6	4317.7	4411.4	9652.3	nd
T13	38.12	3285.7	7296.6	5534.3	3285.7	4958.4	2312.4
T14	38.03	4670.3	8192.0	8075.4	11196.4	11196.4	2557.0
T15	37.94	4122.8	3521.1	8290.7	6721.7	5317.0	2630.2
T16	37.86	2232.8	1929.2	2306.5	5593.7	5304.9	3605.5
T17	37.77	2075.4	2455.9	3092.3	10695.7	6074.8	5593.7
T18	37.69	2238.5	2450.3	4448.0	3085.2	1771.7	5198.0
T19	8.52	1149.9	1914.2	1808.4	945.1	678.9	nd
T20	8.24	2657.3	1725.3	1092.6	914.8	1284.0	253.4
T21	7.97	1572.0	2773.4	1502.7	1502.7	866.7	1325.7
T22	7.70	1320.9	1097.9	1001.2	945.1	2417.3	652.5
T23	7.42	589.1	1002.2	1002.2	772.4	544.4	656.4

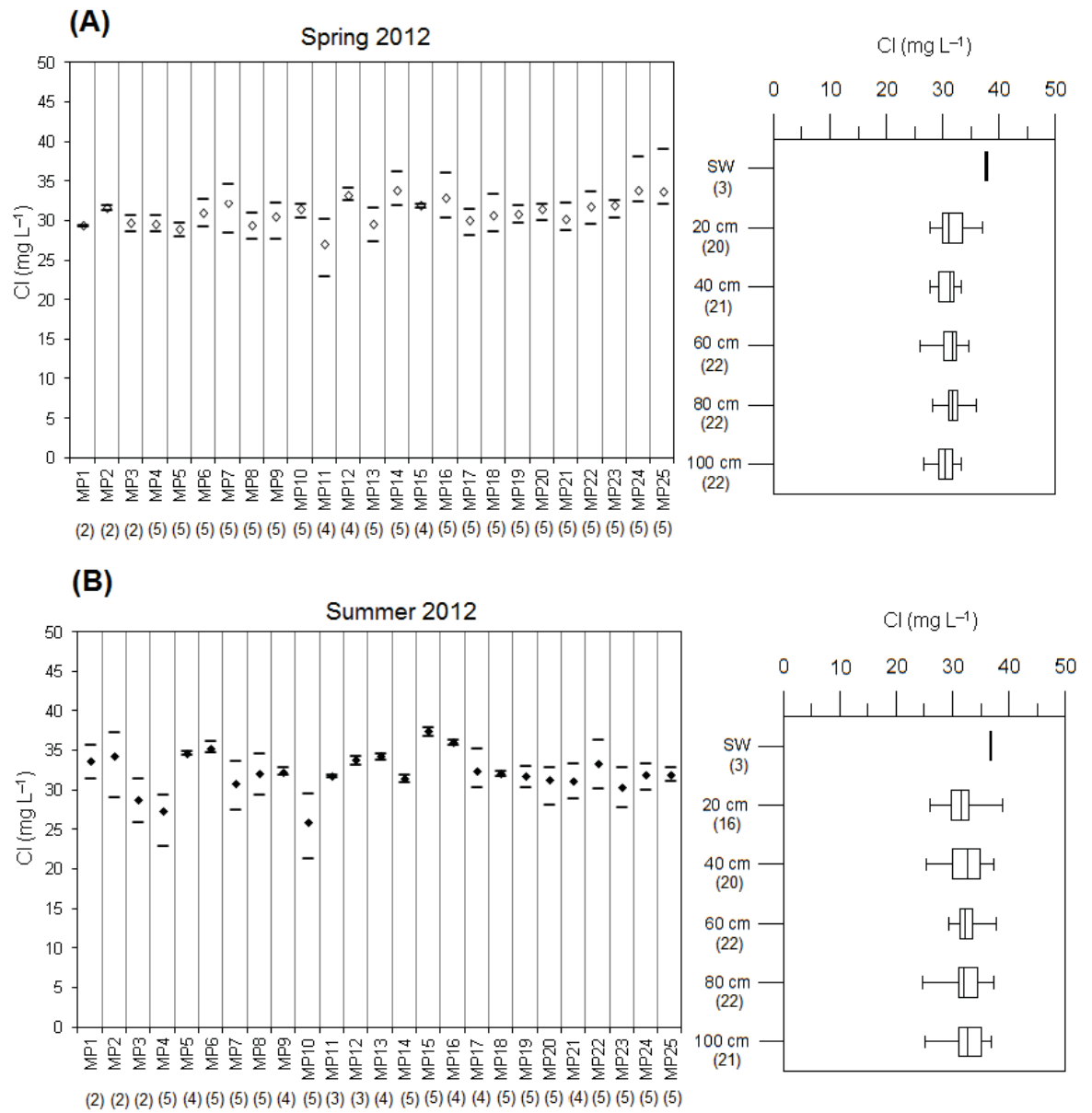
Appendix D Supplementary water quality data

(D1) Final pH and electrical conductivity (EC) measured in-situ during sampling of alluvial monitoring network for the spring and summer 2012 snapshot campaigns. pH and EC measured during the HydraSleeve campaign in the Permo-Triassic sandstone also included. See Section 6.3 in Chapter 6 for further details.

	March 2012		August 2012	
	pH (pH units)	EC ($\mu\text{S cm}^{-1}$)	pH (pH units)	EC ($\mu\text{S cm}^{-1}$)
Location				
BH1	7.52	1145	7.04	1102
BH2	7.01	731	6.92	720
BH3	7.12	684	7.2	701
BH4	7.19	598	7.08	561
BH5	7.23	517	7.07	545
BH6	7.34	434	7.12	498
BH7	7.21	457	7.14	513
BH8	7.48	415	7.66	423
BH9	7.68	449	7.94	481
BH10	7.26	509	7.03	506
BH11	7.35	521	7.63	564
BH12	7.16	590	7.58	593
BH13	7.39	541	7.15	584
BH14	7.36	466	nd	nd
Drainage ditch	7.45	510	7.01	534
Seepage zone	7.54	693	7.49	789
MP26 20 cm	6.99	664	7.07	621
MP26 100 cm	6.96	587	7.03	688
River Tern	7.94	755	7.96	792
<i>Permo-Triassic sandstone</i>				
HBE	7.1	753	nd	nd
HBW	7.31	661	nd	nd
HGO 20m	7.79	498	nd	nd
HGO 40m	7.68	502	nd	nd
HGA 35 m	7.64	623	nd	nd
HGA 50 m	7.55	556	nd	nd
HGA 80 m	7.46	545	nd	nd

nd = no data available

(D2) Chloride (Cl^-) data for the riverbed mini-piezometer samples showing reach-scale variability and depth variability for **(A)** Spring 2012 snapshot **(B)** Summer 2012 snapshot. See Section 6.3 in Chapter 6 for further details.



Appendix E Correlation matrices

(E1) Spearman's rank correlation between N_{Cl} and redox variables and between redox variables for reach-scale samples (mini-piezometers and alluvial monitoring points where $N_{Cl} = <3$) over both Spring and Summer 2012 snapshots. See Section 6.3 in Chapter 6 for further details.

		N_{Cl}	DO	NO_3	SO_4	CH_4	DOC
N_{Cl}	Spearman Correlation	1	.132	.482	.201	-.307	-.544
	p (2-tailed)	.	.496	.008	.295	.105	.029
	N	29	29	29	29	29	16
DO	Spearman Correlation	.132	1	.249	.033	-.068	.121
	p (2-tailed)	.496	.	.193	.865	.726	.656
	N	29	29	29	29	29	16
NO_3	Spearman Correlation	.482	.249	1	.312	-.293	-.576
	p (2-tailed)	.008	.193	.	.099	.123	.019
	N	29	29	29	29	29	16
SO_4	Spearman Correlation	.201	.033	.312	1	-.446	-.326
	p (2-tailed)	.295	.865	.099	.	.015	.217
	N	29	29	29	29	29	16
CH_4	Spearman Correlation	-.307	-.068	-.293	-.446	1	.662
	p (2-tailed)	.105	.726	.123	.065	.	.005
	N	29	29	29	29	29	16
DOC	Spearman Correlation	-.544	.121	-.576	-.326	.662	1
	p (2-tailed)	.029	.656	.019	.217	.005	.
	N	16	16	16	16	16	16

N = number of samples

(E2) Pearson's correlation between Log₁₀-transformed redox variables for plot-scale samplers. See Section 6.3 in Chapter 6 for further details.

		DO	NO₃	SO₄	Mn	CH₄	DOC
DO	Pearson Correlation	1	-.028	.109	-.071	.086	.240
	p (2-tailed)		.884	.539	.695	.629	.171
	N	34	30	34	33	34	34
NO₃	Pearson Correlation	-.028	1	-.064	-.391	-.515	-.451
	p (2-tailed)	.884		.736	.036	.004	.012
	N	30	30	30	29	30	30
SO₄	Pearson Correlation	.109	-.064	1	-.199	-.274	-.097
	p (2-tailed)	.539	.736		.268	.117	.586
	N	34	30	34	33	34	34
Mn	Pearson Correlation	-.071	-.391	-.199	1	.698	.465
	p (2-tailed)	.695	.036	.268		.000	.006
	N	33	29	33	33	33	33
CH₄	Pearson Correlation	.086	-.515	-.274	.698	1	.502
	p (2-tailed)	.629	.004	.117	.000		.002
	N	34	30	34	33	34	34
DOC	Pearson Correlation	.240	-.451	-.097	.465	.502	1
	p (2-tailed)	.171	.012	.586	.006	.002	
	N	34	30	34	33	34	34

N = number of samples